The Dissertation Committee for Raquel Angelina Martinez
Certifies that this is the approved version of the following Dissertation:

The Demographics and Circumplanetary Disk Properties of Wide Planetary Mass Companions: A Comprehensive Study of *Spitzer*/IRAC Archival Data

Committee:

Adam Kraus, Supervisor

Brendan Bowler

Neal Evans

Dan Jaffe

Kaitlin Kratter

The Demographics and Circumplanetary Disk Properties of Wide Planetary Mass Companions: A Comprehensive Study of *Spitzer*/IRAC Archival Data

by

Raquel Angelina Martinez

Dissertation

Presented to the Faculty of the Graduate School

of The University of Texas at Austin

in Partial Fulfillment

of the Requirements

for the Degree of

Doctor of Philosophy

The University of Texas at Austin

August 2021

Acknowledgments

First, I would like to acknowledge the generous funding support I have received from the Donald D. Harrington Fellows Program, a fellowship I have held my entire time at UT Austin that was truly icing on the cake after I chose to come here. Not only did the fellowship allow me to live comfortably in Austin, but it allowed me to pursue whatever research interests I wanted and introduced me to many amazing scholars in other disciplines at UT. I would also like to acknowledge support from the NASA Earth & Space Science Fellowship program that awarded me the funding to pursue the bulk of this dissertation research.

I would like to thank my committee members Drs. Brendan Bowler, Neal Evans, Dan Jaffe, and Kaitlin Kratter for their guidance over the years. And of course, I will forever be grateful to my advisor, Dr. Adam Kraus, for learning the ins and outs of this department with me as his first recruited student. I am thankful for his mentorship, advocacy, vast astronomy knowledge, and once removed from the stress of looming deadlines, the copious amounts of feedback he has given on any proposal, paper, or piece of writing of mine (this dissertation included), that has undoubtedly prepared me well for the future.

Of the 211 astronomy Ph.D.s granted from U.S. institutions in 2018, the number awarded to women who also identify as Black, African-American or Hispanic/Latinx could be counted on two hands with fingers to spare. This statistic is not due to a lack of science interest or aptitude among Black, Indigenous, and People of Color–it instead speaks to the hurdles and barriers we encounter during the pursuit of an astronomy career. I was very fortunate to land in a department with so many members that were willing to join me in fighting to mitigate and eliminate the toxic environments and relationships that disproportionately cause BIPOC scientists to leave the field. I am so proud of the work I've done with Astronomy on Tap ATX, Girl Day, Women in Astronomy, the TAURUS Program, ISEE PDP, and the Equity & Inclusion Group, and I look forward to hearing about how these activities and causes have carried on after I'm gone. I'd especially like to thank Dr. Caitlin Casey for encouraging my involvement with many of these initiatives, and modeling the type of well-rounded professor I can see myself being. Also, a huge thanks to Dr. Brandon Bozek for his friendship and support with everything

I pursued inside and outside of academia.

One of the things that drew me to the UT Austin Department of Astronomy was the collegial and friendly environment of its graduate students. I have had so many fun times with the friends I have made in this department, as well as others all over campus, who have been there for some of the highest of highs, and a few of the lowest of lows. I am grateful for my cohort Briana Indahl, Benjamin Kidder and Rebecca Tippens for being instant friends and navigating this department with me. I'll miss the sense of adventure and humor of many of the graduate students and postdocs that I've been lucky enough to meet while at UT, including Dreia Carrillo, Jackie Champagne, Sam Factor, Danny Krolikowski, Jessica Luna, Justin Spilker, Sydney Sherman, Matt Stevans, Ben Tofflemire, Zac Vanderbosch, and Jorge Zavala. I also want to thank (and congratulate!) my dear friend Dr. Sinclaire Manning for the many nights of Love Island, sporting events, restaurants, and vent sessions we've had over the years. While I am sad to be leaving all these wonderful people, I look forward to crossing paths in the future and picking up right where we left off.

Lastly, I would like to acknowledge my family back in California and friends all over for their continued love and support during my time deep in the heart of Texas. I am especially thankful for my parents, Ed & Margie, for setting such a great example in how to love, encourage, and support one's family. To my siblings, David & Rosie, thank you for always being there for when I needed a break from the stressors of academia. It has been tough being away from my loved ones the past seven years, especially with the pandemic limiting how much I could see and hug them toward the end, but I cannot wait to be close again very soon.

Abstract

The Demographics and Circumplanetary Disk Properties of Wide Planetary Mass Companions: A Comprehensive Study of *Spitzer*/IRAC Archival Data

Raquel Angelina Martinez, Ph.D.

The University of Texas at Austin, 2021

Supervisor: Adam Kraus

Over the past decade, a growing population of planetary-mass companions (<20 $M_{\rm Jup}$; PMCs) orbiting young stars have been discovered. They are located at wide separations (>100 au) from their young host stars, challenging models of star and planet formation. It is unclear whether these systems represent the low-mass extreme of stellar binary formation, or the high-mass and wide-orbit extreme of planet formation theories, as various formation pathways inadequately explain their physical and orbital aspects. Determining which scenario best reproduces the observed characteristics of PMCs will come once a statistically robust sample of directly imaged planets are found and studied. PMC systems also provide an opportunity to witness planet assembly, thus characterizing the spectral energy distributions of PMCs will help with future interpretation of exoplanet observations.

The extensive *Spitzer*/IRAC data set of nearby young populations has great potential to be mined for wide companions to stars. For my thesis, I developed an automated pipeline to find faint PMCs via point spread function (PSF) subtraction in existing *Spitzer*/IRAC images. I identified candidates for further study and pursued follow-up observations of candidate companion systems as I endeavored to

leverage the wealth of *Spitzer* images to find undiscovered companions.

I discovered two wide-orbit substellar companion systems and described characterization efforts of them. I measured the mid-infrared photometry of 16 wide-orbit companions, compared them to brown dwarfs in star-forming regions and the field, and determined the global disk frequency of young (<15 Myr) wide companions with low masses to be high ($56\% \pm 12\%$). I determined that my PSF-subtraction infrastructure is sensitive to $\sim$2 $M_{\rm Jup}$ companions at ρ>300 au. I also expanded my search for companions to the Taurus star-forming region, constraining the frequency of 0.5–30 $M_{\rm Jup}$ companions on semi-major axes 50–5000 au to <3.7% at a 95% confidence level.

My thesis has set the stage to reveal the demographics of wide-orbit PMCs from which better constraints on the models of extreme binary star and planet formation will emerge, ultimately enhancing our understanding of where these systems come from, how they evolve, and where they fit into the paradigm of star and planet formation.

Table of Contents

List of Tables

List of Figures

Chapter 1: Introduction

Looking back at the research I have pursued on my way toward a Ph.D., a common theme emerges. I have sought to understand the various stages of star and planet formation at their extremes: from high mass stars to objects in the substellar mass regime; from the youngest binaries to systems in the final stages of forming planets; from interesting individual systems to building samples for demographic studies. In this thesis I will present three studies focusing on my work to understand **planetary-mass companions** (M<20 $M_{\rm Jup}$; hereafter **PMCs**) on wide orbits ($a\gtrsim$100 au), an enigmatic population of astrophysical objects that straddles the definition of what is a low-mass brown dwarf and what is a high-mass planet.

The earliest direct-imaging surveys for planetary-mass and brown dwarf companions targeted members of young, nearby stellar associations to more easily detect bright, newly-formed exoplanets a few tens of au away from their hosts. This strategy proved successful with the discovery of 2MASSW J1207334–393254 b, more commonly known as 2M1207 b, the first directly-imaged planetary-mass companion from the VLT/NACO deep imaging survey of austral stars (Chauvin et al. 2004; 2005a; 2010). Ultimately, this survey observed 88 stars finding a total of 3 companions below 25 $M_{\rm Jup}$. Soon thereafter, the HR 8799 exoplanets were discovered as part of the International Deep Planet Survey (IDPS; Kaisler et al. 2003; Marois et al. 2008; Marois 2010; Marois et al. 2010), which leveraged the Keck II, Gemini North, Gemini South, and VLT telescopes in a 14 yr near-infrared imaging campaign. In sum, IDPS surveyed 292 stars and confirmed four exoplanets–all orbiting HR 8799. 2M1207 b and the HR 8799 planets have masses and orbital separations that can be explained by formation within a circumstellar disk, as is thought to be the case for the solar system (Cameron 1978). Additional PMCs on even wider orbits that have been discovered in direct-imaging surveys include 1RXS J160929.1–210524 b (8 $M_{\rm Jup}$, 330 au; Lafrenière et al. 2008a), GSC 06214-00210B (14 $M_{\rm Jup}$, 330 au; Ireland et al. 2011), HD 106906 b (11 $M_{\rm Jup}$, 650 au; Bailey et al. 2014), SR 12 c (6–20 $M_{\rm Jup}$, 1100 au; Kuzuhara et al. 2011), and 2MASS J21265040–8140293 (12–15 $M_{\rm Jup}$, 4500 au; Deacon et al. 2016), which was unexpected given the formation of these systems are hard to explain with prevailing planet formation theories. There are currently 46 confirmed planetary-mass objects <30 $M_{\rm Jup}$

on orbits between 2 and 3500 au that have been discovered via direct-imaging[1]. If a stricter definition of what constitutes a planet is taken, typically M<13 $M_{\rm Jup}$ (the deuterium-burning limit), the number of confirmed directly-imaged planets falls to 26. This represents $<<1\%$ of the known exoplanet population which not only emphasizes the difficulty of exoplanet imaging, but also reveals how unconstrained any conclusions about wide PMCs as a population are because of their rarity.

Even though stellar multiples are the most common outcome of star formation processes (e.g., Heintz 1969; Batten 1973; Duquennoy & Mayor 1991; Raghavan et al. 2010), and thousands of planetary systems have been confirmed (Thompson et al. 2018; Christiansen et al. 2020) since the discovery of 51 Peg b by Mayor & Queloz (1995), the origins of PMC systems are still under debate. But while their dominant formation mechanism is to be determined, discovering and characterizing new and known wide-orbit PMCs with novel techniques offer valuable scientific opportunities to inform our understanding of companion systems and their evolution.

1.1 First Things First: The Canonical Picture of Star Formation

The basic paradigm of individual star formation has not changed much since Shu et al. (1987) initially proposed a four-stage evolutionary process. First, slowly-rotating, unstable cores form within a molecular cloud as ambipolar diffusion eliminates support provided by magnetic fields and turbulence. Second, the core moves away from equilibrium, with the core center moving away sooner and faster thus collapsing from the inside-out, forming a central protostar and disk. Third, the protostar accretes enough material to burn deuterium and drive a stellar wind along its rotational axis. Finally, material from the stellar envelope begins to fall moreso onto the disk than the protostar, widening the opening angle to reveal a newly-formed star with a circumstellar disk. Shu et al. (1987) even "considered" a fifth phase of star formation where the circumstellar disk disappears, though believed it to fall more into the realm of pre-main sequence stellar evolution. This stage of disk dispersal is dominated by viscous accretion at early times (Hartmann

[1]NASA Exoplanet Archive

1998; Ercolano & Pascucci 2017), photo-evaporation at larger radii (e.g., Hollenbach et al. 2000; Dullemond et al. 2007), and to an even lesser extent the environment of the forming star (Scally & Clarke 2001; Adams et al. 2006).

Each of these evolutionary stages have a morphologically-distinct observed counterpart (Lada 1987). Class 0 young stellar objects (YSOs) have spectral energy distributions (SEDs) with $T_{\rm bol}$<70 K (Andre et al. 1993; Myers & Ladd 1993; Barsony 1994). The Lada (1987) classification scheme begins with Class I, II, and III sources which are based on the shape of the YSO SED from the near- to mid-infrared. Class I YSOs are observed to have a substantial infrared excess greater than the central protostar which is generated from the circumstellar envelope. The envelope is cold ($\sim$30 K) and the Class I YSO SED peaks around $\sim$100 μm. At the Class II stage, the surrounding envelope material has fallen onto an optical thick circumstellar disk which emits in the infrared, making the SED broader than the single blackbody expected from the protostar. Radiation from the protostar is responsible for the majority of the flux in a Class II YSO SED, peaking around 1–2 μm. By the Class III phase, the YSO disk has almost entirely dispersed and is barely reflected in the SED.

This picture, while illustrative, does not factor in the influence of binary stars, nor does it provide insight into how planets form, both ubiquitous outcomes that must stem somewhere from within this paradigm. Multiple systems should form early in the star formation process when plenty of material is available to fragment, either from the circumstellar envelope (Offner et al. 2010), or from the circumstellar disk (Adams et al. 1989; Bonnell & Bate 1994a). Planets, on the other hand, begin forming later on in the process, most likely originating from within the circumstellar disk. My thesis work has interrogated the later evolutionary stages of star formation, seeking to specifically understand how wide-orbit PMCs can fit into this picture.

1.2 Companion Formation Theories

Wide-orbit PMCs challenge both formation models for binary stars and planetary systems. It is unclear whether PMCs represent the low-mass extreme of the stellar binary model, or instead are the end result of high-mass and wide-orbit

planet formation theories. Even so, their existence suggests that wide-orbit PMCs are a normal product of star and planet formation. Possible pathways to the production of such systems that have been proposed include the "top-down" process of fragmentation, whether during the direct collapse of a molecular core or gravitational instability (GI) in a circumstellar disk, or a more "bottom-up" approach of core accretion with gas capture. Dynamical scattering by an inner, more massive object also has been suggested to explain a PMC's presence at such wide orbits. However, each explanation does not fully explain the observed physical and orbital characteristics of these systems.

1.2.1 Fragmentation of the Molecular Cloud

PMCs could form similarly to single stars via fragmentation of a collapsing molecular cloud. Prompt fragmentation can occur in a rotating prestellar core during or just after its free-fall collapse, breaking into pieces that orbit one another (e.g., Bodenheimer & Burkert 2001; Tohline 2002). In the early stages of collapse, the prestellar core material is able to cool radiatively because its compressional heating is low. As the collapse accelerates, the amount of heating increases while also decreasing the core's ability to cool. This process also produces binary systems with orbital separations $>$100 au. If instead turbulence is the cause of fragmentation, binary systems with smaller separations of a few 10s of au are produced (Goodwin et al. 2004). Even closer binaries ($<$1 au) can be created if fragmentation occurs later on in the collapse when molecular hydrogen dissociates (Bonnell & Bate 1994b).

Theoretical studies are showing that fragmentation can produce the initial seeds of PMC systems (Burkert et al. 1997). Simulations of hierarchical fragmentation in a 3D medium yield minimum fragment masses of 7 to 10 $M_{\rm Jup}$ (e.g., Low & Lynden-Bell 1976; Silk 1977; Boss 1988), while more recent studies incorporating shocks are able to reach even smaller minimum masses around 3 $M_{\rm Jup}$ (Boyd & Whitworth 2005). There is also some observational evidence of young hierarchical systems, such as 2MASS J$04414565+2301580$ (Todorov et al. 2010; Bowler & Hillenbrand 2015), that exhibit mass ratios and orbital separations consistent with being formed via cloud fragmentation.

While the formation pathway for bodies of the characteristic PMC mass is ap-

parent, the means of avoiding subsequent growth is not. Fragmentation from a collapsing molecular cloud (Bodenheimer & Burkert 2001) severely narrows the time interval when the companion could actually form (<0.5 Myr). If the fragment is formed yet not isolated before the exhaustion of the circumstellar envelope, the companion will then accrete enough material to become an object of brown dwarf mass, or higher (e.g., Bate 2005; Tomida et al. 2013). Fragmentation as a formation pathway for PMCs seems plausible, but the timescales over which the process takes place may be too limiting to form the number of objects that have been observed.

1.2.2 Gravitational Instability

Gravitational instability (GI), also known as "disk instability" or "disk fragmentation", is another "top-down" process that might be a plausible formation channel for PMCs. In the GI model, the protoplanetary disk that forms after free-fall collapse is the main conduit for accretion to occur onto the protostar. At the same time, circumstellar envelope material is accreting onto the protoplanetary disk. If the mass of the disk becomes sufficiently large compared to the mass of the protostar, the disk becomes unstable to spiral-shaped instabilities (e.g., Adams et al. 1989; Laughlin & Korchagin 1996). The instabilities lead to overdensities that result in perturbations of the disk, eventually leading to fragmentation. These fragments can be dense clumps and self-gravitating, remaining bound to its host star. The clumps further contract and eventually grow into binary stars (e.g., Bonnell & Bate 1994a; Tobin et al. 2016), or if certain conditions are met, gas giant planets. Additionally, evidence of episodic accretion has been observed among young protostars (e.g., Herbig 1977a; Dopita 1978; Reipurth 1989; Peneva et al. 2010), that if infrequent enough (∼10 kyr), can create favorable conditions for fragmentation to occur in outer regions of the circumstellar disk (Stamatellos et al. 2011).

Several properties govern whether a disk is able to undergo fragmentation. First, the disk needs to be massive enough for gravity to overcome thermal and centrifugal support. Additionally, it must be able to radiatively cool so that pressure support against collapse is reduced in the disk (Gammie 2001). If both of these are true, the Toomre stability criterion is not satisfied ($Q \equiv \frac{c_s \kappa}{\pi G \Sigma} < 1$; Toomre 1964). Thus, disks that fragment would need to be very cold (low c_s; Kratter et al. 2010)

and very massive (high Σ; e.g., Boss 2011; Vorobyov 2013).

Numerical simulations find disk fragmentation to be a "robust" mechanism for making substellar objects below the hydrogen-burning limit (80 $M_{\rm Jup}$;Stamatellos & Whitworth 2009), though the probability of planetary mass objects (<13 $M_{\rm Jup}$) being formed is still very low ($\sim$3%). The epoch of *in situ* formation would also need to occur during the Class 0/I stage (0.1 to 0.5 Myr) but just as the envelope is exhausted to prevent even further accretion (Dodson-Robinson et al. 2009; Kratter et al. 2010). Disk fragmentation could occur later during the Class II stage, but the disks would need to be unusually massive, and represent a small fraction of that population (Andrews et al. 2013; Vorobyov 2013).

1.2.3 Core Accretion

Another avenue to PMC formation is the "bottom-up" core accretion planet formation model (Safronov 1969; 1972). This process begins within the protostellar disk and involves the build up of a solid, rocky core via collisions and coagulations of micron-sized dust grains into centimeter-sized pebbles. As these pebbles orbit the central star and settle toward the disk midplane, they continue to collide and aggregate into meter-sized boulders, then into kilometer-sized planetesimals, and then terrestrial planets, which eventually will be able to retain a gaseous envelope. At first, the envelope surrounding the forming planet is in hydrostatic equilibrium with the circumstellar envelope and grows steadily (Safronov 1969; Rice & Armitage 2003). When the protoplanet mass reaches a critical mass of $\sim$10 $M_{\oplus}$, runaway gas accretion occurs (e.g., Pollack et al. 1996; Hubickyj et al. 2005; Dodson-Robinson et al. 2008). For a Jupiter-mass planet at 5 au, the initial phase of planetesimal accretion lasts for $\sim 5\times10^5$ yr (Pollack et al. 1996). The second phase of steady solid and gas accretion lasts about 7 Myr, while the third runaway gas accretion phase lasts an additional $\sim 5\times10^5$ yr. Typical protoplanetary disks disperse on faster timescales of a few Myr (e.g., Haisch et al. 2001; Hillenbrand 2005), though Pollack et al. (1996) note that the results of their simulations provide "conservatively long" estimates for the timescale of core accretion to make ice and gas giants. More recent simulations of core accretion have overcome this timescale issue by invoking additional physical processes, such as migration or grain settling (e.g., Alibert et al. 2005a;b; Hubickyj et al. 2005; Youdin & Goodman 2005; Dodson-

Robinson et al. 2008; Lambrechts & Johansen 2012).

In order for gas giant planets to have access to enough material to become critically massive, they must form outside of the "snow line," the location in the protoplanetary disk where the temperature is low enough for water ice to freeze out ($\sim$5 au; e.g., Lewis 1974; Stevenson & Lunine 1988). In fact, many snow lines can exist for any molecule that is able to condense within the protoplanetary disk which have significant implications for the final bulk composition of a planet formed via core accretion (Öberg et al. 2011). Additionally, runaway gas accretion is limited by the gaseous material in proximity to the forming planet which can either be depleted by the forming planet itself or the natural dispersal of the protoplanetary disk.

The $>$10–100 au separations between PMCs and their host stars preclude core accretion models since the $>$100 Myr timescale over which the accretion would occur is much longer than the $\sim$3–5 Myr disk lifetime (Pollack et al. 1996). If instead the kilometer-sized planetesimals can form quickly via streaming instabilities (Youdin & Goodman 2005; Johansen & Youdin 2007), centimeter-sized pebbles can accrete rapidly onto them (Ormel & Klahr 2010; Lambrechts & Johansen 2012), producing critically massive cores before the protoplanetary disk has dispersed. The advent of pebble accretion theory may be the key to producing critically massive cores quickly. Lambrechts & Johansen (2012) are able to reduce the core growth timescale by 3–4 orders of magnitude between semi-major axes of 5–50 au, and produce 10 $M_{\oplus}$ cores in under 1 Myr at 100 au, though their simulations do not extend past that orbital separation.

1.2.4 Dynamical Origins

Dynamical processes have been proposed as a possible origin of the PMC population. Lafrenière et al. (2008b) suggested in their discovery paper of 1RXS J160929.1–210524 b (8 $M_{\rm Jup}$, 330 au) that a combination of core accretion, which can successfully build a gas giant planet $<$10 au away from its host, and interactions with either other massive planets in the system or the circumstellar disk could result in the system's observed orbital characteristics. Simulations of the first scenario, planet-planet scattering, show that PMCs can end up on orbits $>$100 au, with eccentricities $\gtrsim$0.4 (Scharf & Menou 2009; Veras et al. 2009).

Simulations of the second scenario, Type II orbital migration, have been used to explain the inward movement from beyond the "snow line" of "hot Jupiters", gas giants that have orbital periods $P<10$ days. In some situations, gas giant planets can migrate to larger orbital separations beyond the "snow line" where they formed (Veras & Armitage 2004; Pepliński et al. 2008). The planet is massive enough to interact tidally with the surrounding protoplanetary disk, creating a gap at its orbital location. The gas outside of this location will cross the gap, effectively locking the planet's orbit with the viscous motion of the disk, usually causing orbital decay (Ward 1997). On the other hand, to facilitate this inward accretion, the disk must move some of its material outward to conserve angular momentum. If a massive planet happens to be in this outer region, its semi-major axis can grow to be as large as $\sim$50 au (Veras & Armitage 2004; Martin et al. 2007).

Recent observing campaigns have ruled out such dynamical origins of PMCs. Dedicated searches for potential scatterers have not found PMC systems to have higher multiplicity occurrence rates than in the field (Bryan et al. 2016). Additional follow-up measurements of orbital arcs are finding PMCs to have low eccentricities (e.g., Ginski et al. 2014; Pearce et al. 2019), precluding ejection (Veras et al. 2009; Nagasawa & Ida 2011). Notably, the discovery of "substellar" disks around PMCs suggest ejection is not a plausible formation mechanism because the scattering event would likely disrupt the disk (Bowler et al. 2011). While migratory processes are able to move gas giant planet away from their formation location beyond the "snow line", the resultant orbital separations are $\lesssim$100 au, the typical radius of the circumstellar disk. For wide PMC systems with $a>>100$ au, no disk material is present for the forming planet to interact with, suggesting additional or alternative migration mechanisms need to be invoked for PMCs to have dynamical origins.

1.3 Determining the Dominant Formation Mechanism of Wide PMCs

Though the primary formation mechanism for the small number of PMCs known is still an open question in the field, my thesis work will enable the empirical tests needed to help unite theory to observations as more PMCs are found.

Even in the absence of population statistics, PMCs still offer a valuable scientific opportunity on a per system basis. PMCs' large separations (>2″) and moderate contrasts make them more amenable to direct imaging and spectroscopic study compared to planets located at smaller separations orbiting older stars. For instance, Mohanty et al. (2007) obtained J-band imaging and $H + K$ band low-resolution spectroscopy of 2M1207 b, finding it underluminous for its temperature, age, and distance, possibly due to a circum(sub)stellar disk. Multiple studies of the HR 8799 b, c, and d planets measured their colors to be redder than expected, suggesting dusty clouds and non-equilibrium CO/CH_4 in their atmospheres (Marois et al. 2008; Lafrenière et al. 2009; Metchev et al. 2009; Bowler et al. 2010). Bonnefoy et al. (2013) build the SED of β Pic b from 1–5 μm and determined the planet's atmosphere was dusty and its properties on the edge of core accretion capabilities, emphasizing the need for further explorations of parameter space to reproduce the specific observed properties of the system. So if wide-orbit PMCs *did* form similarly to planets, studying PMC atmospheres would provide much needed insight into the more "traditional" giant planets that orbit very close to their host stars.

PMCs also offer the opportunity to observe planet assembly in action, as some have already been shown to accrete from circumplanetary disks (e.g., Seifahrt et al. 2007; Schmidt et al. 2008; Bowler et al. 2014; Zhou et al. 2014). The different formation mechanisms described above predict different accretion histories, and thus observable differences in the companion's SED at young ages (Spiegel & Burrows 2012; Mordasini 2013). For wide PMCs that form in circumstellar disks, gaps would open and material outside of the gap would flow toward the protoplanet, some falling into the planet's Hill sphere and accreting onto a circumplanetary disk (Ayliffe & Bate 2009; Lubow et al. 1999). Accretion of hydrogen gas onto the protoplanet generates observable Hα emission, significantly decreasing the contrast between the star and companion (Eisner 2015; Zhu 2015). The directly-imaged planet PDS 70 b (5–9 $M_{\rm Jup}$, 22 au; Keppler et al. 2018; Müller et al. 2018) is an exemplary accreting system that has not only had its Hα emission detected, but also UV excess from hydrogen continuum emission (Zhou et al. 2021). Wide-orbit PMCs are relatively easy to observe and can be studied in greater detail than their shorter period, planetary analogs. Detecting PMC atmospheres will help with future interpretation of observations of "bona fide" planets, giving us a peek into the

planet formation processes that, so far, have been too difficult to observe.

With only 8 directly imaged PMCs known on orbits with semi-major axes greater than 100 au (Bowler 2016), PMC demographics and occurrence rates suffer from inadequate statistics. In my thesis, I describe my efforts to increase the number of wide PMC systems known. Once many more PMCs have been found, companion mass functions (CMFs), semi-major axis distributions, and companion mass ratio distributions (CMRDs) can be studied on a statistical basis. Should PMCs form from the direct collapse of a molecular cloud, their semi-major axis distribution would just be a continuation of the binary star semi-major axis distribution out to thousands of au. A similar preference for fragmentation over core accretion emerges if the PMC CMF also looks like an extension of the "top-heavy" binary star CMF rather than a "bottom-heavy" planetary CMF (e.g., Reggiani et al. 2016; Wagner et al. 2019). If a combination of core accretion and fragmentation processes are present, the semi-major axis distribution of PMCs should be bimodal (Boley 2009). Also, determining whether a companion is mutually inclined to a remnant debris disk provides clues as to the dominant formation route. Similar conclusions can be made when studying the orbital architectures of multi-planet systems. Relative metallicity and abundance ratios between PMC and host star are also expected to differ, depending on whether the object formed from a cloud with its star, or from a disk (Öberg et al. 2011). Whether these objects form like planets or stars, they represent an extreme version of either. The demographics and properties of PMCs constrain the extreme limit of their formation mechanism.

1.4 Optimizing the Discovery of Wide PMCs

Our ability to observe and study these systems in any detail has been largely due to state-of-the-art direct imaging techniques and steady improvements in adaptive optics (AO). While high-resolution imaging surveys utilized AO to successfully identify gas giant and substellar companions (e.g., Chauvin et al. 2004; Lafrenière et al. 2008b; Marois et al. 2008; Ireland et al. 2011; Kraus et al. 2011; 2014a; Nielsen et al. 2019), these have come at a high observational cost. Large-aperture telescopes with AO typically confirm one PMC per 50 to 100 stars observed (Ireland et al. 2011), with each observation being on the order of tens of

minutes in length. Thus, a dedicated survey would typically discover one PMC every 2 to 3 nights of telescope time. One way to more efficiently find widely separated PMCs is to search publicly available data sets. The main crux of my thesis was to develop an automated pipeline to find faint PMCs of stars via point spread function (PSF) subtraction in existing *Spitzer*/IRAC images, with the ultimate goal of identifying promising candidates for further characterization with ground-based telescopes, discovering new PMCs and characterizing their properties in order to test formation models.

As a testament to the fruitful exploitation of existing data sets to search for wide substellar companions, Kraus & Hillenbrand (2007) leveraged the archival 2MASS data set to investigate the wide binary population of 3 nearby young associations; Taurus-Auriga, Chameleon I, and Upper Scorpius. By using existing point source catalogs and developing their own point source fitting procedure, they were able to find over 100 candidate binaries with almost 40 previously unidentified. Aller et al. (2013) later performed a similar study that used both optical Pan-STARRS (Kaiser et al. 2002) and near-infrared UKIDSS (Lawrence et al. 2007) catalogs to identify 30 candidate wide-orbit PMCs. Follow-up spectroscopy of 14 of these systems revealed two new companions and confirmed two companions previously identified via photometry in Upper Scorpius. Unfortunately, their strategy of requiring optical detections to initially identify candidate PMCs not only biased their study against lower mass systems but also against systems embedded in the molecular cloud from which they formed. Also, relying solely on photometric catalogs does not probe very close to the host star, since wide-field surveys use very conservative algorithms for identifying point sources. For such a study, one would need to work with the survey images and model the point spread functions (PSFs) of the bright primary stars in more detail to probe down to solar system orbital scales.

1.4.1 Leveraging the *Spitzer* Archive

In my thesis, I have overcome these limitations by using the infrared data products of the *Spitzer Space Telescope* (Werner et al. 2004) and by fitting and subtracting the Infrared Array Camera (IRAC) PSF. The *Spitzer* mission has obtained a wealth of deep and wide imaging of nearby molecular clouds and cores (e.g., Padgett et al. 2006; Evans et al. 2009; Rebull et al. 2011; Dunham et al. 2015). By span-

ning a range of wavelengths from 3.6 to 160 μm, *Spitzer* allowed astronomers to peer inside obscured regions of the sky and gained more knowledge regarding the characteristics of star-forming regions in the solar neighborhood. Properties such as stellar association membership, binary frequency and disk populations are only a few examples of the science enabled by the mission. In particular, the extensive *Spitzer*/IRAC data set of nearby star-forming regions and associations has great potential to be mined for undiscovered wide companions to stars.

1.4.2 Targeting Star-forming Regions

The optics of IRAC provide for diffraction-limited imaging across its four channels (3.6, 4.5, 5.8, and 8 μm), but *Spitzer*'s primary mirror is only diffraction limited for wavelengths greater than 5.4 μm. In-flight full width at half-maximums (FWHMs) for the IRAC PSF are $1\farcs66$, $1\farcs72$, $1\farcs88$, and $1\farcs98$ in each respective channel (Fazio et al. 2004), which means the images are undersampled given the native IRAC pixel scale of $\sim1\farcs22$. While this makes searching for PMCs $<1''$ from their hosts difficult, the *Spitzer*/IRAC FWHMs correspond to resolvable companion separations above 240 au at the distances of Taurus or Upper Scorpius (145 ± 15 pc; Torres et al. 2009). At wide separations (in the background-limited regime), IRAC is even sensitive enough to detect the photospheres of proto-brown dwarfs and protoplanets ($M_{\rm lim}$ = 1 $M_{\rm Jup}$ at 1 Myr and 2 $M_{\rm Jup}$ at 5 Myr, according to the DUSTY models of Chabrier et al. 2000a). *Spitzer*'s limits are even deeper for hosts of circumplanetary disks, which add substantial infrared excesses.

Previous analyses of *Spitzer*/IRAC images have searched for wide-orbit PMC systems in young moving groups that are closer (<100 pc) and older (> 10 Myr) than the regions (>100 pc; <5 Myr) my work scrutinized. Durkan et al. (2016) reanalyzed the images of a sample of 73 young stars with median age 85 Myr and median distance 23.3 pc, and 48 exoplanet hosts with unconstrained ages and median distance 22.6 pc. They detect no planets but constrain a population of 0.5–13 $M_{\rm Jup}$ planets at separations of 100–1000 au with an upper frequency limit of 9% at a 95% confidence level. The Wide-orbit Exoplanet search with InfraRed Direct imaging survey (WEIRD; Baron et al. 2018), identified four candidate companions with red [3.6]–[4.5] colors from their 177 star sample. All were later rejected through follow-up proper motion observations. With Monte Carlo simulations they constrain the

occurrence of 1–13 $M_{\rm Jup}$ PMCs on orbits with semi-major axes of 1000–5000 au to $<$3% at a 95% confidence level.

Different post-processing techniques (i.e. locally-optimized combination of images, principal component analysis, empirical stellar templates) have been used on IRAC images of stars that lie in stellar associations closer to the solar system. This takes advantage of the well-behaved IRAC PSF wings to effectively subtract off flux from a star of interest at $>> \frac{\lambda}{D}$. In my work, I am able to probe closer to a star of interest within the IRAC PSF core at 1–3 $\frac{\lambda}{D}$, which is troublesome due to IRAC's undersampled data. Additionally, PMCs in star-forming regions are more luminous because of their youth, decreasing their relative contrast with their hosts and making them easier to detect in the mid-infrared.

1.4.3 Observing Planets as they Form

As mentioned previously, PMC systems offer the opportunity to witness planet assembly in action, as some wide-orbit PMCs have already been shown to accrete from circumplanetary and circumsubstellar disks (e.g., Seifahrt et al. 2007; Schmidt et al. 2008; Bowler et al. 2014; Zhou et al. 2014). Characterizing the mid-infrared spectral energy distributions (SEDs) of wide-orbit PMCs will help with future interpretation of observations of exoplanets, offering a new perspective on planet formation processes that have been too difficult to observe but might parallel free-floating brown dwarfs like OTS 44 (Joergens et al. 2013).

Almost half of PMCs are observed to harbor disks (46%; Bowler et al. 2017), mostly identified through accretion signatures (e.g., Hα, Paβ, Brγ), red near-infrared colors, or mid-infrared excesses. This high disk frequency is comparable to that observed around isolated young substellar objects but whether wide-orbit companion disks have similar accretion characteristics, disk compositions, and grain sizes is still not yet known. Attempts to observe and characterize PMC disks at radio wavelengths have produced mostly upper limits, which suggests that the dust in PMC disks might actually be more compact and optically thick (e.g., Bowler & Hillenbrand 2015; MacGregor et al. 2017; Wolff et al. 2017; Wu et al. 2017). If so, wide-orbit PMC disks are much better suited for characterization in the mid-infrared.

Theoretical models of circumsubstellar disks were greatly advanced by the

Spitzer Infrared Spectrograph (IRS; Houck et al. 2004), operating from 5–38 μm at $R\sim$600, but many wide-orbit PMCs were discovered *after* the end of *Spitzer*'s cryogenic mission in 2009. *Spitzer's* spatial resolution is even coarser at longer wavelengths, so resolving most PMCs would have been a challenge. Some mid-IR observations of nearby brown dwarfs and planetary-mass objects can be obtained with ground-based telescopes, but these are extremely difficult to conduct due to the Earth's atmosphere and do not extend past 5 μm. In Chapters 2 and 3, I highlight the importance of leveraging *Spitzer* to not only provide an efficient way to build targets of interest but also motivate future observations of PMC systems with the *James Webb Space Telescope* (*JWST*). The *JWST* Mid-InfraRed Instrument (MIRI) Medium Resolution Spectrometer (MRS) will have 10-100$\times$ the sensitivity of *Spitzer*/IRS, allowing for the detailed study of wide-orbit PMC disks for the first time. Observations with *JWST*/MIRI MRS will not only constrain disk sizes and morphologies of wide-orbit PMCs, but also determine disk composition and grain sizes through the identification of spectral features (e.g., amorphous silicate features, PAHs, crystalline silicates, CO_2 absorption).

Discerning whether PMCs have disks is another test of formation models. Disks that resemble those surrounding single, young brown dwarfs imply formation with their host star similar to wide stellar binaries. On the other hand, if the PMCs formed *in situ*, their disks should be larger and more massive due to the reservoir of material surrounding it.

1.5 Outline of Thesis

With this motivation, the main crux of my thesis was to create an automated pipeline to sift through archival images of star-forming regions and known wide-orbit PMC systems from *Spitzer*/IRAC to not only discover wide-orbit planetary-mass companions, but also characterize known and candidate systems in the mid-infrared. I leveraged *Spitzer*'s sensitivity to measure the photometry of any companion that I found or resolved, and ascertained whether that companion harbored a circum(sub)stellar disk.

In Chapter 2, I detail the MCMC-based PSF-fitting pipeline I developed and report its performance on IRAC images of known and candidate companions to

young stars in the star-forming regions of Chameleon, Taurus, and Upper Scorpius. With this initial pipeline demonstration, I utilize *Gaia* DR2 parallax measurements to confirm a new wide-orbit brown dwarf system, 2MASS J$03590986+2009361$, which comprises a 60 $M_{\rm Jup}$ primary and 20 $M_{\rm Jup}$ companion. The companion also shows a mid-infrared excess indicating it may harbor a disk.

In Chapter 3, I send the remaining sample of known wide companion systems with IRAC images through my pipeline infrastructure. I resolve five companions that have not been detected in the *Spitzer* images before, including AB Pic b and ROXs 42B b, determining that I measure photospheric mid-infrared colors of the former but I measure non-photospheric colors of the latter. I also estimate the global disk frequency of young, wide-orbit PMCs to be $56\% \pm 12\%$.

In Chapter 4, I present the preliminary pipeline results of a general search for Jupiter-mass companions on wide orbits of a 209-member sample of Taurus members. I build upon my PSF-subtraction framework by adding an automated method for signaling the presence of significant positive residuals in PSF-subtracted IRAC images. I find 11 systems of interest that appear to harbor candidate companions or have extended residual flux remaining after primary PSF subtraction. I report the discovery of a $\rho = 2\farcs98$ (780 au), $M = 30$ $M_{\rm Jup}$ companion to 2MASS J05160577+2236151. The survey is up to 93% complete to 5 $M_{\rm Jup}$ companions at $\sim$1000 au, and I constrain the frequency of 0.5–30 $M_{\rm Jup}$ companions on semi-major axes 50–5000 au to $<$3.7% at a 95% confidence level.

In Chapter 5, I discuss ongoing and future directions for my pipeline and interesting wide PMC systems that I have analyzed in my work, and provide a brief summary of the results from my thesis.

Chapter 2: Searching for Wide Companions and Identifying Circum(sub)stellar Disks through PSF-Fitting of *Spitzer*/IRAC Archival Images[1]

2.1 Abstract

Direct imaging surveys have discovered wide-orbit planetary-mass companions that challenge existing models of both star and planet formation, but their demographics remain poorly sampled. We have developed an automated binary companion point spread function (PSF) fitting pipeline to take advantage of *Spitzer*'s infrared sensitivity to planetary-mass objects and circum(sub)stellar disks, measuring photometry across the four IRAC channels of 3.6 μm, 4.5 μm, 5.8 μm, and 8.0 μm. We present PSF-fitting photometry of archival *Spitzer*/IRAC images for 11 young, low-mass ($M \sim 0.044$–0.88 $M_{\odot}$; M7.5–K3.5) members of three nearby star-forming regions (Chameleon, Taurus, and Upper Scorpius; $d \sim$150 pc; $\tau \sim$1–10 Myr) that host confirmed or candidate faint companions at $\rho = 1\farcs68 - 7\farcs31$. We recover all system primaries, six confirmed, and two candidate low-mass companions in our sample. We also measure non-photospheric $[3.6] - [8.0]$ colors for three of the system primaries, four of the confirmed companions, and one candidate companion, signifying the presence of circumstellar or circum(sub)stellar disks. We furthermore report the confirmation of a $\rho = 4\farcs66$ (540 au) companion to [SCH06] J0359+2009 which was previously identified as a candidate via imaging over five years ago, but was not studied further. Based on its brightness ($M_{[3.6]} = 8.53$ mag), we infer the companion mass to be $M = 20 \pm 5\ M_{\rm Jup}$ given the primary's model-derived age of 10 Myr. Our framework is sensitive to companions with masses less than 10 $M_{\rm Jup}$ at separations of $\rho = 300$ AU in nearby star-forming regions, opening up a new regime of parameter space that has yet to be studied in detail, discovering planetary-mass companions in their birth environments and revealing their circum(sub)stellar disks.

[1]This chapter has been published as Martinez, R. A. & Kraus, A. L. 2019, AJ, 158, 134. The dissertation author was the primary investigator and author of this publication.

2.2 Introduction

The vast majority of exoplanets have been discovered via the radial velocity (Wright et al. 2011) or transit (Thompson et al. 2018) planet-search methods but the detailed study of their atmospheres and assembly is hindered by their close proximity to bright stellar hosts. Advancing techniques in high-contrast imaging are enabling the detailed study of gas giant planets on wider orbits, providing insight into their formation conditions, atmospheric composition, and circumplanetary environments. Direct imaging surveys typically target nearby young stellar moving groups and associations because contrast ratios between companion and host star is lowest at early ages. These searches have uncovered an interesting population of planetary-mass companions ($\lesssim$20 $M_{\rm Jup}$; hereafter PMCs) located at wide separations ($>$100 au) from their host stars, such as 1RXSJ1609B (8 $M_{\rm Jup}$, 330 au; Lafrenière et al. 2008b), GSC 06214–00210B (14 M_{Jup}, 330 au; Ireland et al. 2011), and HD 106906 b (11 $M_{\rm Jup}$; 650 au; Bailey et al. 2014). Yet only eight confirmed planets and 15 candidate planets or PMCs on orbits with semi-major axes greater than 100 au have been directly-imaged (Bowler 2016) indicating PMC demographics and occurrence rates suffer from inadequate statistics.

While the deuterium-burning limit at $\approx$13 $M_{\rm Jup}$ is commonly used as the boundary between what is a giant planet or brown dwarf, that mass definition is still a matter of debate (e.g., Schneider et al. 2011; Hatzes & Rauer 2015; Bowler 2016). In this work we adopt a definition of "planetary-mass" $\leq$ 20 $M_{\rm Jup}$ recognizing that the giant planet and brown dwarf companion mass functions overlap between 5–30 $M_{\rm Jup}$ (Wagner et al. 2019).

The mere existence of PMCs suggests that such objects are a viable, albeit rare, outcome of star and planet formation. A recent meta-analysis of imaging surveys by Bowler (2016) found the occurrence rate of planets with masses between 5 and 13 $M_{\rm Jup}$ to be $<$2.1%. Ireland et al. (2011) found an occurrence rate of planets between 6 and 20 $M_{\rm Jup}$ to be 4% around solar-type stars, suggesting a slightly more optimistic frequency. However, star and planet formation models are inadequately predicting the occurrence rate of wide-orbit PMC systems, and it is still unclear whether they represent the low-mass extreme of the stellar binary formation process, or instead are the end result of high-mass and wide-orbit planet formation process. Opacity-limited fragmentation during the collapse of a molecular cloud

can form bodies of the characteristic PMC mass (e.g., Low & Lynden-Bell 1976; Silk 1977; Boss 1988; Boyd & Whitworth 2005) but if the fragment forms before it is isolated from the exhaustion of the circumstellar envelope (<0.1 Myr; Bodenheimer & Burkert 2001), it will accrete enough material to become an object of brown dwarf mass or higher (e.g., Bate 2005; Tomida et al. 2013). Gravitational instability (GI) models might be a plausible alternative formation channel for PMCs should the circumstellar disks they form within be atypically massive and cold enough (e.g., Kratter et al. 2010; Boss 2011; Vorobyov 2013) to undergo fragmentation, though the epoch of *in situ* formation would also need to occur during the Class 0/I stage (0.1 to 0.5 Myr) just as the envelope is exhausted to prevent any further accretion (e.g., Kratter et al. 2010; Dodson-Robinson et al. 2009). Disk fragmentation could occur later during the Class II stage, but those disks would also need to be unusually massive (e.g., Andrews et al. 2013; Vorobyov 2013).

From the planet formation perspective, the large separations between PMCs and their host stars disfavor core accretion models since the >100 Myr timescale required to assemble a core is much longer than the ∼3–5 Myr disk lifetime (Pollack et al. 1996). Dynamical processes like ejection could explain the origins of the PMC population. However, scatterers have not been found (Bryan et al. 2016; Pearce et al. 2019) and measurements of PMC orbital arcs suggest they have low eccentricities (Ginski et al. 2014; Schwarz et al. 2016), precluding ejection.

Thermal disk emission and accretion signatures have been detected from wide-orbit PMCs and substellar companions at a variety of wavelengths. Early searches for ultra-low mass companions identified objects potentially harboring disks through their near-infrared colors. Ireland et al. (2011) speculated that GSC 06214–00219 b could have a disk based on its red $K' - L'$ color. Spectroscopic follow-up of the system by Bowler et al. (2011) confirmed the presence of a disk by observing strong Paβ emission. Kraus et al. (2014a) found the majority of their PMC sample to have redder $K' - L'$ than free-floating young objects which could indicate the ubiquity of disks around wide low-mass companions. Additional signs of outflows and accretion signaling disks surrounding wide-orbit PMCs have been observed with Hα line emission and continuum excess in the optical (e.g., Bowler et al. 2014; Zhou et al. 2014). Determining the disk properties of wide-orbit PMCs will help provide additional constraints on their formation pathway. The

presence of substellar disks suggest ejection is not a plausible formation mechanism for PMCs because the the scattering event would likely disrupt the disk (Bowler et al. 2011).

The *Spitzer* mission has obtained a wealth of wide and deep imaging of nearby molecular clouds and cores, including complete Infrared Array Camera (IRAC; Fazio et al. 2004) maps of every major star-forming region within 300 pc (e.g., Evans et al. 2009) across its four channels (3.6, 4.5, 5.8, and 8 μm; Ch 1,..., Ch 4). The extensive *Spitzer*/IRAC data set of nearby star-forming regions and associations has great potential to be mined for undiscovered wide companions to stars. *Spitzer*/IRAC is capable of resolving companion projected separations of $1\farcs7$ to $2\farcs0$, corresponding to 240 to 290 au at the distances of Taurus or Upper Scorpius ($\sim$145 pc; Torres et al. 2009, de Zeeuw et al. 1999) and sensitive to the photospheres of proto-brown dwarfs and protoplanets (M_{lim} = 1 $M_{\rm Jup}$ at 1 Myr and 2 $M_{\rm Jup}$ at 5 Myr; Chabrier et al. 2000b). *Spitzer*'s limits are even deeper for hosts of circumplanetary disks, which add substantial infrared excesses.

In this paper, we report the results of a pilot study to recover and to measure the mid-infrared photometry of confirmed and candidate low-mass companions of young stars in *Spitzer*/IRAC imaging and to determine whether they host circum(sub)stellar disks. In Sections 2 and 3, we describe our target sample and the archival *Spitzer*/IRAC observations used. We describe our MCMC based PSF-fitting routine in Section 4. In Section 5, we present the results of our analysis of the IRAC images and highlight interesting individual systems. Finally in Section 6, we discuss the performance of our PSF-fitting routine.

2.3 Target Sample

Our target sample is built from systems with confirmed or candidate low-mass companions previously discovered in the star-forming regions of Chameleon I (179 pc, 2–3 Myr; Voirin et al. 2018, Luhman 2004), Taurus-Auriga (145 ± 15 pc, 1–2 Myr; Torres et al. 2009, Kraus & Hillenbrand 2009a), and Upper Scorpius (145 pc, 5–10 Myr; de Zeeuw et al. 1999, Preibisch et al. 2002, Pecaut et al. 2012) from the multiplicity surveys of Lafrenière et al. (2008a) and Kraus & Hillenbrand (2012). We also include in our sample a small number of systems observed by Kraus & Hillen-

brand (2012) that might be a part of an older distributed population of Taurus (5–10 Myr; Wichmann et al. 1996, Slesnick et al. 2006, Kraus et al. 2017). These young regions are compelling targets because they offer increased sensitivity to PMCs retaining residual heat from formation. There is also a high likelihood of finding companions harboring disks, which would add substantial infrared excess.

From this larger sample, we then identify systems that also have archival *Spitzer*/IRAC observations available. In-flight full width at half-maximums (FWHMs) for the IRAC PSF are $1\farcs66$, $1\farcs72$, $1\farcs88$, and $1\farcs98$ in each respective channel, corresponding to resolvable companion separations above 240 au at the distances of Taurus or Upper Scorpius. IRAC is also sensitive enough to detect photospheres of proto-brown dwarfs and protoplanets ($M_{\rm lim}$ = 1 $M_{\rm Jup}$ at 1 Myr and 2 $M_{\rm Jup}$ at 5 Myr; Chabrier et al. 2000b) at wide separations in the background-limited regime. Our sample was intentionally constructed to span a range of primary brightness, contrast, and projected separation to test our ability to recover astrophysical sources and sufficiently probe those axes of parameter space. Most of the systems in the target sample have high-precision astrometry gathered from previous adaptive optics (AO) imaging. We used these measurements to experiment with the effects of using informative priors.

Lafrenière et al. (2008a) examined 126 stars ranging in mass from $\sim$0.1–3$M_{\odot}$ in Chameleon I. Using the ESO Very Large Telescope AO imaging system, they found 30 binary and six triple systems. We chose CHXR 28 and Sz 41 from that study for our target sample. Kraus & Hillenbrand (2012) used Keck laser guide star AO to study 78 stars in Taurus-Auriga and Upper Scorpius, finding 45 candidate companions. We chose five candidate systems from that survey for our sample: 2MASS J03590986+2009361, 2MASS J04554970+3019400, 2MASS J05373850+2428517, 2MASS J16111711–2217173, and 2MASS J16151116–2420153. We also incorporate four more systems into our target sample not studied in the aforementioned surveys: FU Tau AB (Luhman et al. 2009), FW Tau (Kraus et al. 2014a), 2MASS J16101918–2502301 (Aller et al. 2013), and 2MASS J16103196–1913062 (Aller et al. 2013).

The primary spectral types for the 11 systems in our target sample range from K3.5 to M7.5 and the primary K_s-band magnitudes range from 7.69 mag to 13.25 mag. The projected separations and K_s-band contrasts of the candidate and con-

firmed companions range from $1\farcs684$ to $7\farcs313$ and 0.32 to 7.27 mag, respectively. Four of the confirmed low-mass companions in these systems are known to have disks; FU Tau B, FW Tau C, Sz 41 B, and USco 1610–2502 B. The combined target primary properties are given in Table 2.1 and system properties in Table 2.2.

Table 2.1: Primary Properties for Test Case Systems

2MASS	Other Name	SpT	K_s (mag)	$W1$ (mag)	$W2$ (mag)	Ref.
J03590986+2009361	[SCH06] J0359099+2009362	M4.75	12.53	12.22	11.96	1
J04233539+2503026	FU Tau A	M7.25	9.32	8.60	7.82	2
J04292971+2616532	FW Tau AB	M4	9.39	9.20	8.93	3
J04554970+3019400		M6	11.86	11.50	11.17	1
J05373850+2428517	[SCH06] J0537385+2428518	M5.25	10.78	10.60	10.34	1
J11075588–7727257	CHXR 28 Aa,Ab	K6	7.69	6.99	7.50	4
J11122441–7637064	Sz 41 A	K3.5	8.00	6.61	6.20	4
J16101918–2502301	USco 1610–2502 A	M1	8.36	8.24	8.20	5,6
J16103196–1913062	USco 1610–1913 A	K7	8.99	8.74	8.67	5,6
J16111711–2217173	[SCH06] J16111711–22171749	M7.5	13.25	13.07	12.74	1
J16151116–2420153	[SCH06] J16151115–24201556	M6	13.17	12.98	12.76	1

NOTES — The primaries for FW Tau and CHXR 28 are actually close binaries but treated as single stars because they are spatially unresolved at the angular scale of *Spitzer*/IRAC observations. Primary properties obtained from the following references: (1) Kraus & Hillenbrand (2012); (2) Luhman et al. (2009); (3) Kraus et al. (2014a); (4) Lafrenière et al. (2008a); (5) Kraus & Hillenbrand (2009b); (6) Aller et al. (2013).

Table 2.2: Properties of Test Case Confirmed and Candidate Companions

2MASS	Other Name	Separation (arcsec)	Position Angle (deg)	ΔK_s (mag)	Ref.
J03590986+2009361 B	[SCH06] J0359099+2009362 B	4.660 ± 0.005	264.275 ± 0.003	1.965 ± 0.005	1
J04233539+2503026 B	FU Tau B	5.72 ± 0.10	123.2 ± 1.0	4.01 ± 0.10	2
J04292971+2616532 C	FW Tau C	2.295 ± 0.003	295.0 ± 0.5	5.93 ± 0.04	3
J04554970+3019400 c1		7.313 ± 0.007	129.15 ± 0.02	1.77 ± 0.05	1
J05373850+2428517 c1	[SCH06] J0537385+2428518 c1	1.684 ± 0.008	152.84 ± 0.14	7.27 ± 0.13	1
J11075588–7727257 B	CHXR 28 B	1.818 ± 0.003	115.9 ± 0.1	0.32 ± 0.04	4
J11122441–7637064 B	Sz 41 B	1.977 ± 0.001	162.5 ± 0.1	2.35 ± 0.03	4
J16101918–2502301 B	USco 1610–2502 B	4.896 ± 0.002	241.24 ± 0.02	2.90 ± 0.05	5,6
J16103196–1913062 B	USco 1610–1913 B	5.820 ± 0.009	114.01 ± 0.10	3.83 ± 0.05	5,6
J16111711–2217173 c1	[SCH06] J16111711–22171749 c1	4.207 ± 0.004	344.41 ± 0.02	5.66 ± 0.05	1
J16151116–2420153 c1	[SCH06] J16151115–24201556 c1	5.100 ± 0.005	141.03 ± 0.01	4.74 ± 0.02	1

NOTES — An object is labeled as “c#" to reflect that they are unconfirmed candidate companions. System properties obtained from the following references: (1) Kraus & Hillenbrand (2012); (2) Luhman et al. (2009); (3) Kraus et al. (2014a); (4) Lafrenière et al. (2008a); (5) Kraus & Hillenbrand (2009b); (6) Aller et al. (2013).

2.4 Observations

All targets were observed by the *Spitzer Space Telescope* (Werner et al. 2004) with the Infrared Array Camera (IRAC; Fazio et al. 2004) during the cryogenic phase of the mission. IRAC operates with four filters in the mid-infrared; 3.6, 4.5, 5.8, and 8.0 μm. The IRAC detector has 256×256 pixels with a pixel scale of $1\farcs22$.

Observations of the 11 members of our target sample appear in ten different sets of IRAC data, with exposure times of 0.4 s, 1.0 s, 10.4 s, 26.8 s, and 96.8 s. Almost all targets had data taken across the four IRAC channels, but USco 1610–1913 did not have any Channel 1 or Channel 3 observations. Specific details about the *Spitzer*/IRAC programs and data products used are listed in Table 2.3.

Table 2.3: Target Sample *Spitzer*/IRAC Observations

2MASS	No. of Frames				$T_{\rm exp}$	AOR	Date	PID	PI
	Ch 1	Ch 2	Ch 3	Ch 4	(s)		(UT)		
J03590986+2009361	4	4	4	4	0.4, 10.4	26469888	2009 Mar 20	50584	D. Padgett
J04233539+2503026		3		3	0.4, 10.4	3964672	2005 Feb 23	37	G. Fazio
	2	1	2	1	0.4, 10.4	19028224	2007 Mar 30	30816	D. Padgett
	1	1	1	1	0.4, 10.4	19028480			
J04292971+2616532	3	3	3	3	0.4, 10.4	3963392	2004 Mar 07	37	G. Fazio
	1	1	2	1	0.4, 10.4	11232256	2005 Feb 23	3584	D. Padgett
	1	1	1	1	0.4, 10.4	11236096	2005 Feb 24		
	8	8	8	8	1.0	14609920	2006 Mar 24	20386	P. Myers
	8	8	8	8	1.0	14610176	2006 Mar 25		
J04554970+3019400	2	2	1	2	0.4, 10.4	3965696	2004 Feb 14	37	G. Fazio
	1		1		0.4	12663552	2005 Feb 20		
	6	3	6	3	10.4				
		1		1	0.4, 10.4	26476544	2008 Nov 01	50584	D. Padgett
J05373850+2428517	4	4	4	4	0.4, 10.4	26478336	2008 Oct 31	50584	D. Padgett
J11075588–7727257	6	3	7	3	0.4, 10.4	3960320	2004 Jun 10	37	G. Fazio
J11122441–7637064	3	6	3	7	0.4, 10.4	3651328	2004 Jul 04	6	G. Fazio
		1		1	0.4, 10.4	5662976	2004 Jul 21	173	N. Evans
J16101918–2502301	2	2	2	2	0.4, 10.4	5670912	2004 Aug 12	173	N. Evans
J16103196–1913062		9		9	1.2	13868288	2005 Sep 15	20069	J. Carpenter
		8		8	10.4	13874944	2005 Aug 23		
J16111711–2217173		1		1	0.4	15843072	2005 Aug 24	20103	L. Hillenbrand
	5	5	5	5	10.4				
J16151116–2420153		1		1	0.4	15837440	2005 Aug 24	20103	L. Hillenbrand
	5	5	5	5	10.4				

We work with IRAC's cryogenic-phase corrected basic calibrated data (CBCD) and uncertainty (CBUNC) files. Mosaics were not used due to the complicated be-

havior of the IRAC PSF (see Data Analysis section). We use images with exposure times of 10.4 s or less to avoid saturation.

All data were reduced with the *Spitzer* Science Center software pipeline version S18.25.0. No further reduction or processing of the images was performed.

2.5 Data Analysis

2.5.1 The IRAC PSF

Previous analyses of *Spitzer*/IRAC images have searched for wide-orbit PMC systems, taking advantage of IRAC's well-behaved PSF wings at $>> \lambda/D$. Marengo et al. (2006) first established that *Spitzer*/IRAC has the ability to detect PMCs in the background-limited regime in their search for companions orbiting ϵ Eridani. Similar studies of Vega, Fomalhaut, and ϵ Eridani IRAC images by Janson et al. (2015) utilized more sophisticated post-processing techniques (i.e., locally-optimized combination of images, principal component analysis, empirical stellar templates) to demonstrate that *Spitzer* was sensitive to PMCs that lie closer to their host stars. Durkan et al. (2016) reanalyze archival *Spitzer*/IRAC direct imaging surveys of nearby stars to constrain the frequency of giant planets orbiting out to 1000 au. Most recently, Baron et al. (2018) reported first results from the Wide-orbit Exoplanet search with InfraRed Direct Imaging (WEIRD) survey constraining the occurrence of Jupiter-like companions on orbits between 1000 and 5000 au. These studies focused their investigations on regions closer ($d < 100$ pc) and older ($\tau > 10$ Myr) than the regions we analyze in this work ($d > 100$ pc; $\tau < 10$ Myr).

Our framework is probing the IRAC PSF at 1–3 λ/D, where companion identification is difficult due to it being undersampled at the native $1\farcs22$ pixel scale. To overcome this obstacle when measuring photometry on IRAC images via point source fitting, a PRF (or "effective PSF") was developed by the *Spitzer* Science team that combined information regarding the IRAC PSF, detector sampling, and intrapixel sensitivity variations. Twenty-five total PRFs are provided that represent 25 different locations (5×5 grid) on the 256×256 pixel IRAC detector. Each PRF for a given detector location is $5\times$ oversampled, thus to create the proper PSF for any given position on the detector, one must interpolate the original 5×5 grid of PRFs to the centroid position, shift the PRF to the appropriate "pixel phase," then

sample the individual PRF at regular intervals corresponding to single CCD pixel increments.

We use a modified version of IRACSIM [2] (Ingalls et al. 2016), an Interactive Data Language (IDL) package built to model the pointing, imaging, and Fowler sampling behavior of *Spitzer*/IRAC Channels 1 and 2 in the post-cryogenic mission. Ingalls et al. (2016) rescale the cryogenic PRFs to accommodate the change in intra-pixel sensitivity during *Spitzer*'s warm mission, using these modified PRFs to define the reference frame of a point source to be modeled in native pixel units. We incorporate these imaging modules into our pipeline by adapting them to use the original core PRFs from the cold mission instead, and adding the ability to generate PSFs for IRAC channels 3 and 4.

2.5.2 MCMC PSF Subtraction

Due to the complicated behavior of the IRAC PSF, we adopt an Markov Chain Monte Carlo (MCMC) formalism to fully explore the resulting posterior probability density function for the system parameters. The PSF model is described by seven parameters, three of which are "image-specific" (and hence have independent values for each image) and four of which are "system-specific" (and hence are shared between all images of a target). The three image-specific parameters are x-pixel coordinate of the primary centroid (x), y-pixel coordinate of the primary centroid (y), and image background (b), while the four system-specific parameters are primary peak pixel value (n), separation (ρ), position angle (PA), and contrast (Δm). We use the χ^2 goodness-of-fit between the image and PSF model as our likelihood function. The priors associated with each parameter are presented in Table 2.4. We use uniform priors for x, y, n, and Δm. We constrain x and y to be within four pixels of the initial primary centroid estimate. We also constrain Δm to be between -2 and 10 mag, allowing for the possibility of a companion being brighter in the IRAC channels than the primary.

[2] http://dx.doi.org/10.5281/zenodo.46270

Table 2.4: MCMC Fit Model Parameters

Parameter	Symbol	Prior	Constraints
Image-Specific Fit			
x-centroid	x	Uniform	$[x_0 - 4, x_0 + 4]$
y-centroid	y	Uniform	$[y_0 - 4, y_0 + 4]$
Background	b	Normal[a]	
System-Specific Fit			
Peak Pixel Flux	n	Uniform	None
Projected Separation	ρ	Normal[b]	...
Position Angle	P.A.	Normal[b]	...
Contrast	Δm	Uniform	$[-2, 10]$

[a]Normal prior on the background was based on the pixel value distribution within a 30-pixel radius of the primary.

[b]Normal prior on these parameters were based on prior adaptive optics imaging results presented Table 2.2.

The automated PSF-fitting pipeline performs an MCMC analysis by exploring the posterior PDF using the standard Metropolis-Hastings algorithm with Gibbs sampling. We use four walkers (chains) of 56,000 total jumps each, but break this chain up into three separate MCMC fits. The pipeline first runs a 140,000 jump chain fitting all seven parameters for all of the IRAC images available at a given exposure time of a system, then iterates twice between a 80,000 jump chain image-specific parameter fit and a 60,000 jump chain system-specific parameter fit. The first 10 percent of the chains are removed as burn-in. Images were not analyzed if the initial estimate for the target system primary centroid was within 12 pixels of the IRAC CCD edge. In Figure 2.1 we present example images as a target system is processed through our pipeline. We show example posterior probability distributions for two target systems in Figures 2.2 and 2.3.

2.6 Results

By developing the framework to accurately model and subtract off the flux of bright primary stars, we now can take advantage of *Spitzer*'s extraordinary sensitivity to study wide low-mass companions near the diffraction limit. Previous analyses of archival *Spitzer*/IRAC images have searched for wide companions in

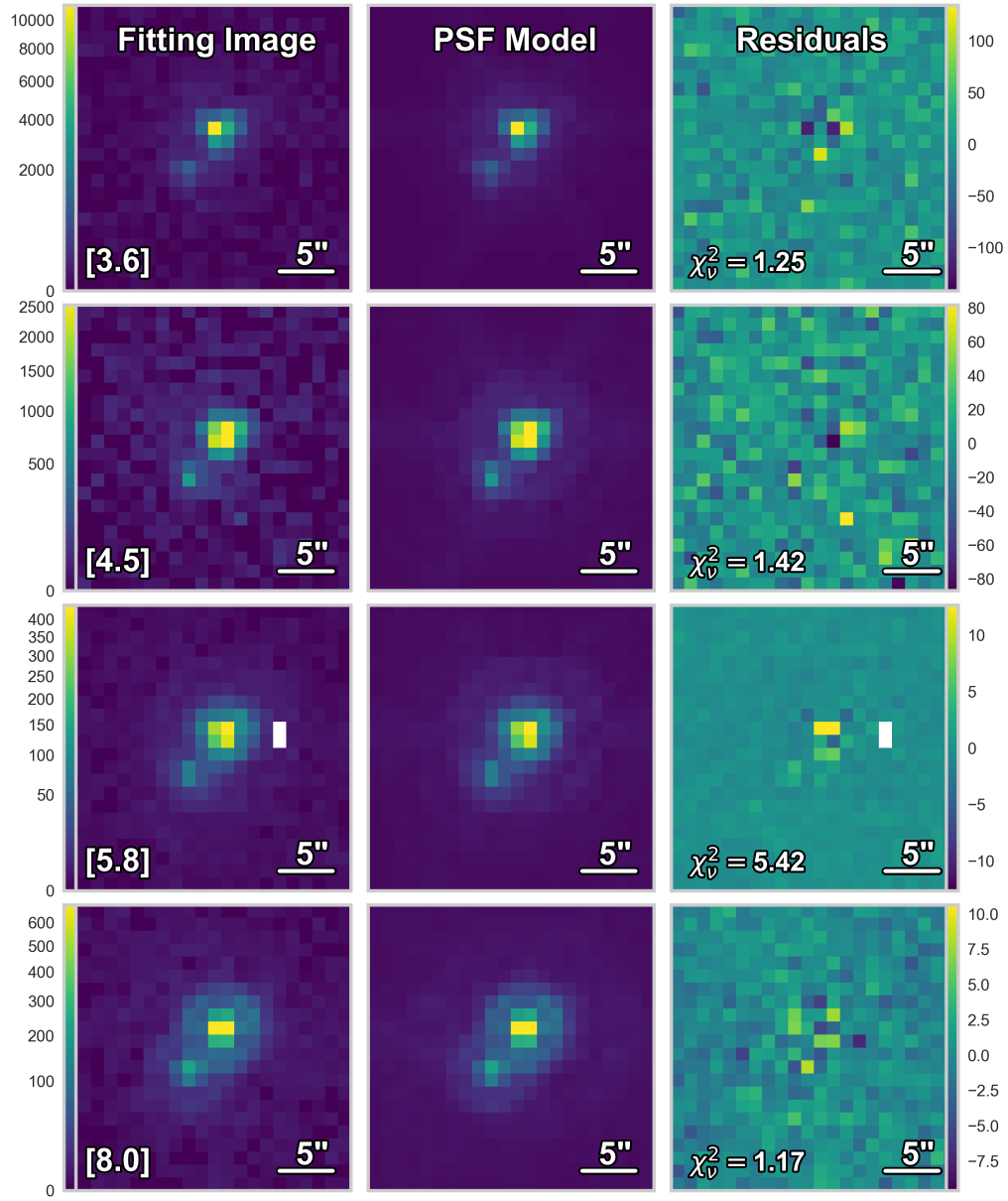

Figure 2.1: Images of USco 1610–2502 at four stages of the PSF-fitting pipeline. The pipeline has been generalized to perform PSF-subtraction across all four channels (rows) should images be available. **Column 1:** The background-subtracted fitting image in units of Data Number per second (DN/s) presented with a square root stretch. **Column 2:** The best-fit PSF model in units of DN/s and also presented with a square root stretch. **Column 3:** The residuals left over after the PSF model is subtracted from the background subtracted fitting image, plotted with a linear color scale. Cosmic rays (for example, white pixels in row 3, column 1) that fall near the system are masked prior to PSF-fitting. Note that the remaining residuals appear similar to the noise near the primary star, indicating a good fit.

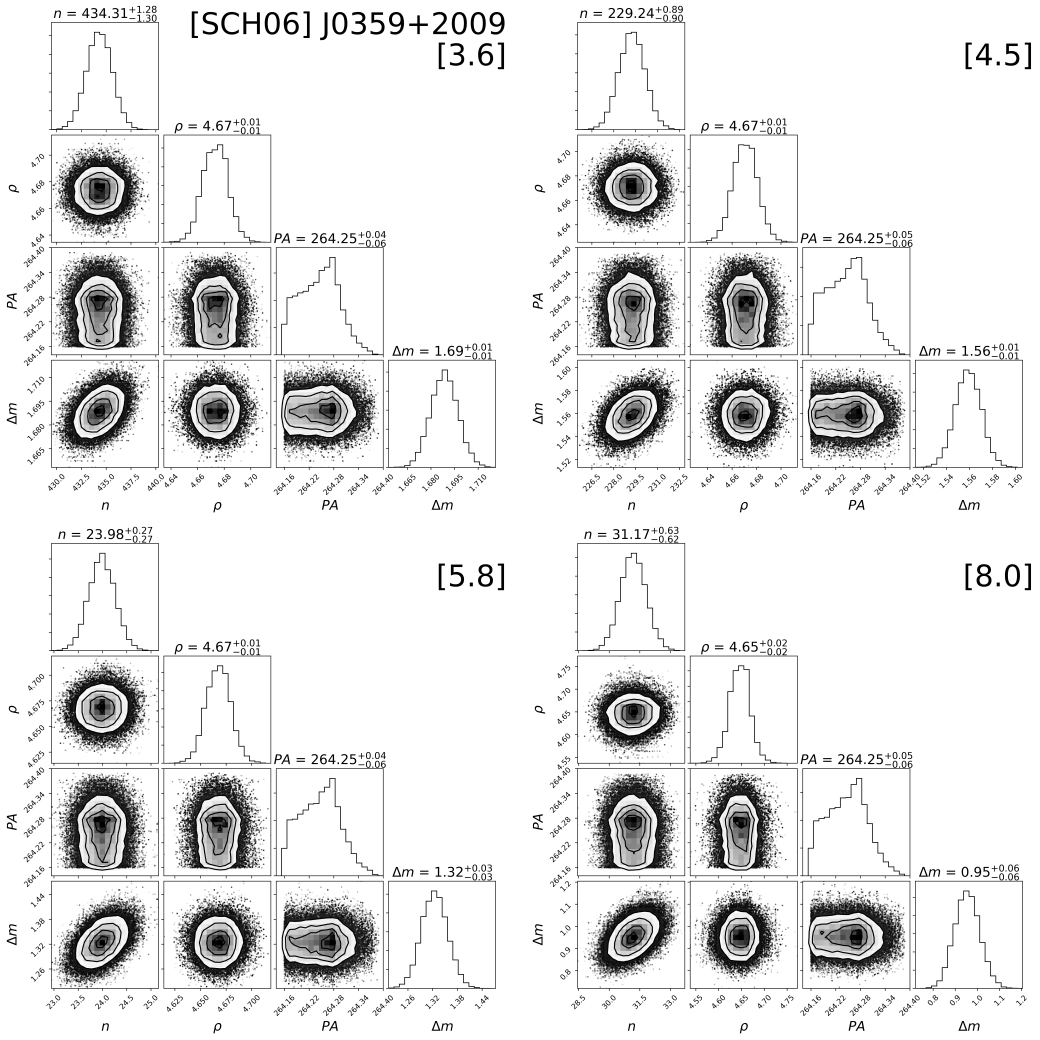

Figure 2.2: J 0359+2009]Posterior probability distributions of the four system-specific parameters fit to the images of [SCH06] J0359+2009, an example system that had its candidate companion detected by our pipeline. No strong covariances are present due to the strong prior on the astrometry from previous adaptive optics imaging. The asymmetric appearance of the PA marginalized posterior probability density results from the pixelation of the IRAC PSF models.

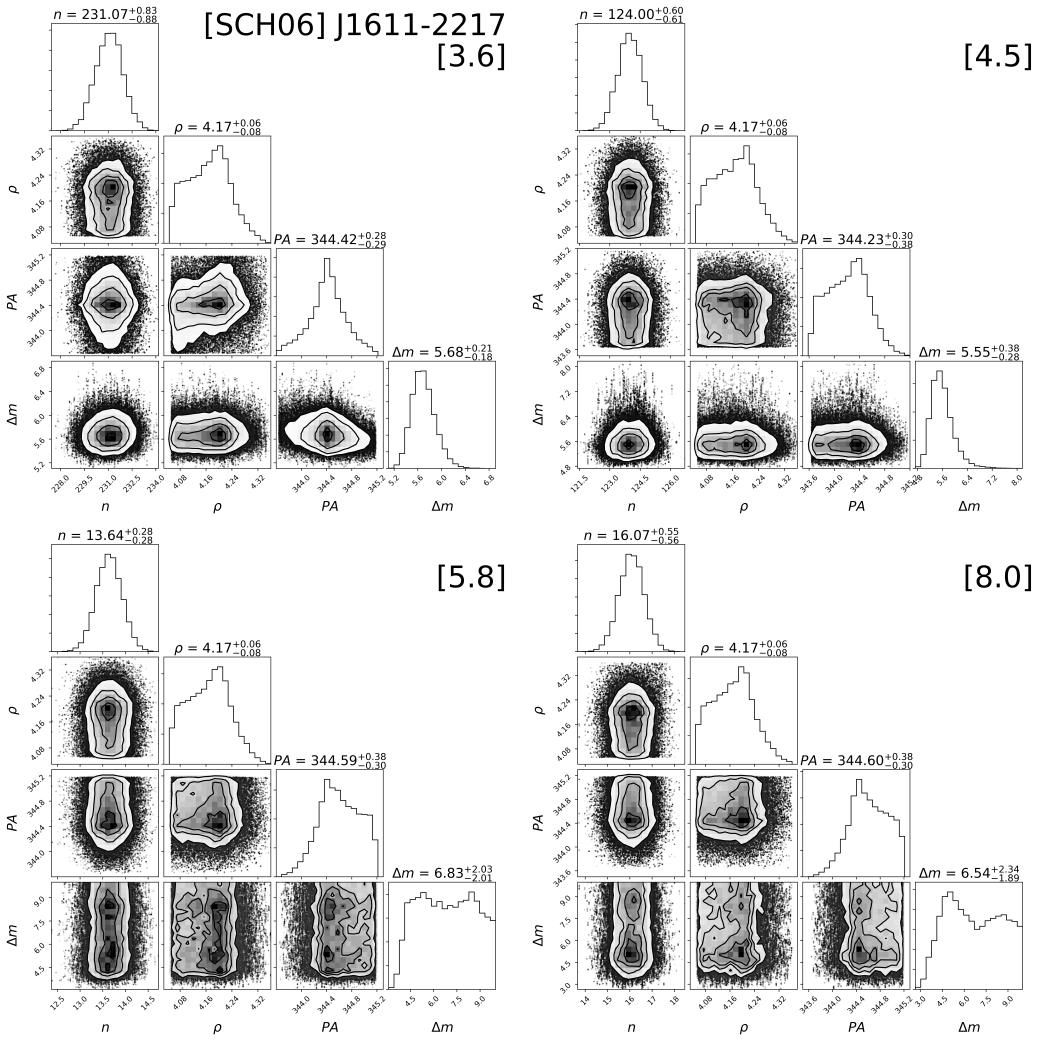

Figure 2.3: J
1611-2217]Posterior probability distributions of the four system-specific parameters fit to the images of [SCH06] J1611-2217, an example system where the candidate companion was not detected by our pipeline. The projected separation and PA marginalized posterior probability densities are still well-constrained because of the strong prior on the astrometry from previous adaptive optics imaging. The marginalized posterior probability densities for Δm in Channels 1 and 2 appear constrained but inspection of stacked residuals images reveal no companion detected above our 3-σ detection limit (see Section 2.6.3). The marginalized posterior probability densities for Δm in Channels 3 and 4 are unconstrained.

young moving groups that are closer (< 100 pc) and older (> 10 Myr) than the regions represented in our target sample (e.g., Durkan et al. 2016; Baron et al. 2018). Although they were able to take advantage of the well-behaved IRAC PSF wings at $>> \lambda/D$ when searching for wide companions, they do so when the contrast between primary star and companion is more severe. Moreover, some wide PMCs within the more distant star-forming regions harbor disks, so some of our targets should have detectable excesses in the mid-infrared, further improving detectability and offering an opportunity to investigate disk evolution and dispersal in low-mass companions to stars. Our MCMC-based PSF fitter is finally opening up a regime of parameter space that has yet to be studied in detail and will reveal low-mass companions, whether they have disks, and the properties of those disks.

2.6.1 Detections

Our reprocessing of the IRAC images yielded detection of all 11 system primaries, six confirmed, and two candidate low-mass companions. The targets were processed independently by channel, with a simultaneous fit of all images in that channel. The best-fit system parameters as determined by our pipeline are presented in Table 2.5. IRAC magnitudes in each channel for the primary stars are calculated from the best-fit primary flux, while for the confirmed or candidate low-mass companions the best-fit contrast is also used. The primary magnitudes span $7.30 < [3.6] < 12.89$ in Channel 1 and $5.35 < [8.0] < 12.70$ in Channel 4. The magnitudes of detected confirmed or candidate companions span $8.59 < [3.6] < 13.88$ in Channel 1 and $8.06 < [8.0] < 13.90$ in Channel 4. Three candidate low-mass companions were not detected by our pipeline (2MASS J05373850+2428517 c1, 2MASS J16111711–2217173 c1, and 2MASS J16151116–2420153 c1). The candidate companion to 2MASS J04554970+3019400 was detected in *Gaia* DR2 (Gaia Collaboration et al. 2018) with measured $\pi = 0.27 \pm 0.10$ mas, making it an unassociated background star. Photometry for the primary stars and candidate or confirmed companions of our target sample are shown in Table 2.6. We show stacked residuals images of four example target systems in Figure 2.4.

Table 2.5: Best-Fit System Properties of Detected Companions and Neighbors

2MASS	Other Name	Separation (arcsec)	Position Angle (deg)	Δ[3.6] (mag)	Δ[4.5] (mag)	Δ[5.8] (mag)	Δ[8.0] (mag)
J03590986+2009361 B	[SCH06] J0359099+2009362 B	4.67 ± 0.01	264.2 ± 0.1	1.69 ± 0.01	1.56 ± 0.01	1.32 ± 0.03	0.95 ± 0.06
J04233539+2503026 B	FU Tau B	5.68 ± 0.04	123.4 ± 0.3	4.05 ± 0.05	4.32 ± 0.04	4.24 ± 0.02	4.12 ± 0.01
J04292971+2616532 B	FW Tau C	2.22 ± 0.10	292.6 ± 2.2	4.74 ± 0.08	4.39 ± 0.05	4.43 ± 0.07	3.99 ± 0.06
J04554970+3019400 c1[a]		7.34 ± 0.01	129.0 ± 0.2	2.45 ± 0.01	2.63 ± 0.01	2.86 ± 0.05	3.33 ± 0.12
J11075588–7727257 B	CHXR 28 B	1.87 ± 0.04	117.0 ± 0.7	0.52 ± 0.01	0.47 ± 0.01	0.51 ± 0.04	0.60 ± 0.03
J11122441–7637064 B	Sz 41 B	1.97 ± 0.01	162.6 ± 0.2	2.20 ± 0.01	2.06 ± 0.01	2.37 ± 0.04	2.72 ± 0.02
J16101918–2502301 B	USco 1610–2502 B	4.90 ± 0.01	241.2 ± 0.3	2.63 ± 0.02	2.33 ± 0.03	2.18 ± 0.01	1.64 ± 0.01
J16103196–1913062 B	USco 1610–1913 B	5.83 ± 0.01	113.6 ± 0.4	...	3.46 ± 0.01	...	3.41 ± 0.02

If an entry in Δm is missing, no IRAC data existed for that object in that channel. The astrometric precision reflects that of the input priors. The candidate companions to 2MASS J05373850+2428517, 2MASS J16111711–2217173, and 2MASS J16151116–2420153 were not recovered.

[a]The candidate companion to 2MASS J04554970+3019400 was detected in *Gaia* DR2 (Gaia Collaboration et al. 2018) with measured $\pi = 0.27 \pm 0.10$ mas, making it an unassociated background star.

Table 2.6: *Spitzer*/IRAC Photometric Measurements for Test Case Sample

2MASS	Other Name	$[3.6]_{\rm P}$ (mag)	$[4.5]_{\rm P}$ (mag)	$[5.8]_{\rm P}$ (mag)	$[8.0]_{\rm P}$ (mag)	$[3.6]_{\rm N}$ (mag)	$[4.5]_{\rm N}$ (mag)	$[5.8]_{\rm N}$ (mag)	$[8.0]_{\rm N}$ (mag)
J03590986+2009361	[SCH06] J0359099+2009362	12.20 ± 0.02	12.08 ± 0.02	12.05 ± 0.02	12.00 ± 0.03	13.88 ± 0.02	13.64 ± 0.02	13.37 ± 0.04	12.95 ± 0.06
J04233539+2503026	FU Tau	8.35 ± 0.02	7.74 ± 0.02	7.29 ± 0.02	6.53 ± 0.02	12.39 ± 0.05	12.06 ± 0.05	11.53 ± 0.02	10.65 ± 0.02
J04292971+2616532	FW Tau	9.01 ± 0.02	8.90 ± 0.02	8.84 ± 0.02	8.85 ± 0.02	13.75 ± 0.08	13.29 ± 0.05	13.27 ± 0.07	12.84 ± 0.06
J04554970+3019400		11.34 ± 0.02	11.15 ± 0.02	10.93 ± 0.02	10.58 ± 0.02	13.80 ± 0.02	13.78 ± 0.02	13.79 ± 0.05	13.91 ± 0.12
J05373850+2428517	[SCH06] J0537385+2428518	10.41 ± 0.02	10.33 ± 0.02	10.25 ± 0.02	10.23 ± 0.02	> 12.37	> 13.25	> 13.65	> 13.82
J11075588–7727257	CHXR 28	7.99 ± 0.02	8.00 ± 0.02	7.81 ± 0.02	7.83 ± 0.02	8.51 ± 0.02	8.47 ± 0.02	8.32 ± 0.04	8.44 ± 0.04
J11122441–7637064	Sz 41	7.31 ± 0.02	6.87 ± 0.02	6.39 ± 0.02	5.35 ± 0.02	9.50 ± 0.02	8.93 ± 0.02	8.76 ± 0.05	8.07 ± 0.03
J16101918–2502301	USco 1610–2502	8.27 ± 0.02	8.33 ± 0.02	8.25 ± 0.02	8.19 ± 0.02	10.90 ± 0.03	10.67 ± 0.03	10.43 ± 0.02	9.83 ± 0.02
J16103196–1913062	USco 1610–1913	...	8.68 ± 0.02	...	8.58 ± 0.02	...	12.13 ± 0.02	...	12.00 ± 0.02
J16111711–2217173	[SCH06] J16111711–22171749	12.86 ± 0.02	12.75 ± 0.02	12.66 ± 0.03	12.72 ± 0.04	> 17.75	> 17.66	> 15.40	> 14.81
J16151116–2420153	[SCH06] J16151115–24201556	12.79 ± 0.02	12.71 ± 0.02	12.64 ± 0.02	12.69 ± 0.04	> 17.79	> 17.71	> 15.68	> 14.56

Subscript “P" denotes the primary star of the test case sample system while subscript “N" denotes the confirmed companion, candidate companion, or neighbor. If an entry is missing, no IRAC data existed for that object in that channel.

In Table 2.7 we derive companion masses for our target sample using our measured $[3.6]$ photometry (or $[4.5]$ for USco 1610–1913 which does not have Channel 1 images available) and the BT-Settl evolutionary models of Allard et al. (2012). We use *Gaia* DR2 distance estimates from Bailer-Jones et al. (2018), or if an estimate did not exist, the canonical distance to the star-forming region of which the system is a member to determine absolute magnitudes.

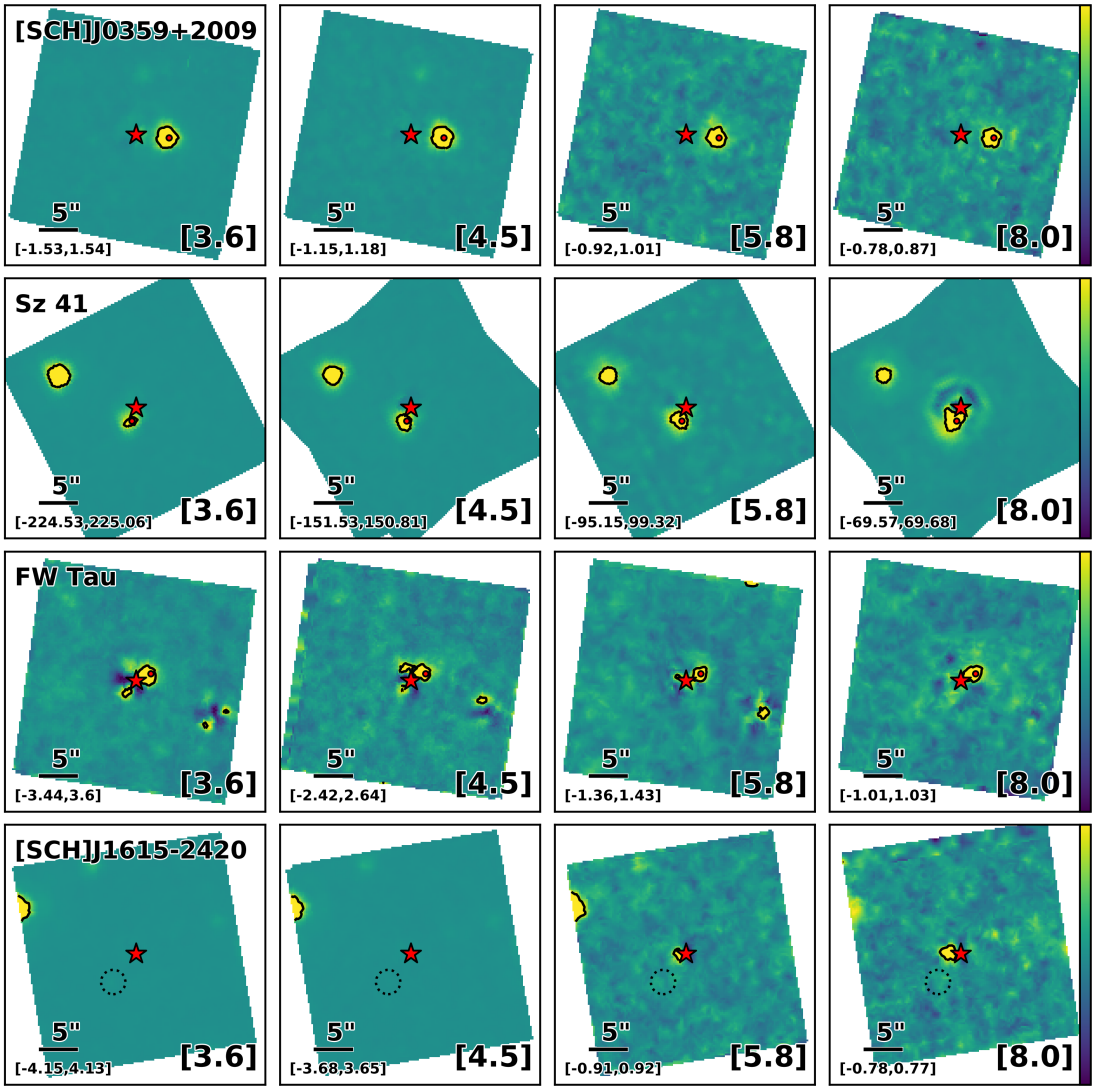

Figure 2.4: J 0359+2009, Sz 41, FW Tau, and [SCH06]J1615–2420 across all four IRAC channels]Stacked residuals images for [SCH06] J0359+2009, Sz 41, FW Tau, and [SCH06]J1615–2420 (rows) across all four IRAC channels (columns). Images were generated by combining individual residual images after the primary PSF had been subtracted, placing each on a final grid with a pixel scale 5 times smaller than the original IRAC pixel scale of 1.″22, shifting to a common origin, and rotating so that north is up and east is left. The stacked residuals images are displayed with a linear color scale and 5-σ contours overlaid. The minimum and maximum pixel value of the color bar are given in the bottom lefthand corner in units of DN/s. A red star denotes the position of the primary while a red or dashed circle denotes the expected position of the companion. **First row:** [SCH06] J0359+2009 is an example of a straightforward companion detection. See Section 2.6.2 for more details on this system. **Second row:** Sz 41 is the brightest member of our sample ($M_{[3.6]}$=0.89) and appears saturated in Channel 4 as evidenced by the ring-like structure in the residuals surrounding the primary location. We are still able to measure photometry for the system that agrees with previous measurements. The other bright object to the upper left of the system is a known background giant. **Third row:** Residuals images for FW Tau C, which we are able to resolve across all four IRAC channels for the first time. See Sections 2.6.2 and 2.7.2 for more details on this system. **Fourth row:** the candidate companion of [SCH06] J1615–2420 was not detected by our pipeline. A dotted circle is placed at its expected location. The bright object to the upper left is another Upper Sco member.

Table 2.7: Derived Masses

2MASS	Other Name	Distance (pc)	$M_{[3.6]}$ (mag)	Age (Myr)	Reference	Mass[a]
J03590986+2009361 B	[SCH06] J0359099+2009362 B	117.4 ± 2.3	8.53 ± 0.05	$5 - 10$	1	$15 - 16\ M_{\rm Jup}$
J04233539+2503026 B	FU Tau B	131.2 ± 2.6	6.80 ± 0.07	$1 - 2$	2	$22 - 29\ M_{\rm Jup}$
J04292971+2616532 C	FW Tau C	145 ± 15	7.94 ± 0.24	$1 - 2$	2	$10 - 14\ M_{\rm Jup}$[b]
J04554970+3019400 c1		2920 ± 1360	0.96 ± 0.80	...	...	...
J05373850+2428517 c1	[SCH06] J0537385+2428518 c1	114.5 ± 1.2	> 7.08	$1 - 2$	1	$< 25\ M_{\rm Jup}$
J11075588–7727257 B	CHXR 28 B	202.1 ± 10.4	1.98 ± 0.11	$2 - 3$	3	$1.2 - 1.5\ M_{\odot}$
J11122441–7637064 B	Sz 41 B	192.7 ± 0.8	3.08 ± 0.02	$2 - 3$	3	$0.47 - 0.61\ M_{\odot}$
J16101918–2502301 B	USco 1610–2502 B	152.0 ± 1.9	4.99 ± 0.04	$5 - 10$	4, 5	$0.18 - 0.28\ M_{\odot}$
J16103196–1913062 B	USco 1610–1913 B	132.9 ± 1.3	6.51 ± 0.03[c]	$5 - 10$	4, 5	$34 - 73\ M_{\rm Jup}$
J16111711–2217173 c1	[SCH06] J16111711–22171749 c1	213.1 ± 18.3	> 11.11	$5 - 10$	4, 5	$< 10\ M_{\rm Jup}$
J16151116–2420153 c1	[SCH06] J16151115–24201556 c1	143.8 ± 4.5	> 12.00	$5 - 10$	4, 5	$< 10\ M_{\rm Jup}$

Age ranges for target systems obtained from the following references: (1) Slesnick et al. (2006); (2) Kraus & Hillenbrand (2009a); (3) Luhman (2004); (4) de Zeeuw et al. (1999); (5) Pecaut et al. (2012).

[a]A model-derived mass is not meaningful for the neighbor to J04554970+3019400 because it is a background star. For candidate companions that could not be confirmed, we list the mass or mass limit that would be consistent with that photometry.

[b]The nature of FW Tau C is a matter of debate since different aspects of its observations are consistent with either a substellar companion surrounded by an edge-on disk or a PMC embedded in a low inclination disk. See Sections 2.6.2 and 2.7.2 for further discussion.

[c]No [3.6] images were available for USco 1610–1913. The listed absolute magnitude and derived mass are based on the [4.5] magnitude measured in this work.

In Figure 2.5 we present a color-magnitude diagram of $[3.6] - [8.0]$ versus $[3.6]$ showing the 10 system primaries, four confirmed low-mass companions, and one candidate companion detected in Channels 1 and 4, as well as Upper Scorpius members with both *Gaia* DR2 parallaxes and *Spitzer*/IRAC photometric measurements from Luhman & Mamajek (2012). We also show the intrinsic photospheric mid-infrared color-magnitude sequences from BT-Settl models (Allard et al. 2012) for 1 and 10 Myr objects in dashed light blue and black lines, respectively. We use these $[3.6] - [8.0]$ colors to assess the presence of excess emission due to a disk since intrinsic photospheric colors can vary with spectral type. Three primaries have $[3.6] - [8.0]$ color more than 3-σ above their intrinsic photosphere color (Sz 41, FU Tau, and 2MASS J0455+3019) while one candidate and four confirmed wide companions have $[3.6] - [8.0]$ color more than 3-σ above their expected intrinsic photosphere color. Tables 2.8 and 2.9 list the primary and secondary IRAC colors of our target sample across all channels, respectively. We also show the H–R diagram positions of our entire target sample in Figure 2.6.

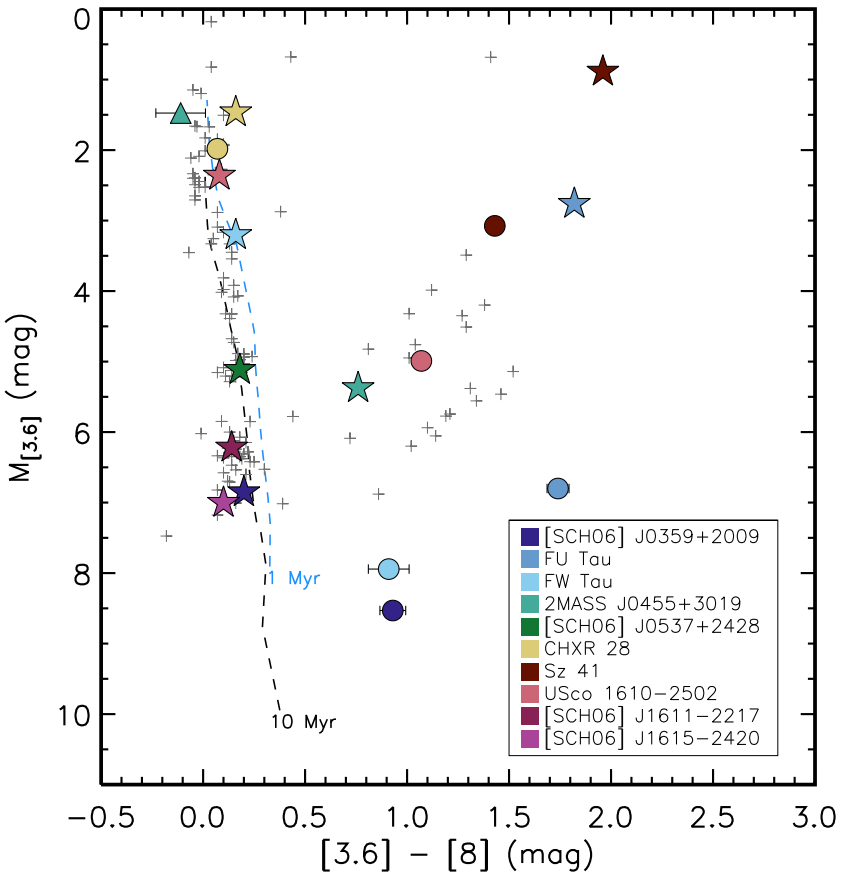

Figure 2.5: a
nd [8.0] measurements]*Spitzer*/IRAC color-magnitude diagram for our target systems and Upper Scorpius members with IRAC [3.6] and [8.0] measurements from Luhman & Mamajek (2012). Absolute $[3.6]$ magnitudes were determined using *Gaia* DR2 distance estimates from Bailer-Jones et al. (2018), or if an estimate did not exist, the canonical distance to the star-forming region of which the system is a member. The primary components of the target sample members are indicated as stars while the confirmed companions are indicated as filled circles. The nearby neighbor to 2MASS J0455+3019 is an unassociated background star and is denoted by a teal triangle. Also indicated are the intrinsic photospheric $[3.6] - [8.0]$ colors from BT-Settl models of Allard et al. (2012) at 1 and 10 Myr, using dashed light blue and black lines, respectively. Three sample primaries and five secondaries have $[3.6] - [8.0]$ colors indicative of a circumstellar or circum(sub)stellar disks.

Table 2.8: Measured Mid-IR Colors for Primaries

2MASS	Other Name	$[3.6]-[4.5]$ (mag)	$[3.6]-[5.8]$ (mag)	$[3.6]-[8.0]$ (mag)	$[4.5]-[5.8]$ (mag)	$[4.5]-[8.0]$ (mag)	$[5.8]-[8.0]$ (mag)	Disk? Y/N
J03590986+2009361	[SCH06] J0359099+2009362	0.11 ± 0.02	0.15 ± 0.03	0.20 ± 0.03	0.04 ± 0.03	0.09 ± 0.03	0.05 ± 0.03	N
J04233539+2503026	FU Tau A	0.61 ± 0.02	1.06 ± 0.02	1.82 ± 0.02	0.45 ± 0.02	1.21 ± 0.02	0.76 ± 0.02	Y
J04292971+2616532	FW Tau AB	0.11 ± 0.02	0.17 ± 0.02	0.16 ± 0.02	0.06 ± 0.02	0.05 ± 0.02	-0.01 ± 0.02	N
J04554970+3019400		0.19 ± 0.02	0.42 ± 0.02	0.77 ± 0.02	0.23 ± 0.02	0.58 ± 0.02	0.35 ± 0.02	Y
J05373850+2428517	[SCH06] J0537385+2428518	0.09 ± 0.02	0.16 ± 0.02	0.18 ± 0.02	0.08 ± 0.02	0.09 ± 0.02	0.02 ± 0.02	N
J11075588–7727257	CHXR 28 Aa,Ab	-0.01 ± 0.02	0.18 ± 0.03	0.16 ± 0.03	0.18 ± 0.03	0.16 ± 0.03	-0.02 ± 0.03	N
J11122441–7637064	Sz 41 A	0.44 ± 0.02	0.92 ± 0.02	1.96 ± 0.02	0.48 ± 0.02	1.53 ± 0.02	1.04 ± 0.02	Y
J16101918–2502301	USco 1610–2502 A	-0.06 ± 0.02	0.02 ± 0.02	0.08 ± 0.02	0.08 ± 0.02	0.14 ± 0.02	0.06 ± 0.02	N
J16103196–1913062	USco 1610–1913 A	...	...	...	...	0.09 ± 0.02	...	N
J16111711–2217173	[SCH06] J16111711–22171749	0.11 ± 0.02	0.20 ± 0.03	0.14 ± 0.04	0.09 ± 0.03	0.03 ± 0.04	-0.06 ± 0.05	N
J16151116–2420153	[SCH06] J16151115–24201556	0.07 ± 0.02	0.15 ± 0.03	0.10 ± 0.04	0.07 ± 0.03	0.02 ± 0.04	-0.05 ± 0.04	N

If an entry is missing, either no IRAC data existed for that object or no images were adequately fit in that IRAC Channel.

Table 2.9: Measured Mid-IR Colors for Detected Companions and Neighbors

2MASS	Other Name	$[3.6]-[4.5]$ (mag)	$[3.6]-[5.8]$ (mag)	$[3.6]-[8.0]$ (mag)	$[4.5]-[5.8]$ (mag)	$[4.5]-[8.0]$ (mag)	$[5.8]-[8.0]$ (mag)	Disk? Y/N
J03590986+2009361 B	[SCH06] J0359099+2009362 B	0.24 ± 0.03	0.51 ± 0.04	0.94 ± 0.07	0.27 ± 0.04	0.69 ± 0.07	0.42 ± 0.07	Y
J04233539+2503026 B	FU Tau B	0.33 ± 0.07	0.86 ± 0.06	1.74 ± 0.05	0.53 ± 0.05	1.41 ± 0.05	0.88 ± 0.03	Y
J04292971+2616532 C	FW Tau C	0.46 ± 0.10	0.48 ± 0.11	0.91 ± 0.10	0.02 ± 0.09	0.45 ± 0.08	0.44 ± 0.09	Y
J04554970+3019400 c1		0.02 ± 0.03	0.00 ± 0.05	-0.11 ± 0.12	-0.01 ± 0.05	-0.13 ± 0.12	-0.12 ± 0.13	N
J11075588–7727257 B	CHXR 28 B	0.05 ± 0.03	0.19 ± 0.05	0.08 ± 0.04	0.15 ± 0.05	0.03 ± 0.04	-0.12 ± 0.06	N
J11122441–7637064 B	Sz 41 B	0.57 ± 0.03	0.75 ± 0.05	1.44 ± 0.03	0.18 ± 0.05	0.86 ± 0.03	0.69 ± 0.05	Y
J16101918–2502301 B	USco 1610–2502 B	0.24 ± 0.04	0.47 ± 0.03	1.08 ± 0.03	0.23 ± 0.04	0.84 ± 0.03	0.61 ± 0.02	Y
J16103196–1913062 B	USco 1610–1913 B	...	...	...	...	0.14 ± 0.03	...	N

If an entry is missing, either no IRAC data existed for that object or no images were adequately fit in that IRAC Channel.

2.6.2 Notes on Individual Systems

Our reprocessing of IRAC images yielded detections of one candidate and six confirmed low-mass companions and one unassociated neighbor. Five of the companions have $[3.6]-[8.0]$ colors more than 3-σ above their expected intrinsic photosphere color. We describe four of them in more detail in the following sections.

[SCH06] J0359+2009 B: A New Wide Companion Near the Planet–Brown Dwarf Boundary

Slesnick et al. (2006) first identified 2MASS J03590986+2009361 (hereafter [SCH06] J0359+2009) as a potential member of an older distributed population of Taurus, proposed by Wichmann et al. (1996). Observational follow-up conducted by Kraus & Hillenbrand (2012) identified a candidate low-mass companion in the vicinity of [SCH06] J0359+2009 at projected separation $\rho = 4\farcs66$. No further targeted observations to confirm association have been reported in the literature and the nature of the candidate companion has remained unclear.

Gaia DR2 (Gaia Collaboration et al. 2018) measure $(\mu_\alpha, \mu_\delta, \pi) = (4.95 \pm 0.37$ mas $\mathrm{yr}^{-1}, -14.14 \pm 0.20$ mas $\mathrm{yr}^{-1}, 8.49 \pm 0.16$ mas) for the primary and $(\mu_\alpha, \mu_\delta, \pi) = (2.85 \pm 1.69$ mas $\mathrm{yr}^{-1}, -16.49 \pm 0.98$ mas $\mathrm{yr}^{-1}, 7.27 \pm 0.87$ mas) for the candidate companion. These measurements are consistent with the expected Taurus proper motion ($\mu = (+6, -20)$ mas yr^{-1}; Kraus et al. 2017), as well as comovement and codistance for the two objects to within 1.5-σ. With these additional data we confirm association and report the discovery of a new low-mass companion (hereafter [SCH06] J0359+2009 B; see Figure 2.7).

In Table 2.10 we summarize Pan-STARRS optical (PS1; Chambers et al. 2016), 2MASS near-infrared (Cutri et al. 2003) and the *Spitzer*/IRAC mid-infrared photometry measured in this work for both [SCH06] J0359+2009 A and [SCH06] $J0359{+}2009$ B. We use these data to analyze the SEDs of the [SCH06] J0359+2009 system. We fit solar metallicity BT-Settl model atmospheres (Allard et al. 2012) spanning effective temperatures between 2000 and 3500 K ($\Delta T_{\rm eff} = 100$ K) fixed at $\log$ g $= 4.0$, which is appropriate for late M dwarfs with ages $\tau > 5$ Myr from evolutionary models. We also fit for $E(B-V)$ using the extinction curve of Fitzpatrick (1999) spanning from 0.0 to 0.2 mag in steps of 0.01 mag. For the primary

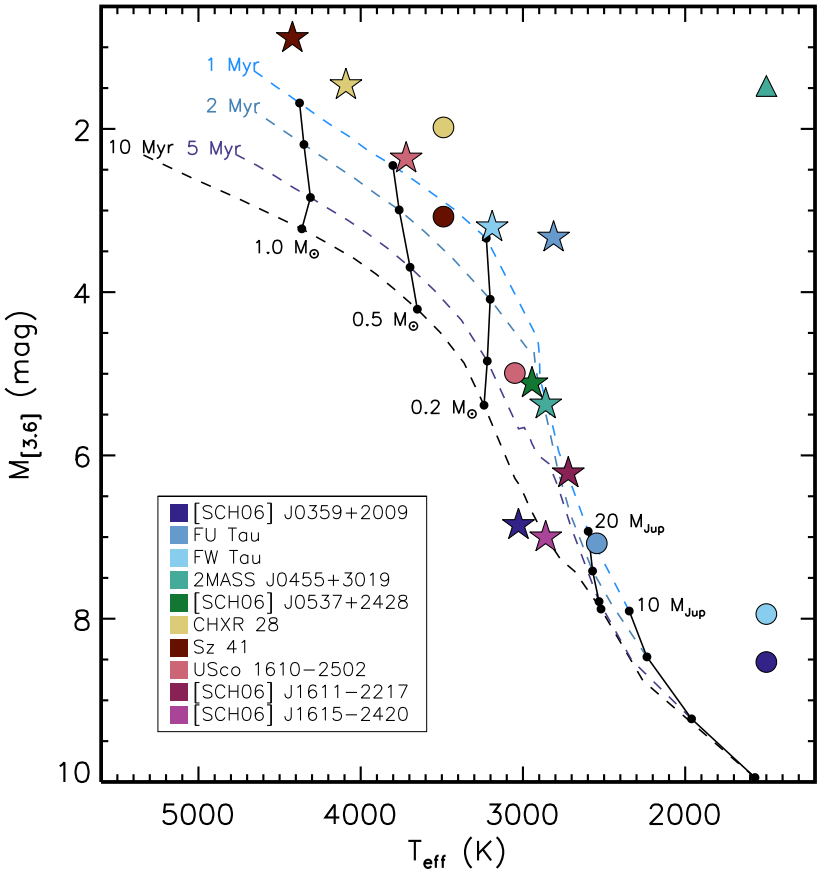

Figure 2.6: H-R diagram for our target systems. The primary components of the target sample members are indicated as stars and confirmed secondary components indicated as circles. We use $T_{\rm eff}$ measurements reported in the literature for objects that were spectroscopically derived from spectral types, or we estimate them based on optical spectral types from the literature and the spectral type to temperature conversion from Herczeg & Hillenbrand (2014). The 1, 2, 5, and 10 Myr isochrones of Allard et al. (2012) are plotted (dashed lines) with 10 $M_{\rm Jup}$, 20 $M_{\rm Jup}$, 0.2 $M_{\odot}$, 0.5 $M_{\odot}$, and 1.0 $M_{\odot}$ iso-mass tracks (solid lines). The secondary components to [SCH06] J0359+2009 (dark blue circle) and FW Tau (light blue circle), and nearby neighbor to 2MASS J0455+3019 (teal triangle) are indicated at their corresponding $M_{[3.6]}$ but not placed on this diagram because they do not have independent temperature estimates.

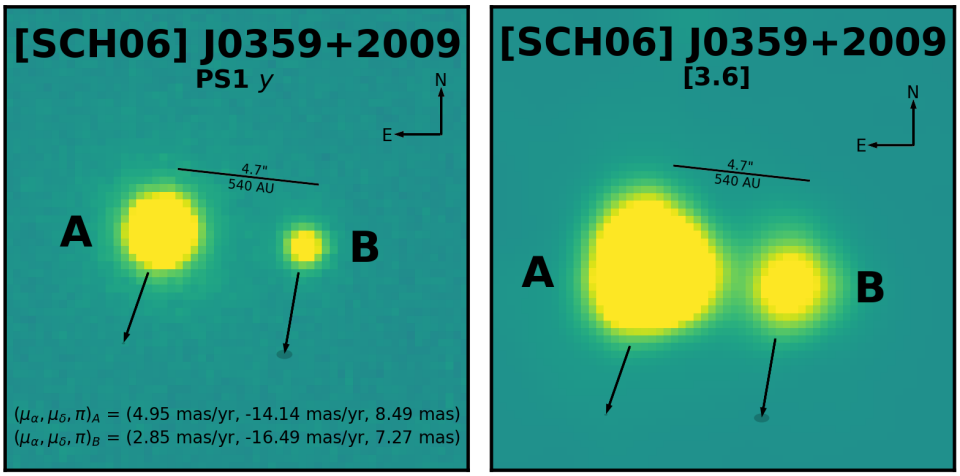

Figure 2.7: J 0359+2009 system]Pan-STARRS y-band (left) and IRAC Ch 1 (right) images of the [SCH06] J0359+2009 system. [SCH06] J0359+2009 B is located at a separation of $4\farcs7$ (540 au). Proper motion vectors for [SCH06] J0359+2009 A and B are shown as black arrows indicating the direction of motion; the length of the vectors have been magnified to scale to make them visible. The proper motion errors are also shown at the ends of the proper motion vectors as shaded gray ellipses. Given the component masses and projected separation (see Section 2.6.2), this system appears to be an older analog of ultrawide brown dwarf pairs like FU Tau (Luhman et al. 2009).

we fit PS1 $grizy$, 2MASS JHK and *Spitzer*/IRAC photometric data using χ^2 minimization. We fit only the PS1 $rizy$, 2MASS JHK and IRAC $[3.6]$ photometric data for the companion. We present the SEDs of both [SCH06] J0359+2009 and [SCH06] J0359+2009 B in Figure 2.8.

Table 2.10: [SCH06] J0359+2009 Photometry

Filter	Wavelength (μm)	A Flux (mag)	B Flux (mag)	Reference
$g_{\rm P1}$	0.481	19.56 ± 0.02[a]	> 21.25[a]	1
$r_{\rm P1}$	0.617	18.28 ± 0.02[a]	> 19.49[a]	1
$i_{\rm P1}$	0.752	16.29 ± 0.02[a]	19.58 ± 0.02[a]	1
$z_{\rm P1}$	0.866	15.34 ± 0.02[a]	18.10 ± 0.02[a]	1
$y_{\rm P1}$	0.962	14.86 ± 0.02[a]	17.25 ± 0.02[a]	1
J	1.235	13.48 ± 0.03	15.48 ± 0.07	2
H	1.662	12.83 ± 0.03	14.79 ± 0.06	2
K_s	2.159	12.53 ± 0.03	14.42 ± 0.07	2
$[3.6]$	3.6	12.20 ± 0.02	13.88 ± 0.02	This work
$[4.5]$	4.5	12.08 ± 0.02	13.64 ± 0.02	This work
$[5.8]$	5.8	12.05 ± 0.02	13.37 ± 0.04	This work
$[8.0]$	8.0	12.00 ± 0.03	12.95 ± 0.06	This work

[a]AB magnitudes

References – (1) Chambers et al. (2016), (2) Cutri et al. (2003)

The best-fitting model for [SCH06] J0359+2009 A is $T_{\rm eff} = 2900 \pm 50$ K and $E(B-V) = 0.09^{+0.02}_{-0.015}$ mag while for [SCH06] J0359+2009 B the best-fitting model is $T_{\rm eff} = 2400 \pm 50$ K and $E(B-V) = 0.00 \pm 0.03$ mag. Although the best-fit SEDs of [SCH06] J0359+2009 A and B have discrepant $E(B-V)$ of ~ 0.1 mag, wide binary pairs in Taurus have been found to have differing reddening values of similar amounts (Herczeg & Hillenbrand 2014) due to the systematic uncertainty in atmospheric models of young low-mass objects (e.g., Dupuy et al. 2010), in addition to the young objects themselves likely harboring spots that change the emergent spectrum (e.g., Gully-Santiago et al. 2017). We infer system masses from predictions of BT-Settl evolutionary models (see Figure 2.9) based on their absolute $[3.6]$ magnitude and the best-fitting model $T_{\rm eff}$. We estimate [SCH06] J0359+2009 A to have a mass of $60 \pm 10 M_{\rm Jup}$ and the companion to have a mass of $20 \pm 5 M_{\rm Jup}$. The

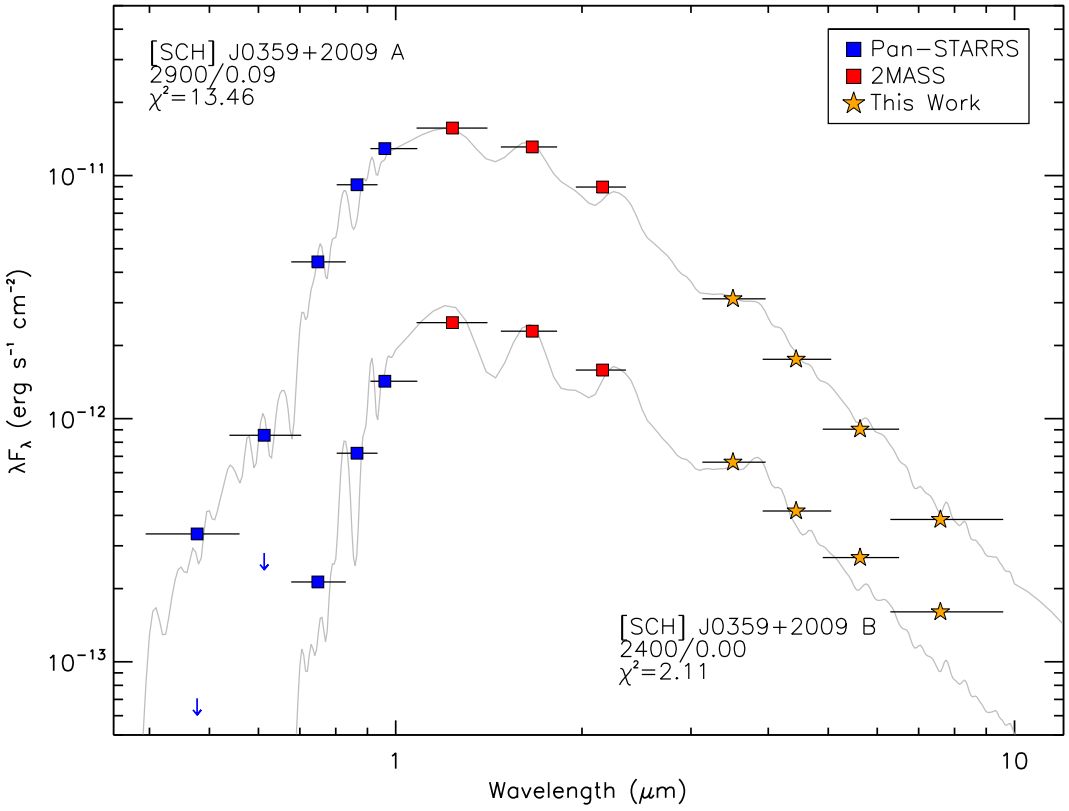

Figure 2.8: J
0359+2009 and its companion [SCH06] J0359+2009 B]Spectral energy distributions of [SCH06] J0359+2009 and its companion [SCH06] J0359+2009 B. Photometric uncertainties are smaller than the symbol sizes. An $E(B-V) = 0.09^{+0.02}_{-0.015}$ mag, $T_{\rm eff} = 2900 \pm 50$ K BT-Settl model best fits the photometry of the primary for wavelengths > 0.4 μm. An $E(B-V) = 0.00 \pm 0.03$ mag, $T_{\rm eff} = 2400 \pm 50$ K BT-Settl model best fits the $0.7 - 3.6$ μm photometry of the companion. Both models are plotted in gray. The bandpasses of the photometric filters are plotted as horizontal lines. The excess flux seen in $[5.8]$ and $[8.0]$ is likely due to the presence of a circumplanetary/circum(sub)stellar disk.

H-R diagram positions are nominally consistent with isochronal ages of 10-20 Myr, though those ages appear to be underestimated by most current models (e.g., Feiden 2016). As seen in Figure 2.8, the *Spitzer*/IRAC 8 μm photometry for [SCH06] J0359+2009 B disagrees with the best-fitting model at >8-σ. This is consistent with our measured mid-infrared excess of $[3.6] - [8.0] = 0.94 \pm 0.07$ mag which is discrepant with the color of a M9 photosphere at the 7.9-σ level and L0 photosphere at the 4.4-σ level as measured empirically by Luhman et al. (2010). Given the component masses and projected separation, this system appears to be an older analog of ultrawide brown dwarf pairs like FU Tau (Luhman et al. 2009).

Kraus & Hillenbrand (2012) identified a second candidate companion in the vicinity of [SCH06] J0359+2009 A at projected separation $\rho = 5\farcs95$ and P.A.$= 99°$. This source was not in our original target sample nor do we detect it (see Figure 2.4, top row). We derive upper limits on its IRAC photometry of $[3.6] > 18.8$ mag, $[4.5] > 18.0$ mag, $[5.8] > 16.5$ mag, and $[8.0] > 15.4$ mag based on our detection limits discussed in Section 2.6.3.

FU Tau

FU Tau AB is an isolated wide binary with $\rho = 5\farcs7$ (Luhman et al. 2009), or 750 au at its parallactic distance (131.2 pc; Gaia Collaboration et al. 2018). Using spectroscopic observations in the optical, Luhman et al. (2009) estimate the spectral type of the primary to be M7.25 and the secondary to be M9.25, deriving model-dependent masses for FU Tau A and B to be 50 $M_{\rm Jup}$ and 15 $M_{\rm Jup}$, respectively. We clearly detect FU Tau B in all four IRAC channels. Both FU Tau A and B show significant excess with $[3.6] - [8.0] = 1.83 \pm 0.02$ mag for the primary and $[3.6] - [8.0] = 1.77 \pm 0.08$ mag for the secondary. This confirms the previous detection of this disk as detailed in Luhman et al. (2009). FU Tau A also shows signs of variability. Observations taken in 2007 exist of FU Tau in all four channels. Observations were also taken for FU Tau in 2005, but only in Channels 2 and 4. Visual inspection of the residual images produced by our pipeline suggested Channels 2 and 4 were not well fit by the same contrast values across both epochs. We ran the individual epochs of FU Tau observations through our pipeline to quantify the variability. We measure $[4.5] = 7.67 \pm 0.02$ and $[8.0] = 6.41 \pm 0.02$ for the 2005 observations while we measure $[4.5] = 7.84 \pm 0.02$ and $[8.0] = 6.68 \pm 0.02$ in the 2007

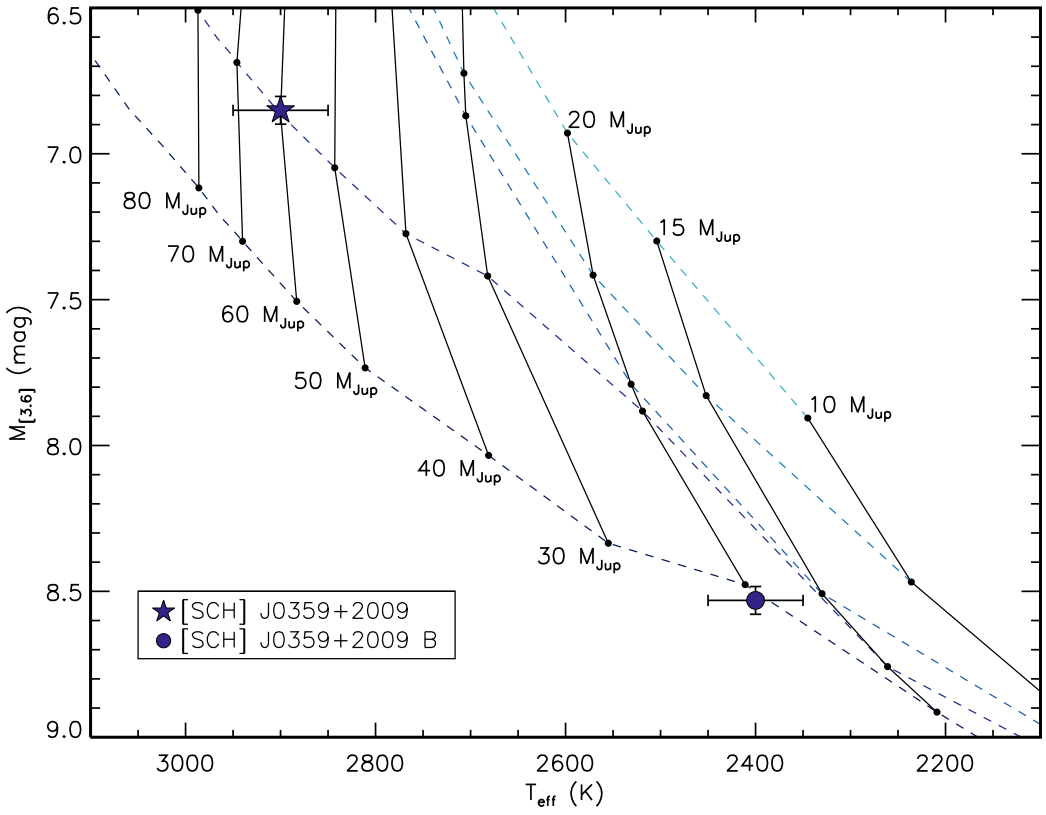

Figure 2.9: J 0359+2009 and its companion]H-R diagram for [SCH06] J0359+2009 and its companion. For both components, the temperatures are estimated from our SED fits (Section 5.2.1; Figure 2.8). The 1, 2, 5, 10, and 20 Myr isochrones of Allard et al. (2012) are plotted (dashed lines) with mass tracks (solid lines) from 10 $M_{\rm Jup}$ to 80 $M_{\rm Jup}$. The H-R diagram positions are nominally consistent with isochronal ages of 10-20 Myr, though those ages appear to be underestimated by most current models (e.g., Feiden 2016). The position of the primary indicates a mass of 60 ± 10 $M_{\rm Jup}$ while the position of the companion indicates a mass of 20 ± 5 $M_{\rm Jup}$.

images. The FU Tau B photometry does not change significantly between epochs, suggesting the variability is due to the primary. In addition to this, FU Tau A is overluminous compared to the 1 Myr isochrone. Luhman et al. (2009) posit that this may be due to FU Tau A itself being an unresolved binary, though this solution would not account for all of the overluminosity. Stelzer et al. (2010) obtained *Chandra* X-ray observations which suggested that atypical magnetic activity or accretion is present in FU Tau A and hence that severe rotation and magnetic field effects might be reducing the efficiency of convection, affecting its place on the H–R diagram.

More recent observations of the primary suggest its spectral type is slightly earlier at ∼M6.5−M7 (e.g., Scholz et al. 2012; Herczeg & Hillenbrand 2014). To assess whether the overluminosity of the primary continues into the IRAC channels, we converted the spectral types of FU Tau A (M6.5) and B (M9.25) to effective temperatures using the relation from Herczeg & Hillenbrand (2014). We also adopt a distance of 131.2 pc from Gaia Collaboration et al. (2018) which is closer than the 140 pc distance that had been assumed in previous studies. The significant overluminosity of the primary persists across all IRAC channels and we show the example for Channel 1 in Figure 2.10. FU Tau A is above the BT-Settl 1 Myr isochrone of Allard et al. (2012) by 2.36, 2.33, 2.31, and 2.24 mag in the IRAC channels. These results are of similar magnitude to the ~ 2 mag overluminosity found in the J band by Scholz et al. (2012), though we do not confirm their claim of overluminosity for FU Tau B.

FW Tau

FW Tau AB is a close binary system of young M5.5 stars that harbors a third component (hereafter FW Tau C) at $\rho = 2\farcs3$. The nature of FW Tau C is a matter of debate since different aspects of its observations are consistent with either a substellar companion surrounded by an edge-on disk or a PMC embedded in a low inclination disk (e.g., Kraus et al. 2015; Caceres et al. 2015; Wu & Sheehan 2017). Kraus et al. (2014a) first confirmed FW Tau C as a comoving wide-separation companion with near-infrared observations using the Keck-II 10m telescope and NIRC2, and given its luminosity they estimated its mass to be $10 \pm 4\,M_{\rm Jup}$ for system ages between 1-5 Myr (Chabrier et al. 2000b). More recent ALMA Cycle 3

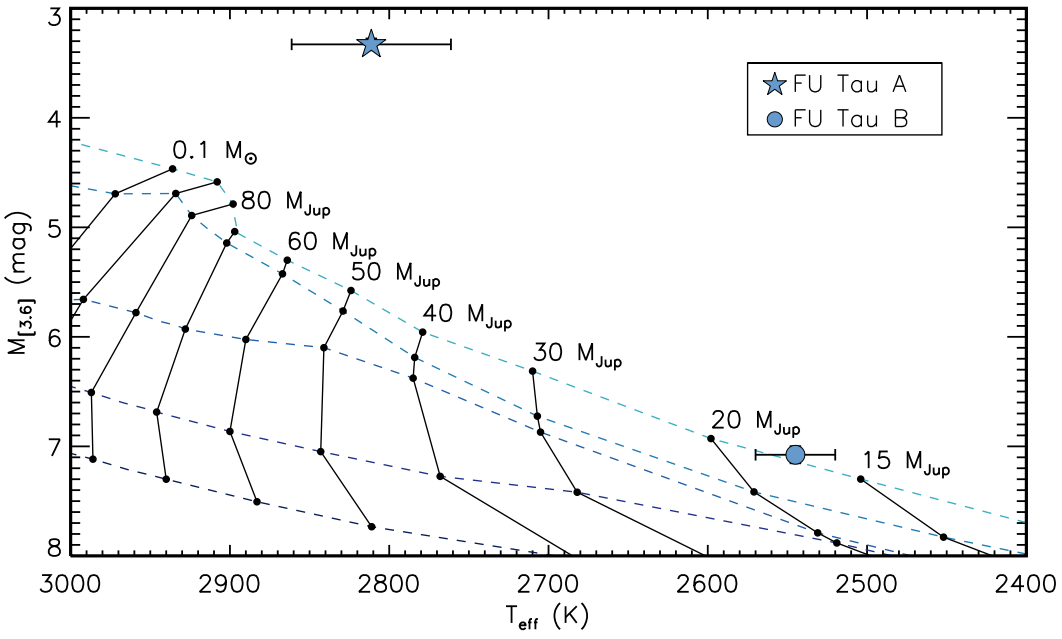

Figure 2.10: H-R diagram for FU Tau AB. For both components, $T_{\rm eff}$ was determined using the temperature scale for young stars from Herczeg & Hillenbrand (2014). The 1, 2, 5, 10, and 20 Myr isochrones of Allard et al. (2012) are plotted (dashed lines) with mass tracks (solid lines) from 15 $M_{\rm Jup}$ to 0.1 $M_{\odot}$. FU Tau A is significantly overluminous compared to the 1 Myr isochrone.

observations and modeling performed by Wu & Sheehan (2017) place the dynamical mass of FW Tau C closer to $\sim 0.1\ M_{\odot}$, but with a moderate disk inclination that does not explain its faint luminosity.

We are able to resolve FW Tau C and measure its mid-infrared photometry in all four IRAC channels. We measure the mid-infrared excess of FW Tau C to be $[3.6] - [8.0] = 0.91 \pm 0.10$ mag. The 8 μm flux offers the prospect of an independent test between the proposed explanations, as the predicted SED for each case varies most at 8–12 μm. We discuss this comparison further in Section 2.7.

USco 1610–2502

2MASS J16101918–2502301 (hereafter USco 1610–2502) is a member of Upper Sco (Preibisch et al. 1998) with a spectral type of M1. Its companion, USco 1610–2502 B, was confirmed to be a comoving companion by Aller et al. (2013), who measured a spectral type of M5.5 and a projected separation of $\rho = 5\farcs1$.

We have analyzed the SED of USco 1610–2502 B in a similar fashion as for the [SCH06] J0359+2009 system. We fit all PS1 and 2MASS photometry from the literature and include *Spitzer*/IRAC [3.6] and *WISE* Band 1 photometry. The best-fitting model for USco 1610–2502 B is $T_{\rm eff} = 2900 \pm 50$ K and $E(B-V) = 0.03 \pm 0.025$ mag. Figure 2.11 shows the best fitting model for USco 1610–2502 B as well as available photometry between 0.4 and 24 μm. There is no evidence for a circumstellar disk surrounding the primary but USco 1610–2502 B has a significant excess of $[3.6] - [8.0] = 1.08 \pm 0.03$ mag. USco 1610–2502B also has 2MASS $K_S - [3.6] = 0.36 \pm 0.06$ mag which is consistent with the colors of young stellar photospheres (Luhman et al. 2010). This confirms the "transitional disk" designation from Luhman & Mamajek (2012). Barenfeld et al. (2016) measured a 0.88 mm continuum flux of 0.30 ± 0.14 mJy and estimate an upper limit on the dust disk mass to be $<$0.5 $M_{\oplus}$.

Cieza et al. (2007) introduced a two-parameter scheme to understand the SED morphology of transitional disks based on identifying the longest wavelength at which the observed flux is dominated by stellar photosphere, $\lambda_{turnoff}$, and the slope of the IR excess, α_{excess}, between $\lambda_{turnoff}$ and 24 μm. In this classification system, $\lambda_{turnoff}$ corresponds to the dust temperature, and therefore size, of the inner hole, while α_{excess} indicates the sharpness of the inner hole. Disks completely

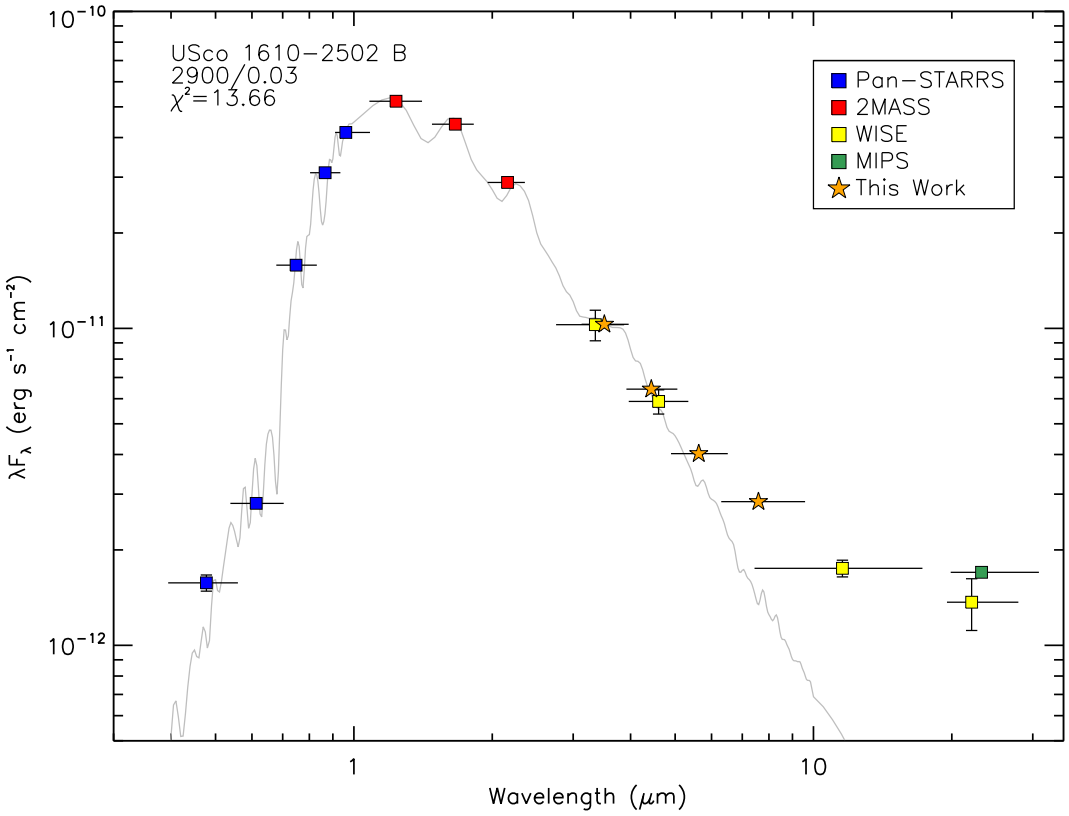

Figure 2.11: Spectral energy distribution of USco 1610–2502 B. Photometric uncertainties are smaller than the symbol sizes if not shown. An $E(B-V) = 0.03 \pm 0.025$ mag, $T_{\rm eff} = 2900 \pm 50$ K BT-Settl model (gray) best fits the photometry of the primary for wavelengths between 0.4 and 3.6 μm. The bandpasses of the photometric filters are plotted as horizontal lines. The excess flux seen for wavelengths > 4.5 μm is indicative of an irradiated disk with some grain growth and grain settling toward the midplane.

cleared of inner-hole dust have large and positive α_{excess} values, while disks undergoing significant grain growth and dust settling have large, negative α_{excess} values (Dullemond & Dominik 2004). For USco 1610–2502 B, $\lambda_{turnoff} = 5.8$ μm and $\alpha_{excess} = -0.61$, indicative of an irradiated disk with some grain growth and grain settling toward the midplane. No mid-infrared spectroscopy exists for USco 1610–2502 B so it is not yet possible to constrain its inner hole size in the absence of millimeter imaging (Espaillat et al. 2012).

2.6.3 Detection Limits

We evaluated the sensitivity to low-mass companions in terms of contrast for each target system individually by image and channel as a function of radial separation from the primary star. We performed aperture photometry by measuring the flux inside 100 randomly drawn apertures of radius 1 FWHM at each radius from the central star. We calculated the mean and standard deviation of these 100 fluxes to find the limiting flux and converted this value into *Spitzer*/IRAC magnitudes to obtain 3-σ limits. We also evaluated the sensitivity to low-mass companions in terms of contrast for each target system with the central star subtracted from the image in the same manner. The results of these calculations are presented as contrast curves in Figure 2.12 and Figure 2.13 for Channels 1 and 4, respectively. The curves show that the detectable contrast between central star and companion grows with increasing distance from the primary. For the images without primary PSF subtraction, a plateau is reached after $\sim 8\farcs5$ which corresponds to physical separations of 1000 au for the closest member of our target sample (114.5 pc) and 1800 au for the furthest (213.1 pc). Detectable contrast limits inward of $8\farcs5$ improve after PSF subtraction by an average of 5.5 magnitudes in Channel 1 and to the background noise-limit in Channel 4 for the majority of our target sample.

We convert our contrast curves into limiting masses using the BT-Settl evolutionary models of Allard et al. (2012) at 5 Myr and the measured absolute magnitudes of our target sample in each IRAC Channel. The contrast and mass limits reached as a function of radial separation from the PSF-subtracted images are presented in Tables 2.11 and 2.12, respectively. The 5 Myr BT-Settl evolutionary model does not go below 10 $M_{\rm Jup}$ ($M_{[3.6]} > 9.227$ mag) so we do not quote lower mass companions even though we are sensitive to them. Using the older COND-based

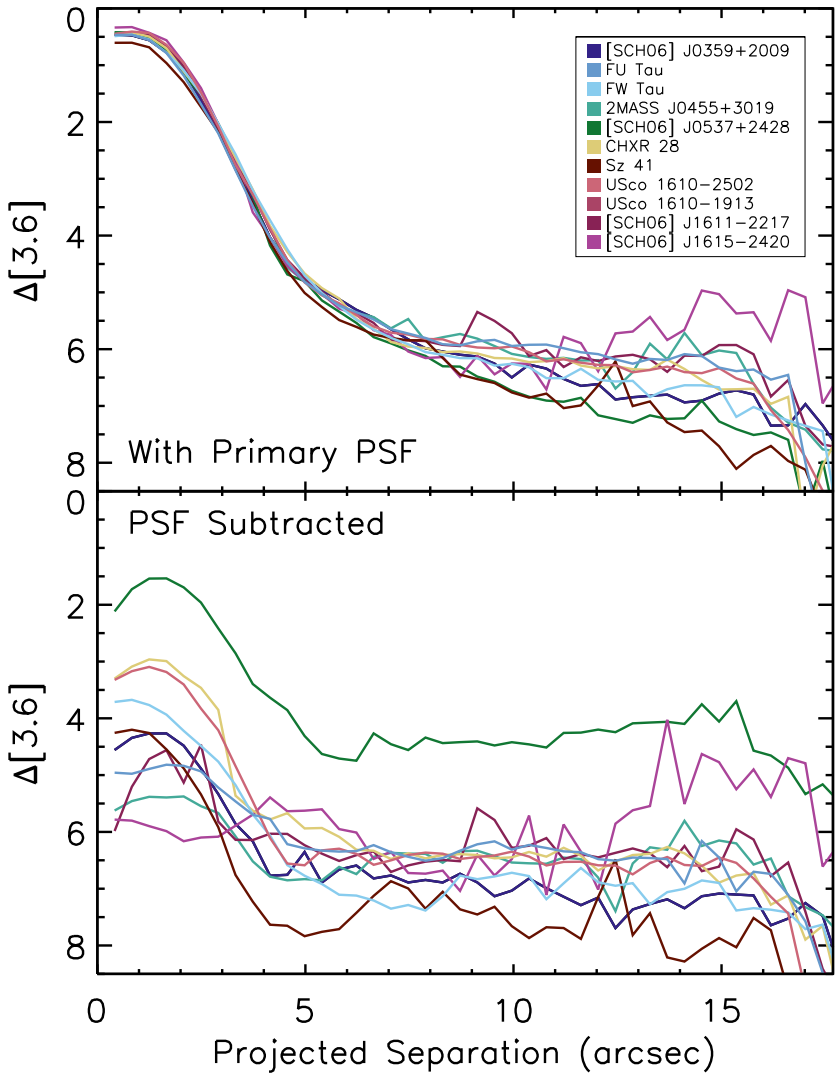

Figure 2.12: Contrast limits for the stacked IRAC Channel 1 images of our target sample. The top panel shows the contrast curves prior to PSF subtraction as a function of projected separation from the primary star in arcseconds. The bottom panel shows the corresponding contrast curve once the primary PSF has been subtracted.

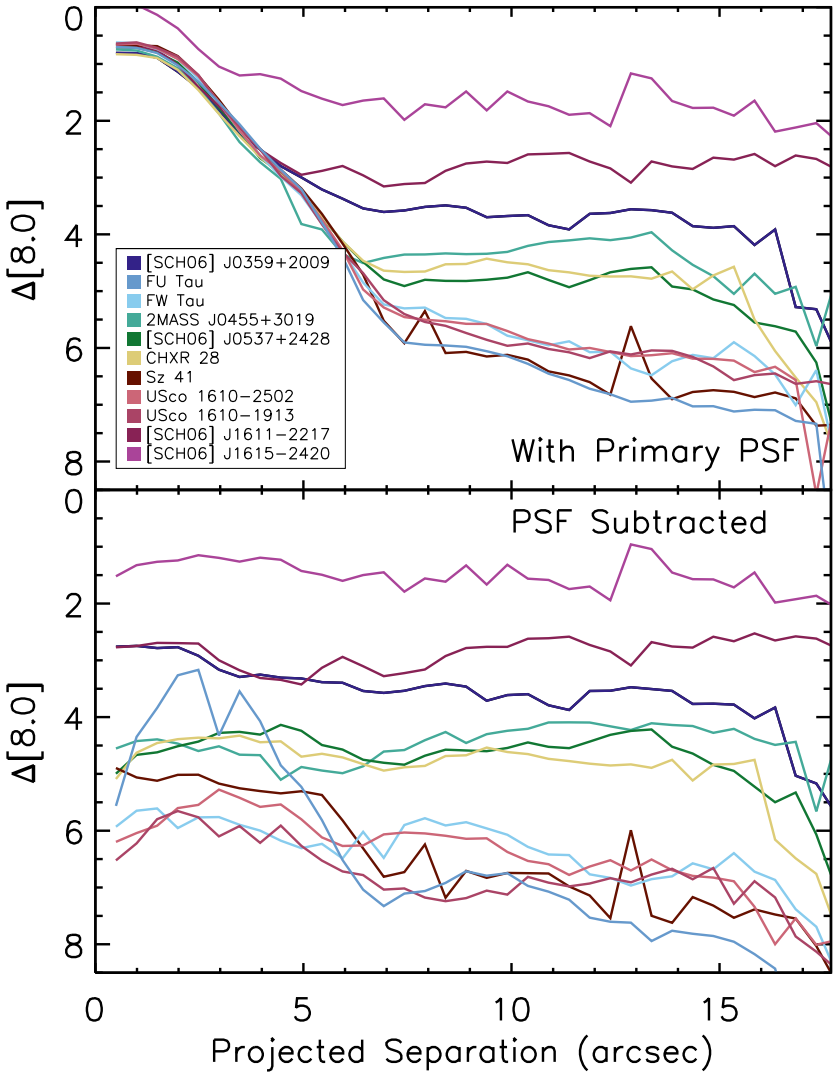

Figure 2.13: Same as Figure 2.12 but for IRAC Channel 4.

of models of Allard et al. (2001) we find we are sensitive to companion masses as low as 0.8 $M_{\rm Jup}$ at $10''$ away from a 1 Myr system and 2.9 $M_{\rm Jup}$ at $10''$ away from a 10 Myr system.

Table 2.11: Companion Contrast Limits

Target	Distance (pc)	Ch.	M (mag)	Exp. Time (s)	Contrast (mag) at ρ =(arcsec)									
					0.5	1.0	1.5	2.0	3.0	4.0	5.0	7.0	10.0	12.0
2MASS J03590986+2009361	117.4	1	6.85	10.4	4.51	4.31	4.27	4.44	5.45	6.55	6.38	6.77	7.01	7.17
		2	6.73	10.4	4.98	4.80	4.74	4.92	5.48	5.83	5.89	5.99	6.33	6.03
		3	6.70	10.4	3.52	3.57	3.63	3.77	4.23	4.42	4.53	4.29	4.26	4.34
		4	6.65	10.4	2.76	2.75	2.78	2.77	3.17	3.26	3.33	3.57	3.61	3.54
2MASS J04233539+2503026	131.2	1	2.76	0.4	4.91	4.90	4.78	4.73	5.17	5.86	6.07	6.31	6.13	6.37
		2	2.15	0.4	4.23	4.32	4.45	4.63	5.35	6.31	6.75	6.75	7.19	6.75
		3	1.70	10.4	4.91	4.87	4.85	4.80	4.83	5.92	6.96	6.91	7.23	7.44
		4	0.94	10.4	...	5.61	4.22	3.54	4.30	4.27	5.40	7.14	6.89	7.54
2MASS J04292971+2616532	145	1	3.20	1.0	6.87	6.46	6.10	5.95	5.93	6.75	8.07	8.27	7.65	7.66
		2	3.09	1.0	6.22	5.71	5.44	5.35	5.65	6.81	6.77	6.83	6.67	6.69
		3	3.03	10.4	6.52	6.37	6.40	6.53	7.18	7.68	8.38	6.98	6.66	6.74
		4	3.04	10.4	5.75	5.62	5.56	5.78	5.72	5.97	6.19	5.75	5.92	6.80
2MASS J04554970+3019400	156	1	5.37	10.4	5.81	5.64	5.35	5.20	5.60	6.45	6.81	6.44	6.40	6.11
		2	5.18	10.4	6.28	5.81	5.51	5.31	5.65	6.39	6.67	6.23	6.57	5.93
		3	4.96	10.4	4.74	4.37	4.30	4.43	4.90	5.12	5.00	4.83	4.48	4.11
		4	4.61	10.4	4.40	4.50	4.63	4.61	4.35	4.14	4.20	4.58	3.99	3.68
2MASS J05373850+2428517	114.5	1	5.12	10.4	2.04	1.65	1.54	1.67	2.52	3.55	4.33	4.43	4.42	4.20
		2	5.04	10.4	6.31	5.96	5.55	5.34	5.45	6.24	7.16	7.02	6.69	6.70
		3	4.96	10.4	4.60	4.50	4.58	4.83	5.65	5.77	5.65	5.66	5.53	5.53
		4	4.94	10.4	4.99	4.66	4.62	4.51	4.28	4.29	4.27	4.81	4.52	4.40
2MASS J11075588–7727257	202.1	1	1.46	0.4	3.21	3.07	3.00	3.09	4.13	5.03	5.45	6.46	6.44	6.53
		2	1.47	0.4	3.92	3.82	3.69	3.60	3.48	4.49	4.77	5.63	5.85	5.74

Table 2.11 continued on next page

Table 2.11 *(continued)*

Target	Distance (pc)	Ch.	M (mag)	Exp. Time (s)	Contrast (mag) at ρ =(arcsec)									
					0.5	1.0	1.5	2.0	3.0	4.0	5.0	7.0	10.0	12.0
		3	1.27	0.4	4.66	4.35	4.15	4.14	4.32	4.49	4.85	5.20	4.63	4.48
		4	1.30	0.4	5.11	4.64	4.48	4.38	4.36	4.40	4.50	4.82	4.57	4.81
2MASS J11122441–7637064	192.7	1	0.89	0.4	4.57	4.49	4.65	4.89	6.00	6.97	7.81	6.73	7.67	6.79
		2	0.46	0.4	7.32	5.83	5.47	5.63	6.91	7.69	7.66	7.10	8.12	7.99
		3	-0.03	0.4	4.94	4.78	4.77	4.84	5.24	5.66	6.08	6.10	5.58	5.94
		4	-1.07	0.4	4.88	4.95	5.12	4.97	5.18	5.25	5.38	6.78	6.73	7.34
2MASS J16101918–2502301	152	1	2.36	0.4	4.95	4.84	4.80	4.79	5.41	6.33	7.11	6.58	6.59	6.66
		2	2.42	0.4	5.03	4.74	4.65	4.71	5.11	5.38	5.67	5.23	5.77	5.49
		3	2.34	10.4	4.60	4.61	4.54	4.54	4.95	5.41	5.79	6.44	6.45	6.46
		4	2.28	10.4	6.63	6.50	6.28	5.90	5.49	5.50	6.02	6.33	6.32	6.76
2MASS J16103196–1913062	132.9	2	3.06	1.2	9.59	7.36	6.66	6.43	6.63	7.23	7.53	7.31	7.27	7.34
		4	2.96	10.4	5.75	5.49	5.36	5.16	5.15	5.67	6.18	7.00	7.63	7.28
2MASS J16111711–2217173	213.1	1	6.22	10.4	5.82	5.00	4.62	5.03	5.89	6.07	6.24	6.66	6.28	6.44
		2	6.11	10.4	5.37	4.99	4.72	6.16	6.08	5.51	5.72	5.83	6.08	5.72
		3	5.70	10.4	4.78	4.47	4.38	4.22	3.96	3.81	3.71	3.76	3.54	3.49
		4	6.08	10.4	2.77	2.75	2.69	2.70	3.01	3.31	3.40	3.27	2.73	2.76
2MASS J16151116–2420153	143.8	1	7.00	10.4	5.79	5.84	5.95	6.13	6.04	5.50	5.63	6.37	6.41	6.96
		2	6.92	10.4	4.84	4.88	5.32	6.16	7.69	8.43	6.03	6.25	5.61	4.96
		3	6.85	10.4	3.53	3.37	3.36	3.44	3.96	4.23	4.17	4.14	3.41	3.30
		4	6.90	10.4	1.52	1.32	1.26	1.24	1.20	1.20	1.43	1.50	1.37	1.76

Table 2.12: Companion Mass Limits

Target	Distance (pc)	Ch.	M (mag)	Exp. Time (s)	Mass Limit ($M_{\rm Jup}$) at ρ =(arcsec)									
					0.5	1.0	1.5	2.0	3.0	4.0	5.0	7.0	10.0	12.0
2MASS J03590986+200936	117.4	1	6.84	10.4	<10	<10	<10	<10	<10	<10	<10	<10	<10	<10
		2	6.73	10.4	<10	<10	<10	<10	<10	<10	<10	<10	<10	<10
		3	6.76	10.4	<10	<10	<10	<10	<10	<10	<10	<10	<10	<10
		4	6.79	10.4	<10	<10	<10	<10	<10	<10	<10	<10	<10	<10
2MASS J04233539+2503026	131.2	1	2.76	0.4	21	21	23	23	19	14	13	11	12	11
		2	2.15	0.4	37	35	33	29	22	15	12	12	<10	12
		3	1.70	10.4	31	32	32	33	33	20	13	13	11	<10
		4	0.94	10.4	...	31	140	240	130	130	35	16	18	13
2MASS J04292971+2616532	145	1	3.20	1.0	<10	<10	<10	11	11	<10	<10	<10	<10	<10
		2	3.09	1.0	<10	13	14	15	13	<10	<10	<10	<10	<10
		3	3.03	10.4	<10	<10	<10	<10	<10	<10	<10	<10	<10	<10
		4	3.04	10.4	10	12	12	10	11	<10	<10	10	<10	<10
2MASS J04554970+3019400	156	1	5.37	10.4	<10	<10	<10	<10	<10	<10	<10	<10	<10	<10
		2	5.18	10.4	<10	<10	<10	<10	<10	<10	<10	<10	<10	<10
		3	4.96	10.4	<10	<10	<10	<10	<10	<10	<10	<10	<10	<10
		4	4.61	10.4	<10	<10	<10	<10	<10	11	10	<10	12	14
2MASS J05373850+2428517	114.5	1	5.12	10.4	27	32	34	32	22	14	<10	<10	<10	<10
		2	5.04	10.4	<10	<10	<10	<10	<10	<10	<10	<10	<10	<10
		3	4.96	10.4	<10	<10	<10	<10	<10	<10	<10	<10	<10	<10
		4	4.94	10.4	<10	<10	<10	<10	<10	<10	<10	<10	<10	<10
2MASS J11075588–7727257	202.1	1	1.46	0.4	240	260	280	260	110	38	30	19	19	19
		2	1.47	0.4	120	130	150	160	170	50	40	26	24	25

Table 2.12 continued on next page

Table 2.12 *(continued)*

Target	Distance	Ch.	M	Exp. Time	Mass Limit ($M_{\rm Jup}$) at ρ =(arcsec)									
	(pc)		(mag)	(s)	0.5	1.0	1.5	2.0	3.0	4.0	5.0	7.0	10.0	12.0
		3	1.27	0.4	49	78	110	110	81	71	42	34	50	69
		4	1.30	0.4	34	46	58	70	71	67	56	40	49	40
2MASS J11122441–7637064	192.7	1	0.89	0.4	130	140	120	80	30	20	14	22	15	21
		2	0.46	0.4	19	39	57	46	23	17	17	21	14	15
		3	-0.03	0.4	170	190	200	190	140	78	45	44	84	50
		4	-1.07	0.4	420	390	340	390	330	300	280	67	72	37
2MASS J16101918–2502301	152	1	2.36	0.4	25	26	27	27	20	14	<10	12	12	11
		2	2.42	0.4	22	25	26	26	21	19	17	20	16	18
		3	2.34	10.4	27	27	28	28	23	19	16	12	12	12
		4	2.28	10.4	10	12	12	15	18	18	14	12	12	<10
2MASS J16103196–1913062	132.9	2	3.06	1.2	<10	<10	<10	<10	<10	<10	<10	<10	<10	<10
		4	2.96	10.4	11	13	14	16	16	12	<10	12	<10	<10
2MASS J16111711–2217173	213.1	1	6.22	10.4	<10	<10	<10	<10	<10	<10	<10	<10	<10	<10
		2	6.11	10.4	<10	<10	<10	<10	<10	<10	<10	<10	<10	<10
		3	5.70	10.4	<10	<10	<10	<10	<10	<10	<10	<10	<10	10
		4	6.08	10.4	10	10	11	11	<10	<10	<10	<10	10	10
2MASS J16151116–2420153	143.8	1	7.00	10.4	<10	<10	<10	<10	<10	<10	<10	<10	<10	<10
		2	6.92	10.4	<10	<10	<10	<10	<10	<10	<10	<10	<10	<10
		3	6.85	10.4	<10	<10	<10	<10	<10	<10	<10	<10	<10	<10
		4	6.90	10.4	13	15	15	16	16	16	14	14	16	11

2.7 Discussion

2.7.1 Optimizing the Search for Wide PMCs with Spitzer

The under-sampled PSF of *Spitzer*/IRAC has made detection of exoplanets in the mid-infrared difficult, especially at small angular separations ($\sim \lambda/D$) that most closely approach solar-system scales. Here, we have shown that our framework to model the IRAC PSF is successful at recovering known or candidate companions at a wide range of projected separations from their hosts. Previous analyses of archival *Spitzer*/IRAC images have placed initial constraints on the frequency of gas giant companions on wide orbits. Durkan et al. (2016) find companions with 0.5–13 $M_{\rm Jup}$ at separations of 100–1000 au occur with an upper frequency limit of 9% based on a sample of 121 stars. Baron et al. (2018) probe further separations of 1000–5000 au in their 177 star sample, finding an occurrence rate of $< 3\%$ for 1–13 $M_{\rm Jup}$ companions. As mentioned previously, both surveys searched for wide companion systems in young moving groups that are closer (< 100 pc) and older (> 10 Myr) than the regions from which our target sample was created. Because of this, the contrast between primary star and companion is more severe in those surveys. We have shown that our pipeline can measure photometry at a few λ/D in 1–10 Myr star-forming regions that are > 100 pc away. Our pipeline will enable a systematic exploration of the demographics and properties (e.g., companion mass functions, semi-major axis distributions, disk frequencies) of wide-orbit, low-mass companions systems for samples of discrete stars in future work.

Nine systems in our target sample have had their IRAC photometry measured previously. When comparing our measurements to the latest IRAC measurement reported almost all agree within the errors. Exceptions to this are the brightest systems in our sample whose multiplicity was determined with AO imaging after the IRAC photometric measurements were reported (e.g., CHXR 28, Sz 41) or primaries with significant variability between epochs (FU Tau A). In addition, Sz 41 A is saturated in Channel 4 as seen in Figure 2.4 by the characteristic ringed appearance in the PSF subtraction residuals. We are still able to resolve the companion and measure its photometry. The measured total flux from our pipeline agrees with the previous reported flux.

The presence of bright, unassociated stars in or just outside the 25×25 fitting

image mostly does not hinder the quality of the measured photometry significantly for our sample. One exception, 2MASS J04554970+3019400, is $\sim 30''$ away from HD 31305, a $V = 7.6$ mag A0 star. While its primary photometry is unaffected, the photometry of the neighbor is contaminated by stray light that is not effectively modeled by the background parameter. In these cases, fitting and subtracting off the flux of the nearby bright star prior to PSF subtraction with our framework could allow the companion to be more accurately fit.

[SCH06] J0359+2009 and [SCH06] J0537+2428 were the only targets that had not had their IRAC photometry measured and reported in the literature. These targets were located at the outskirts of canonical star-forming regions and until recently not studied in detail. Now with *Gaia* revealing so many more young systems, it is possible to evaluate whether they have wide companions and circumstellar disks, as well as re-evaluate interesting systems or systems where multiplicity was determined later.

More broadly, the Mid-Infrared Instrument (MIRI) on the *James Webb Space Telescope* will provide key insight by constraining disk sizes for young planetary-mass companions known and discovered prior to its launch. Previous searches for disk emission at radio wavelengths have yielded mostly upper limits which suggests wide-orbit PMCs may have smaller, hotter disks and are more suited for characterization in the mid-infrared (Wu et al. 2017). Our framework provides an efficient way to build targets of interest to be studied with *JWST* and the ELTs coming online in the next decade.

2.7.2 The Nature of FW Tau

As we described in 2.6.2, two scenarios have been proposed to explain FW Tau C: a PMC embedded in a low inclination disk or a substellar companion surrounded by an edge-on disk. Caceres et al. (2015) constructed the FW Tau system SED from near-infrared to millimeter wavelengths to explore the possible interpretations via disk modeling. Although they did not come to a definitive conclusion about the nature of FW Tau C with the limited data available, their models differ most in SED shape and brightness in the mid-infrared from 3–10 μm (see Figure 3 of Caceres et al. 2015).

We can independently test the proposed scenarios because we have resolved

FW Tau C across all IRAC channels. We find that the brightness of the IRAC photometry is more consistent with the edge-on disk model in Channels 1, 2, and 4 but also note that the SED shape across the four IRAC channels is actually more coincident with the PMC model (see Figure 2.14). Given the conflicting indications of this object's nature from across its SED, the enhanced sensitivity, spatial resolution, and wavelength coverage (3–30 μm) of MIRI may ultimately resolve its true nature.

2.8 Summary

We have developed an MCMC-based PSF fitter to re-analyze archival *Spitzer*/IRAC images of 11 young, low-mass stars with varying spectral types that host faint confirmed or candidate companions at a range of projected separations. Our framework accurately models the flux of the system allowing us to measure the mid-infrared photometry for any astrophysical source in the vicinity of young stars of interest. We recover six confirmed, and two candidate low-mass companions, two of which have never had *Spitzer*/IRAC photometry reported in the literature previously. One of these, [SCH06] J0359+2009 B, is a new companion with mass $20 \pm 5 M_{\rm Jup}$ and $[3.6] - [8.0]$ color indicative of a circum(sub)stellar disk. Using the evolutionary models of Allard et al. (2012), we show that we are sensitive to companions $< 10\,M_{\rm Jup}$ in the IRAC images. Our PSF-fitting framework is finally opening up a regime of parameter space that has yet to be studied in detail, revealing low-mass companions and whether they host disks.

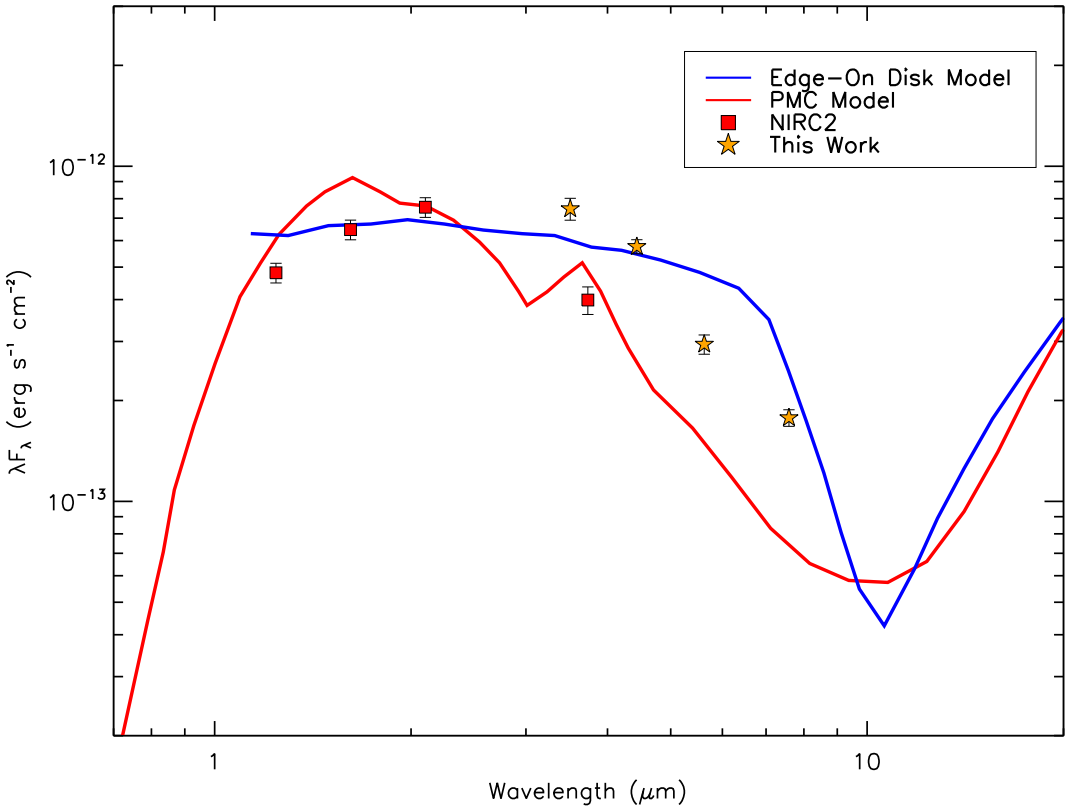

Figure 2.14: SED for the two proposed scenarios for the nature of the FW Tau system. The blue and red lines are the brown-dwarf/edge-on-disk model and PMC model from Caceres et al. (2015), respectively. The red squares are the NIRC2 photometric observations obtained by Kraus et al. (2014a) while the orange stars are the *Spitzer*/IRAC photometric measurements from this work. The brightness of the IRAC photometry is more consistent with the edge-on disk model in Channels 1, 2, and 4 but we note that the SED shape across the four IRAC channels appears to be more coincident with the PMC model.

Chapter 3: A Mid-Infrared Study of Directly-Imaged Planetary-Mass Companions using Archival *Spitzer*/IRAC Images[1]

3.1 Abstract

The atmospheres and accretion disks of planetary-mass and substellar companions provide an unprecedented look into planet and moon formation processes. In our ongoing effort to leverage the extraordinary sensitivity of the *Spitzer*/Infrared Array Camera (IRAC) at 3.6, 4.5, 5.8, and 8.0 μm to study wide planetary-mass and substellar companions near the diffraction limit, we present point-spread function (PSF) fitting photometry of archival *Spitzer*/IRAC images for nine stars (G0–M4+M7) in nearby star-forming regions or stellar associations that host companions at separations of $\rho = 1\farcs17 - 12\farcs33$. We detect all system primaries in all four IRAC channels and recover eight low-mass companions in at least one IRAC channel for our sample, five of which have not been resolved previously in IRAC images. We measure non-photospheric $[3.6] - [8.0]$ colors for four of the system companions (DH Tau B, 2M0441 B, SR 12 c, ROXs 42B b), confirming or indicating the presence of circumstellar or circum(sub)stellar disks. We detect fluxes consistent with photospheric emission for four other companions (AB Pic b, CHXR 73 b, 1RXS J1609 b, HD 203030 b) that are unlikely to host disks. Combined with past detections of accretion or disk indicators, we determine the global disk frequency of young (<15 Myr) wide companions with masses near the deuterium-burning limit to be $56\% \pm 12\%$.

3.2 Introduction

Dedicated exoplanet-finding surveys, such as the NASA *Kepler* mission (Borucki et al. 2010), have revolutionized our understanding of mature planetary system populations, but the formation and evolutionary processes that lead to their properties are still not well understood. The detailed study of exoplanets

[1]This chapter has been submitted for publication in The Astronomical Journal. The dissertation author was the primary investigator and author of this publication.

on an individual basis is usually hindered by the close proximity of the exoplanet to its bright stellar host. The atmospheres of transiting exoplanets can be characterized via transmission spectroscopy (e.g., Deming et al. 2013; Kreidberg et al. 2014; Wakeford et al. 2017), but this limits the planetary systems that can be studied to those with semi-major axes <1 au. Systems with planets orbiting on wider orbits have been observed via spectroscopy behind adaptive optics (AO; Patience et al. 2010; Barman et al. 2011; Konopacky et al. 2013; Haffert et al. 2019; Petrus et al. 2020) but these observations are difficult and expensive. Direct-imaging surveys of nearby star-forming regions have found an interesting population of wide-orbit (>100 au), planetary-mass companions (<20 $M_{\rm Jup}$; hereafter PMCs), such as 1RXS J160929.1–210524 b (8 $M_{\rm Jup}$, 330 au; Lafrenière et al. 2008b), GSC 06214–00210 B (14 $M_{\rm Jup}$, 330 au; Ireland et al. 2011), and HD 106906 b (11 $M_{\rm Jup}$, 650 au; Bailey et al. 2014). These systems have far more favorable separations and contrasts for the detailed study of gas giant atmospheres on larger semi-major axes. In addition, at young ages these systems also offer a unique view of moon-forming circumplanetary disks.

Most observations of directly-imaged exoplanets and planetary-mass companions have been made in the near-infrared (1–3 μm). Self-luminous exoplanets and planetary-mass objects emit substantial amounts of energy in the mid-infrared yet very few systems have been studied redward of the L-band (3 μm). From the ground, mid-infrared observations of exoplanets and PMCs are technically challenging, while from space, many systems were discovered after the cryogenic mission of the *Spitzer Space Telescope* (Werner et al. 2004) ended in 2009, and/or fall near or inside its diffraction limit. Extending the wavelength coverage of these objects into the mid-infrared to better fit spectral energy distributions (SEDs) will lead to more precise estimates of their physical properties and further constrain models of substellar and exoplanet atmospheres (e.g., Leggett et al. 2008; Bonnefoy et al. 2010; 2014). Utilizing the available mid-infrared observations that do exist of these systems are crucial for planning additional follow-up observations with next-generation facilities like the *James Webb Space Telescope* (*JWST*).

PMCs also frequently harbor disks, mostly identified through accretion signatures (e.g., line emission in Hα, Paβ, Brγ), red near-infrared colors, or mid-infrared excesses. Bowler et al. (2017) found $46\% \pm 14\%$ of young (<15 Myr) substellar (<20

$M_{\rm Jup}$) companions with existing moderate-resolution spectroscopy had detectable Paβ emission. This high disk frequency is comparable to that observed around isolated young substellar objects (Luhman et al. 2010; Esplin & Luhman 2017; Luhman & Esplin 2020) but it is not clear whether wide-orbit companion disks and isolated circum(sub)stellar disks have similar accretion rates, disk compositions, and grain size distributions. Observations of PMC disks at radio wavelengths have produced only upper limits, which suggests that the dust in PMC disks might actually be more compact and optically thick (e.g., Bowler & Hillenbrand 2015; MacGregor et al. 2017; Wolff et al. 2017; Wu et al. 2017). If so, wide-orbit PMC disks are much better suited for identification and characterization in the mid-infrared.

In Martinez & Kraus (2019) (hereafter Paper I), we presented an automated point-spread function (PSF) subtraction pipeline to leverage the *Spitzer* archive in the search for wide-orbit planetary-mass companions and identify excesses from circum(sub)stellar disks. Here, we apply our infrastructure to the remaining sample of known wide-orbit PMCs. In Sections 3.3 and 3.4, we describe our sample and PSF-fitting framework. We present the results of our image analysis and pipeline performance in Section 3.5. Finally in Section 3.6, we consider the mid-infrared photometry of the wide companions in our sample in the context of other young low-mass stars and brown dwarfs, and discuss the global disk frequency of PMCs.

3.3 Sample and *Spitzer* Observations

In Paper I the sample of wide-companion systems was chosen to test the feasibility of recovery via PSF-subtraction over a broad range of separations and contrast ratios. Here, we constructed a new sample to include other low-mass companions with potentially planetary mass that plausibly fit within those detection limits. We then identified systems with archival *Spitzer*/Infrared Array Camera (IRAC; Fazio et al. 2004) observations from its cryogenic mission. Six of the companions have not been resolved in *Spitzer*/IRAC, while three companions have had IRAC photometry reported in the literature previously. Seven of the systems belong to the young star-forming regions or stellar associations of Taurus, Carina, Chameleon, Upper Scorpius, and ρ Ophiuchus, while two are young field objects. We target the young field objects because their lower distances provide good sen-

sitivity to both mass and projected separation.

IRAC operated with four filters in the mid-infrared: 3.6, 4.5, 5.8, and 8.0 μm. The IRAC detector has 256×256 pixels with a pixel scale of $1\farcs22$. We work with IRAC's cryogenic-phase corrected basic data (CBCD) and uncertainty (CBUNC) files. All data were reduced with the *Spitzer* Science Center software pipeline version S18.25.0. We used the high-precision astrometry measurements of the companions from previous high-contrast AO observations as priors in our Markov Chain Monte Carlo (MCMC) fits (see Section 3.4).

The combined sample primary properties are given in Table 3.1 and system properties in Table 3.2. The specific details about the *Spitzer*/IRAC programs and data products are listed in Table 3.3.

Table 3.1: Primary Properties of Directly-Imaged Substellar Companion Systems

2MASS	Other Name	K_s (mag)	$W1$ (mag)	$W2$ (mag)	SpT	A_V (mag)	Distance (pc)	Age (Myr)	Ref.
J04294155+2632582	DH Tau	8.18	7.65	7.12	M1	1.4	133.3 ± 0.4	2 ± 1	1
J04414565+2301580	2M0441 Aab	9.85	9.70	9.47	M4.3; M7	0.2	$122.9^{+1.1}_{-0.9}$	2 ± 1	2–4
J06191291–5803156	AB Pic	6.98	7.28	6.91	K1	0.27	50.13 ± 0.03	45 ± 4	5, 6
J11062877–7737331	CHXR 73	10.70	10.52	10.21	M3	6.5[c]	$190.0^{+3.3}_{-3.0}$	2 ± 1	7
J13164653+0925269	GJ 504	4.03	4.20	5.30	G0	0.0	17.57 ± 0.04	$100 - 6500$	8
J16093030–2104589	1RXS J1609	8.92	8.79	8.78	M0	0.9	$137.8^{+0.3}_{-0.4}$	11 ± 2	9
J16271951–2441403	SR 12 AB	8.41	8.29	8.16	K4; M2.5	1.8[c]	$112.5^{+5.8}_{-5.3}$	3 ± 2	10, 11
J16311501–2432436	ROXs 42B	8.67	8.48	8.37	M0	2.4	$145.4^{+0.5}_{-0.7}$	3 ± 2	12, 13
J21185820+2613500	HD 203030	6.65	6.98	6.70	K0	0.03	$39.23^{+0.03}_{-0.04}$	$130 - 400$	14, 15

[a]2MASS Point Source Catalog (Cutri et al. 2003)

[b]CatWISE Source Catalog (Marocco et al. 2020). The $W1$ and $W2$ values reported for AB Pic and GJ 504 are lower than in AllWISE (Cutri et al. 2021) likely because of saturation.

[c]A_V converted from A_J.

NOTES — *Gaia* EDR3 parallactic distances are used from Bailer-Jones et al. (2021) except for SR 12 AB, where we use its *Gaia* DR2 parallactic distance from Bailer-Jones et al. (2018).

REFERENCES — (1) Itoh et al. (2005); (2) Todorov et al. (2010); (3) Todorov et al. (2014); (4) Bowler & Hillenbrand (2015); (5) Chauvin et al. (2005b); (6) Bonnefoy et al. (2010); (7) Luhman et al. (2006); (8) Kuzuhara et al. (2013); (9) Lafrenière et al. (2008b); (10) Kuzuhara et al. (2011); (11) Bowler et al. (2014); (12) Kraus et al. (2014a); (13) Currie et al. (2014); (14) Metchev & Hillenbrand (2006); (15) Miles-Páez et al. (2017)

Table 3.2: Properties of Directly-Imaged Substellar Companions

2MASS (Primary)	Other Name (Companion)	Separation (arcsec)	Position Angle (deg)	Filter	Δm (mag)	Ref.
J04294155+2632582	DH Tau B	2.31 ± 0.02	138.5 ± 0.1	K'	5.92	1–4
J04414565+2301580	2M0441 Bab	12.325 ± 0.007	238.0 ± 0.1	K_s	3.31	5–7
J06191291–5803156	AB Pic b	5.453 ± 0.025	175.25 ± 0.34	K_s	7.16	8, 9
J11062877–7737331	CHXR 73 b	1.30 ± 0.03	234.9 ± 1.0	K_s	4.70	10
J13164653+0925269	GJ 504 B	2.483 ± 0.015	326.46 ± 0.36	L'	12.90	11, 12
J16093030–2104589	1RXS J1609 b	2.219 ± 0.002	27.7 ± 0.1	K_s	7.25	13, 14
J16271951–2441403	SR 12 C	8.673 ± 0.153	166 ± 2[a]	K_s	6.16	15, 16
J16311501–2432436	ROXs 42B b	1.172 ± 0.002	270.09 ± 0.17	K_s	6.34	17–19
J21185820+2613500	HD 203030 B	11.923 ± 0.021	108.76 ± 0.12	K_s	9.56	20, 21

[a]P.A. estimated from Fig. 1 of Kuzuhara et al. (2011).

NOTES — Uncertainties listed were used as input errors on the P.A. prior.

REFERENCES — (1) Itoh et al. (2005); (2) Bonnefoy et al. (2014); (3) Zhou et al. (2014); (4) Kraus et al. (2014a); (5) Todorov et al. (2014); (6) Bowler & Hillenbrand (2015); (7) Kraus & Hillenbrand (2009b); (8) Chauvin et al. (2005b); (9) Bonnefoy et al. (2014); (10) Luhman et al. (2006); (11) Kuzuhara et al. (2013); (12) Skemer et al. (2016); (13) Lafrenière et al. (2008b); (14) Wu et al. (2015); (15) Kuzuhara et al. (2011); (16) Bowler et al. (2014); (17) Kraus et al. (2014a); (18) Currie et al. (2014); (19) Bowler et al. (2014); (20) Metchev & Hillenbrand (2006); (21) Miles-Páez et al. (2017)

Table 3.3: *Spitzer*/IRAC Observations

2MASS	No. of Frames				$T_{\rm exp}$	AOR	Date	PID	PI
	Ch 1	Ch 2	Ch 3	Ch 4	(s)		(UT)		
J04294155+2632582	3	3	3	3	0.4/10.4	3963392	2004 Mar 7	37	G. Fazio
	1	1	1	1	0.4/10.4	11232256	2005 Feb 23	3584	D. Padgett
	1	1	1	1	0.4/10.4	11236096	2005 Feb 24	3584	D. Padgett
J04414565+2301580	0/5	1/5	0/5	1/5	1.0/26.8	18364160	2007 Mar 28	30540	J. Houck
J06191291–5803156	9	9	9	9	0.4/10.4	15174656	2005 Sep 18	20795	P. Lowrance
J11062877–7737331	2	2	2	2	0.4/10.4	3960320	2004 Jun 10	37	G. Fazio
J13164653+0925269	1/5	0/5	1/5	0/5	1.0/26.8	3921920	2004 Jan 9	34	G. Fazio
		1/5		1/5	1.0/26.8	18010368	2006 Jul 9	30298	K. Luhman
J16093030–2104589	1/5		1/5		0.4/10.4	15844608	2005 Aug 24	20103	L. Hillenbrand
		9		9	1.2	13872384	2006 Mar 26	20069	J. Carpenter
J16271951–2441403	2	3	2	3	0.4/10.4	3652096	2004 Mar 7	6	G. Fazio
	2	2	2	2	0.4/10.4	5771008	2004 Mar 28	177	N. Evans
J16311501–2432436	2/2	2/2	2/2	2/2	0.4/10.4	5752320	2004 Mar 28	177	N. Evans
	2	2	2	2	10.4	5756928	2004 Mar 29	177	N. Evans
J21185820+2613500	16/16	16/16	16/16	16/16	1.0/26.8	23036416	2008 Jun 19	40489	S. Metchev
	16/16	16/16	16/16	16/16	1.0/26.8	23796480	2007 Nov 15	40489	S. Metchev

3.4 Data Analysis

Previous analyses of *Spitzer*/IRAC images have searched for wide-orbit PMC systems by taking advantage of IRAC's well-behaved PSF wings at $>> \lambda/D$ (e.g., Janson et al. 2015; Durkan et al. 2016; Baron et al. 2018). Our framework is optimized for probing the IRAC PSF at 1–5 λ/D, where companion identification is difficult because the PSF is undersampled at the native $1\farcs22$ pixel scale. Classical PSF-modeling techniques, such as "locally optimized combination of images" (LOCI; Lafrenière et al. 2007) or principal component analysis, require more pixels to adequately model the primary star PSF. We use the framework described in Paper I to model the point spread functions of the system components in the IRAC images. To summarize, we use the point response function (PRF, or effective PSF; Hoffman 2005) developed by the *Spitzer* Science team to generate model PSFs at any position on the IRAC detector. We then fit a two-source PSF model in each image performing a MCMC analysis using a Metropolis-Hastings algorithm with Gibbs sampling. The PSF model is described by seven parameters: x-pixel coordinate of the primary centroid (x), y-pixel coordinate of the primary centroid (y), image background (b), peak pixel value of the primary (n), projected separation (ρ), position angle (PA), and contrast (Δm). In addition, image pixel values greater than 90% of the saturation limit were masked. We adopt priors on separation and position angle from past high-resolution imaging results, listed in Table 3.2.

Table 3.4: Best-Fit System Properties of Detected Companions

2MASS (Primary)	Other Name (Companion)	Separation (arcsec)	Position Angle (deg)	$\Delta[3.6]$ (mag)	$\Delta[4.5]$ (mag)	$\Delta[5.8]$ (mag)	$\Delta[8.0]$ (mag)
J04294155+2632582	DH Tau B	2.22 ± 0.18	137.30 ± 1.5	5.74 ± 0.24	5.30 ± 0.17	4.79 ± 0.16	4.38 ± 0.15
J04414565+2301580	2M0441 Bab	12.35 ± 0.01	237.4 ± 0.1	2.67 ± 0.01	2.41 ± 0.01	2.17 ± 0.01	1.80 ± 0.01
J06191291–5803156	AB Pic b	5.52 ± 0.09	175.4 ± 0.3	6.34 ± 0.06	5.95 ± 0.07	5.65 ± 0.30	5.58 ± 0.16
J11062877–7737331	CHXR 73 b	1.24 ± 0.03	228.5 ± 3.8	3.59 ± 0.04	3.81 ± 0.06	...	2.94 ± 0.12
J16093030–2104589	1RXS J1609 b	2.14 ± 0.11	27.0 ± 0.6	...	6.04 ± 0.15	...	...
J16271951–2441403	SR 12 c	8.62 ± 0.05	164.8 ± 0.6	5.83 ± 0.07	5.08 ± 0.03	5.05 ± 0.07	4.16 ± 0.03
J16311501–2432436	ROXs 42B	1.17 ± 0.03	263.6 ± 4.8	...	4.30 ± 0.08	...	4.55 ± 0.11
J21185820+2613500	HD 203030 b	12.025 ± 0.004	108.69 ± 0.02	8.27 ± 0.01	7.88 ± 0.01	6.97 ± 0.02	6.84 ± 0.02

NOTES — If an entry in Δm is missing, the companion was not detected in that channel.

The MCMC analysis is conducted in two stages to determine image-specific parameters (x, y, b) separately from system-specific parameters (n, ρ, PA, Δm). We ran four MCMC chains with 140,000 steps each, discarding the first 10% of each chain as "burn-in". The weighted average median (x, y)-centroid, ρ, PA, and Δm generated by the MCMC fit is used to create individual PSF models of each system component from which aperture photometry using a $10''$ radius is measured. The zero-points of IRAC Channels 1–4 are 280.9 ± 4.1, 179.7 ± 2.6, 115.0 ± 1.7, and 64.9 ± 0.9 Jy, respectively.

Some members of the sample have nearby neighbors with flux that could influence the results of the pipeline fit. The neighbors of DH Tau, 2MASS J04414565+2301580 and 2MASS J04414489+2301513 (hereafter 2M0441 A and 2M0441 B), and CHXR 73 are within $15''$ of the primary centroid and unsaturated. We use the same PSF model described above to fit and subtract each neighbor within each individual IRAC image prior to being put through the pipeline. SR 12 is $\sim$25$''$ away from a bright and saturated young stellar object, 2MASS J16272146–2441430 (YLW 13B). Although this object is well outside of the pipeline fitting region,the wings of its flux can still affect the PSF-fitting results. For this system we use the high-dynamic range PSF from Marengo et al. (2006) to model this bright neighbor and subtract off its contaminating flux (Figure 3.1).

After the MCMC runs, stacked residual images are created by combining individual residual images after the primary PSF has been subtracted, placing each on a final grid with a pixel scale five times smaller than the original IRAC pixel scale of $1\farcs22$, shifting to a common origin, and rotating so that north is up and east is left. PSF subtraction occurs on the original data, not on mosaiced or subsampled images, because of the complicated nature of the IRAC PSF and because subsampling the images prior to PSF-fitting would introduce covariance between adjacent pixels. We perform aperture photometry on these subsampled stacked residuals images to determine detection limits around each primary. We use apertures with radii equal to the FWHM in each channel ($1\farcs66$, $1\farcs72$, $1\farcs88$, $1\farcs98$). The FWHMs are larger than the IRAC pixel scale ($1\farcs22$), thus all covariant pixels contribute to the measured aperture flux.

To evaluate the sensitivity of our PSF-fitting framework to substellar companions in the IRAC images of our sample, we performed aperture photometry on the

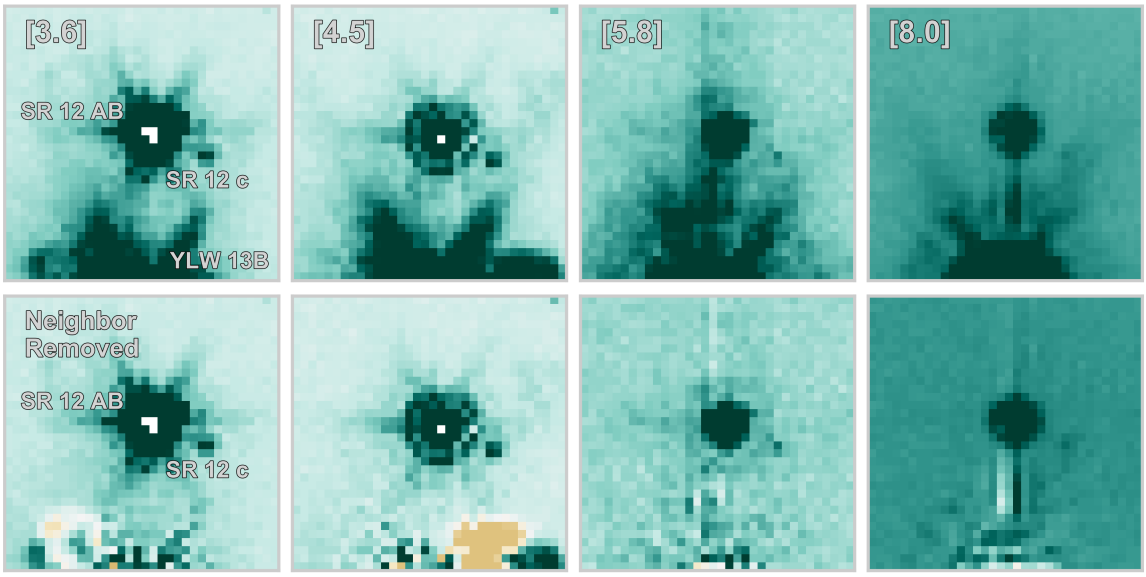

Figure 3.1: Individual IRAC images of SR 12 before (top row) and after (bottom row) YLW 13B, a nearby young stellar object, is removed. High-dynamic range PSFs were used to model the bright PSF wings of YLW 13B which were then subtracted off to minimize contamination when determining the system parameters of SR 12.

stacked images before and after PSF-subtraction. We measured the flux inside 100 randomly drawn apertures of radius 1 FWHM at $\mathrm{FWHM}/4$ ($0\farcs42$, $0\farcs43$, $0\farcs47$, $0\farcs50$) intervals radially outward from the primary star. The mean and standard deviation of these fluxes is used to determine the limiting flux and is then converted into *Spitzer*/IRAC magnitudes to obtain 4-σ limits. For a given target, the companion height above (or below) the 4-σ detection limit at that radius can be used to infer the systematic uncertainty due to residual primary-PSF structure in our modeling framework photometry. For example, if photometry measured for a companion is equal to the 4-σ limit, its systematic flux uncertainty would be 25%, or $\sim$0.24 mag, while a 5-σ detection would have a systematic flux uncertainty of 20%, or $\sim$0.20 mag. With $\sim$36, 34, 28, and 25 independent apertures in a search radius of $10''$ around a primary star, the probability of measuring a spurious $>$4-σ signal is 0.003%.

We then convert our detection limit curves into mass detection limits using the BT-Settl evolutionary models of Allard et al. (2012) at the reported literature ages and *Gaia* parallactic distances of our sample systems.

3.5 Results

3.5.1 Detections

Our reprocessing of the IRAC images yielded detections in one or more filters for eight out of our sample of nine substellar companions. The one system whose companion was not detected, GJ 504, had the brightest primary (K_s=4.03 mag) and largest expected contrast ($>$12 mag), but we are still able to assess a robust upper limit. We present the final system parameters as determined by our pipeline in Table 3.4. The contrasts reported are marginalized values of the parameters as measured by our MCMC fits and we note that the contrast errors reflect only the statistical uncertainty. The projected separations and position angles reflect the input priors from previous adaptive optics imaging such that the information in the *Spitzer*/IRAC images is entirely devoted to measuring companion contrast. IRAC magnitudes for the primary stars and substellar companions are calculated from the PSF models, assuming the median MCMC fit parameters, and are included in Table 3.5.

Table 3.5: Photometry for Sample Systems

Filter	Primary Magnitude (mag)	Secondary Magnitude (mag)	Ref.
2MASS J04294155+2632582 (DH Tau)			
F775W	...	20.2 ± 0.03	1
F850LP	...	18.0 ± 0.02	1
J	9.767 ± 0.021	15.71 ± 0.05	2,3
H	8.824 ± 0.026	14.96 ± 0.04	2,3
K_s	8.178 ± 0.026	14.19 ± 0.02	2,3
[3.6]	7.58 ± 0.02	13.32 ± 0.24	This work
[4.5]	7.21 ± 0.02	12.51 ± 0.17	This work
[5.8]	7.10 ± 0.02	11.89 ± 0.16	This work
[8.0]	6.76 ± 0.02	11.13 ± 0.15	This work
2MASS J04414565+2301580 (2M0441 AB)			
$y_{\rm P1}$	12.06 ± 0.01	16.10 ± 0.01	4
J	10.74 ± 0.02	14.42 ± 0.03	2
H	10.10 ± 0.02	13.73 ± 0.03	2
K_s	9.85 ± 0.02	13.16 ± 0.03	2
[3.6]	9.59 ± 0.02	12.26 ± 0.02	This work
[4.5]	9.48 ± 0.02	11.89 ± 0.02	This work
[5.8]	9.32 ± 0.02	11.48 ± 0.02	This work
[8.0]	9.19 ± 0.02	10.96 ± 0.02	This work
2MASS J06191291–5803156 (AB Pic)			
B_T	10.24 ± 0.02	...	5
$G_{\rm RP}$	9.29 ± 0.01	...	6
$G_{\rm BP}$	8.21 ± 0.01	...	6
J	7.58 ± 0.02	16.18 ± 0.10	2,7
H	7.09 ± 0.02	14.69 ± 0.10	2,7
K_s	6.98 ± 0.02	14.14 ± 0.08	2,7
[3.6]	6.89 ± 0.02	13.22 ± 0.06	This work

Table 3.5 continued on next page

Table 3.5 *(continued)*

Filter	Primary Magnitude (mag)	Secondary Magnitude (mag)	Ref.
[4.5]	6.89 ± 0.02	12.87 ± 0.07	This work
[5.8]	6.85 ± 0.02	12.50 ± 0.65	This work
[8.0]	6.83 ± 0.02	12.41 ± 0.16	This work
2MASS J11062877–7737331 (CHXR 73)			
$G_{\rm RP}$	15.76 ± 0.01	...	6
F625W	19.03 ± 0.08	...	8
F775W	...	24.07 ± 0.13	8
F850LP	...	21.35 ± 0.04	8
J	12.67 ± 0.03	17.87 ± 0.30	2,9
H	11.32 ± 0.02	16.52 ± 0.30	2,9
K_s	10.70 ± 0.02	15.40 ± 0.25	2,9
[3.6]	10.30 ± 0.02	13.94 ± 0.05	This work
[4.5]	10.24 ± 0.02	14.03 ± 0.06	This work
[5.8]	10.12 ± 0.02	>14.01	This work
[8.0]	10.14 ± 0.02	13.06 ± 0.12	This work
2MASS J13164653+0925269 (GJ 504)			
J	4.13 ± 0.02	19.78 ± 0.10	10
H	3.88 ± 0.02	20.01 ± 0.10	10
K_s	3.81 ± 0.02	19.38 ± 0.11	10
L'	3.80 ± 0.02	16.70 ± 0.17	10
[3.6]	3.84 ± 0.02	>8.02	This work
[4.5]	3.90 ± 0.02	>7.56	This work
[5.8]	3.79 ± 0.02	>9.05	This work
[8.0]	3.78 ± 0.02	>8.32	This work
2MASS J16093030–2104589 (1RXS J1609)			
$I_{\rm DENIS}$	10.99 ± 0.03	...	11
$z'_{\rm VISAO}$	10.60 ± 0.06	21.24 ± 0.15	12
$Y_{s,\rm VISAO}$	10.43 ± 0.10	...	12

Table 3.5 continued on next page

Table 3.5 *(continued)*

Filter	Primary Magnitude (mag)	Secondary Magnitude (mag)	Ref.
J	9.82 ± 0.03	17.85 ± 0.12	2,13
H	9.12 ± 0.02	16.86 ± 0.07	2,13
K_s	8.92 ± 0.02	16.15 ± 0.05	2,13
[3.6]	8.77 ± 0.02	>13.75	This work
[4.5]	8.79 ± 0.02	14.82 ± 0.15	This work
[5.8]	8.71 ± 0.02	>13.36	This work
[8.0]	8.69 ± 0.02	>14.16	This work
2MASS J16271951–2441403 (SR 12)			
$g_{\rm P1}$	13.09 ± 0.02	...	4
$z_{\rm P1}$	...	19.03 ± 0.04	4
$y_{\rm P1}$	...	17.82 ± 0.04	4
J	9.42 ± 0.02	...	2
H	8.63 ± 0.04	...	2
K_s	8.41 ± 0.04	14.42 ± 0.07	2
[3.6]	8.16 ± 0.02	13.99 ± 0.07	This work
[4.5]	8.10 ± 0.02	13.18 ± 0.03	This work
[5.8]	8.05 ± 0.02	13.09 ± 0.07	This work
[8.0]	8.01 ± 0.02	12.17 ± 0.04	This work
2MASS J16311501–2432436 (ROXs 42B)			
$g_{\rm P1}$	15.07 ± 0.01	...	4
$r_{\rm P1}$	13.49 ± 0.1	...	4
$i_{\rm P1}$	12.51 ± 0.1	...	4
$z_{\rm P1}$	11.81 ± 0.1	...	4
$y_{\rm P1}$	11.47 ± 0.1	...	4
J	9.91 ± 0.02	...	2
H	9.02 ± 0.02	...	2
K_s	8.67 ± 0.02	...	2
$J_{\rm NIRC2}$	...	16.99 ± 0.07	14

Table 3.5 continued on next page

Table 3.5 *(continued)*

Filter	Primary Magnitude (mag)	Secondary Magnitude (mag)	Ref.
$H_{\rm NIRC2}$	...	15.88 ± 0.06	14
$K'_{\rm NIRC2}$	...	15.01 ± 0.05	14
$L'_{\rm NIRC2}$	...	14.15 ± 0.09	14
[3.6]	8.36 ± 0.02	>10.98	This work
[4.5]	8.36 ± 0.02	13.44 ± 0.56	This work
[5.8]	8.25 ± 0.02	>12.54	This work
[8.0]	8.28 ± 0.02	12.82 ± 0.11	This work
2MASS J21185820+2613500 (HD 203030)			
B_T	9.39 ± 0.02	...	5
$G_{\rm BP}$	8.94 ± 0.01	...	6
$G_{\rm RP}$	8.69 ± 0.01	...	6
J	7.07 ± 0.02	18.77 ± 0.08	2,15
H	6.73 ± 0.02	17.57 ± 0.08	2,15
K_s	6.65 ± 0.02	16.21 ± 0.10	2,16
[3.6]	6.73 ± 0.02	15.01 ± 0.02	This work
[4.5]	6.76 ± 0.02	14.63 ± 0.02	This work
[5.8]	6.88 ± 0.02	13.84 ± 0.02	This work
[8.0]	6.61 ± 0.02	13.44 ± 0.03	This work

NOTES — If an entry is missing, that filter was not used in the component's SED fit.

REFERENCES — (1) Zhou et al. (2014); (2) Cutri et al. (2003); (3) Itoh et al. (2005); (4) Chambers et al. (2016); (5) Høg et al. (2000); (6) Gaia Collaboration et al. (2018); (7) Chauvin et al. (2005b); (8) Hubble Legacy Archive; (9) Luhman et al. (2006); (10) Skemer et al. (2016); (11) Epchtein et al. (1997); (12) Wu et al. (2015); (13) Lachapelle et al. (2015); (14) Kraus et al. (2014a); (15) Miles-Páez et al. (2017); (16) Metchev & Hillenbrand (2006)

In Figure 3.2, we present example pipeline results for an individual system, AB Pic. We show stacked images of the original data and final system model as well as stacked residuals images after the PSF models are subtracted. After subtracting the

primary star PSF, a statistically significant positive residual is seen at the expected position of AB Pic b. This residual disappears after subtracting the best-fit system PSFs, indicating that it is a robust detection across all IRAC filters.

Not all companions were detected in every IRAC channel. Generally, companions were not detected or had less constrained photometry in Channel 3 (5.8 μm), suggesting a possible PSF mismatch between templates and data in that channel. CHXR 73 b was detected in Channels 1, 2, and 4. ROXs 42B b was detected in Channels 2 and 4. 1RXS J160929.1–210524 b (herafter 1RXS J1609 b) was detected only in Channel 2. These three objects had the smallest projected separations ($1\farcs2 - 2\farcs2$) of the sample. ROXs 42B b and 1RXS J1609 b also had the largest K_s-band contrasts which could explain the difficulty of detection in the other IRAC channels. Our measured photometry in Channel 4 (8.0 μm) of ROXs 42B b suggests it may have a long-wavelength excess, making its detection easier. In Figure 3.3, we show stacked residuals images after the primary PSF has been subtracted, highlighting the companion detection in either Channel 2 or Channel 4 for these systems, as well as DH Tau.

In Figure 3.4, we present a color-magnitude diagram of $M_{[3.6]}$ vs. [3.6]–[8.0] color for the nine primaries and seven companions that were detected in those filters. We also show the intrinsic photospheric mid-infrared color-magnitude sequences from the BT-Settl models of Allard et al. (2012) for 1, 10, 100, and 500 Myr. Typically an object with [3.6]–[8.0] color significantly redder than the intrinsic photospheric isochrone on this diagram is interpreted as excess emission due to a disk. Based on this criterion, two primaries and seven companions appear red and may harbor circum(sub)stellar disks, but we will explore whether a more nuanced disk criterion is needed in Section 3.6.

We detect the photospheres of AB Pic b, CHXR 73 b, and HD 203030 b while companions with significant [3.6]–[8.0] color excess are DH Tau B, SR 12 c, and ROXs 42B b. Although 1RXS J1609 b was not detected in Channels 1, 3, or 4, an SED fit of literature photometry and our Channel 2 measurement indicate we detected its photosphere (see Section 3.5.3).

2M0441 AB actually comprise a quadruple system consisting of two bound low-mass binaries (Todorov et al. 2010; 2014; Bowler & Hillenbrand 2015, and references therein). Mid-infrared excess has been identified for both pairs (Luhman

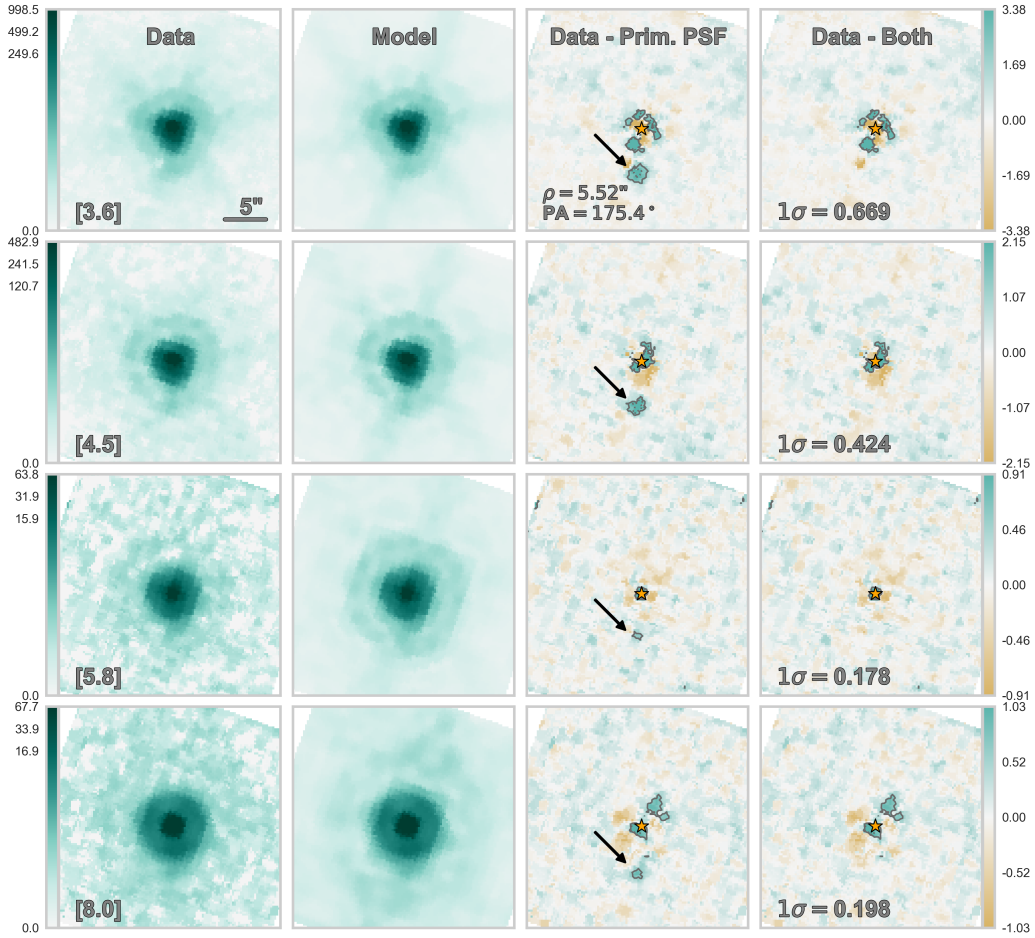

Figure 3.2: Stacked images of AB Pic across all four IRAC channels (rows) after it has gone through the PSF-fitting pipeline. All fits were conducted within the CBCD images at the native plate scale, but to convey the full data set, the images here were generated by combining individual frames after they had been re-scaled to $0\farcs24$/pixel ($\sim 5\times$ smaller than the original IRAC pixel scale), shifted to a common origin, and rotated so that north is up and east is left. Columns 1 and 2 show the original IRAC data of AB Pic and the median two-source PSF model, respectively, displayed with a logarithmic color scale (leftmost color bar). Column 3 shows the residuals left behind after only the primary PSF model is subtracted from the data. Column 4 shows the residuals left behind after the two-source PSF model is subtracted from the data. Both Columns 3 and 4 are displayed with a linear color scale (rightmost color bar) and 3- and 5-σ contours overlaid with solid and dotted lines, respectively. The standard deviation of the pixel values is displayed in the lower left-hand corner of Column 4 in units of DN/s. After subtracting the primary star PSF, a statistically significant positive residual is seen at the expected position of AB Pic b. This residual disappears after subtracting the best-fit system PSFs, indicating that it is a robust detection across all IRAC filters.

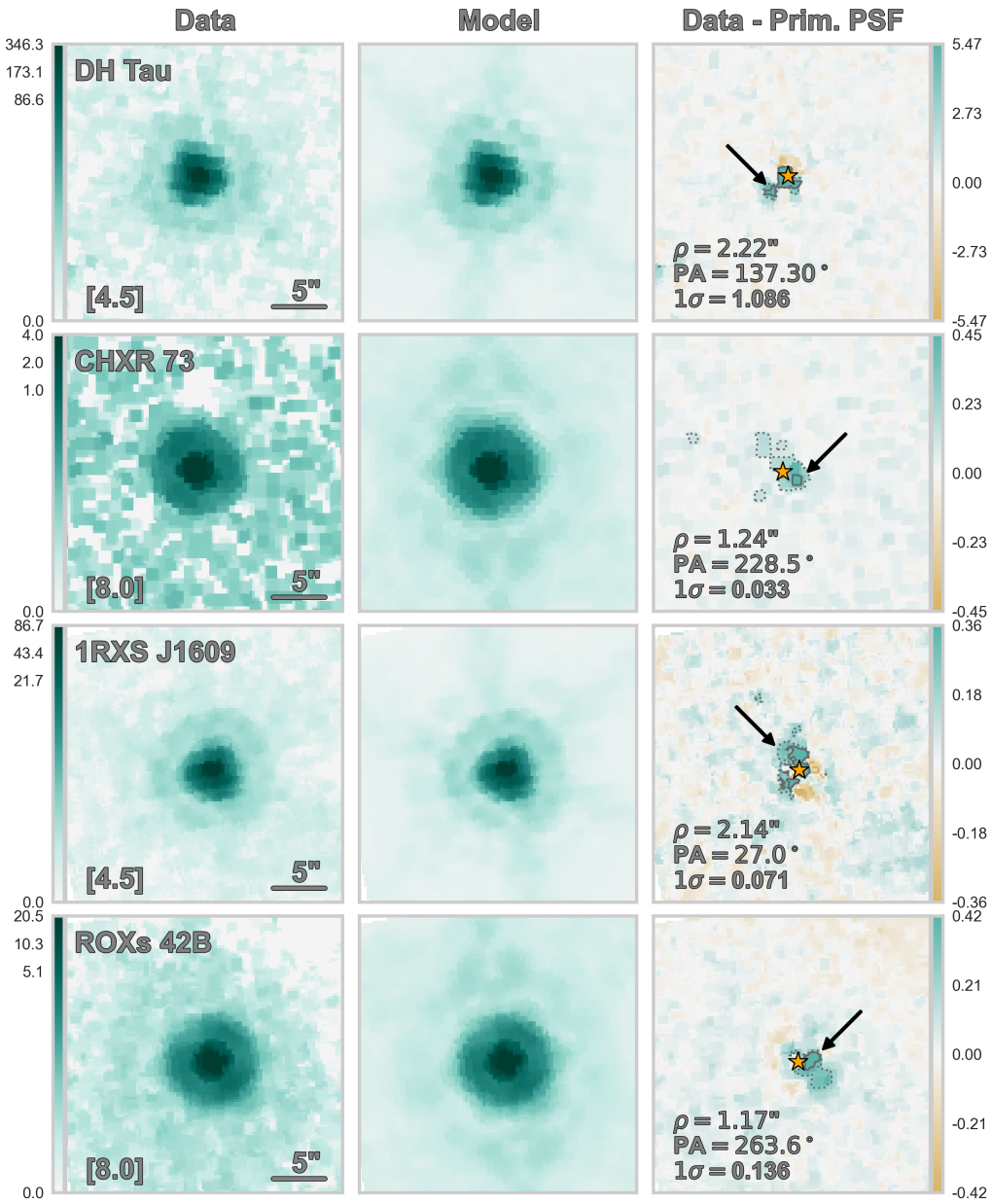

Figure 3.3: Stacked images of DH Tau, CHXR 73, 1RXS J1609, and ROXs 42B, the other four systems besides AB Pic (shown in Figure 3.2) with companions that are newly resolved in this work. Columns 1 and 2 show the original IRAC data and the median two-source PSF model, respectively, displayed with a logarithmic color scale (leftmost color bar). Column 3 shows the residuals left behind after only the primary PSF model is subtracted from the data. Column 3 is displayed with a linear color scale (rightmost color bar) with 3- and 5-σ contours overlaid with solid and dotted lines, respectively. For each panel north is up and east is left.

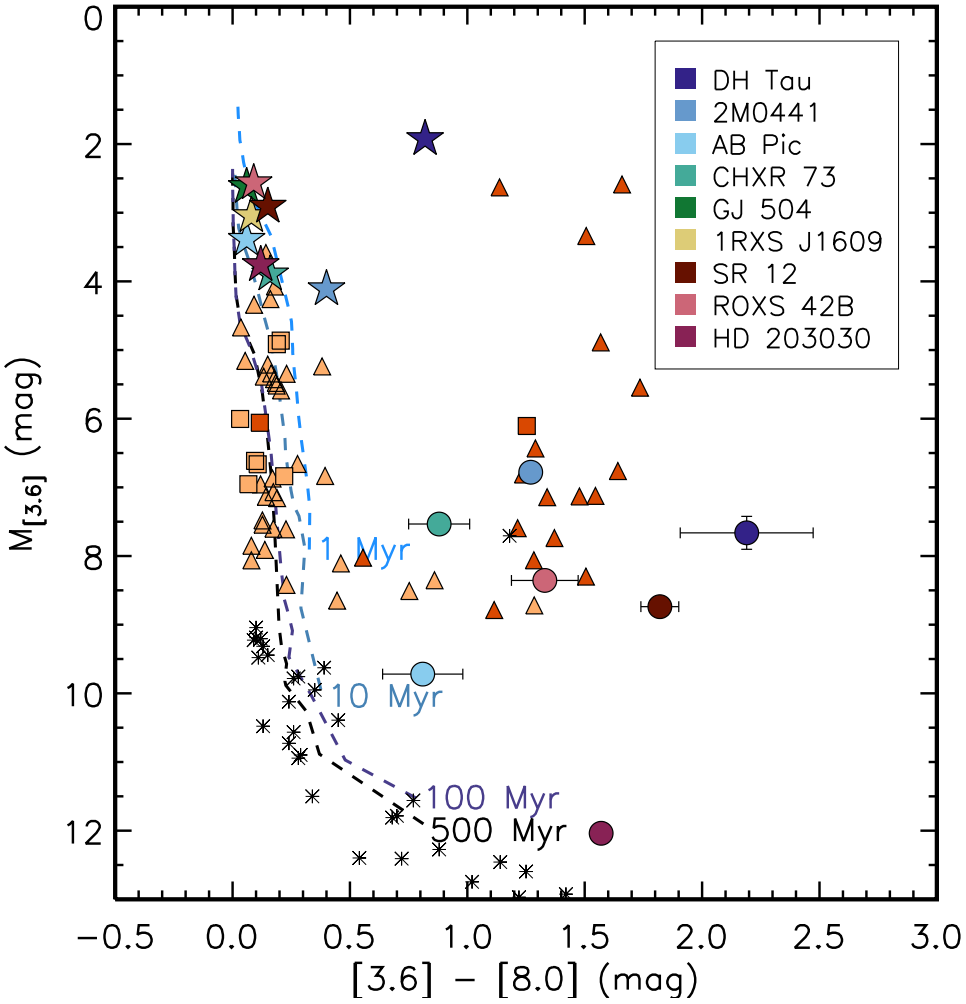

Figure 3.4: Color-magnitude diagram for our sample detected in both Channels 1 (3.6 μm) and 4 (8.0 μm). For comparison, we include young >M7 brown dwarfs members of the Taurus (triangles; Esplin & Luhman 2017) and Upper Scorpius (squares; Luhman & Esplin 2020) star-forming regions. Orange symbols represent disk-free members while red symbols denote disk-bearing members. We also include field brown dwarfs from Dupuy & Liu (2012), indicated as asterisks. $M_{[3.6]}$ was determined from *Gaia* EDR3 parallactic measurements (Bailer-Jones et al. 2021) of each system primary. The primary components are indicated as filled stars while substellar companions are indicated as filled circles. Also displayed are the intrinsic photospheric [3.6]-[8.0] colors from BT-Settl models of Allard et al. (2012) at 1, 10, 100, and 500 Myr (dashed lines). Not shown are the companions to GJ 504 and 1RXS J1609 which were not detected in either channels 1 or 4. ROXs 42B b was not detected in Channel 1 by our pipeline but shown here as an L'-band detection from Kraus et al. (2014a). The companions of our sample appear to be significantly redder than the BT-Settl isochrones, in line with previous comparisons between young and old free-floating brown dwarfs (Dupuy & Liu 2012; Liu et al. 2016). The mid-infrared colors of the companions are similar to disk-bearing free-floating brown dwarfs in young star-forming regions.

et al. 2010; Adame et al. 2011; Bulger et al. 2014), indicating at least one component of each binary harbors a circum(sub)stellar disk. We readily confirm this excess with our pipeline in the *Spitzer* images but determining the mid-infrared flux contributions from the individual components of 2M0441 B is beyond the scope of this paper.

3.5.2 Detection Limits and Mass Sensitivity

Our PSF-fitting results yield sensitive upper limits on the companions that we did not detect, as well as for the presence of additional companions in these systems. We present the contrast and mass limits reached in the PSF-subtracted images as a function of radial separation in Tables 3.6 and 3.7, and show the Channel 4 detection limits in Figure 3.5 (See Section 3.4 for the details of the detection limit calculation).

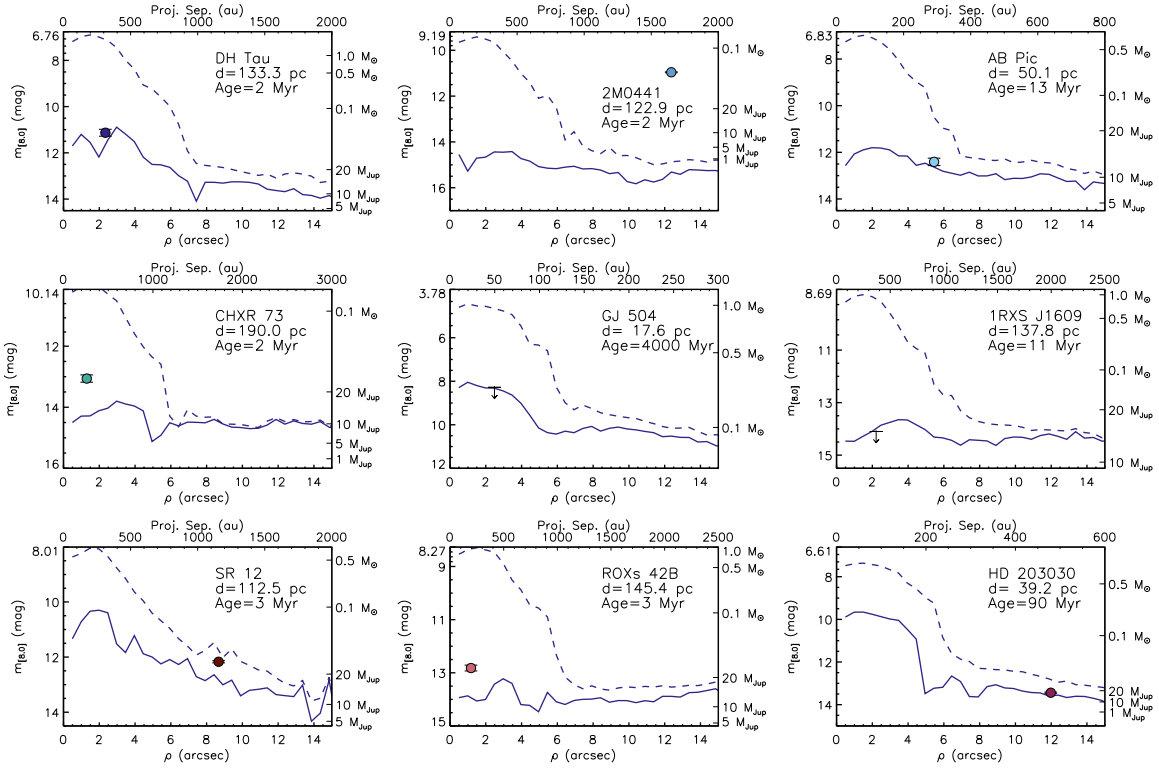

Figure 3.5: Contrast limits determined from the stacked IRAC Channel 4 images of our sample. The dashed blue line indicates the contrast curves prior to PSF subtraction as a function of separation from the primary in arcseconds. The solid blue line indicates the corresponding contrast curve after the median two-source PSF model has been subtracted. The top of each leftside y-axis lists the primary magnitude as measured by the pipeline. The contrast curves are presented in terms of apparent magnitudes as well as mass calculated by using the *Gaia* EDR3 parallax distance estimates of Bailer-Jones et al. (2021), literature age determinations, and BT-Settl isochrones (Allard et al. 2012).

Table 3.6: Companion Contrast Limits

2MASS	Distance	Ch.	M	Exp. Time	Contrast (mag) at ρ =(arcsec)									
	(pc)		(mag)	(s)	0.5	1.0	1.5	2.0	3.0	4.0	5.0	7.0	10.0	12.0
J04294155+2632582	133.3	1	1.96	0.4	4.79	4.49	4.36	4.46	5.08	5.76	6.46	6.23	6.45	6.22
		2	1.66	0.4	5.02	4.75	4.62	4.55	4.85	5.76	6.00	5.59	5.73	6.03
		3	1.48	10.4	4.20	4.04	4.22	4.36	4.73	6.52	7.35	6.80	6.74	6.83
		4	1.14	10.4	4.94	4.45	4.80	5.39	4.15	4.81	5.74	6.59	6.50	6.88
J04414565+2301580	122.9	1	4.13	26.8	3.19	2.15	1.87	1.64	2.43	5.72	7.90	7.53	7.63	7.59
		2	4.01	26.8	4.75	4.65	4.84	5.02	6.43	7.04	7.51	7.37	7.46	7.05
		3	3.87	26.8	6.76	5.99	6.03	6.18	6.45	7.94	8.21	7.16	7.26	6.71
		4	3.74	26.8	5.37	6.08	5.52	5.47	5.26	5.54	5.90	5.89	6.56	6.37
J06191291–5803156	50.1	1	3.39	0.4	...	6.90	6.26	6.37	6.96	7.23	7.79	7.33	7.66	7.57
		2	3.39	0.4	5.89	5.81	5.99	6.19	6.57	7.60	7.01	7.28	7.18	6.99
		3	3.35	0.4	6.53	6.49	5.83	5.78	6.54	6.34	6.29	6.32	6.14	6.04
		4	3.33	0.4	5.74	5.24	5.06	4.97	5.08	5.36	5.66	6.13	6.29	6.15
J11062877–7737331	190.0	1	3.91	10.4	4.73	4.58	4.46	4.53	5.14	5.89	6.66	6.82	7.09	7.10
		2	3.85	10.4	6.06	5.76	5.84	5.59	5.79	6.99	6.64	6.46	6.61	6.45
		3	3.73	10.4	3.80	3.64	3.62	3.74	4.29	5.10	5.14	5.29	5.55	4.99
		4	3.75	10.4	4.36	4.15	4.14	3.97	3.67	3.83	4.96	4.35	4.53	4.30
J13164653+0925269	17.6	1	2.62	1.0	5.95	5.10	4.54	4.28	4.36	5.89	6.21	7.35	7.58	7.70
		2	2.68	1.0	5.12	4.82	4.54	4.02	3.47	3.59	5.28	7.10	7.07	7.09
		3	2.58	1.0	6.43	5.20	4.96	5.06	5.41	5.45	6.85	7.24	7.11	7.31
		4	2.56	1.0	4.51	4.27	4.42	4.53	4.68	5.27	6.39	6.56	6.42	6.76
J16093030–2104589	137.8	1	3.07	10.4	4.28	3.98	3.90	4.01	4.61	6.40	7.58	7.26	7.53	7.51
		2	3.09	1.2	6.16	6.21	6.38	6.47	6.33	6.95	7.11	7.11	7.26	7.02

Table 3.6 continued on next page

Table 3.6 *(continued)*

2MASS	Distance (pc)	Ch.	M (mag)	Exp. Time (s)	Contrast (mag) at ρ =(arcsec)									
					0.5	1.0	1.5	2.0	3.0	4.0	5.0	7.0	10.0	12.0
		3	3.01	10.4	5.24	4.88	4.73	4.71	5.05	5.75	7.19	6.57	6.45	6.26
		4	2.99	1.2	5.78	5.78	5.58	5.40	5.06	4.99	5.36	5.90	5.62	5.52
J16271951–2441403	112.5	1	2.90	10.4	5.87	4.91	4.55	4.55	4.90	6.13	7.47	6.96	7.06	7.02
		2	2.84	10.4	4.64	4.13	4.04	3.99	5.64	6.28	6.66	6.78	6.76	7.04
		3	2.79	10.4	4.72	4.37	4.21	4.20	4.82	5.74	5.94	5.79	5.83	6.07
		4	2.75	10.4	3.32	2.70	2.33	2.29	3.53	3.26	4.01	4.14	5.35	5.36
J16311501–2432436	145.4	1	2.55	0.4	4.27	4.00	3.90	4.00	4.82	5.24	5.72	5.42	5.84	5.60
		2	2.55	0.4	5.93	5.40	5.00	4.73	4.40	4.46	4.69	4.80	5.03	5.08
		3	2.47	10.4	4.40	4.13	4.01	4.12	4.78	5.54	6.79	6.67	7.04	6.87
		4	2.47	10.4	5.65	5.59	5.78	5.70	4.95	5.92	6.11	5.76	5.78	5.61
J21185820+2613500	39.2	1	3.76	26.8	7.27	4.70	4.25	4.13	4.36	4.77	6.89	7.56	7.73	7.66
		2	3.79	26.8	...	6.78	5.57	4.66	4.11	4.09	5.62	7.36	7.24	7.69
		3	3.91	26.8	1.66	1.26	1.18	1.27	1.42	2.18	3.86	6.55	7.49	7.22
		4	3.64	26.8	3.28	3.05	3.05	3.15	3.38	3.90	6.85	6.40	6.66	6.98

Table 3.7: Companion Mass Limits

2MASS	Distance (pc)	Ch.	M (mag)	Exp. Time (s)	Mass Limit ($M_{\rm Jup}$) at ρ =(arcsec)									
					0.5	1.0	1.5	2.0	3.0	4.0	5.0	7.0	10.0	12.0
J04294155+2632582	133.3	1	1.96	0.4	30	35	38	36	25	16	10	12	10	12
		2	1.66	0.4	30	35	37	38	33	19	16	21	19	16
		3	1.48	10.4	47	51	47	44	36	12	6	10	11	10
		4	1.14	10.4	37	48	40	29	56	39	23	13	14	11
J04414565+2301580	122.9	1	4.13	26.8	21	38	44	50	33	<1	<1	<1	<1	<1
		2	4.01	26.8	7	8	6	5	<1	<1	<1	<1	<1	<1
		3	3.87	26.8	<1	<1	<1	<1	<1	<1	<1	<1	<1	<1
		4	3.74	26.8	2	<1	1	2	3	1	<1	<1	<1	<1
J06191291–5803156	50.1	1	3.39	0.4	...	9	11	11	8	7	5	7	5	6
		2	3.39	0.4	13	13	13	12	10	7	9	8	8	9
		3	3.35	0.4	10	10	13	13	10	11	11	11	11	12
		4	3.33	0.4	12	15	15	15	15	14	13	11	10	10
J11062877–7737331	190.0	1	3.91	10.4	9	10	11	10	5	<1	<1	<1	<1	<1
		2	3.85	10.4	<1	1	1	2	1	<1	<1	<1	<1	<1
		3	3.73	10.4	16	18	18	17	12	6	6	5	3	7
		4	3.75	10.4	10	12	12	13	16	15	6	10	9	11
J13164653+0925269	17.6	1	2.62	1.0	130	190	250	280	270	140	120	81	78	77
		2	2.68	1.0	180	200	230	300	390	370	170	84	84	84
		3	2.58	1.0	100	180	190	190	160	160	88	82	84	80
		4	2.56	1.0	240	270	250	230	220	170	99	93	98	88
J16093030–2104589	137.8	1	3.07	10.4	34	50	54	48	24	12	7	8	7	7
		2	3.09	1.2	13	13	12	12	12	10	10	10	9	10

Table 3.7 continued on next page

Table 3.7 *(continued)*

2MASS	Distance (pc)	Ch.	M (mag)	Exp. Time (s)	Mass Limit ($M_{\rm Jup}$) at ρ =(arcsec)									
					0.5	1.0	1.5	2.0	3.0	4.0	5.0	7.0	10.0	12.0
		3	3.01	10.4	17	19	20	20	18	14	9	11	12	12
		4	2.99	1.2	14	14	15	15	17	18	16	13	14	15
J16271951–2441403	112.5	1	2.90	10.4	10	19	23	23	19	8	<1	2	1	1
		2	2.84	10.4	21	26	27	28	12	7	4	4	4	2
		3	2.79	10.4	19	23	25	25	18	11	9	10	10	8
		4	2.75	10.4	38	53	68	69	34	39	27	26	13	13
J16311501–2432436	145.4	1	2.55	0.4	30	34	36	34	24	19	14	17	13	15
		2	2.55	0.4	12	16	20	23	27	26	23	22	20	19
		3	2.47	10.4	27	30	33	31	23	15	5	6	4	5
		4	2.47	10.4	13	13	12	12	19	11	9	12	12	13
J21185820+2613500	39.2	1	3.76	26.8	18	72	100	110	91	69	22	15	13	14
		2	3.79	26.8	...	24	40	69	100	100	39	17	19	13
		3	3.91	26.8	460	550	560	540	520	350	110	23	8	13
		4	3.64	26.8	190	230	230	210	180	130	18	24	21	15

Our detection limit curves show that prior to PSF subtraction detectable companion contrasts plateau past $8''$, corresponding to projected physical separations of $\sim$150 au for the closest sample member (17.5 pc; GJ 504) and $\sim$1600 au for the furthest (191.0 pc; CHXR 73). Within $8''$, detectable contrasts improve by as much as 7 mag in Channel 1 and 5.5 mag in Channel 4.

While we do not detect the companion of GJ 504 in the images, we can place a limit on its $L-$[8.0] color using previous AO imaging results in the L-band from Skemer et al. (2016) and our work. We find $L - [8.0] < 8.38$ mag.

3.5.3 SED Fits

Optical and near-infrared photometry from the literature can be used with our new *Spitzer*/IRAC mid-infrared photometry to analyze the SEDs of our sample systems. We fit system components with solar metallicity BT-Settl model atmospheres (Allard et al. 2012) spanning effective temperatures between 1000 and 7000 K ($\Delta T_{\rm eff} = 100$ K) fixed at either $\log g = 3.5$ (2M0441 B and CHXR 73) or $\log g = 4.0$ which is appropriate for young dwarfs according to BT-Settl evolutionary models. We convolve the model atmospheric spectra with filter transmission profiles to generate synthetic photometric measurements and find the χ^2-minimizing scale factor between the model photometry and the observed photometry for each object. We also fit $E(B-V)$ as a free parameter using the extinction curve of Fitzpatrick (1999) in steps of 0.01 mag.

In Figure 3.6, we show the SED fits for the systems in our sample. We show our new *Spitzer*/IRAC photometry as red stars and the literature photometry used in our fits as blue squares. We also include the best-fit BT-Settl model for the primary and companion in gray. In Table 3.5, we list all the photometry used in each SED fit for each system, in addition to our measured photometry from the pipeline parameters. In Table 3.8, we summarize the properties found from our fits. We discuss the SED fits of specific systems in Section 3.5.4, and interpret potential companion mid-infrared excesses further in Section 3.6.

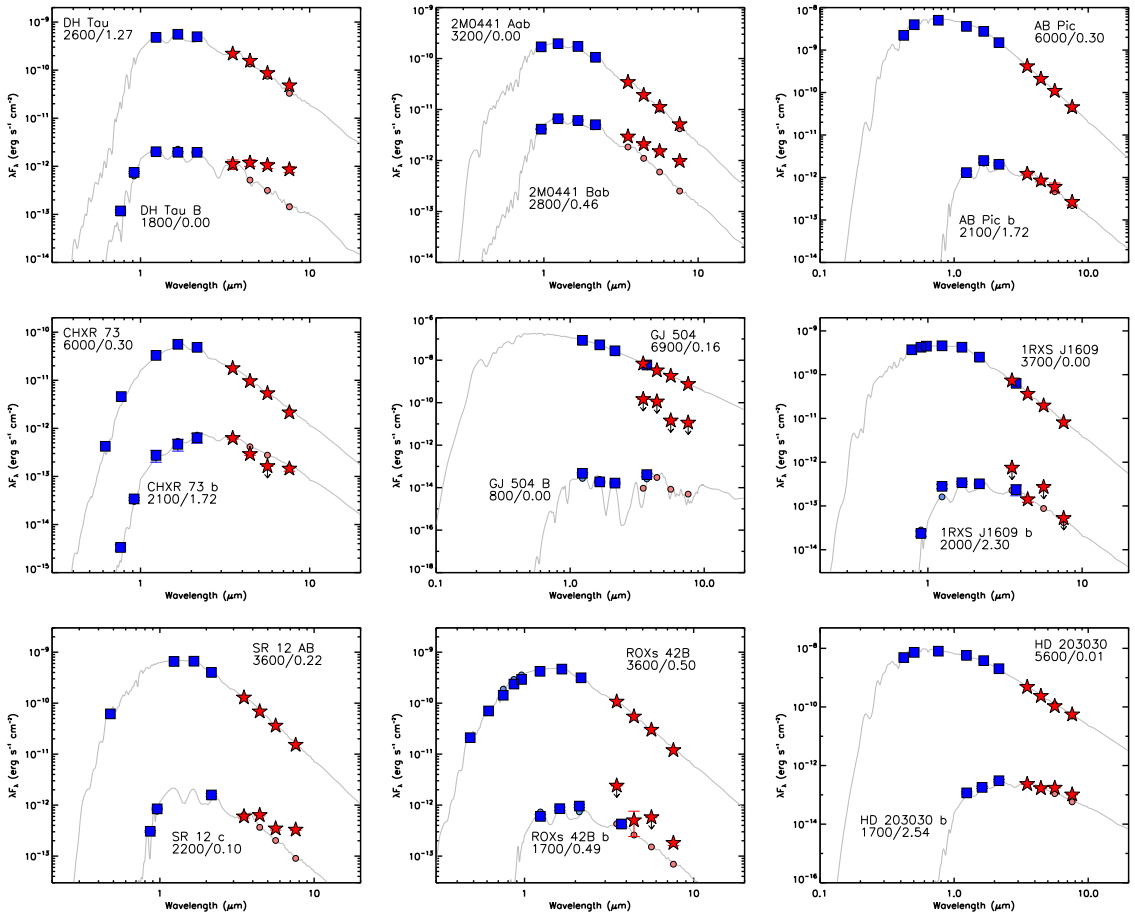

Figure 3.6: Spectral energy distributions of our sample. We fit system components with solar metallicity BT-Settl model atmospheres (Allard et al. 2012) and fit $E(B-V)$ individually as a free parameter. SED-fitting results ($T_{\rm eff}$/$E(B-V)$) for each component of our wide companion systems are plotted near the reddened best-fit model. Literature photometry for the systems is plotted as blue squares while *Spitzer*/IRAC photometry from this work is indicated as red stars. Synthetic photometry of the best fit model is also plotted as blue circles for the literature filters used or red circles at the IRAC channels. Specific filters and photometry used in our SED fits for the entire sample are listed in Table 3.5. SED-fitting results for the entire sample, including the χ^2_ν of each fit and $[8.0]_{mod} - [8.0]_{obs}$ magnitude excess, are listed in Table 3.8.

Table 3.8: SED-fitting Results for Sample Systems

Parameter	Primary	Companion
2MASS J04294155+2632582 (DH Tau)		
$T_{\rm eff}$ (K)	2600 ± 100	1800 ± 50
$E(B-V)$ (mag)	1.27 ± 0.06	0.00 ± 0.02
χ^2_ν	0.65	6.07
$[8.0]_{mod} - [8.0]_{obs}$ (mag)	0.41	1.94
2MASS J04414565+2301580 (2M0441)		
$T_{\rm eff}$ (K)	3200 ± 100	2800 ± 50
$E(B-V)$ (mag)	0.00 ± 0.02	0.46 ± 0.04
χ^2_ν	0.36	3.11
$[8.0]_{mod} - [8.0]_{obs}$ (mag)	0.23	1.47
2MASS J06191291–5803156 (AB Pic)		
$T_{\rm eff}$ (K)	6000 ± 100	2100 ± 100
$E(B-V)$ (mag)	0.30 ± 0.02	1.72 ± 0.17
χ^2_ν	4.12	1.16
$[8.0]_{mod} - [8.0]_{obs}$ (mag)	0.08	0.21
2MASS J11062877–7737331 (CHXR 73)		
$T_{\rm eff}$ (K)	3700 ± 50	1600 ± 50
$E(B-V)$ (mag)	2.15 ± 0.04	1.42 ± 0.09
χ^2_ν	0.36	0.79
$[8.0]_{mod} - [8.0]_{obs}$ (mag)	-0.07	-0.07
2MASS J13164653+0925269 (GJ 504)		
$T_{\rm eff}$ (K)	6900 ± 200	800 ± 100
$E(B-V)$ (mag)	0.16 ± 0.04	0.00 ± 0.18
χ^2_ν	2.78	12.17
$[8.0]_{mod} - [8.0]_{obs}$ (mag)	0.06	$<$8.41
2MASS J16093030–2104589 (1RXS J1609)		
$T_{\rm eff}$ (K)	3700 ± 50	2000 ± 100
$E(B-V)$ (mag)	0.00 ± 0.01	2.30 ± 0.13
χ^2_ν	0.60	3.93
$[8.0]_{mod} - [8.0]_{obs}$ (mag)	0.02	$<$0.26
2MASS J16271951–2441403 (SR 12)		
$T_{\rm eff}$ (K)	3600 ± 50	2200 ± 50
$E(B-V)$ (mag)	0.22 ± 0.01	0.10 ± 0.05
χ^2_ν	1.14	4.76

Table 3.8 continued on next page

Table 3.8 *(continued)*

Parameter	Primary	Companion
$[8.0]_{mod} - [8.0]_{obs}$ (mag)	0.04	1.41
2MASS J16311501–2432436 (ROXs 42B)		
$T_{\rm eff}$ (K)	3600 ± 50	1700 ± 50
$E(B-V)$ (mag)	0.50 ± 0.02	0.49 ± 0.18
χ^2_ν	4.29	4.20
$[8.0]_{mod} - [8.0]_{obs}$ (mag)	0.01	1.04
2MASS J21185820+2613500 (HD 203030)		
$T_{\rm eff}$ (K)	5600 ± 50	1700 ± 50
$E(B-V)$ (mag)	0.01 ± 0.02	2.54 ± 0.14
χ^2_ν	8.79	1.41
$[8.0]_{mod} - [8.0]_{obs}$ (mag)	0.13	0.62

3.5.4 Notes on Two Individual Systems

Our reprocessing of the IRAC images yielded detection of all nine primaries and eight substellar companions, five of which have not been resolved in the IRAC filters. We describe two systems in more detail in the following sections.

DH Tau

DH Tau is a protoplanetary disk host with spectral type M1 (Herbig 1977b; Watson et al. 2009). It is an actively accreting classical T Tauri star with previously detected mid-infrared excess (Valenti et al. 1993; Meyer et al. 1997; Luhman et al. 2006; 2010). DH Tau hosts a substellar companion at projected separation $\rho = 2.3$ ($\sim$310 au at its *Gaia* distance of $\sim$135 pc; Itoh et al. 2005; Bailer-Jones et al. 2021). The companion mass was initially estimated to be $\sim$30–50 $M_{\rm Jup}$ but comparison of its bolometric luminosity to newer evolutionary models revealed a lower mass of $\sim$11 $M_{\rm Jup}$ (Luhman et al. 2006; Kraus et al. 2014a; Bowler 2016), closer to the planet–brown dwarf boundary. Hydrogen emission lines and a UV continuum excess indicate active accretion onto DH Tau B (Zhou et al. 2014; Bonnefoy et al. 2014) but emission from the circum(sub)stellar disk has not been detected (Wu et al. 2020).

We resolve DH Tau B and measure its mid-infrared photometry in all IRAC

channels (see Fig 3.3 for Channel 2 detection). As we described in 3.5.3 and show in Figure 3.6, we use *Hubble Space Telescope* (*HST*) optical (Zhou et al. 2014), Two Micron All Sky Survey (2MASS) near-infrared (Cutri et al. 2003), and the *Spitzer*/IRAC 3.6 μm photometry measured in this work to analyze the SEDs of DH Tau A and B. The best-fitting model for DH Tau A is $T_{\rm eff} = 2600 \pm 100$ K and $E(B-V) = 1.27 \pm 0.06$ mag and for DH Tau B, the best-fitting model is $T_{\rm eff} = 1800 \pm 50$ K and $E(B-V) = 0.00 \pm 0.02$ mag. The 8 μm photometry for DH Tau B disagrees with the best-fitting model at 6-σ. We find the mid-infrared color of DH Tau B to be [3.6]–[8.0]$= 2.19 \pm 0.28$ mag which is discrepant with the Luhman et al. (2010) empirical color of an M9 dwarf atmosphere at the 6.4-σ level. This red color indicates a clear mid-infrared excess consistent with presence of circum(sub)stellar disk.

We use our 3.6 μm photometric measurement, DH Tau's *Gaia* parallactic distance (133.3 pc; Bailer-Jones et al. 2021), and Taurus's adopted age of $\tau \sim 2$ Myr to estimate the mass of DH Tau B to be $M = 17 \pm 3\ M_{\rm Jup}$, consistent with previous mass determinations ($M = 18 \pm 4\ M_{\rm Jup}$; Kraus et al. 2014a).

AB Pic

AB Pic is a K2 star originally considered a member of the Tucana-Horologium association ($\tau \sim 40$ Myr; Song et al. 2003; Kraus et al. 2014b; Bell et al. 2015). Torres et al. (2008) later re-assessed AB Pic to be a member of Carina, another young moving group (YMG) with age $\tau \sim 30$ Myr (e.g., Bell et al. 2015; Miret-Roig et al. 2018). Recently, Booth et al. (2021) has revised the age of Carina to be younger and only 13 Myr.

Chauvin et al. (2005b) observed AB Pic to host a planetary-mass companion, AB Pic b, at projected separation $5\farcs5$ or 275 au at its 50 pc distance. Near-infrared spectroscopic observations measure the spectral type of the wide companion to be L0-L1 (Bonnefoy et al. 2014). Near-infrared spectroscopy of the companion has not detected emission line accretion indicators (Bonnefoy et al. 2014), nor has the companion been detected at wavelengths longer than L' filter (Rameau et al. 2013; Pérez et al. 2019).

We detect AB Pic b in all four IRAC channels, finding its mid-infrared color to be $[3.6]-[8.0] = 0.81 \pm 0.17$ mag. AB Pic b is redder than younger stellar pho-

tospheres by 1-σ (Luhman et al. 2010). Using near-infrared photometric measurements from Chauvin et al. (2005b) and the mid-infrared photometry found in this work, we analyze the SED of AB Pic b similarly as we described previously for DH Tau B (see Figure 3.6) allowing $E(B-V)$ to range up to 2.0 mag. The best-fitting models for AB Pic A and b have $T_{\rm eff} = 6000 \pm 100$ K and $T_{\rm eff} = 2100 \pm 100$ but with discrepant $E(B-V)$ of 0.30 ± 0.02 mag and 1.72 ± 0.17 mag, respectively. The amount of reddening for the primary is consistent with previous measurements (0.27 ± 0.02 mag; van Belle & von Braun 2009). The significantly higher value found for AB Pic b could indicate the presence of an as of yet unresolved circum(sub)stellar disk, though the observations allow a substantial range of possible values. Our observed 8 μm flux disagrees with the model photosphere at the 1.2-σ level. Fixing the companion color excess to agree with the primary at $E(B-V) = 0.30$ mag results in a cooler best-fitting model with $T_{\rm eff} = 1700$ K. For this model photosphere, the observed 8 μm flux from our work disagrees only at the 0.6-σ level. We therefore conclude that there is not yet compelling evidence that AB Pic b hosts a disk or shows a mid-infrared excess.

Using our 3.6 μm photometric measurement, the *Gaia* parallactic distance (50.1 pc; Bailer-Jones et al. 2021), and revised age of Carina ($\tau \sim 13$ Myr), we estimate the mass of AB Pic b to be $M = 11 \pm 1\ M_{\rm Jup}$. This new mass estimate is $\sim$2 $M_{\rm Jup}$ lower than if an age of 30 Myr were assumed for AB Pic and places the companion firmly below the deuterium-burning limit.

3.5.5 Companions with Previous IRAC Photometric Measurements

2M0441 AB

Esplin et al. (2014) report IRAC photometry of $m_{[4.5]} = 9.48 \pm 0.02$ mag, $m_{[5.8]} = 9.37 \pm 0.03$ mag, and $m_{[8.0]} = 9.22 \pm 0.03$ mag for 2M0441 A in Channels 2–4 (Channel 1 is saturated). For 2M0441 B, they report $m_{[3.6]} = 12.26 \pm 0.02$ mag, $m_{[4.5]} = 11.88 \pm 0.02$ mag, $m_{[5.8]} = 11.53 \pm 0.03$ mag, and $m_{[8.0]} = 11.00 \pm 0.03$ mag. Our pipeline IRAC photometry agrees with these prior measurements within the error bars, and through our PSF-fitting procedure that masks saturated pixels, we are able to recover a Channel 1 magnitude for the the primary that is consistent with its

overall SED shape.

HD 203030

Miles-Páez et al. (2017) observed HD 203030 with *Spitzer*/IRAC (Program ID 40489) at two distinct epochs to utilize roll subtraction to obtain photometry of HD 203030 b that was minimally contaminated by its host bright stellar halo. No photometry is reported for HD 203030, but they do report IRAC photometry of $m_{[3.6]} = 14.99 \pm 0.02$ mag, $m_{[4.5]} = 14.73 \pm 0.02$ mag, $m_{[5.8]} = 14.39 \pm 0.05$ mag, and $m_{[8.0]} = 14.15 \pm 0.04$ mag for HD 203030 b. We initially fit the first epoch long-exposure images of HD 203030 and found our Channel 1 pipeline photometry of $m_{[3.6]} = 15.01 \pm 0.02$ mag agreed with their measurement, but we measured higher fluxes for all other channels ($m_{[4.5]} = 14.63 \pm 0.02$ mag, $m_{[5.8]} = 13.84 \pm 0.02$ mag, and $m_{[8.0]} = 13.44 \pm 0.03$ mag). No ground-based photometry at wavelengths greater than 3 μm have been reported in the literature.

To explore this discrepancy further, we use our pipeline infrastructure to fit all of the IRAC images available simultaneously for each exposure time, as well as the individual epochs separately. In the 1 s exposures, the primary is not saturated and we measure its photometry to be $m_{[3.6]} = 6.64 \pm 0.02$ mag, $m_{[4.5]} = 6.68 \pm 0.02$ mag, $m_{[5.8]} = 6.63 \pm 0.02$ mag, and $m_{[8.0]} = 6.63 \pm 0.02$ mag across the IRAC channels for the first epoch, and $m_{[3.6]} = 6.66 \pm 0.02$ mag, $m_{[4.5]} = 6.68 \pm 0.02$ mag, $m_{[5.8]} = 6.64 \pm 0.02$ mag, and $m_{[8.0]} = 6.63 \pm 0.02$ mag for the second. The IRAC photometry is consistent with the Band 1 (3.5 μm), 2 (4.6 μm), and 3 (12.0 μm) mid-infrared photometry reported in the AllWISE catalog Cutri et al. (2021) ($W1 = 6.66 \pm 0.07$, $W2 = 6.63 \pm 0.02$, $W3 = 6.63 \pm 0.02$). In the 26.8 s exposures, our pipeline measures $m_{[3.6]} = 6.73 \pm 0.02$ mag, $m_{[4.5]} = 6.76 \pm 0.02$ mag, $m_{[5.8]} = 6.88 \pm 0.02$ mag, and $m_{[8.0]} = 6.61 \pm 0.02$ mag across the IRAC channels for the first epoch, and $m_{[3.6]} = 6.80 \pm 0.02$ mag, $m_{[4.5]} = 6.79 \pm 0.02$ mag, $m_{[5.8]} = 6.69 \pm 0.02$ mag, and $m_{[8.0]} = 6.61 \pm 0.02$ mag for the second, suggesting a systematic uncertainty of 0.1–0.2 mag for the brightness of the primary when its PSF core is saturated. This variation is still smaller than the $\sim$0.5–0.7 mag discrepancy between our photometric measurements for the companion and those of Miles-Páez et al. (2017), indicating that if there is an issue in our analysis, it comes when fitting the companion and after the primary PSF has been subtracted.

The intrinsic photospheric colors of late-M and L dwarfs are typically determined by combining photometric observations with parallax measurements (e.g., Patten et al. 2006; Luhman et al. 2010; Filippazzo et al. 2015; Faherty et al. 2016). A L7.5 field dwarf should have $K_s - [3.6] = 1.13$ mag, $[3.6] - [4.5] = -0.02$ mag, $[4.5] - [5.8] = 0.32$ mag, and $[5.8] - [8.0] = 0.23$ mag in the IRAC channels, according to Dupuy & Liu (2012). Both $[3.6] - [4.5]$ colors measured for HD 203030 b by Miles-Páez et al. (2017) and in this work are $\sim$0.3–0.4 mag redder than expected, although consistent with younger planetary-mass objects (e.g., Filippazzo et al. 2015; Faherty et al. 2016; Liu et al. 2016). In the other channels, the colors measured by Miles-Páez et al. (2017) agree with a field L7.5 photosphere, while our photometry continues to be significantly redder. Miles-Páez et al. (2017) measure $[3.6] - [8.0] = 0.84 \pm 0.04$ which is ~ 0.3 mag redder than expected but still within the upper envelope of the rms scatter of the Dupuy & Liu (2012) sample. We measure $[3.6] - [8.0] = 1.57 \pm 0.04$ mag. This color excess could potentially indicate the presence of a circum(sub)stellar disk if confirmed, but given the disagreement with Miles-Páez et al. (2017), such an interpretation should be treated with caution.

To test if this color excess might emerge from our reduction procedures, in Figure 3.7 we show the stacked image output for our pipeline fits of the first epoch of long-exposure IRAC images. A significant positive residual is present at the expected location of HD 203030 b when only the primary PSF is subtracted, and no significant structure remains at that location when both primary and companion PSFs are subtracted, though in Channels 3 and 4, there appears to be a slight oversubtraction. The maximum pixel value at the location of HD 203030 b prior to PSF subtraction is 0.1359 DN/s and 0.2507 DN/s, respectively in those channels. After PSF subtraction, the minimum pixel value is –0.0058 DN/s and –0.0237 DN/s. This over-subtraction would result in a maximum flux overestimation of 0.05 mag and 0.10 mag in Channels 3 and 4, still not enough to explain the differences between our IRAC photometry and those of Miles-Páez et al. (2017).

To estimate a systematic uncertainty from PSF modeling, we consider the rms of flux values measured at the radial separation of the companion around HD 203030 when calculating the detection limit in the PSF-subtracted images. In Channel 3, we find the rms to be 3.26 DN/s which is 20.0% of the flux measured for HD

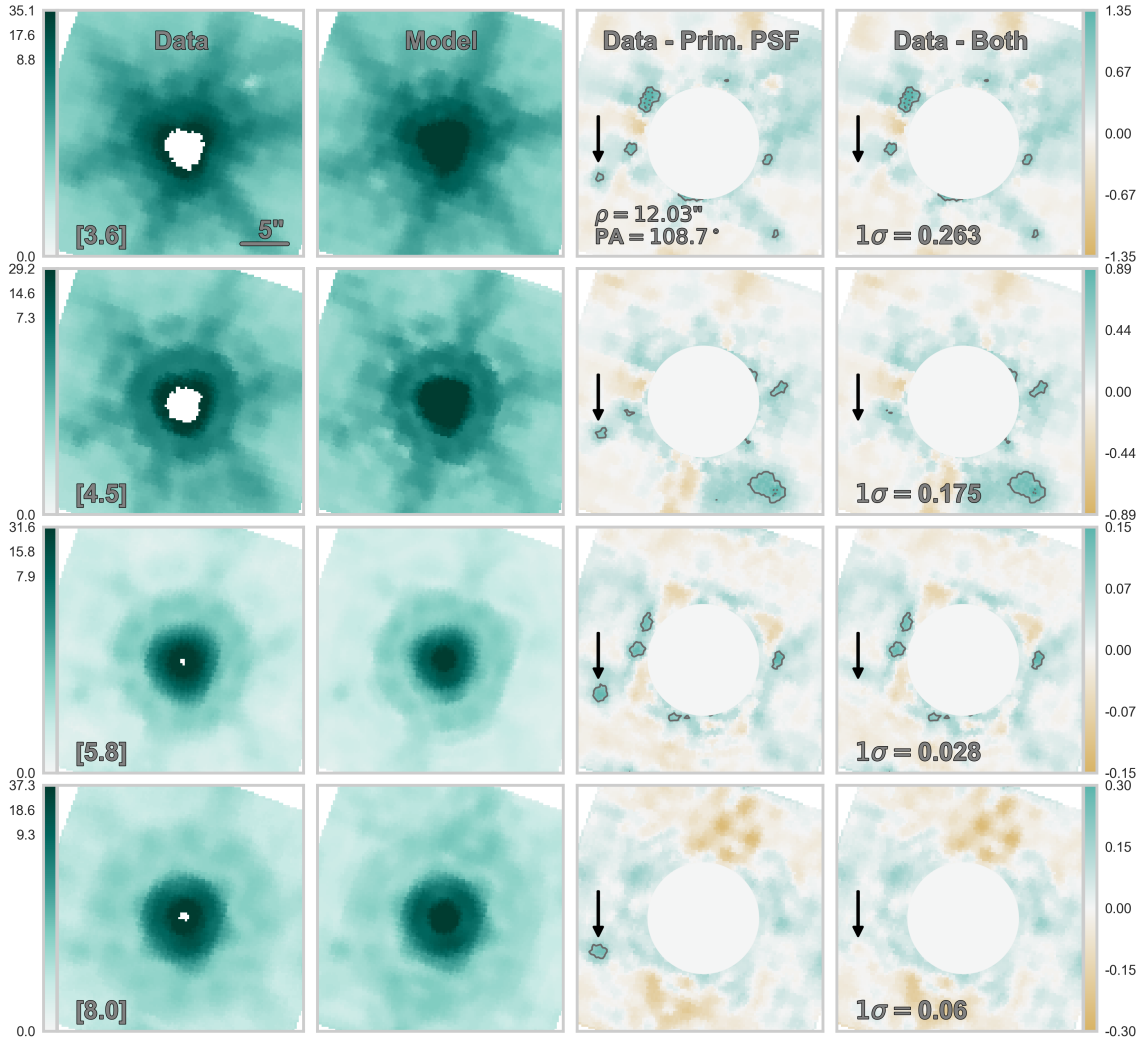

Figure 3.7: Stacked images of HD 203030 across all four IRAC channels (rows) after its first epoch images have gone through the PSF-fitting pipeline. The images were generated in the same fashion as AB Pic in Figure 3.2. Columns 1 and 2 show the original IRAC data of HD 203030 and the median two-source PSF model, respectively, displayed with a logarithmic color scale (leftmost color bar). Column 3 shows the residuals left behind after only the primary PSF model is subtracted from the data. Column 4 shows the residuals left behind after the two-source PSF model is subtracted from the data. The standard deviation of the pixel values outside a $\sim 6''$ radius from the primary centroid is displayed in the lower left-hand corner of Column 4 in units of DN/s. Both Columns 3 and 4 are displayed in a linear color scale (rightmost color bar) with the area within $\sim 6''$ of the primary centroid masked, and 3- and 5-σ contours overlaid with solid and dotted lines, respectively. After subtracting the primary star PSF, a statistically significant positive residual is seen at the expected position of HD 203030 b. This residual disappears after subtracting the best-fit system PSFs and no significant structure is left behind at the location of the companion.

203030 b. Similarly in Channel 4, we find the rms of flux values to be 9.23 DN/s, or 19.6% of the measured flux of the companion. We therefore conclude that there is no clear evidence of systematic errors in our PSF fit, as the overluminosity would be a 4–5-σ effect for each of the [5.8] and [8.0] filters, which sample the IRAC PSF in different ways. However, it is unlikely this discrepancy can be resolved without further observations to independently determine its mid-infrared brightness.

SR 12

Observations of SR 12 were a part of the *Spitzer* c2d Legacy survey (Evans et al. 2009) that imaged five nearby molecular clouds with the IRAC and MIPS instruments. Various studies (e.g., Cieza et al. 2007; 2009; Gutermuth et al. 2009; Günther et al. 2014; Esplin & Luhman 2020) have reported IRAC photometry for SR 12 AB from these data, ranging from 8.16–8.27 mag at 3.6 μm, 8.16–8.25 mag at 4.5 μm, 7.99–8.12 mag at 5.8 μm, and 8.03–8.12 mag at 8.0 μm, with typical uncertainties between 0.02 and 0.06 mag. Our pipeline photometry for SR 12 AB agrees with these previous measurements within the uncertainties in Channels 1, 3, and 4, though our measurement is $\sim$0.06 mag brighter in Channel 2.

The c2d IRAC photometry for SR 12 c is $m_{[3.6]} = 13.65 \pm 0.08$, $m_{[4.5]} = 13.60 \pm 0.03$ mag, $m_{[5.8]} = 13.20 \pm 0.28$ mag, and $m_{[8.0]} = 12.50 \pm 0.37$ (Cieza et al. 2007; Alves de Oliveira et al. 2010; Günther et al. 2014). Our Channel 1 and 2 photometry are significantly discrepant ($m_{[3.6]} = 13.99 \pm 0.07$, $m_{[4.5]} = 13.18 \pm 0.03$ mag), but we are able to constrain SR 12 c's Channel 3 and Channel 4 photometry to $m_{[5.8]} = 13.09 \pm 0.07$ mag, and $m_{[8.0]} = 12.17 \pm 0.04$ mag.

SR 12 c has a spectral type of M9-L0 (e.g., Kuzuhara et al. 2011; Bowler et al. 2014; Santamaría-Miranda et al. 2018) and thus its photosphere should have a K_s–[3.6] color of $\sim$0.6–0.7 mag based on empirical measurements of late M dwarfs (e.g., Patten et al. 2006; Luhman et al. 2010). Kuzuhara et al. (2011) reported ground-based photometry of $K_s = 14.57 \pm 0.03$ mag with their discovery of SR 12 c. Combining this K_s-band measurement with our IRAC Channel 1 photometry gives $K_s - [3.6] = 0.58 \pm 0.08$ mag, consistent with a detection of an M9 photosphere. We also measure $[3.6] - [8.0] = 1.82 \pm 0.08$ mag which indicates the companion harbors a disk. Santamaría-Miranda et al. (2018) identified numerous emission line accretion tracers in the spectrum of SR 12 c, confirming this disk.

The 4.5 μm photometry we measure for the companion is the most discrepant from previous studies. No *WISE* photometry has been reported for SR 12 c either, likely due to its crowded environment. Since our photometry of SR 12 AB agrees with previously reported values, any uncertainties would likely come from PSF subtraction. We again consider the rms of flux values measured at the radial separation of the companion around SR 12 AB when calculating the detection limit in the PSF-subtracted images. We find at 4.5 μm the rms to be 12.7 DN/s which is 6.4% of the flux measured for SR 12 c. Similarly at 5.8 μm, we find the rms of flux values to be 4.63 DN/s, or 14.2% of the measured flux of the companion. We conclude here that any large-scale deviation from an M9 photosphere may be outlining the SED of the disk harbored by SR 12 c.

As we mentioned in Section 3.4, SR 12 is $25''$ away from YLW 13B, a bright and saturated young stellar object. The discrepancies between the c2d companion photometry and ours photometry could be a result of the c2d pipeline's handling of bright neighbors, especially in Channel 1. Conversely, if there is a disk excess in the IRAC bands then it seems likely that we either overestimate the brightness at 4.5 μm or underestimate the brightness at 5.8 μm.

3.6 Discussion

Free-floating young brown dwarfs are observed to follow color-magnitude sequences that are distinct from older brown dwarfs (e.g., Allers et al. 2010; Liu et al. 2016; Faherty et al. 2016). In the near-infrared young brown dwarfs are redder in $J - K$ colors, suggesting enhanced dust abundances (e.g., Woitke & Helling 2004; Barman et al. 2011) or lower surface gravities (e.g., Burrows et al. 1997; Kirkpatrick et al. 2006; Looper et al. 2008). Determining whether wide-orbit PMCs also follow the trends previously established for free-floating brown dwarfs into the mid-infrared could point to formation pathway commonalities. Deviations would imply differing formation processes and redder colors could indicate the presence of circum(sub)stellar disks.

3.6.1 Absolute Magnitude Trends with Spectral Type

A star forms with a large radius that subsequently contracts in its pre-main sequence phase, which might result in an observable difference between the luminosities of young stars and substellar objects than those of the field. These objects would also appear brighter in the *Spitzer*/IRAC bands, especially the later spectral types and objects that harbor disks.

Figure 3.8 shows absolute magnitude-spectral type diagrams plotting $M_{[3.6]}$ through $M_{[8.0]}$ versus spectral type for the detected wide-orbit companions in our sample (filled circles) as well as others from Paper I (FU Tau B, FW Tau C, SCH J0359 B, USco 1610 B), ROXs 12 B, GQ Lup B, and GSC 6214 B (purple upside down triangles). We complement these data with late-M to early-L brown dwarfs from the Taurus and Upper Sco star-forming regions (Esplin & Luhman 2017; Luhman & Esplin 2020). The absolute magnitudes for the individual PMCs were calculated from either the *Gaia* EDR3 or DR2 parallactic measurements (Bailer-Jones et al. 2021; 2018), or if not available, from the adopted distance to the star-forming region. Individual association members are color-coded red if they are thought to harbor a disk from measured mid-infrared excess, or orange if they are thought to be disk-free. We also indicate the expected field polynomial sequence as determined by Dupuy & Liu (2012) (solid line; dark gray) as well as the young ($\tau < 1$ Gyr, $\tau \sim 5$–150 Myr; Faherty et al. 2016, Liu et al. 2016) ultracool dwarf polynomial sequence from Faherty et al. (2016) (dashed line; light gray).

In general, brown dwarfs with spectral types <M8 are 1–2 magnitudes brighter than the YMG polynomial sequence, while substantial overlap begins between the YMG sequence and brown dwarfs with spectral types >M8. This overluminosity above the field sequence is expected as the young objects have not yet contracted to their final radii. DH Tau B, 2M0441 B, CHXR 73 b, and ROXs 42B b are consistently above the YMG polynomial sequence, as well as FU Tau B. These wide companions orbit host stars that are among the very young regions ($\tau \sim 1$–3 Myr; Taurus, Chameleon, Ophiuchus). AB Pic b is the only PMC in our sample that is consistently below the YMG sequence. The high scatter within these sequences suggests that magnitudes alone do not provide a sensitive view of which objects are outliers.

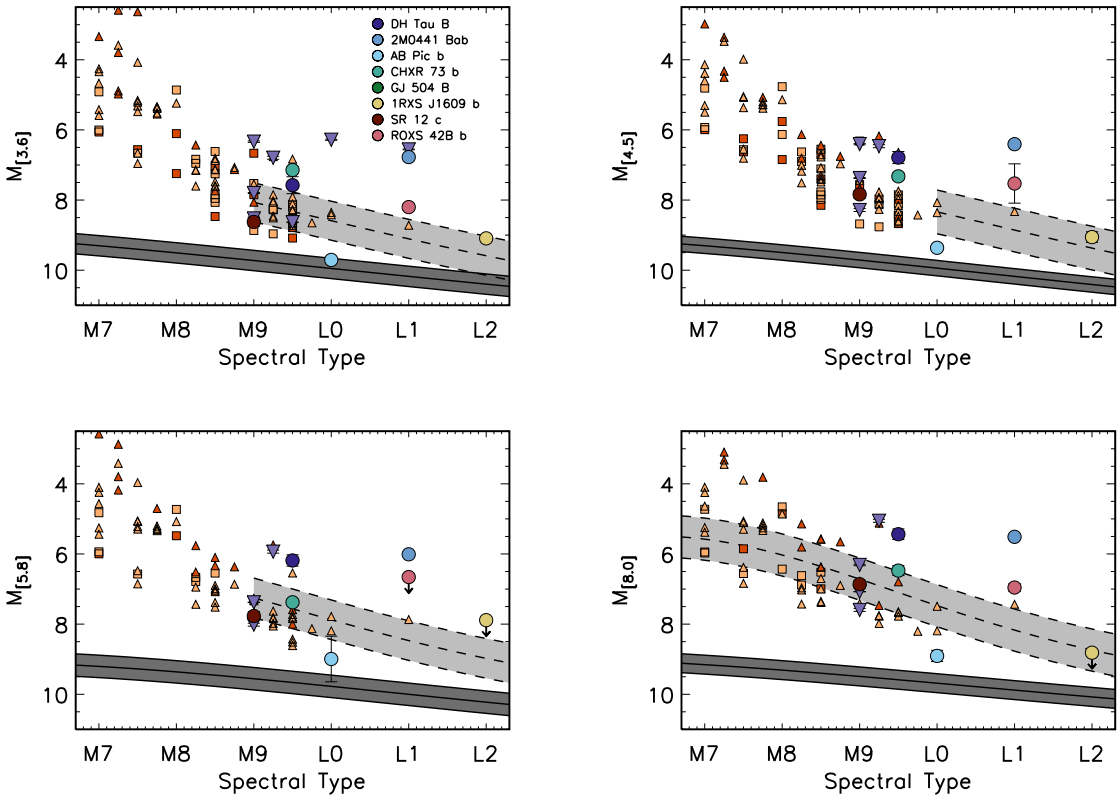

Figure 3.8: $M_{[3.6]}$ through $M_{[8.0]}$ vs. spectral type for the $\leq$L2 wide-orbit PMC samples of this work and Paper I (purple upside triangles), in addition to the young Taurus and Upper Sco brown dwarfs (depicted as in Figure 3.4). We also indicate the expected field polynomial sequence of Dupuy & Liu (2012) (solid line; dark gray) and the young ultracool dwarf polynomial sequence from Faherty et al. (2016) (dashed line; light gray). The young objects sit above the field sequence, but the dynamic range is not high enough in magnitude space to distinguish between disk-bearing and disk-free members.

3.6.2 Color Trends of Wide-orbit Companions in the Mid-Infrared

The colors of wide-orbit PMCs provide a more nuanced view of their non-photospheric behavior. The colors of our sample are expected to be close to zero given their range in spectral types, thus objects with non-zero colors are potentially interesting.

In Figure 3.9 we show [3.6]–[8.0] color as a function of spectral type for the same systems as described above for Figure 3.8. We again indicate the Taurus (triangles) and Upper Sco (squares) members as disk-bearing (red) or disk-free (orange), and include the field and YMG member polynomial sequences of Dupuy & Liu (2012) (solid line; dark gray) and Faherty et al. (2016) (dashed line; light gray).

DH Tau B, 2M0441 B, AB Pic b, CHXR 73 b, SR 12 c, and ROXs 42B b are significantly redder than the field polynomial sequence. The young ($\tau \sim 2$–10 Myr) Taurus and Upper Sco disk-hosting and disk-free members also readily differentiate themselves in the [3.6]–[8.0] color space.

Interestingly, the disk-bearing members fall right in line with the continuation of the YMG ($\sim$20–120 Myr) dwarf sequence. The detected PMCs of this sample also are consistent with the YMG sequence except for DH Tau B, which is already known to show active accretion. 2M0441 B, SR 12 c, and ROXs 42B b are above the average YMG polynomical sequence color for their spectral type which could be due to the youth of the systems or the presence of circum(sub)stellar disks. There also is the possibility that some YMG members may also harbor circum(sub)stellar disks.

3.6.3 Identifying Disk-Hosting PMCs in Color-Color Space

Identifying disk hosts in color-color space removes reliance on spectral type measurements that can be highly uncertain. In Figure 3.10 we show [3.6]–[8.0] vs. K_s–[3.6] color for our PMC sample and the young Taurus and Upper Sco brown dwarfs, depicted as in Figures 3.8 and 3.9. We also include the expected color-color sequence of 5 Myr BT-Settl and AMES-Dusty isochrones as a theoretical comparison.

Five of the wide orbit PMCs in this work (DH Tau B, 2M0441B, ROXs 42B b,

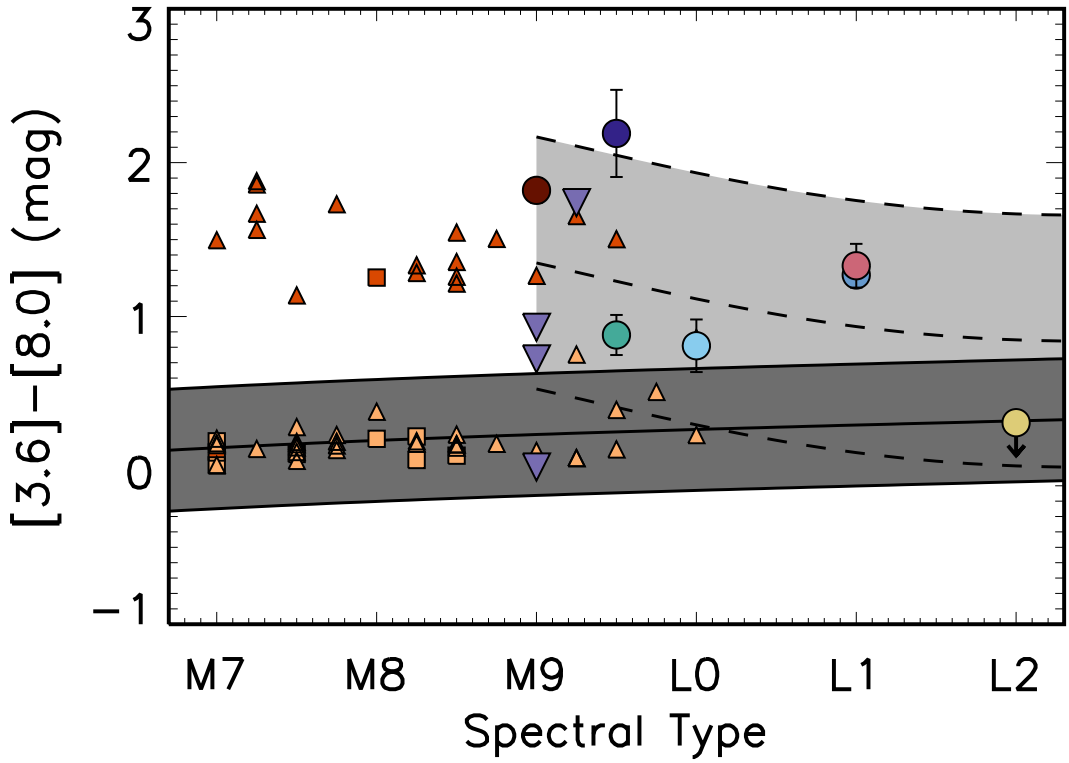

Figure 3.9: [3.6]–[8.0] color as a function of spectral type for our sample.We include the wide-orbit PMC sample from Paper I, and the young Taurus and Upper Sco brown dwarfs, depicted as in Figures 3.4 and 3.8. Also included are field and young moving group (YMG) member polynomial sequences of Dupuy & Liu (2012) (solid line; dark gray) and Faherty et al. (2016) (dashed line; light gray). The dynamic range is refined enough in color space for the disk-bearing objects to clearly sit above the disk-free objects.

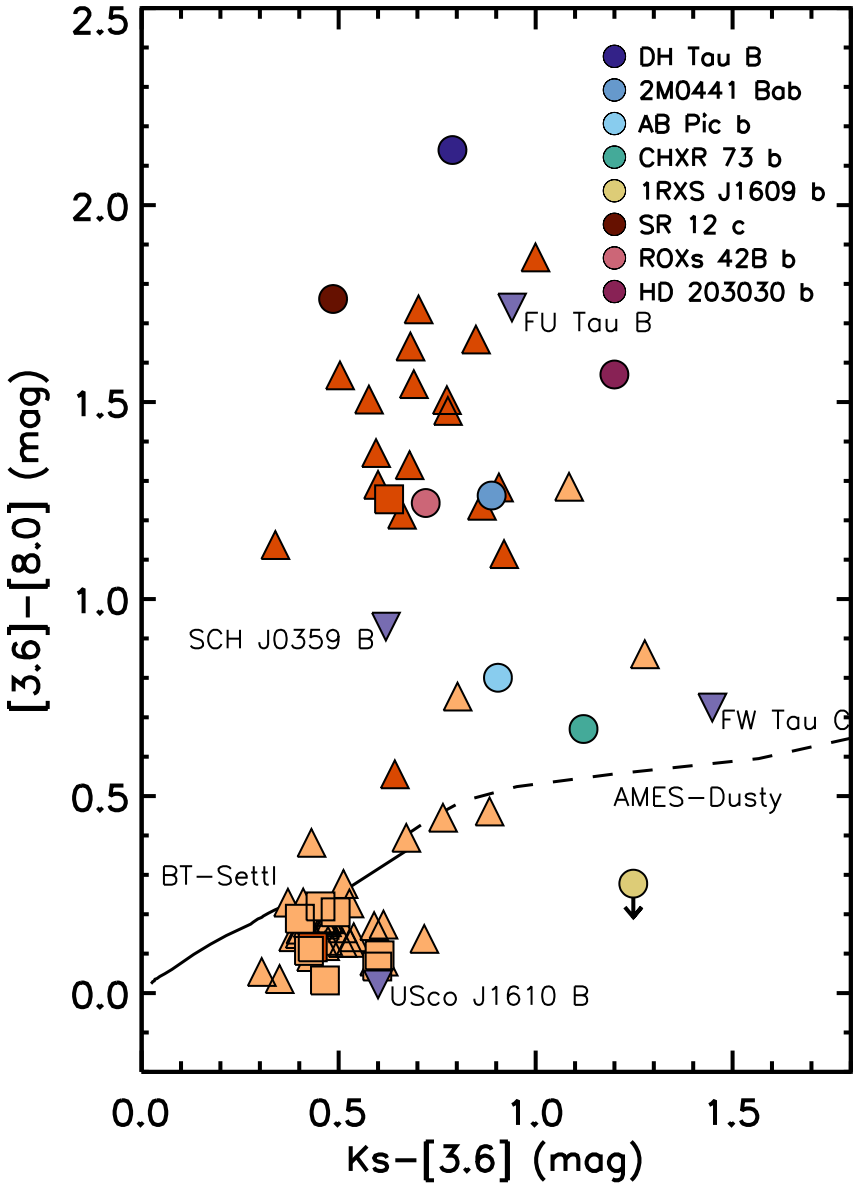

Figure 3.10: [3.6]–[8.0] vs. K_s–[3.6] color for our sample companions, the Paper I wide-orbit PMC sample, and the young Taurus and Upper Sco brown dwarfs, depicted as in Figures 3.4, 3.8 and 3.9. We also include the expected color-color sequence of 5 Myr BT-Settl and AMES-Dusty isochrones. The disk-bearing objects are clear outliers in this particular color-color space, providing a criterion to say DH Tau B, 2M0441 B, ROXs 42B, and SR 12 c appear to host disks.

SR 12 c, and HD 203030 b), along with two from Paper I (FU Tau B and SCH J0359 B) have colors consistent with young disk-bearing brown dwarfs. However, HD 203030 b is is the latest spectral type of our sample (L7.5) thus its position in this parameter space is likely explained by differences in late-L atmospheric characteristics rather than the presence of a circum(sub)stellar disk. Only one object in this combined sample, the more massive USco 1609 B ($M \sim 70\ M_{\rm Jup}$), falls among the disk-free young brown dwarfs. AB Pic b and CHXR 73 b fall outside of the disk-free locus, along with a few late-type disk-free members, but their locations are consistent with predictions from the AMES-Dusty models (Chabrier et al. 2000b; Allard et al. 2001). FW Tau C sits furthest from the disk-hosting and disk-free objects, but given the ongoing debate over whether it a more massive object hosting an edge-on disk (Wu & Sheehan 2017), it might be expected to have anomalous colors.

3.6.4 Disk Fraction of Wide-Orbit PMCs

Determining the presence of circumstellar disks around young star-forming region members has been a useful tool to infer the dominant formation pathway of substellar objects, as well as their planet-forming capabilities. Similarly, identifying and characterizing the disks harbored by PMCs offers a direct avenue to study planet assembly and evolution, as well as potential satellite formation.

Mass-dependent disk evolution has been observed for stars and brown dwarfs in young star-forming regions or associations through the measurement of disk fractions. Luhman et al. (2010) found the disk fraction for solar-type stars in Taurus ($\tau \sim 2$ Myr) to be ∼75% and the disk fraction for lower-mass stars (0.01–0.3 $M_{\odot}$) to be ∼45%. For the older Upper Sco OB association ($\tau \sim 10$ Myr), Carpenter et al. (2006) find <1% of stars more massive than K0 have circumstellar disks while the disk fraction for K0–M5 stars is 19%. Substantial disk fractions persisting for stars <1 $M_{\odot}$ and substellar objects indicate disk dispersal is less efficient and that planet formation timescales are longer. We can now begin to quantify whether these disk frequency trends continue for wide-orbit PMCs. For instance, Bowler et al. (2017) found $46\% \pm 14\%$ of young (<15 Myr) substellar (<20 $M_{\rm Jup}$) companions have detectable Paβ emission, indicating that accretion disks are very common around wide-orbit PMCs. Here, we incorporate our findings into previous disk fraction

determinations and explore their global frequency.

Combining the nine PMC systems from this work with three from Paper 1, ten belong to star-forming regions or associations with $\tau < 15$ Myr: DH Tau, SCH J0359, FU Tau, FW Tau, 2M0441, AB Pic, CHXR 73, ROXs 42B, 1RXS J1609, and SR 12. Since 2M0441 is an interesting quadruple system comprised of close binary pairs, they should be considered separately and not incorporated into our disk fraction calculation. Thus, six of these companions have disk-like mid-infrared excesses determined from this work, suggesting a disk frequency of $67\% \pm 16\%$ for PMCs with $\tau < 15$ Myr. The two older PMC systems in our sample, GJ 504 and HD 203030, host companions that do not have disk-like mid-infrared excesses.

Previous PMC disk fraction determinations from Bowler et al. (2017) and Bryan et al. (2020) required emission line accretion signatures or UV continuum excess detections to designate a companion as a disk host, potentially underestimating their occurrence rate measurement because of the variability of these signatures or the overall faintness of the disk. Here we combine our PMC sample disk determinations with their findings, updating ROXs 42B b and SR 12 c as disk-bearing, giving a disk fraction of $56\% \pm 12\%$. This confirms that PMCs harboring circum(sub)stellar disks is very common at young ages. Even within our <15 Myr age bin, hints of PMC disk evolution may be emerging since two of the three companions with no mid-infrared excess from this work had system ages above 5 Myr. Increasing the sample of >5 Myr PMC systems with and without circum(sub)stellar disks will ultimately confirm whether the rate at with which they host disks follows that observed of star-forming region members.

3.7 Summary

We have used our MCMC-based PSF formalism to reanalyze *Spitzer*/IRAC images of nine stars known to host faint planetary-mass companions, examining higher contrast systems and closer-in separations than our previous work to measure the mid-infrared photometry of the companions. We report new IRAC photometry for all nine primaries in our sample and eight of the companions, five of which have not been resolved in IRAC images before.

For one of the newly resolved companions, AB Pic b, we use our photometry

and the updated system age of 13 Myr (Booth et al. 2021) to estimate its mass at $M = 11 \pm 1\ M_{\rm Jup}$, placing the companion firmly below the deuterium-burning limit. We also measure an 8.0 μm excess for ROXs 42B b, a companion not thought to harbor a disk due to a lack of observed emission line accretion signatures. We also confirm mid-infrared excesses from the previously suggested disks around DH Tau B, 2M0441 B, and SR 12 c, and detect likely photospheric emission from four companions that do not show evidence of disks (AB Pic b, CHXR 73 b, 1RXS J1609 b, HD 203030 b).

We find for our sample from Paper I and this work that $67\% \pm 16\%$ of young (<15 Myr) wide-orbit PMCs harbor disks. Combined with past detections of disk indicators to wide-orbit PMCs, we find a global young disk fraction of $56\% \pm 12\%$, signifying that both accreting and non-accreting PMC disks are very common. The increasing likelihood that the disks surrounding wide-orbit PMCs are compact and optically thick, and thus easier to study in the mid-infrared (Wu et al. 2017), highlights the importance of leveraging *Spitzer* to motivate future observations of PMC systems in the *JWST* era.

Chapter 4: Automated Search for Wide Companions in Taurus

4.1 Abstract

We report the results from a general search for Jupiter-like companions on wide orbits (>50 au) around members of the Taurus star-forming region (τ∼2 Myr, d∼145 pc; Torres et al. 2008). The well-constrained age of the Taurus complex, along with the moderate contrasts and wide separations of these companions, make them prime targets for detailed follow-up characterization via spectroscopy, which would provide valuable insights for exoplanet atmosphere models at young ages. We search for these companions in *Spitzer*/Infrared Array Camera images from its cryogenic phase in archival images at 3.6, 4.5, 5.8, and 8.0 μm. We use the point-spread function (PSF) fitting framework introduced in Martinez & Kraus (2019) to subtract the primary PSF, then search for significant residuals in the resultant images in an automated fashion. We also describe our method for signaling the presence of significant positive residuals post-primary PSF subtraction in a target's images. In our sample of 209 stars, we find 11 systems of interest that appear to harbor candidate companions or have extended residual flux remaining after primary PSF subtraction. We report the discovery of a $\rho = 2\farcs98$ (780 au) companion to 2MASS J05160577+2236151. Based on its brightness ($M_{[3.6]} = 7.13$ mag), we infer the companion mass to be $M = 30\ M_{\rm Jup}$ given the primary's model-derived age of 5 Myr. Our survey is up to 93% complete to 5 $M_{\rm Jup}$ companions at ∼1000 au, and from our survey completeness we constrain the frequency of 0.5–30 $M_{\rm Jup}$ companions on semi-major axes 50–5000 au to <3.7% at a 95% confidence level.

4.2 Introduction

The earliest direct-imaging surveys for planetary-mass and brown dwarf companions targeted members of young, nearby stellar associations to more easily detect bright, newly-formed exoplanets a few tens of au away from their hosts. This strategy proved successful with the discovery of 2MASSW J1207334–393254 b, more commonly known as 2M1207 b, the first directly-imaged planetary-mass companion from the VLT/NACO deep imaging survey of austral stars (Chauvin

et al. 2004; 2005a; 2010). Soon thereafter, the HR 8799 exoplanets were discovered as part of the International Deep Planet Survey (IDPS; Kaisler et al. 2003; Marois et al. 2008; Marois 2010; Marois et al. 2010). 2M1207 b and the HR 8799 planets have masses and orbital separations that can be explained by formation within a circumstellar disk, as is thought to be the case for the solar system (Cameron 1978). Additional PMCs on even wider orbits that have been discovered in direct-imaging surveys include 1RXS J160929.1–210524 b (8 $M_{\rm Jup}$, 330 au; Lafrenière et al. 2008a), GSC 06214-00210B (14 $M_{\rm Jup}$, 330 au; Ireland et al. 2011), HD 106906 b (11 $M_{\rm Jup}$, 650 au; Bailey et al. 2014), SR 12 c (6–20 $M_{\rm Jup}$, 1100 au; Kuzuhara et al. 2011), and 2MASS J21265040–8140293 (12–15 $M_{\rm Jup}$, 4500 au; Deacon et al. 2016), which was unexpected given the formation of these systems are hard to explain with prevailing planet formation theories. There are currently 46 confirmed planetary-mass objects $<$30 $M_{\rm Jup}$ on orbits between 2 and 3500 au that have been discovered via direct-imaging[1]. If a stricter definition of what constitutes a planet is taken, typically $M<$13 $M_{\rm Jup}$ (the deuterium-burning limit), the number of confirmed directly-imaged planets falls to 26. This represents $<<1\%$ of the known exoplanet population which not only emphasizes the difficulty of exoplanet imaging, but also reveals how unconstrained any conclusions about wide PMCs as a population are because of their rarity.

We report here the preliminary results of a general search for wide companions in the Taurus star-forming region ($\tau\sim$2 Myr, $d\sim$145 pc; Torres et al. 2008) using the PSF-subtraction framework first described in Martinez & Kraus (2019) (hereafter Paper I). We search for these companions in archival *Spitzer*/IRAC images to leverage its sensitivity in the mid-infrared, and take advantage of young PMCs' higher luminosities, decreasing the relative contrast with their hosts and making them easier to detect. In Section 4.3, we describe how we construct our sample of Taurus members. Sections 4.4 and 4.5 describe the *Spitzer* observations and our analysis of the IRAC images. We present the results of our survey in Section 4.6. Finally, we discuss the statistical findings of our survey and the constraints it makes on the wide planetary-mass companion occurrence rate in Section 4.7.

[1]NASA Exoplanet Archive

4.3 Survey Sample

We target members of the Taurus star-forming regions for our search for wide companions for their youth, uniform formation environment, and well-characterized binarity. Young, forming planets are intrinsically brighter in the mid-infrared due to retention of residual heat from formation, making lower mass companions easier to detect. We therefore use the most recent Taurus census from Krolikowski et al. (2021) to form our sample, focusing on their "core" Gaussian mixture model groups C1-L1551, C2-L1495, C3-L1517, C4-L1517-Center, C5-L1536, C6-L1524, C7-L1527-B213, and C8-B213, assigned based on *Gaia* EDR3 (Gaia Collaboration et al. 2021) parallaxes, proper motions, and positions. For this work, we do not fit most members of the distributed groups because the ages of these groups are older and less constrained, but also because their IRAC coverage is less complete having only been discovered recently. However, we did include the sample of Slesnick et al. (2006) which comprised a number of distributed population Taurus members that were specifically targeted by *Spitzer*/IRAC Program ID 50584 (PI: D. Padgett).

We then identify systems that also have archival *Spitzer*/Infrared Array Camera (IRAC; Fazio et al. 2004) observations from its cryogenic mission. Many targets in the sample have images obtained during the warm *Spitzer* mission, but we do not fit them due to the PSF changes. Groups C9-118Tau and C10-118TauE were not fit because they had no *Spitzer*/IRAC coverage. We use the binarity flags from Krolikowski et al. (2021) to ensure we only fit single stars to ease the interpretation of any detections and their implications for models of planet formation. The fitting of Taurus binaries will comprise a sample for a future search of PMCs. In Figure 4.1 we show a map of our sample within Taurus superimposed upon the dust reddening map of Schlafly et al. (2014). In total, two B stars, two A stars, four G stars, 21 K stars, and 180 M stars were fit in the sample. The stellar properties of the sample are given in Table 4.1.

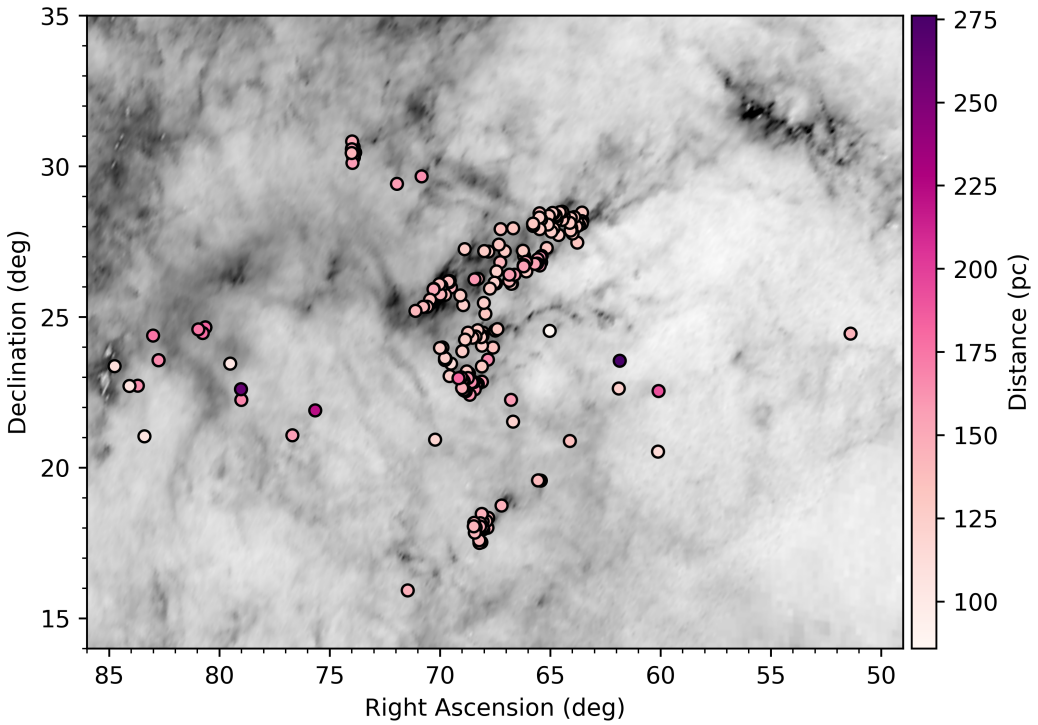

Figure 4.1: The 209 targets from our Taurus sample superimposed on the dust reddening map of Schlafly et al. (2014).

Table 4.1: Primary Properties and *Spitzer*/IRAC Observations of Taurus Sample

2MASS J	Other Name	RA	Dec	Distance (pc)	SpT	# of Images (Ch 1, Ch 2, Ch 3, Ch 4)	Program ID(s)
03253316+2426577		03 25 33.16	+24 26 57.7	145.0	M4.5	4, 4, 4, 4	50584
04002202+2232384		04 00 22.02	+22 32 38.4	191.7	M4.75	4, 4, 4, 4	50584
04002788+2031591		04 00 27.88	+20 31 59.1	114.5	M5.75	4, 4, 4, 4	50584
04072456+2332553		04 07 24.56	+23 32 55.3	276.1	M4	4, 4, 4, 4	50584
04073502+2237394		04 07 35.02	+22 37 39.4	125.2	M5	4, 4, 4, 4	50584
04131414+2819108	LkCa 1	04 13 14.14	+28 19 10.8	130.3	M6.25	5, 6, 5, 6	6, 30816
04141188+2811535	L04-01	04 14 11.88	+28 11 53.5	131.1	M4.5	4, 5, 4, 5	6, 30816
04141358+2812492	FM Tau	04 14 13.58	+28 12 49.2	129.5	M3.5	5, 4, 5, 4	6, 30816
04141458+2827580	FN Tau	04 14 14.58	+28 27 58.0	131.3	K3	5, 4, 5, 4	6, 30816
04141700+2810578	CW Tau	04 14 17.00	+28 10 57.8	133.5	M4.5	6, 5, 6, 5	6, 30816
04141760+2806096	CIDA 1	04 14 17.60	+28 06 09.6	128.2	M5.2	4, 4, 4, 4	6, 30816
04144739+2803055	XEST 20-066	04 14 47.39	+28 03 05.5	133.0	M4.5	5, 9, 5, 9	6, 37, 30816
04150515+2808462	CIDA 2	04 15 05.15	+28 08 46.2	133.5	M3.25	2, 3, 2, 3	30816
04150651+2728136		04 15 06.51	+27 28 13.6	130.9	M8.5	7, 6, 7, 6	6, 37, 30816
04151471+2800096	KPNO-Tau 1	04 15 14.71	+28 00 09.6	131.5	M4	4, 4, 4, 4	6, 30816
04153916+2818586	L09-01	04 15 39.16	+28 18 58.6	132.1	M5.2	4, 2, 4, 2	30816
04155799+2746175	L09-02	04 15 57.99	+27 46 17.5	133.8	M4.75	4, 2, 4, 2	30816
04161210+2756385	L04-02	04 16 12.10	+27 56 38.5	130.2	M4.5	4, 3, 4, 3	6, 30816
04161407+2758275	2MASS J04161407+2758275 N	04 16 14.07	+27 58 27.5	130.8	M4.75	5, 5, 5, 5	6, 30816
04161726+2817128		04 16 17.26	+28 17 12.8	134.1	M6.25	2, 2, 3, 2	30816
04161885+2752155	L06-03	04 16 18.85	+27 52 15.5	129.6	M1.3	4, 4, 5, 4	6, 30816
04162725+2053091		04 16 27.25	+20 53 09.1	137.0	M5	4, 4, 4, 4	50584
04162810+2807358	LkCa 4	04 16 28.10	+28 07 35.8	126.1	M2.3	8, 9, 9, 9	6, 3584, 30816
04173372+2820468	CY Tau	04 17 33.72	+28 20 46.8	134.9	M5	7, 10, 7, 11	6, 3584, 30816
04174955+2813318	KPNO-Tau 10	04 17 49.55	+28 13 31.8	129.8	M3.7	5, 6, 5, 6	6, 3584, 30816
04174965+2829362	V410 X-ray 1	04 17 49.65	+28 29 36.2	127.2	M5.75	4, 6, 4, 6	6, 3584, 30816
04181710+2828419	V410 Anon 13	04 18 17.10	+28 28 41.9	126.8	M5.9	8, 3, 8, 3	3584
04183030+2743208	KPNO-Tau 11	04 18 30.30	+27 43 20.8	128.9	M7.5	6, 4, 6, 4	6, 3584
04185115+2814332	KPNO-Tau 2	04 18 51.15	+28 14 33.2	129.0	M5.25	5, 6, 4, 7	6, 37, 3584
04185813+2812234	IRAS 04158+2805	04 18 58.13	+28 12 23.4	126.8	M5.9	10, 5, 10, 5	3584, 6

Table 4.1 continued on next page

Table 4.1 *(continued)*

2MASS J	Other Name	RA	Dec	Distance (pc)	SpT	# of Images (Ch1, Ch2, Ch3, Ch4)	Program ID(s)
04190110+2819420	V410 X-ray 6	04 19 01.10	+28 19 42.0	130.9	M5.5	4, 4, 4, 4	6, 3584
04190197+2822332	V410 X-ray 5	04 19 01.97	+28 22 33.2	129.8	M3.75	3, 6, 3, 6	37, 3584, 30008
04192520+2756133		04 19 25.20	+27 56 13.3	129.2	K8	4, 6, 4, 6	6, 3584
04192625+2826142	V819 Tau	04 19 26.25	+28 26 14.2	125.6	M5.3	4, 6, 4, 6	6, 3584
04193545+2827218	FR Tau	04 19 35.45	+28 27 21.8	127.7	M3.25	5, 5, 5, 5	37, 3584
04194819+2750007		04 19 48.19	+27 50 00.7	130.5	M6.5	2, 2, 2, 2	3584
04200674+2432268		04 20 06.74	+24 32 26.8	85.8	M4	2, 2, 2, 2	30816
04201611+2821325	L09-03	04 20 16.11	+28 21 32.5	127.2	M3.5	2, 2, 2, 2	3584
04202555+2700355	L04-04	04 20 25.55	+27 00 35.5	162.4	M5.5	3, 2, 3, 2	462
04202606+2804089	IRAS 04171+2756	04 20 26.06	+28 04 08.9	132.0	M4.5	4, 3, 4, 3	462, 3584
04203918+2717317	XEST 16-045	04 20 39.18	+27 17 31.7	124.2	M5.75	2, 3, 2, 3	462
04213459+2701388	L04-05	04 21 34.59	+27 01 38.8	165.8	M6	2, 2, 3, 2	462
04213965+2649143		04 21 39.65	+26 49 14.3	161.9	M6.25	3, 2, 3, 2	462
04214013+2814224	XEST 21-026	04 21 40.13	+28 14 22.4	127.8	M2.3	5, 5, 5, 5	37, 462
04214323+1934133	IRAS 04187+1927	04 21 43.23	+19 34 13.3	145.8	M2.4	3, 6, 3, 6	37, 42
04214631+2659296	CFHT Tau 10	04 21 46.31	+26 59 29.6	160.5	M5	3, 3, 4, 3	462
04215482+2642372		04 21 54.82	+26 42 37.2	157.0	M1.5	3, 3, 3, 3	462
04215563+2755060	DE Tau	04 21 55.63	+27 55 06.0	138.9	G0	5, 8, 5, 8	37, 3584
04215740+2826355	RY Tau	04 21 57.40	+28 26 35.5	126.4	G4	8, 5, 8, 5	37, 3584
04215884+2818066	HD 283572	04 21 58.84	+28 18 06.6	128.4	M6	5, 2, 5, 2	37, 3584
04220496+1934483	RX J0422.1+1934	04 22 04.96	+19 34 48.3	144.4	M3.5	8, 8, 8, 8	37, 30540
04221332+1934392	XEST 01-062	04 22 13.32	+19 34 39.2	139.4	M8.5	5, 5, 5, 5	30540
04221675+2654570	CFHT Tau 21	04 22 16.75	+26 54 57.0	157.2	M3	4, 3, 4, 3	462
04222404+2646258	XEST 11-087	04 22 24.04	+26 46 25.8	153.8	M1	3, 4, 3, 4	462, 3584
04224786+2645530	IRAS 04196+2638	04 22 47.86	+26 45 53.0	152.5	M3	2, 2, 2, 2	3584
04230607+2801194	L06-18	04 23 06.07	+28 01 19.4	130.5	M2	5, 5, 5, 5	37, 3584
04230776+2805573	IRAS 04200+2759	04 23 07.76	+28 05 57.3	127.5	M6	2, 4, 2, 4	3584
04242090+2630511	L06-20	04 24 20.90	+26 30 51.1	127.9	M4.5	5, 7, 5, 7	37, 3584
04242321+2650084	SSTtau 042423.2+265008	04 24 23.21	+26 50 08.4	156.9	M6.25	2, 2, 2, 2	3584
04242646+2649503	CFHT Tau 9	04 24 26.46	+26 49 50.3	159.6	K1	4, 4, 4, 4	173, 3584
04244506+2701447	J1-4423	04 24 45.06	+27 01 44.7	129.3	M0.6	7, 9, 7, 10	37, 462, 3584

Table 4.1 continued on next page

Table 4.1 *(continued)*

2MASS J	Other Name	RA	Dec	Distance (pc)	SpT	# of Images (Ch1, Ch2, Ch3, Ch4)	Program ID(s)
04244815+2643161	V1201 Tau	04 24 48.15	+26 43 16.1	150.2	K0	4, 4, 4, 4	173, 3584
04244904+2643104	HD 283641	04 24 49.04	+26 43 10.4	148.9	M1	4, 4, 4, 4	173, 3584
04244926+2643030		04 24 49.26	+26 43 03.0	156.2	M5	3, 4, 3, 4	173, 3584
04245021+2641006		04 24 50.21	+26 41 00.6	156.0	M6	5, 5, 5, 5	37, 3584
04245708+2711565	IP Tau	04 24 57.08	+27 11 56.5	133.0	M6	4, 2, 4, 2	3584
04262939+2624137	KPNO-Tau 3	04 26 29.39	+26 24 13.7	157.0	M3	2, 4, 2, 2	3584
04264449+2756433		04 26 44.49	+27 56 43.3	129.3	M5.1	5, 5, 5, 5	37, 3584
04264516+2131408		04 26 45.16	+21 31 40.8	121.6	M4.75	4, 4, 4, 4	50584
04265732+2606284	KPNO-Tau 13	04 26 57.32	+26 06 28.4	124.8	K7	5, 5, 5, 5	37, 3584
04270469+2606163	DG Tau	04 27 04.69	+26 06 16.3	141.4	M9.5	5, 5, 5, 5	37, 3584
04270739+2215037		04 27 07.39	+22 15 03.7	159.4	M6.75	4, 4, 4, 4	50584
04272467+2624199		04 27 24.67	+26 24 19.9	158.1	M4.5	5, 3, 5, 3	3584, 30816
04272799+2612052	KPNO-Tau 4	04 27 27.99	+26 12 05.2	129.3	M5.5	2, 2, 2, 2	3584
04281566+2711110		04 28 15.66	+27 11 11.0	135.9	M8.25	2, 4, 2, 4	3584
04285053+1844361		04 28 50.53	+18 44 36.1	146.5	M7.25	0, 3, 0, 3	42
04290068+2755033	L06-08	04 29 00.68	+27 55 03.3	142.8	K6	5, 5, 5, 5	37, 3584
04290498+2649073	IRAS 04260+2642	04 29 04.98	+26 49 07.3	132.2	B9	4, 2, 4, 2	3584
04291983+2724153	HD 28354	04 29 19.83	+27 24 15.3	130.0	M3	3, 3, 4, 3	173, 3584
04293606+2435556	XEST 13-010	04 29 36.06	+24 35 55.6	124.1	M7.5	5, 5, 5, 5	37, 3584
04294568+2630468	KPNO-Tau 5	04 29 45.68	+26 30 46.8	130.7	M1.1	5, 7, 5, 7	37, 3584
04295156+2606448	IQ Tau	04 29 51.56	+26 06 44.8	123.5	M8.5	5, 5, 5, 5	37, 3584
04295950+2433078		04 29 59.50	+24 33 07.8	130.8	M5.5	6, 4, 6, 3	139, 3584
04300724+2608207	KPNO-Tau 6	04 30 07.24	+26 08 20.7	135.1	M8.5	2, 2, 2, 2	3584
04302365+2359129	CFHT Tau 16	04 30 23.65	+23 59 12.9	127.4	M8.25	8, 9, 8, 9	37, 3584
04305718+2556394	KPNO-Tau 7	04 30 57.18	+25 56 39.4	126.7	K8	5, 7, 5, 7	37, 3584
04311444+2710179	JH 56	04 31 14.44	+27 10 17.9	132.0	M5.5	3, 4, 3, 4	3584
04311578+1820072	MHO 9	04 31 15.78	+18 20 07.2	141.2	M4.25	4, 4, 4, 4	6
04311907+2335047		04 31 19.07	+23 35 04.7	166.9	M8	4, 2, 3, 2	3584
04312405+1800215	MHO 4	04 31 24.05	+18 00 21.5	144.7	M7.5	4, 8, 4, 8	6
04313613+1813432	LkHa 358	04 31 36.13	+18 13 43.2	139.1	M0.9	3, 2, 3, 2	6
04314644+2506236		04 31 46.44	+25 06 23.6	127.7	M5	2, 4, 2, 4	3584

Table 4.1 continued on next page

Table 4.1 *(continued)*

2MASS J	Other Name	RA	Dec	Distance (pc)	SpT	# of Images (Ch1, Ch2, Ch3, Ch4)	Program ID(s)
04315919+2711190		04 31 59.19	+27 11 19.0	125.6	M6.25	2, 3, 2, 3	3584
04320329+2528078	L06-11	04 32 03.29	+25 28 07.8	127.7	K5.5	5, 13, 5, 13	37, 139, 3584
04320926+1757227	L 1551-51	04 32 09.26	+17 57 22.7	143.0	K6	3, 5, 3, 5	6, 37
04321540+2428597	Haro 6-13	04 32 15.40	+24 28 59.7	125.6	M6.7	8, 5, 8, 5	37, 3584
04321583+1801387	V826 Tau	04 32 15.83	+18 01 38.7	143.1	K7	2, 4, 2, 4	6, 37
04321606+1812464	MHO 5	04 32 16.06	+18 12 46.4	146.9	M6.5	6, 3, 6, 3	6
04321786+2422149	CFHT Tau 7	04 32 17.86	+24 22 14.9	125.7	M7.75	2, 2, 2, 2	3584
04322210+1827426	MHO 6	04 32 22.10	+18 27 42.6	144.3	M5	5, 3, 5, 3	6, 37
04322329+2403013	L06-12	04 32 23.29	+24 03 01.3	130.7	M4.75	4, 4, 4, 4	3584
04322415+2251083	L09-08	04 32 24.15	+22 51 08.3	149.6	M6	5, 5, 5, 5	37, 3584
04322464+2321382		04 32 24.64	+23 21 38.2	128.5	M0.1	12, 10, 10, 10	37, 139, 3584
04322627+1827521	MHO 7	04 32 26.27	+18 27 52.1	146.4	M5.3	5, 3, 5, 3	6, 37
04323028+1731303	GG Tau Bb	04 32 30.28	+17 31 30.3	147.7	M7.5	3, 3, 3, 3	37
04323058+2419572	FY Tau	04 32 30.58	+24 19 57.2	128.3	M0.5	12, 10, 10, 11	37, 139, 3584
04323176+2420029	FZ Tau	04 32 31.76	+24 20 02.9	130.0	K7.5	7, 6, 7, 6	37, 3584
04324107+1809239	RX J0432.6+1809	04 32 41.07	+18 09 23.9	142.5	M5	0, 4, 0, 4	6, 37
04324373+1802563	L 1551-55	04 32 43.73	+18 02 56.3	147.7	K6	3, 4, 3, 4	6, 37
04325119+1730092	LH 0429+17	04 32 51.19	+17 30 09.2	144.9	M8.25	0, 1, 0, 1	173
04325323+1735337	V1321 Tau	04 32 53.23	+17 35 33.7	142.2	M1.5	2, 2, 2, 2	173
04330781+2616066	KPNO-Tau 14	04 33 07.81	+26 16 06.6	175.8	M6.5	10, 10, 11, 10	37, 30540, 30816
04330945+2246487	CFHT Tau 12	04 33 09.45	+22 46 48.7	157.2	M4	8, 6, 8, 5	37, 30816
04331003+2433433	V830 Tau	04 33 10.03	+24 33 43.3	129.7	M0.5	13, 10, 13, 10	37, 30540, 30816
04331907+2246342	IRAS 04303+2240	04 33 19.07	+22 46 34.2	129.3	M0.4	5, 5, 5, 5	37, 3584
04332621+2245293	XEST 17-036	04 33 26.21	+22 45 29.3	163.3	M4.5	2, 3, 2, 3	30816
04333278+1800436		04 33 32.78	+18 00 43.6	145.1	M1	0, 3, 0, 3	37
04333297+1801004	HD 28867 B	04 33 32.97	+18 01 00.4	144.9	B9	0, 3, 0, 3	37
04333405+2421170	GI Tau	04 33 34.05	+24 21 17.0	128.9	K6.5	5, 5, 5, 5	37, 3584
04333456+2421058	GK Tau	04 33 34.56	+24 21 05.8	132.3	M8.25	3, 14, 3, 14	94, 3584
04334171+1750402	L09-10	04 33 41.71	+17 50 40.2	143.6	M4	3, 3, 3, 3	37
04334298+2235566		04 33 42.98	+22 35 56.6	160.1	M5.2	5, 5, 5, 6	37, 462
04334465+2615005	L09-11	04 33 44.65	+26 15 00.5	160.2	K5.5	5, 5, 5, 5	37, 30816

Table 4.1 continued on next page

Table 4.1 *(continued)*

2MASS J	Other Name	RA	Dec	Distance (pc)	SpT	# of Images (Ch1, Ch2, Ch3, Ch4)	Program ID(s)
04334871+1810099	DM Tau	04 33 48.71	+18 10 09.9	143.1	M3	3, 3, 3, 3	37
04335200+2250301	CI Tau	04 33 52.00	+22 50 30.1	160.9	M1.5	6, 5, 6, 5	37, 3584, 30816
04335283+1803166		04 33 52.83	+18 03 16.6	144.2	M5	3, 0, 3, 0	37
04340619+2418508		04 34 06.19	+24 18 50.8	133.7	M0.6	5, 6, 5, 6	37, 3584, 20302
04341099+2251445	JH 108	04 34 10.99	+22 51 44.5	164.9	M7	6, 5, 6, 5	37, 30816
04341527+2250309	CFHT Tau 1	04 34 15.27	+22 50 30.9	161.4	M7	2, 2, 2, 2	30816
04343609+2225143		04 34 36.09	+22 25 14.3	161.4	M0	5, 3, 5, 4	3584, 30816
04344544+2308027		04 34 45.44	+23 08 02.7	163.8	M5.25	2, 3, 2, 3	3584, 30816
04345542+2428531	AA Tau	04 34 55.42	+24 28 53.1	127.5	M6.75	2, 2, 2, 2	3584
04345693+2258358	XEST 08-003	04 34 56.93	+22 58 35.8	163.2	M3.2	5, 7, 6, 7	37, 30816
04345923+1733379		04 34 59.23	+17 33 37.9	146.3	M7.25	4, 2, 4, 2	3584
04350850+2311398	CFHT Tau 11	04 35 08.50	+23 11 39.8	128.2	M0.3	12, 19, 12, 20	37, 3584, 20302
04351316+1725496		04 35 13.16	+17 25 49.6	141.7	M7.25	2, 3, 2, 3	37, 3584
04352020+2232146	HO Tau	04 35 20.20	+22 32 14.6	153.0	M5.75	6, 6, 6, 6	37, 30816
04352737+2414589	DN Tau	04 35 27.37	+24 14 58.9	126.1	M4	2, 2, 2, 2	3584
04353164+2715081		04 35 31.64	+27 15 08.1	125.7	M4.5	2, 2, 2, 2	3584
04354183+2234115	KPNO-Tau 8	04 35 41.83	+22 34 11.5	162.7	M5	6, 6, 6, 5	37, 3584, 30816
04354203+2252226	XEST 08-033	04 35 42.03	+22 52 22.6	160.6	K2	8, 6, 7, 6	37, 3584, 30816
04354733+2250216	HQ Tau	04 35 47.33	+22 50 21.6	159.1	M2.75	8, 7, 8, 7	37, 3584, 30816
04354778+2523436		04 35 47.78	+25 23 43.6	119.4	M2	9, 4, 8, 4	173, 3584, 20302
04355109+2252401	KPNO-Tau 15	04 35 51.09	+22 52 40.1	182.6	M8.5	10, 5, 10, 5	37, 3584, 30816
04355143+2249119	KPNO-Tau 9	04 35 51.43	+22 49 11.9	159.4	M2	10, 9, 9, 9	37, 3584, 30816
04355209+2255039	XEST 08-047	04 35 52.09	+22 55 03.9	170.0	K4	13, 8, 13, 8	37, 3584, 30816
04355277+2254231	HP Tau	04 35 52.77	+22 54 23.1	160.7	M2	9, 6, 9, 6	37, 3584, 30816
04355286+2250585	XEST 08-049	04 35 52.86	+22 50 58.5	166.3	G2	11, 8, 11, 8	37, 3584, 30816
04355415+2254134	HP Tau/G2	04 35 54.15	+22 54 13.4	166.1	K7	5, 3, 3, 3	30816
04355683+2352049	V1324 Tau	04 35 56.83	+23 52 04.9	126.5	M5.75	8, 4, 7, 4	173, 3584, 20302
04355694+2351472		04 35 56.94	+23 51 47.2	127.8	K5	7, 5, 7, 5	37, 3584
04355892+2238353	XEST 09-042	04 35 58.92	+22 38 35.3	147.7	M1	3, 4, 3, 4	30816
04355949+2238291	SSTtau 043559.4+223829	04 35 59.49	+22 38 29.1	166.9	M7.5	9, 9, 11, 9	37, 3584, 30816
04361038+2259560	CFHT Tau 2	04 36 10.38	+22 59 56.0	181.3	M7.75	7, 7, 7, 7	37, 3584, 30816

Table 4.1 continued on next page

Table 4.1 *(continued)*

2MASS J	Other Name	RA	Dec	Distance (pc)	SpT	# of Images (Ch1, Ch2, Ch3, Ch4)	Program ID(s)
04361909+2542589	LkCa 14	04 36 19.09	+25 42 58.9	125.7	M1	9, 4, 7, 4	3584, 30816
04363893+2258119	CFHT Tau 3	04 36 38.93	+22 58 11.9	164.3	M5.5	12, 14, 13, 14	37, 94
04380007+2327167		04 38 00.07	+23 27 16.7	113.0	M5.25	2, 2, 2, 2	3584
04380083+2558572	L04-07	04 38 00.83	+25 58 57.2	138.1	M5	7, 5, 7, 5	37, 3584
04381486+2611399	L04-08	04 38 14.86	+26 11 39.9	138.4	M0.3	5, 5, 5, 5	37, 3584
04381561+2302276	V1117 Tau	04 38 15.61	+23 02 27.6	125.4	M6	2, 2, 2, 2	3584
04382134+2609137	GM Tau	04 38 21.34	+26 09 13.7	139.8	M7.25	2, 4, 3, 4	3584
04382858+2610494	DO Tau	04 38 28.58	+26 10 49.4	138.3	M5	5, 5, 6, 5	37, 3584
04385859+2336351		04 38 58.59	+23 36 35.1	125.4	M4.25	2, 0, 2, 0	3584
04390163+2336029		04 39 01.63	+23 36 02.9	125.9	M6	4, 0, 4, 0	3584
04390396+2544264	L04-09	04 39 03.96	+25 44 26.4	139.5	M7	7, 5, 7, 5	37, 3584
04390571+2338112		04 39 05.71	+23 38 11.2	125.9	M5	4, 4, 4, 4	3584
04390637+2334179		04 39 06.37	+23 34 17.9	124.2	M7.5	2, 0, 2, 0	3584
04390940+2324007		04 39 09.40	+23 24 00.7	125.7	M6	2, 4, 2, 4	3584
04394488+2601527	ITG 15	04 39 44.88	+26 01 52.7	144.2	K4	5, 5, 5, 5	37, 3584
04394748+2601407	CFHT Tau 4	04 39 47.48	+26 01 40.7	137.4	K9.75	5, 5, 5, 5	37, 3584
04395574+2545020	IC 2087	04 39 55.74	+25 45 02.0	145.9	M3	10, 13, 10, 13	37, 139, 173, 3584
04400800+2605253	IRAS 04370+2559	04 40 08.00	+26 05 25.3	150.5	M5.5	8, 13, 8, 13	37, 139, 173, 3584
04405340+2055471		04 40 53.40	+20 55 47.1	118.8	M5.	4, 4, 4, 4	50584
04410826+2556074	ITG 33	04 41 08.26	+25 56 07.4	137.3	M7.75	4, 17, 4, 18	139, 3584
04411078+2555116	ITG 34	04 41 10.78	+25 55 11.6	139.6	M5.1	8, 5, 5, 5	37, 3584
04414825+2534304	L04-12	04 41 48.25	+25 34 30.4	141.3	M2.3	5, 5, 5, 5	37, 3584
04422101+2520343	CIDA 7	04 42 21.01	+25 20 34.3	141.9	M7.25	5, 5, 5, 5	37, 3584
04422776+2939448		04 42 27.76	+29 39 44.8	158.1	M0.4	3, 3, 3, 3	37
04430309+2520187	GO Tau	04 43 03.09	+25 20 18.7	146.3	M2.5	2, 2, 2, 2	173
04432023+2940060	CIDA 14	04 43 20.23	+29 40 06.0	159.0	M6.25	26, 8, 26, 8	37, 94, 30540
04474859+2925112	DS Tau	04 47 48.59	+29 25 11.2	156.4	K2	6, 6, 6, 6	37
04552333+3027366	L04-14	04 55 23.33	+30 27 36.6	152.7	M5.25	10, 6, 10, 6	37, 50584
04553695+3017553	LkCa 19	04 55 36.95	+30 17 55.3	155.7	M4.7	9, 7, 9, 7	37, 50584
04554046+3039057	L04-15	04 55 40.46	+30 39 05.7	155.0	A1	11, 14, 12, 14	37, 50584
04554535+3019389	L04-16	04 55 45.35	+30 19 38.9	146.1	M5	9, 11, 9, 11	37, 50584

Table 4.1 continued on next page

Table 4.1 *(continued)*

2MASS J	Other Name	RA	Dec	Distance (pc)	SpT	# of Images (Ch1, Ch2, Ch3, Ch4)	Program ID(s)
04554582+3033043	AB Aur	04 55 45.82	+30 33 04.3	159.0	M5.6	9, 13, 9, 13	37, 50584
04554757+3028077	L04-17	04 55 47.57	+30 28 07.7	156.4	M4.5	14, 14, 14, 13	37, 50584
04554801+3028050	L04-18	04 55 48.01	+30 28 05.0	142.6	A1	9, 8, 9, 8	37, 50584
04554820+3030160	XEST 26-052	04 55 48.20	+30 30 16.0	159.1	M5.25	3, 3, 3, 3	37
04554822+3020165	HD 31305	04 55 48.22	+30 20 16.5	178.4	M4	8, 10, 8, 10	37, 50584
04555288+3006523	L04-20	04 55 52.88	+30 06 52.3	149.8	M5	3, 3, 3, 3	37
04555605+3036209	XEST 26-062	04 55 56.05	+30 36 20.9	156.1	G4	7, 6, 7, 8	37, 50584
04555636+3049374	L04-21	04 55 56.36	+30 49 37.4	143.7	M3.5	7, 4, 7, 5	37, 50584
05023773+2154045		05 02 37.73	+21 54 04.5	223.2	M4.25	4, 4, 4, 4	50584
05064662+2104296		05 06 46.62	+21 04 29.6	157.8	M5.25	4, 4, 4, 4	50584
05160212+2214528		05 16 02.12	+22 14 52.8	168.0	M5	4, 4, 4, 4	50584
05160577+2236151		05 16 05.77	+22 36 15.1	262.7	M4	4, 4, 4, 4	50584
05180285+2327127		05 18 02.85	+23 27 12.7	103.3	M5	4, 4, 4, 4	50584
05223326+2439251		05 22 33.26	+24 39 25.1	179.8	M4.75	8, 8, 8, 8	50584
05223346+2439197		05 22 33.46	+24 39 19.7	183.3	M4.5	8, 8, 8, 8	50584
05230197+2428085		05 23 01.97	+24 28 08.5	179.6	M4	4, 4, 4, 4	50584
05234996+2435236		05 23 49.96	+24 35 23.6	175.0	M6	4, 4, 4, 4	50584
05310205+2333576		05 31 02.05	+23 33 57.6	165.8	M4	8, 8, 8, 8	50584
05310261+2334020		05 31 02.61	+23 34 02.0	166.2	M4	8, 8, 8, 8	50584
05320210+2423028		05 32 02.10	+24 23 02.8	176.1	M5	4, 4, 4, 4	50584
05333627+2102276		05 33 36.27	+21 02 27.6	106.8	M4.5	4, 4, 4, 4	50584
05344797+2243139		05 34 47.97	+22 43 13.9	164.0	M4.25	4, 4, 4, 4	50584
05361898+2242426		05 36 18.98	+22 42 42.6	107.7	M4.75	4, 4, 4, 4	50584
05390093+2322079		05 39 00.93	+23 22 07.9	111.2	M6	4, 4, 4, 4	50584

NOTES — *Gaia* EDR3 parallactic distances are from Bailer-Jones et al. (2021) except for 2MASS J03253316+2426577, where we use the median distance to Taurus.

4.4 *Spitzer* Observations

All targets in the sample were observed by the *Spitzer Space Telescope* (Werner et al. 2004) with IRAC (Fazio et al. 2004) during the cryogenic phase of the mission, which operated at four mid-infrared filters: 3.6, 4.5, 5.8, and 8.0 μm. The IRAC detector is 256×256 pixels with pixel scale $\sim 1\farcs22$ per pixel, making its total field of view $312'' \times 312''$. The IRAC PSF FWHM ranges from $1\farcs66$ in Channel 1 (3.6 μm) to $1\farcs98$ in Channel 4 (8.0 μm) corresponding to resolvable companions with separations above 200 au at the median 145 pc distance of Taurus.

Observations of the 209 members of our sample appear in 12 different sets of IRAC data. While the exposure times of the images range from 0.4 to 96.8 s, in this work we use only the 10.4 s images to limit the number of targets that would suffer from saturation. Images with shorter and longer exposure times, as well as warm mission images, will be re-analyzed in future work. All data were reduced with the *Spitzer* Science Center software pipeline version S18.25.0. Specific details about the entire sample's *Spitzer* programs and data used are presented in Table 4.1.

4.5 Image Analysis

We use the point-spread function (PSF) fitting infrastructure described in Martinez & Kraus (2019) to process the available IRAC images of our sample. To summarize, we use the point response function (PRF, or effective PSF; Hoffman 2005) developed by the *Spitzer* Science team to generate models PSFs at any position on the IRAC detector. Image pixel values greater than 90% of the IRAC saturation limit in that channel were masked. We then fit a single-source PSF model at an estimated position of the target in each image performing a Markov Chain Monte Carlo (MCMC) analysis using a Metropolis-Hastings algorithm with Gibbs sampling. The PSF model is described by four parameters: x-pixel coordinate of the target centroid (x), y-pixel coordinate of the target centroid (y), image background (b), and peak pixel value of the target (n).

The MCMC analysis is conducted in two stages to determine image-specific parameters (x, y, b) separately from the system-specific parameter (n). We ran four MCMC chains with a total of 140,000 steps across these two stages, discarding the first 10% of each chain as "burn-in". We then use the weighted average median

n generated by the MCMC fit to appropriately scale an individual PSF model of the target from which aperture photometry using a $10''$ radius is measured. We measure photometry from a PSF model as opposed to the original IRAC images to avoid inclusion of nearby companions contributing to the final flux measurement and make use of the standard IRAC aperture corrections[2].

After an MCMC run completes for one target in one channel, we create stacked images that subsample the original CBCD images to 1/5 of the IRAC pixel scale ($\sim 0\farcs24$), move to a common origin, rotate so that north is up and east is left before they are combined. We perform aperture photometry on these subsampled stacked images to determine the contrast sensitivities of the pipeline around each primary. We use aperture radii equal to the FWHM in each channel ($1\farcs66$, $1\farcs72$, $1\farcs88$, $1\farcs98$) which are larger than the $1\farcs22$ IRAC pixel scale, thus covariant pixels will contribute to the final measured fluxes for the detection limits. We measure the flux inside 100 random azimuthal apertures at radial intervals spaced FWHM/4 between the target centroid out to $15''$. We then calculate the mean and standard deviation of these fluxes to determine the 4-σ limiting flux at a given projected separation for the target.

We convert the *Spitzer* magnitude contrast limits into absolute magnitude limits using the *Gaia* EDR3 parallactic distance from Bailer-Jones et al. (2021), then convert these into companion mass limits using the 1 Myr evolutionary models of Chabrier et al. (2000b). These models go down to masses as low as 1 $M_{\rm Jup}$, but are in the MKO filter system, not *Spitzer*. We transform between the filter systems by using the absolute magnitude-spectral type relations of 314 ultracool dwarfs from Dupuy & Liu (2012). First, we use the Dupuy & Liu (2012) $T_{\rm eff}$ vs. Spectral Type relation to extrapolate the Chabrier et al. (2000b) $\sim$20 point grid onto a grid of 250 points between 315 K and 2990 K. We then fit 7^{th}-order polynomials to $K - [X]$ vs. Spectral Type of the Dupuy & Liu (2012) sample (X = IRAC Channels 1, 2, and 4), while for Channel 3, we fit an 8^{th}-order polynomial. This provides a color relation to derive an estimate of an object's mass given our measured IRAC absolute magnitude.

We then searched for statistically significant positive residuals within the stacked and subsampled images by placing an aperture of 1 FWHM on every fifth

[2]IRAC Instrument Handbook

pixel and determining whether the flux contained within the aperture was above the detection limit for that radial separation from the target. If the flux was above the limit, the stacked image pixel was flagged. After this initial grid search was performed, we then find the local maximum of the flagged pixel values to eliminate redundant detections from the same positive residual. We deem a detection as a candidate companion of interest if a positive residual is flagged at the same position in at least 2 IRAC channels, or just once in Channel 4.

For candidate companions, we then fit a two-source PSF model in each image performing a MCMC analysis using a Metropolis-Hastings algorithm with Gibbs sampling. A two-source PSF model differs from a one-source PSF model in that it is described by seven parameters: x-pixel coordinate of the primary centroid (x), y-pixel coordinate of the primary centroid (y), image background (b), peak pixel value of the primary (n), projected separation (ρ), position angle (PA), and contrast (Δm). In addition, image pixel values greater than 90% of the saturation limit were masked.

Similar to the one-source fit, the MCMC analysis is conducted in two stages to determine image-specific parameters (x, y, b) separately from system-specific parameters (n, ρ, PA, Δm). We ran four MCMC chains with 140,000 steps each, discarding the first 10% of each chain as "burn-in". The weighted average median (x, y)-centroid, ρ, PA, and Δm generated by the MCMC fit is used to create individual PSF models of each system component from which aperture photometry using a $10''$ radius is measured.

4.6 Results

Our PSF-fitting results yield sensitive upper limits on the companions that we did not detect, as well as revealing the presence of additional companions in these systems.

4.6.1 Detection Limits

We present the contrast limits reached in the PSF-subtracted images as a function of radial separation in Figure 4.2. We plot each limit individually in gray, but overlaid in light blue is a shaded region that contains 80% of the limits, while the

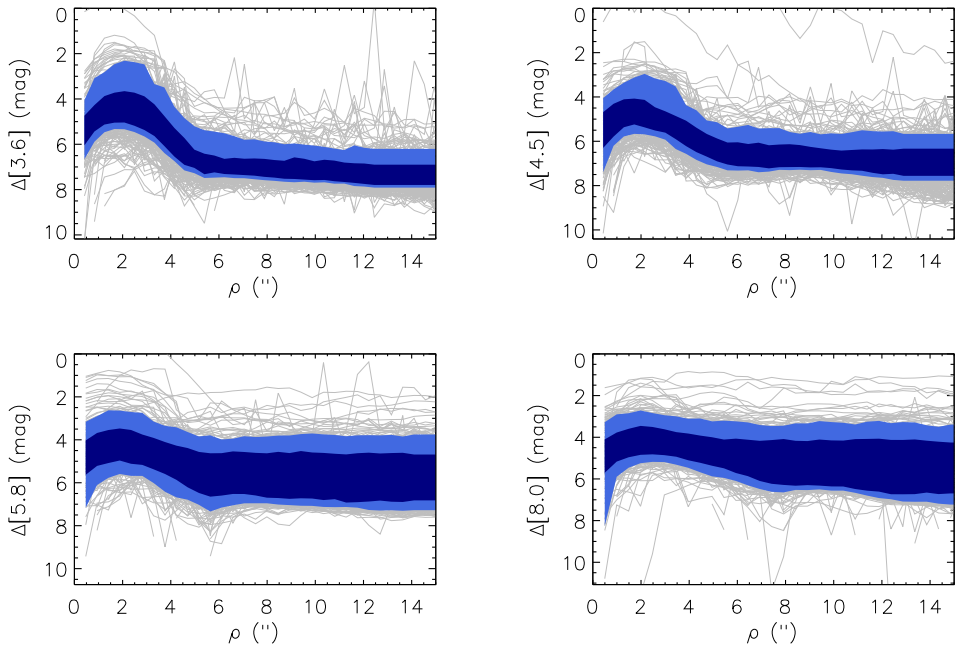

Figure 4.2: 4-σ contrast curves in each of the IRAC Channels for the entire Taurus sample fit in this work. The individual detection limits around each target are plotted in gray. The dark blue shaded areas in each panel contain 50% of the detection limit curves, while the light blue areas contain 80% of the detection limit curves.

dark blue region contains 50% of the limits. Since the achievable contrast for the pipeline depends on the brightness of the star and the background limit, we show in Figure 4.3 the limiting companion flux reached with our pipeline. The light and dark blue shaded regions again contain 80% and 50% of the flux limit curves. Finally, we convert the limiting fluxes into companion mass limits (Figure 4.4; see Section 4.5 for details of our conversion method) using the 1 Myr isochrones of Chabrier et al. (2000b).

Our detection limit curves show that our pipeline achieves a plateau of detectable companion fluxes past $\sim$5″ of 16.5 mag, 16.0 mag, 15.1 mag, and 14.1 mag in Channels 1 through 4, respectively. This angular separation corresponds to projected physical separations of $\sim$725 au at the median distance of the Taurus members in the sample. In companion mass space, the median sensitivity is 2.0 $M_{\rm Jup}$, 2.4 $M_{\rm Jup}$, 2.8 $M_{\rm Jup}$, and 6.0 $M_{\rm Jup}$ past 5″ in the IRAC channels. The larger scatter inside of 5″ is likely the result of bright targets having saturated cores which

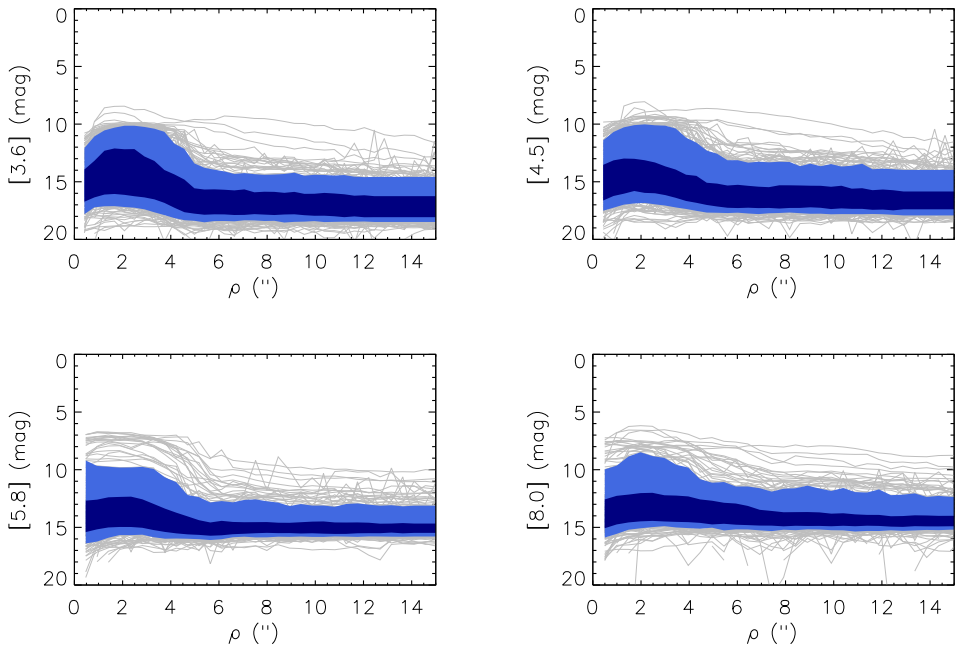

Figure 4.3: 4-σ companion flux limits in each of the IRAC Channels for the entire Taurus sample fit in this work. Similar to Figure 4.2, the individual companion flux limits around each target are plotted in gray, the dark blue shaded areas in each panel contain 50% of the companion flux limit curves, while the light blue areas contain 80% of the companion flux limit curves.

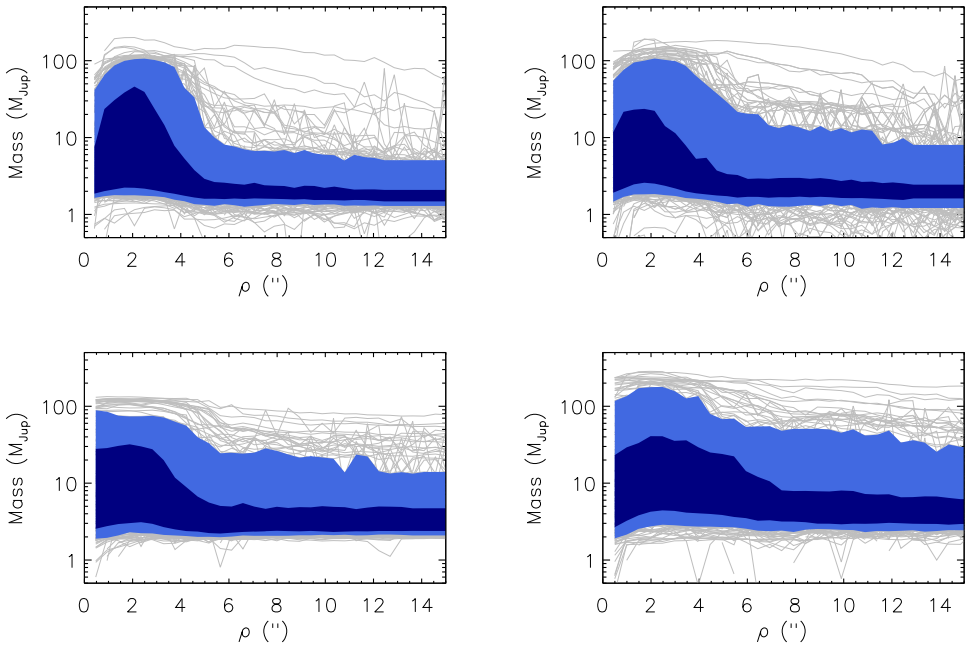

Figure 4.4: 4-σ companion mass limits in each of the IRAC Channels for the entire Taurus sample fit in this work. Similar to Figure 4.2, the individual companion mass limits around each target are plotted in gray, the dark blue shaded areas in each panel contain 50% of the mass limit curves, while the light blue areas contain 80% of the mass limit curves.

were not accurately fit by our PSF model. We did not pre-screen any of the sample's IRAC images for obvious neighbors which manifests as jagged peaks in the contrast and flux limit curves at larger separations. We are not very sensitive to low-mass companions <10 $M_{\rm Jup}$ for some of our targets, which also might be a result of improper PSF subtraction for very saturated stars, or contamination from nearby bright neighbors outside of the fitting radius for our pipeline.

4.6.2 Completeness of Survey

We use the companion mass detection limits of our survey and the Exoplanet Detection Map Calculator (ExoDMC[3]) Python package to determine our survey completeness. ExoDMC is the latest (and first Python-based) version of the Multi-purpose Exoplanet Simulation System (MESS; Bonavita et al. 2012) code that performs statistical analyses of direct imaging surveys. ExoDMC utilizes user-provided information on target stars (i.e., age, distance) and detection limits to estimate the detection probability of a synthetic planet population, producing detection probability maps.

Since a companion's observed projected separation does not necessarily equal the semi-major axis of the system, ExoDMC generates uniformly distributed orbital parameters with a user-provided eccentricity distribution for each semi-major axis and companion mass grid point. Planet distributions take the functional form

$$\frac{d^2N}{dmda} \propto m^{\alpha} a^{\beta}, \tag{4.1}$$

with m being the planet mass and a representing the semi-major axis (Cumming et al. 2008). One of the default planet distributions of ExoDMC is logarithmic in mass and semi-major axis (i.e., $\alpha = \beta = -1$), but we also adapt the code to accommodate the power law distribution from Brandt et al. (2014) with $\alpha = -0.65$ and $\beta = -0.85$, to compare to a model based on the results of high-contrast imaging surveys. We also use a uniform distribution for eccentricity. We allow the mass grid to range between 0.5 to 30 $M_{\rm Jup}$ equally spaced on a logarithmic scale with 60 steps, and the semi-major axis grid to range from 50 to 5000 au, equally spaced on a logarithmic scale with 500 steps. For every grid point, 10^4 planets are simulated

[3] https://github.com/mbonav/Exo_DMC

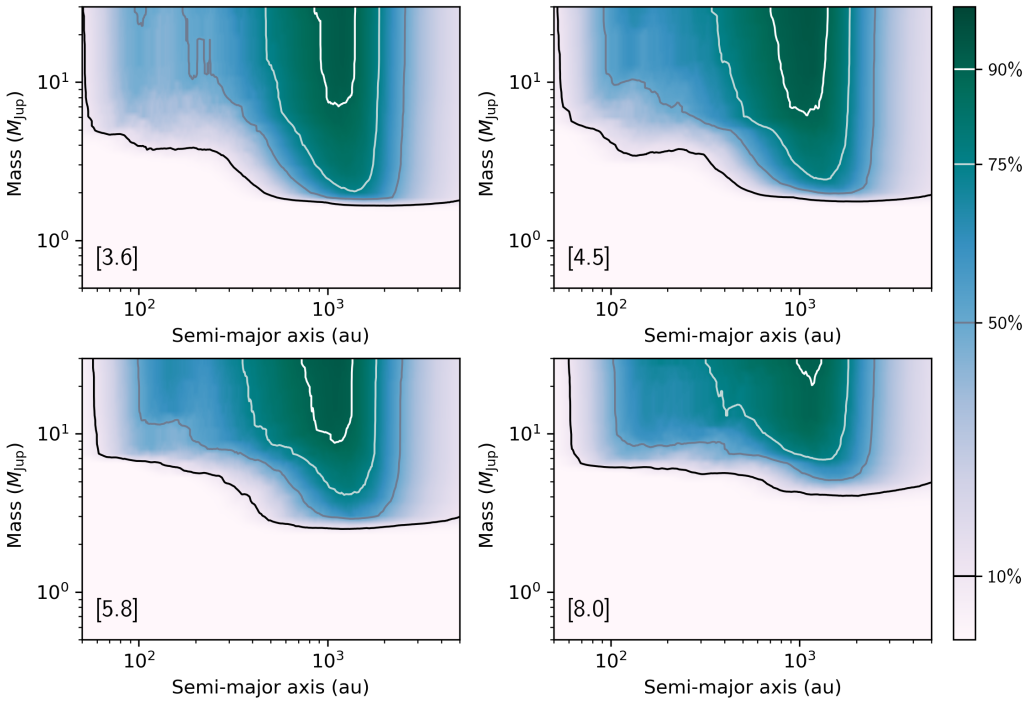

Figure 4.5: Completeness map of our survey for the individual IRAC channels.

with randomly drawn orbital parameters. If the simulated planet mass and separation was above the mass limit, it is considered a detection. Thus, the probability of detection at each point in the grid is the number of simulated planets detected divided by 10^4. These simulations were performed for each target of our sample in each channel.

The median probability of detection in each channel for the entire sample is shown in Figure 4.5. In Channel 1 (3.6 μm), we are generally less sensitive to close-in companions because saturation of the target star affected these images the most. In the other channels, we are sensitive to companions as low as 10 $M_{\rm Jup}$ down to $\sim$100 au away from the star. For both distributions at 3.6 and 4.5μm, we are sensitive to companions as low as 2 $M_{\rm Jup}$ at $\sim$1000 au, while for 5.8 and 8.0 μm at the same semi-major axis, we are sensitive to 3–5 $M_{\rm Jup}$ companion masses.

We combine the individual completeness maps for each star in our sample and

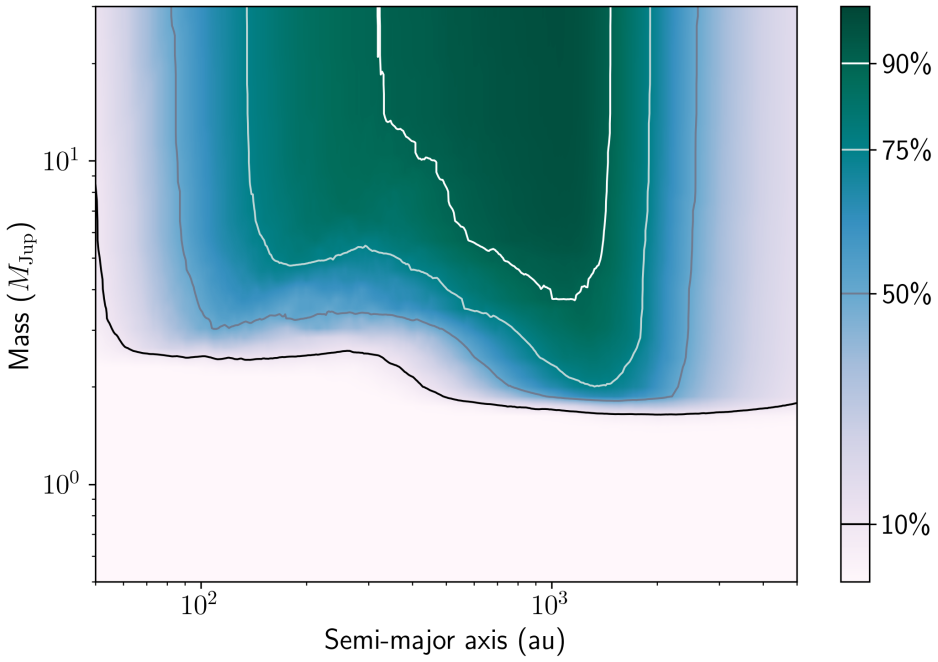

Figure 4.6: Overall completeness map for our Taurus survey showing the probability of detecting a planet of given mass and semi-major axis. The contours indicate 90% (white), 75% (off-white), 50% (gray), and 10% (gray) probability.

in each channel to create an overall completeness map for our Taurus survey. For each star at each grid point, the highest detection probability from the previously constructed IRAC channel completeness maps was taken. These limits were then averaged to generate the overall completeness map, shown in Figure 4.6. In Figure 4.7, we show the mean detection probability as a function of semi-major axis for 2, 3, 5, 10, and 13 $M_{\rm Jup}$ companion masses. The maximum detection probability for each mass is 75% at 1324 au, 88% at 1230 au, 93% at 1071 au, 96% at 1091 au, and 97% at 1081 au.

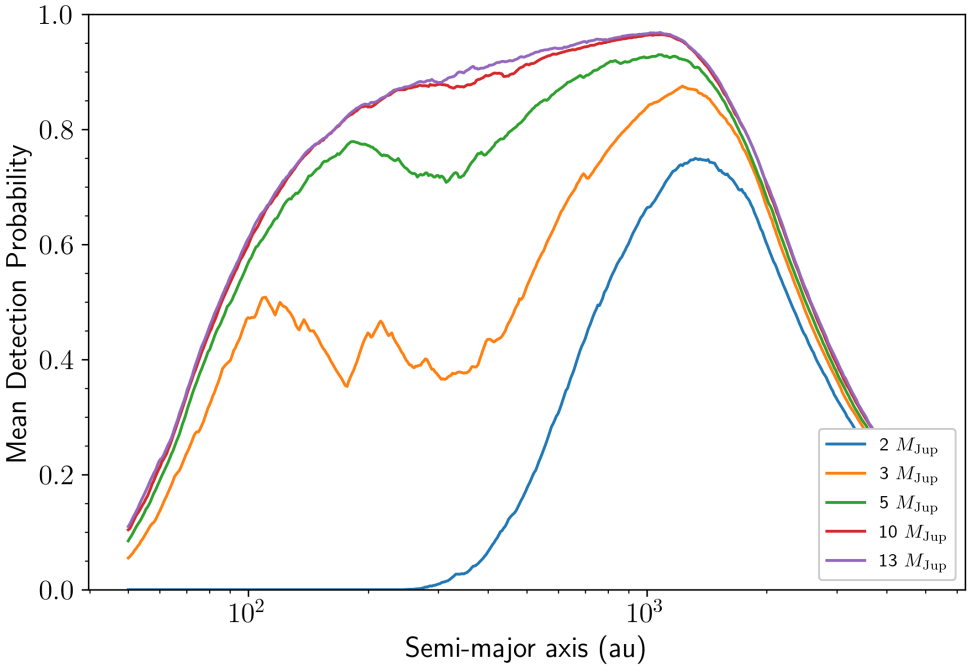

Figure 4.7: Mean detection probability for different companion masses as a function of semi-major axis.

4.6.3 Candidate Two-Channel Detections

As an example to the reader, we list the positive residuals within $5''$ of our sample targets in Table 4.2. In Figures 4.8 and 4.9, we show images generated by custom scripts[4] that download Pan-STARRS 1 (Chambers et al. 2016) y-filter cut outs of a sample target and plot them next to stacked IRAC images before and after PSF-subtraction. The orange dots indicate the locations of any flagged positive residuals. We down-select from initial indications of significant positive residuals by visually inspecting the combination PS1-IRAC cutouts to look for IRAC saturation artifacts or cosmic ray hits that generate false-positives. We cross-check star-like sources in the stacked residuals images with *Gaia* EDR3 (Gaia Collaboration et al. 2021) parallaxes to remove background sources.

Table 4.2: Significant Two-Channel and Channel 4 Residuals within $5''$

2MASS J	ρ ($''$)	P.A. (deg)	Channel	Contrast (mag)
04325323+1735337	3.52	236.3	1	5.53
	3.52	236.3	2	6.10
	3.60	208.3	4	5.20
04390396+2544264	4.81	114.0	4	4.97
04161210+2756385	0.88	56.3	4	4.98
04174965+2829362	4.58	25.2	1	3.97
	4.58	25.2	2	5.21
04193545+2827218	4.58	25.2	1	7.11
	4.58	25.2	2	7.10
04201611+2821325	2.42	315.0	1	4.00
	2.42	315.0	2	4.09
04215563+2755060	4.58	25.2	1	5.49
	4.58	25.2	2	5.24
04230776+2805573	4.18	353.3	4	4.79
04331003+2433433	4.49	135.0	4	6.26
04333456+2421058	4.58	25.2	3	3.28
	4.58	25.2	4	3.49
04352737+2414589	4.58	25.2	2	4.47

Table 4.2 continued on next page

[4] https://github.com/thespacedoctor/panstamps

Table 4.2 *(continued)*

2MASS J	ρ ($''$)	P.A. (deg)	Channel	Contrast (mag)
	4.58	25.2	4	5.45
	4.42	83.7	4	5.59
04214631+2659296	3.60	208.3	1	6.05
	3.60	208.3	2	4.82
04242321+2650084	3.52	33.7	1	5.60
	3.52	33.7	3	4.95
04354733+2250216	4.45	99.5	4	5.48
04554801+3028050	4.49	135.0	4	3.51
04554822+3020165	4.42	83.7	1	6.01
	4.42	83.7	4	5.32
	4.42	83.7	1	6.01
	4.42	83.7	4	5.32
04555288+3006523	4.32	222.7	1	6.52
	4.32	222.7	2	6.58
04002202+2232384	4.49	135.0	4	3.55
05160577+2236151	4.42	186.3	2	2.68
	4.42	186.3	3	2.76
	4.42	186.3	4	2.52
05230197+2428085	3.52	33.7	4	4.08
05320210+2423028	4.81	156.0	1	3.49
	4.81	156.0	2	3.63

4.6.4 PSF-Fitting of Candidate Two-Source Systems

We use the framework described in Paper I to model the point spread functions of 11 candidate two-source systems based on the output of the scripts described in Section 4.6.3. These were chosen for two-source fitting because their stacked residuals images indicated that the system was either a close binary not flagged by Krolikowski et al. (2021), had a star-like residual not seen in the Pan-STARRS z-band image, or had a star-like residual with no *Gaia* parallax. We report the best-fit results from our pipeline for 11 candidate two source systems in Table 4.3. We discuss two systems in more detail in the following sub-sections.

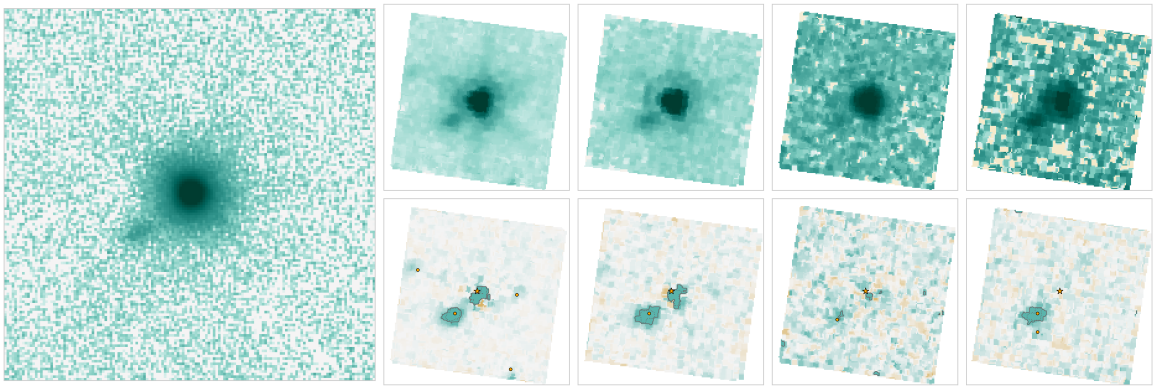

Figure 4.8: Postage stamp images of 2MASS J04270739+2215037. The larger left-hand panel contains PS1 y-band image of the star clearly showing a extended object located $6.5''$ away. The smaller upper panels show the stacked IRAC images of the star for each channel prior to PSF subtraction, while the smaller lower panels show the stacked residuals images after PSF subtraction. The extended residual is seen in each IRAC channel. We discuss this system further in Section 4.6.4.

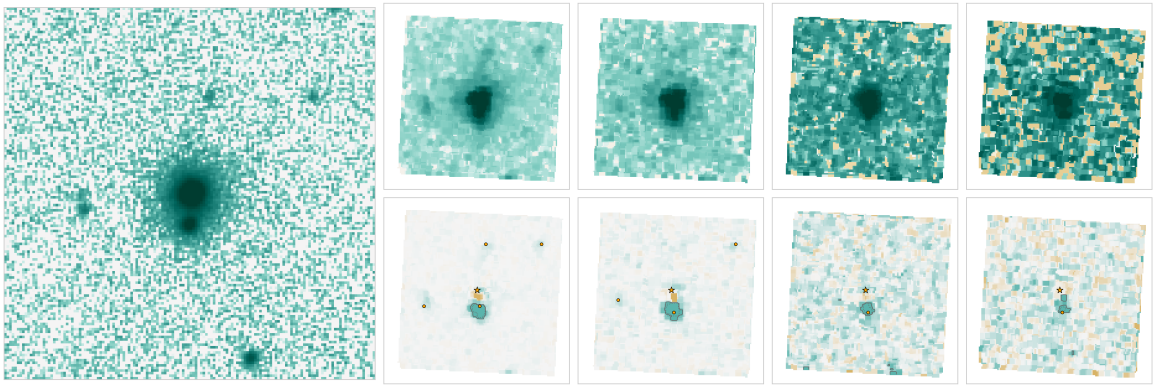

Figure 4.9: Postage stamp images of 2MASS J05160577+2236151 laid out in the same manner as Figure 4.8. In each IRAC channel a significant residual is seen $\sim 3''$ away from 2MASS J05160577+2236151. We further analyze and characterize this system in Section 4.6.4.

Table 4.3: Best-Fit System Properties of Detected Candidate Companions

2MASS J	Separation (arcsec)	Position Angle (deg)	$\Delta[3.6]$ (mag)	$\Delta[4.5]$ (mag)	$\Delta[5.8]$ (mag)	$\Delta[8.0]$ (mag)
04161210+2756385	0.97 ± 0.01	14.6 ± 0.1	-0.02 ± 0.01	0.13 ± 0.01	0.22 ± 0.16	-0.04 ± 0.02
04185115+2814332	3.12 ± 0.14	225.3 ± 4.3	4.45 ± 0.18	4.82 ± 0.21	3.89 ± 0.30	2.51 ± 0.26
04214631+2659296	1.87 ± 0.15	208.8 ± 1.6	3.32 ± 0.27	4.77 ± 0.25	8.12 ± 3.39	4.68 ± 1.88
04270739+2215037	6.54 ± 0.03	127.3 ± 0.5	4.67 ± 0.02	4.47 ± 0.03	4.69 ± 3.34	2.20 ± 0.07
04290068+2755033	6.78 ± 0.17	300.2 ± 3.0	4.11 ± 0.15	4.28 ± 0.27	3.40 ± 0.27	4.58 ± 1.97
04293606+2435556	4.14 ± 0.10	155.2 ± 1.7	6.24 ± 0.08	5.98 ± 0.03	3.19 ± 0.09	4.90 ± 0.15
04340619+2418508	6.95 ± 0.09	20.6 ± 1.4	3.45 ± 0.06	3.36 ± 0.03	2.91 ± 0.25	3.93 ± 3.73
04394488+2601527	1.17 ± 0.03	263.6 ± 4.8	2.94 ± 0.06	1.13 ± 0.08	1.13 ± 0.08	3.26 ± 0.04
04400800+2605253	4.55 ± 0.02	250.6 ± 0.2	4.97 ± 0.03	4.73 ± 0.04	5.40 ± 1.34	5.00 ± 0.02
05160212+2214528	6.19 ± 0.02	143.1 ± 1.0	5.34 ± 0.03	5.26 ± 0.06	4.27 ± 0.08	4.90 ± 0.45
05160577+2236151	2.98 ± 0.01	176.5 ± 0.7	2.22 ± 0.01	2.19 ± 0.03	2.25 ± 0.08	2.09 ± 0.14

2MASS J04270739+2215037: Chance Alignment with Elliptical Galaxy?

Slesnick et al. (2006) first identified 2MASS J04270739+2215037 (hereafter 2M0427+2215) as a potential member of an older distributed population of Taurus, proposed by Wichmann et al. (1996). Krolikowski et al. (2021) place this M6.75 star in their D4-North distributed group with $\tau \sim 2.5$ Myr and $d \sim 143$ pc. There is no evidence of binarity Kraus & Hillenbrand (2012) or infrared excess emission for 2M0427+2215 (Esplin et al. 2014).

After inital PSF-subtraction of the target star, a significant extended residual is seen in each IRAC channel (see Figure 4.8) at $\sim$6.5″. We perform a two-source PSF for this target, finding the extended residual to have $[3.6] = 15.55$ mag, $[4.5] = 15.26$ mag, $[5.8] = 15.37$ mag,and $[8.0] = 12.89$ mag. The Pan-STARRS survey, UKIDSS survey, as well as archival *HST* imaging (PI: K. Luhman) of 2M0427+2215 shows a low surface brightness object in its vicinity (hereafter 2M0427+2215 cc1). In the event that this object happens to be a low mass object within an edge-on disk, we analyze its SED by fitting its Pan-STARRS1 z-band, UKIDSS K-band, and *Spitzer*/IRAC 3.6 μm photometry points to solar metallicity BT-Settl model atmospheres (Allard et al. 2012) spanning effective temperatures between 1000 and 7000 K ($\Delta T_{\rm eff} = 100$ K) fixed at $\log$ g $= 4.0$. We also fit for $E(B-V)$ using the extinction curve of Fitzpatrick (1999) spanning from 0.00 to 1.00 mag in steps of 0.01 mag. We find the best-fit model for the extended object has $T_{\rm eff} = 2500 \pm 50$ K and $E(B-V) = 0.39 \pm 0.03$. We present the SED of both 2M0427+2215 and 2M0427+2215 cc1 in Figure 4.10.

2M0427+2215 cc1 is extremely bright in Channel 4 (8 μm) which could be emission from a circumstellar disk. The optical photometry does not agree with the 2500 K BT-Settl model which could also indicate significant UV continuum excess from an accretion disk. The shape of the candidate companion SED is similar to a late-type stellar or substellar object surrounded by a highly-inclined disk (see Figure 3 of Caceres et al. 2015), but modeling of this possibility is beyond the scope of this work.

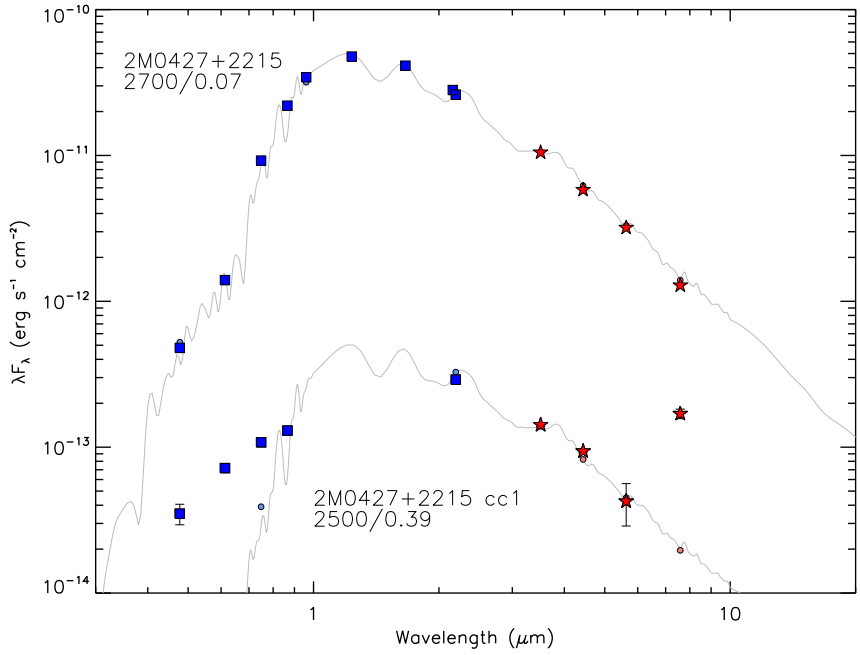

Figure 4.10: Spectral energy distributions of 2M0427+2215 and 2M0427+2215 cc1. The majority of the photometric uncertainties are smaller than the symbol sizes. An $E(B-V) = 0.07 \pm 0.01$ mag, $T_{\rm eff} = 2700 \pm 50$ K BT-Settl model best fits the photometry of the primary. An $E(B-V) = 0.39 \pm 0.03$ mag, $T_{\rm eff} = 2500 \pm 50$ K BT-Settl model best fits the PS1 z, UKIDSS K, and *Spitzer*/IRAC photometry of the extended object. Both models are plotted in gray. 2M0427+2215 cc1 appears to be either a low-mass companion within an edge-on disk or an elliptical galaxy in chance alignment with 2M0427+2215.

2MASS J05160577+2236151 B: A Brown Dwarf Companion at 780 au

Also originally part of the Slesnick et al. (2006) sample of older distributed population of Taurus members, *Gaia* EDR3 parallactic measurements place 2MASS J05160577+2236151 (hereafter 2M0516+2236) ∼260 pc away, further away than what is usually considered a member of the Taurus-Auriga star-forming region (Krolikowski et al. 2021). Slesnick et al. (2006) originally selected this object for spectroscopic observation because of its high position on an optical color-magnitude diagram, and red position on a near-infrared color-color diagram, indicating it may be a pre-main sequence star. They then obtained moderate-resolution spectroscopy of 2M0516+2236 to measure the gravity-sensitive Na I absorption doublet, classifying it as having a low surface gravity and thus a young age similar to Taurus. 2M0516+2236 does not fall near any known young stellar populations, though it is near the locus of the Cas-Tau association (Blaauw 1956).

After subtracting off one PSF at the position of 2M0516+2236 in its IRAC images, a significant residual is seen approximately $3''$ away from its centroid at a position angle around 180° in all four channels (see Figure 4.11). With a two-source fit, we found the companion to have $\rho = 2\farcs98 \pm 0\farcs01$, P.A.$= 176.5^\circ \pm 0.7^\circ$, $\Delta[3.6] = 2.22 \pm 0.01$ mag, $\Delta[4.5] = 2.19 \pm 0.03$ mag, $\Delta[5.8] = 2.25 \pm 0.08$ mag, and $\Delta[3.6] = 2.09 \pm 0.14$ mag.

Previously unknown, bright wide companions may be detected in *Gaia*, which confirm comovement with a primary much faster than waiting for observational follow-up with ground-based telescopes, as was the case for [SCH06] J0359+2009 B (Martinez & Kraus 2019). *Gaia* EDR3 (Gaia Collaboration et al. 2021) measure $(\mu_\alpha, \mu_\delta, \pi) = (5.02 \pm 0.09$ mas yr^{-1}, -16.69 ± 0.06 mas yr^{-1}, 3.76 ± 0.08 mas) for 2M0516+2236 and $(\mu_\alpha, \mu_\delta, \pi) = (4.88 \pm 0.43$ mas yr^{-1}, -16.76 ± 0.30 mas yr^{-1}, 3.89 ± 0.41 mas) for the candidate companion. These measurements are consistent with comovement and codistance for the two objects to within 1-σ. With these additional data we confirm association and report the discovery of a new low-mass companion (hereafter 2M0516+2236 B). The companion is at a projected separation of 780 au for its ∼260 pc distance.

To analyze the SEDs of the 2M0516+2236 system, we fit available Pan-STARRS optical (PS1; Chambers et al. 2016), 2MASS near-infrared (Cutri et al. 2003), UKIDSS near-infrared Lawrence et al. (2012), and the *Spitzer*/IRAC mid-infrared

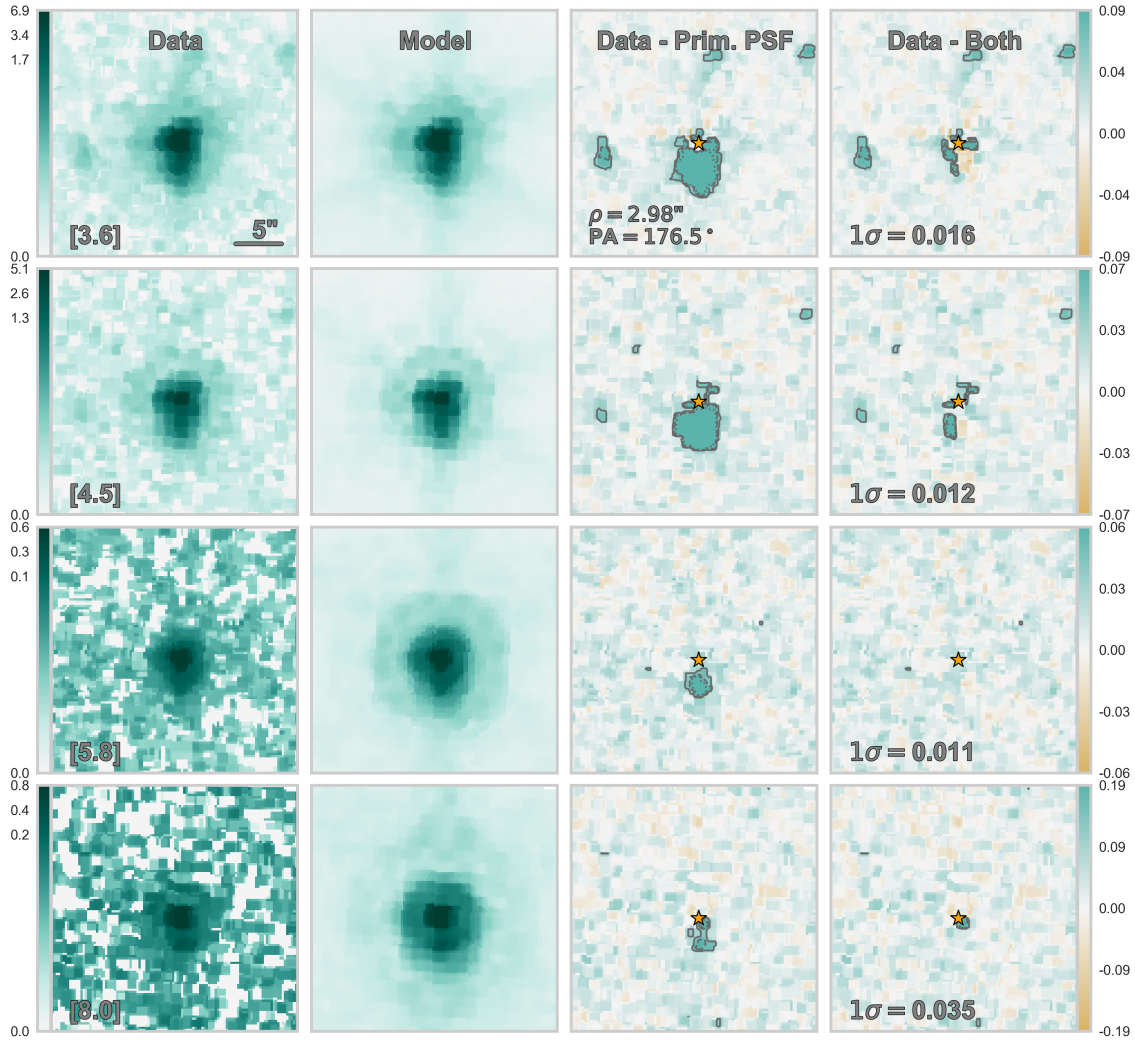

Figure 4.11: Stacked images of 2M0516+2236 across all four IRAC channels (rows) after it has gone through the PSF-fitting pipeline. All fits were conducted within the CBCD images at the native plate scale, but to convey the full data set, the images here were generated by combining individual frames after they had been re-scaled to $0\farcs24$/pixel ($\sim 5\times$ smaller than the original IRAC pixel scale), shifted to a common origin, and rotated so that north is up and east is left. Columns 1 and 2 show the original IRAC data of 2M0516+2236 and the median two-source PSF model, respectively, displayed with a logarithmic color scale (leftmost color bar). Column 3 shows the residuals left behind after only the primary PSF model is subtracted from the data. Column 4 shows the residuals left behind after the two-source PSF model is subtracted from the data. Both Columns 3 and 4 are displayed with a linear color scale (rightmost color bar) and 3-, 5-, and 7-σ contours overlaid with solid and dotted lines, respectively. The standard deviation of the pixel values is displayed in the lower left-hand corner of Column 4 in units of DN/s. After subtracting the primary star PSF, a statistically significant positive residual is seen $3''$ away from 2M0516+2236 at a position angle of $177°$. This residual disappears after subtracting the best-fit system PSFs, indicating that it is a robust detection across all IRAC filters.

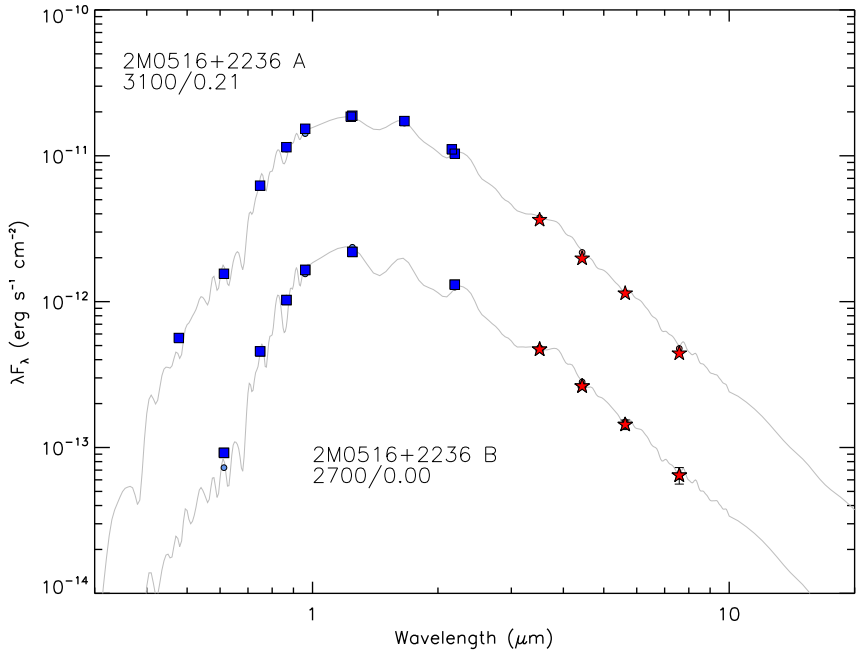

Figure 4.12: Spectral energy distributions of 2M0516+2236 and its companion 2M0516+2236 B. The majority of the photometric uncertainties are smaller than the symbol sizes. An $E(B-V) = 0.21 \pm 0.01$ mag, $T_{\rm eff} = 3100 \pm 50$ K BT-Settl model best fits the photometry of the primary. An $E(B-V) = 0.00 \pm 0.01$ mag, $T_{\rm eff} = 2700 \pm 50$ K BT-Settl model best fits the photometry of the companion. Both models are plotted in gray. There is no evidence of excess flux seen in $[5.8]$ and $[8.0]$, so neither component of this system appears to harbor a circum(sub)stellar disk.

photometry measured in this work. We fit solar metallicity BT-Settl model atmospheres (Allard et al. 2012) spanning effective temperatures between 1000 and 7000 K ($\Delta T_{\rm eff} = 100$ K) fixed at $\log$ g $= 4.0$, which is appropriate for late M dwarfs with ages τ>5 Myr from evolutionary models. We also fit for $E(B-V)$ using the extinction curve of Fitzpatrick (1999) spanning from 0.00 to 1.00 mag in steps of 0.01 mag. For the primary we fit PS1 $grizy$, 2MASS JHK, UKIDSS JK, and all the *Spitzer*/IRAC photometric data using χ^2 minimization. For the companion, we fit only the PS1 $rizy$, UKIDSS JK, and all the *Spitzer*/IRAC photometric data. We present the SEDs of the 2M0516+2236 system in Figure 4.12.

The best-fitting model for 2M0516+2236 A is $T_{\rm eff} = 3100 \pm 50$ K and $E(B-V) = 0.21 \pm 0.01$ mag while for 2M0516+2236 B the best-fitting model is $T_{\rm eff} = 2700 \pm 50$

K and $E(B-V) = 0.00 \pm 0.01$ mag. Although the best-fit SEDs of 2M0516+2236 A and B have discrepant $E(B-V)$ of ~ 0.2 mag, wide binary pairs in Taurus have been found to have differing reddening values of similar amounts (Herczeg & Hillenbrand 2014) due to the systematic uncertainty in atmospheric models of young low-mass objects (e.g., Dupuy et al. 2010), in addition to the young objects themselves likely harboring spots that change the emergent spectrum (e.g., Gully-Santiago et al. 2017). We infer system masses from predictions of BT-Settl evolutionary models (see Figure 4.13) based on their absolute $[3.6]$ magnitude and the best-fitting model $T_{\rm eff}$. We estimate 2M0516+2236 A to have a mass of 0.15 $M_{\odot}$ and the companion to have a mass of 30 $M_{\rm Jup}$. The H–R diagram position of the primary is between an isochronal age of 2 and 5 Myr, while that of the companion is between 5 and 10 Myr. We measure a mid-infrared color of $[3.6]-[8.0] = 0.31 \pm 0.14$ mag which is consistent with the color of a young M7–M8 photosphere as measured empirically by Luhman et al. (2010).

2M0516+2236 is the newest system of a growing sample of unusually wide, low-mass binaries, like FU Tau (Luhman et al. 2009), [SCH06] J0359+2009 B (Martinez & Kraus 2019), and UScoCTIO108 (Béjar et al. 2008). Young brown dwarf binaries usually have smaller orbits (a <10 au) and tend to have equal mass ratios (Kraus & Hillenbrand 2012). Additionally, Kraus & Hillenbrand (2009a) find that young brown dwarf binaries with M_{tot}<0.25 $M_{\odot}$ and projected separations between 500–5000 au are extremely rare (<0.4%), which could indicate that these systems do not fragment from a circumstellar disk, nor is their observed orbital separation a result of dynamical evolution within the post-natal environment.

4.7 Discussion

4.7.1 Planet Frequency

While vetting and confirming the candidate companion detections is ongoing, we can still use an assumed null result and our pipeline companion mass detection limits to place constraints on the frequency of planetary-mass companions on orbits between 50–5000 au, using the formalism described by Carson et al. (2006) and Lafrenière et al. (2007). We detail their methodology here. For a survey of N stars, enumerated j=1...N, we denote the fraction of stars with at least one com-

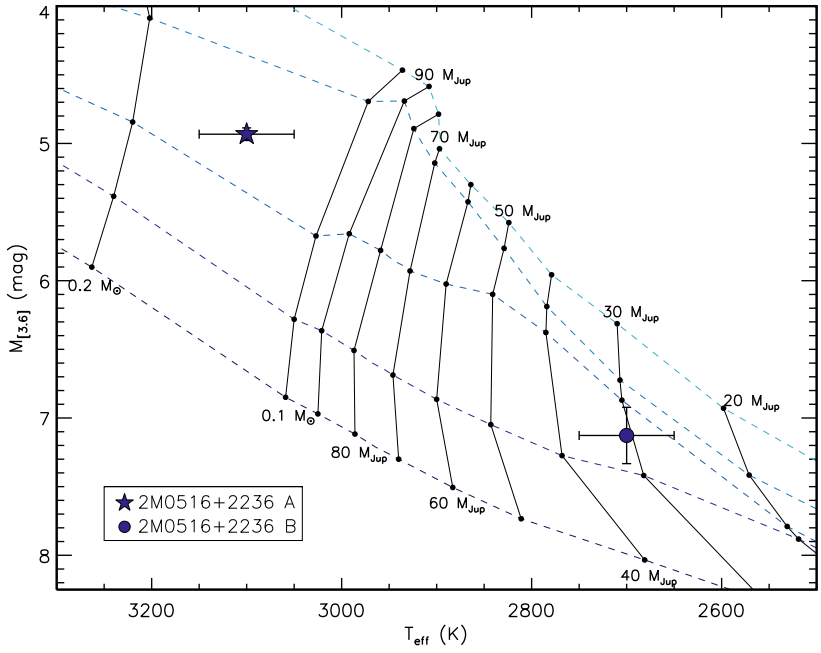

Figure 4.13: H–R diagram for 2M0516+2236 and its companion. For both components, the temperatures are estimated from our SED fits (see Figure 4.12). The 1, 2, 5, 10, and 20 Myr isochrones of Allard et al. (2012) are plotted (dashed lines) with mass tracks (solid lines) from 20 $M_{\rm Jup}$ to 0.2 $M_{\odot}$. The position of the primary indicates a mass of $\sim$0.21 $M_{\odot}$ while the position of the companion indicates a mass of 30 $M_{\rm Jup}$.

panion in the mass interval [m_{min},m_{max}] and semi-major axis [a_{min},a_{max}] as f, and the probability our survey would detect such a companion as p_j. Thus, the probability of detecting a companion orbiting star j is (fp_j), while the probability of not detecting a companion is $(1 - fp_j)$. The detections of a companion about a star of a survey are denoted d_j, where d_j=1 for a detection and d_j=0 for no detection. The binomial likelihood of the data given f is then

$$L\left(\{d_j\}|f\right) = \prod_{j=1}^{N} \left(1 - fp_j\right)^{1-d_j} \cdot \left(fp_j\right)^{d_j} . \tag{4.2}$$

Using Bayes' theorem, the posterior distribution of f given the data is

$$p\left(f|\{d_j\}\right) = \frac{L\left(\{d_j\}|f\right) \cdot p(f)}{\int_0^1 L\left(\{d_j\}|f\right) \cdot p(f)\mathrm{d}f}, \tag{4.3}$$

where $p(f)$ is the prior distribution of f. For this exercise, we use $p(f) = 1$ since we assume no *a priori* knowledge of the wide-orbit massive planet frequency. By integrating the posterior distribution from 0 to f, we can find the upper limit on the planet frequency for a probability matching a desired confidence interval.

For p_j, we use the average probability over the completeness map for a given target. As stated before, we ran two planet simulations: one with logarithmic distributions for both companion mass and semi-major axis ($\alpha = \beta = -1$); and one with the Brandt et al. (2014) power law distributions ($\alpha = -0.65$; $\beta = -0.85$). In total, we simulate $10^4 \times 60 \times 500 \times 209 = 6.27 \times 10^{11}$ planets for each distribution. For the logarithmic default setting of ExoDMC, the grid points were distributed equally on a logarithmic scale between the minimum and maximum mass and between the minimum and maximum semi-major axis. Thus averaging over this completeness map is equivalent to assuming the masses and semi-major axes were distributed uniformly in log. For the power law distribution, we insert code into ExoDMC that transforms an equally spaced linear grid onto a grid with spacings that follow a user-provided power law. Averaging over this completeness map is then equivalent to assuming the user-specified power law distributions. These two choices should yield the same recovery fraction at any given value of companion mass and semi-major axis. However, by varying the density at which we place the grid points, the integrated recovery fractions will not be the same and will reflect

the values appropriate for the choice of distribution model.

For a semi-major axis range of 50–5000 au and companion mass between 0.5 and 30 $M_{\rm Jup}$, we calculate an upper limit on the frequency of substellar companions to be 3.7% at 95% confidence. If we assert the stricter mass definition for a planetary-mass companion ($<$13 $M_{\rm Jup}$), the frequency upper limit is 4.6%. For the Brandt et al. (2014) power law distributions, the companion frequency upper limits are 3.0% for substellar objects $<$30 $M_{\rm Jup}$ and 3.6% for planetary-mass objects $<$13 $M_{\rm Jup}$.

4.7.2 Comparisons to Other Direct-Imaging Survey Occurrence Rates

Ireland et al. (2011) placed some of the first constraints on wide-orbit PMCs in young star-forming regions, finding $\sim$4% of solar-type stars have companions between 6–20 $M_{\rm Jup}$ with semi-major axes between 200–500 au. This occurrence rate was based on 2 companion detections from a sample of 49 stars in Upper Scorpius. Lafrenière et al. (2014) later find three substellar companions among a survey of 91 stars, determining a occurrence rate of substellar companions (5–40 $M_{\rm Jup}$) with orbital separations of 250–1000 au of 4.0% in Upper Sco. Conversely, Janson et al. (2013) find no companions in their survey of 138 stars in Sco–Cen and conclude occurrence rates of $\sim$4% are too high. This shows how differences in sample size, instrument sensitivity, and instrument field of view can significantly alter the interpretation of the small number of detections from direct-imaging multiplicity surveys.

In Table 4.4, we show the measured occurrence rates from a few other direct-imaging surveys of young star-forming regions, as well as searches for wide companions in *Spitzer* data sets, in addition to the companion frequency upper limit we derive in this work. Although we have not yet confirmed our candidate Taurus companions, our results are consistent with the survey results of Ireland et al. (2011) and Lafrenière et al. (2014). Our results are also consistent with the Daemgen et al. (2015) multiplicity survey of Taurus, where they find a substellar companion frequecny of 3.5% based on the detection of two high-likelihood companions. When they include additional candidate companions into their frequency estimate

they find a higher upper limit of $< 8.8\%$.

Table 4.4: Previous Results of Substellar Multiplicity Surveys

Survey	Primary Mass ($M_\odot$ or Sp Ty.)	Separation (au)	Companion Mass ($M_{\rm Jup}$)	Occurrence Rate
Ireland et al. (2011)	[0.5, 1.75]	[200, 500]	[6, 20]	$4.1^{+4.9}_{-1.3}\%$
Lafrenière et al. (2014)	[0.2, 10.0]	[250, 1000]	[5, 40]	$4.0^{+3.0}_{-1.2}\%$
Daemgen et al. (2015)	[0.2, 3.0]	[20, 1500]	<70	$3.5^{+4.3}_{-1.1}\%$[a]
Durkan et al. (2016)	[M4, B1.5]	[100, 1000]	[0.5, 13]	$< 9\%$
Baron et al. (2018)	[M9, B0]	[1000, 5000]	[1, 13]	$< 3\%$
Wallace et al. (2020)	[0.24, 2.65]	[10, 500]	[2, 13]	$< 20\%$
This work	[M9.5, B9]	[50, 5000]	[0.5, 30]	$< 3.7\%$

[a]Daemgen et al. (2015) also calculate an occurrence rate of $< 8.8^{+5.2}_{-2.5}\%$ based on the inclusion of three additional candidate companions.

Durkan et al. (2016) find no new planets in their re-analysis of archival *Spitzer*/IRAC images, constraining the population of 0.5–13 $M_{\rm Jup}$ planets at separations of 100–1000 au with an upper frequency limit of 9% at a 95% confidence level, over twice the upper limit we find for a smaller companion mass interval. In their Monte Carlo simulations to determine the planet frequency they assume a companion mass distribution $\alpha = -1.31$ and a linear semi-major axis distribution, which could account for the difference in our calculated frequency. The Wide-orbit Exoplanet search with InfraRed Direct imaging survey (WEIRD; Baron et al. 2018) also searched for wide companions in *Spitzer*/IRAC images but found an upper frequency limit of 3%, similar to our results for planetary-mass companions (3.0%). They assume logarithmic distributions in companion mass and semi-major axis as we do in our simulations. Given our sample size, survey sensitivity, and lack of confirmed detections, a lower occurrence rate is favored, otherwise the WEIRD survey and our survey would have detected more companions. While the Durkan et al. (2016) frequency upper limit is still allowed by our results, it is likely that our constraint more accurately reflects the underlying mass and separation distributions.

4.8 Summary

We have used our PSF-fitting framework to re-analyze *Spitzer*/IRAC images of Taurus star-forming region members to search for wide-orbit planetary-mass companions around a large sample of stars with well-constrained, young ages. In our sample of 209 stars, we find 11 systems of interest that appear to harbor candidate companions or have extended residual flux remaining after primary PSF subtraction.

We also report the discovery of a ρ=2$\farcs$98 (780 au) companion to 2MASS J05160577+2236151. Based on its brightness ($M_{[3.6]}$=7.13 mag), we infer the companion mass to be M=30 $M_{\rm Jup}$ given the primary's model-derived age of 5 Myr. We also describe a candidate companion to 2MASS J04270739+2215037, which appears to either be a low-mass companion embedded in a circumstellar disk or chance alignment with an elliptical galaxy.

By converting the flux limits of our survey to companion mass limits, we find our survey is up to 93% complete to 5 $M_{\rm Jup}$ companions at $\sim$1000 au. We also constrain the frequency of 0.5–30 $M_{\rm Jup}$ companions on semi-major axes 50–5000 au to $<$3.7% at a 95% confidence level. Adjustments to these calculations will come as further vetting of candidate companions is performed, and post-PSF-subtraction image analysis is refined, which will be explored in future work.

Chapter 5: Future Work and Summary

5.1 Future Work

5.1.1 Outlook for Continued PMC Searches in Large-Sky Surveys

There is still a tremendous opportunity to continue searching for wide companions in *Spitzer*/IRAC data. *Spitzer* observed every major star-forming region within 300 pc, which consists of thousands of stars (e.g., Evans et al. 2009). Probing semi-major axes out to thousands of au is *critical*: binary formation processes are more likely than those of planet formation to work at such distances from the host star. These orbits are outside the field of view of AO instruments ($\sim$3″), making my framework ***uniquely*** able to detect differences in the semi-major axis distributions of wide planetary companion systems.

Other deep, large-scale sky surveys have extensive imaging data of nearby star-forming regions and associations that have great potential to be mined for undiscovered wide companions to stars. My PSF-subtraction infrastructure can be adapted to such surveys as the Pan-STARRS1 3π Survey (PS1; Kaiser et al. 2002) that imaged the sky above $\delta = -30^{\circ}$ in $grizy$; the VISTA Hemisphere Survey (VHS; McMahon et al. 2013) that imaged the southern hemisphere in JK_s; and the UKIRT Infrared Deep Sky Survey (UKIDSS; Lawrence et al. 2007) Galactic Clusters Survey (GCS) that imaged $\sim$1000 deg^2 of sky containing six open clusters and four star-forming regions in $ZYJHK$. The image analysis techniques developed in my thesis can also be extended and applied to an even larger stellar sample when the Vera C. Rubin Observatory project begins acquiring data for the Legacy Survey of Space and Time (LSST; Ivezić et al. 2008) in October 2022. When in full operation, LSST will deliver 20 TB of imaging data every night, eventually observing billions of astrophysical objects across the entire sky during its 10-year survey length.

My pipeline infrastructure has also contributed to the characterization of exoplanets discovered by TESS. Newton et al. (2019) reported the discovery of a transiting planet with radius between that of Neptune and Saturn in the 45 Myr Tucana–Horologium young moving group. The host star, DS Tuc, is a visual binary and my two-source PSF model framework was used to estimate the flux con-

tamination from DS Tuc B and more precisely measure the exoplanet parameters from the DS Tuc A light curve. Observations of young exoplanets orbiting members of young moving groups like DS Tuc Ab provide an excellent opportunity to probe planetary evolution since they are likely still undergoing dynamical and atmospheric changes that occur within the first ∼100 Myr of formation. Numerous binaries like DS Tuc have been observed with *Spitzer* and my pipeline can be applied to such systems to accurately disentangle their flux contributions.

5.1.2 Spectroscopic Follow-Up of Wide-orbit PMCs

Since young PMCs harbor disks, *Spitzer* is well-suited to detect these systems' infrared excesses, enabling the investigation of disk evolution and dispersal in low-mass companions to stars. When candidate circumsubstellar disks are found, moderate-resolution spectroscopy opens the possibility of identifying emission lines associated with accretion from a circumplanetary disks which would provide important clues about the formation routes, mass accretion rates, circumplanetary disk structure, and even possible moon-forming capabilities of other wide-orbit PMC systems. Obtaining spectroscopic observations in the near-infrared also helps determine and/or refine the spectral types and gravity classifications of the components of wide PMC systems, as well as more accurately measure bolometric luminosities which typically rely on broadband photometry. As I have been developing this automated pipeline over the course of my Ph.D., I have also been pursuing spectroscopic observations of wide-orbit planetary systems.

The Hobby-Eberly Telescope 2^{nd} generation Low Resolution Spectrograph (HET/LRS2) is a $6'' \times 12''$ fiber-fed integral field unit (IFU) that allows for wide PMC systems to be observed entirely within its field of view. I have obtained over 30 hours of HET/LRS2 time to observe a small sample of wide-orbit systems and characterize them in the optical. The objects are DH Tau, FU Tau, FW Tau, HD 284149, and [SCH06] J0359+2009 B. In Figure 5.1 I show an IFU image slice of FW Tau at Hα. The companion, FW Tau C, is clearly seen.

Another avenue of investigation I intend to pursue in the near future is further characterization of the new companion I discovered and described in Chapter 2, [SCH06] J0359+2009 B. I was awarded Gemini-N/GNIRS time to observe both components of the system for the first time in the near-infrared to confirm the com-

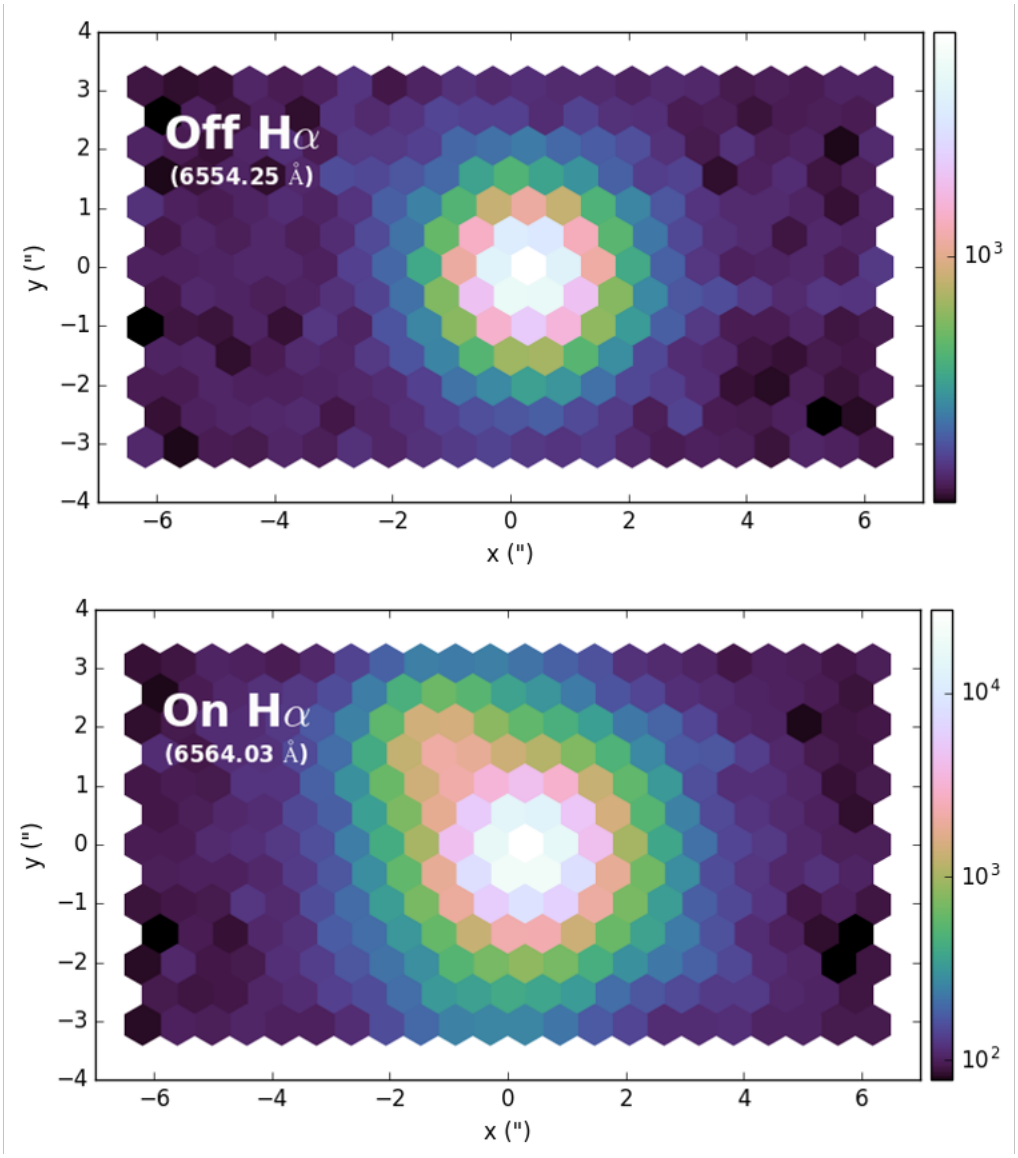

Figure 5.1: HET/LRS2 IFU data slices of the FW Tau system. Top: Only FW Tau AB is seen in continuum data slices adjacent to Hα. Bottom: FW Tau C is clearly detected in emission at Hα to the upper left. Accurate determination of effective temperatures and identification of accretion signatures are necessary to precisely investigate mass accretion rates, circumplanetary disk structure, formation routes, and even possible moon-forming capabilities of the wide companions.

panion's low temperature, low gravity, and planetary mass. Other science goals for studying the system are: (1) to determine the companion's spectral type and gravity classification; (2) confirm its youth and planetary mass; and (3) identify accretion signatures (e.g., Paβ at 1.28 μm; Brγ at 2.16 μm; H_2 1–0 S(0) at 2.12 μm) in the circumsubstellar environment.

I show a preliminary reduction of the HET/LRS2 and GNIRS data of [SCH] J0359+2009 B in Figure 5.2. The companion appears to have a near-infrared spectral type of M9 ± 1 and intermediate gravity based on the Allers et al. (2010) classification scheme. The HET/LRS2 optical IFU data reduction is still being refined, but there are signs of significant Hα variability between two nights of observations (see Figure 5.3).

Spectroscopic data like these are especially important to obtain at young ages when an edge-on disk around a brown dwarf can mimic the expected photospheric properties of a planet, as has been suggested for FW Tau C (e.g., Caceres et al. 2015; Kraus et al. 2015). Furthermore, the launch of the *James Webb Space Telescope* (*JWST*) in 2021 will greatly advance our understanding of wide-orbit PMCs in the mid-infrared since many were discovered *after* the end of *Spitzer*'s cryogenic mission in 2009. For two such targets, [SCH06] J0359+2009 B and ROXs 42B b, my PSF-fitting framework measured *Spitzer*/IRAC 8 μm excesses over their expected intrinsic photospheres, motivating a *JWST* Cycle 1 proposal I led as principal investigator to confirm and characterize their circumsubstellar disks with the Mid-Infrared Instrument (MIRI) Medium Resolution Spectrometer integral field unit. Although my proposal was not selected, my search is continuing to build larger samples of wide PMC systems to be observed that will be extremely relevant to the *JWST* mission. *JWST*/MIRI MRS will have 10–100$\times$ the sensitivity of *Spitzer*/IRS and not only constrain disk sizes and morphologies of wide-orbit PMCs, but also determine disk composition and grain sizes by identifying spectral features.

5.2 Summary and Lessons Learned about PMC Formation and Evolution

In my thesis, I explored the origins and characteristics of wide-orbit planetary-mass and substellar companions by discovering new systems and characterizing

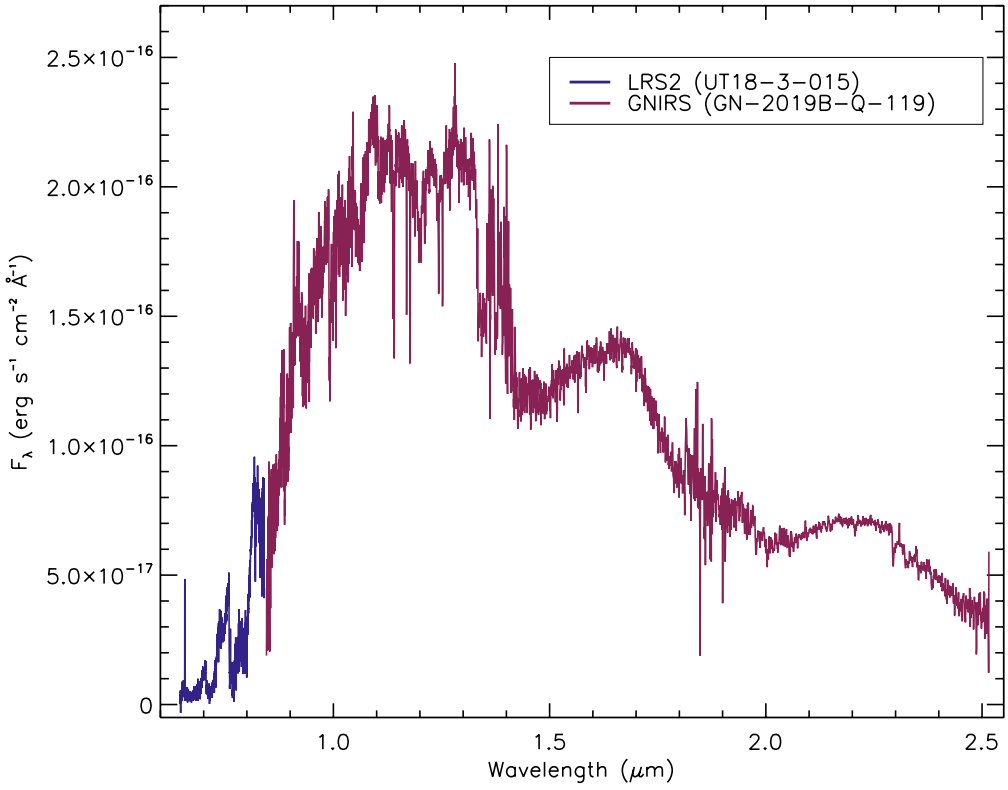

Figure 5.2: Preliminary extracted flux calibrated HET/LRS2 and Gemini-N/GNIRS spectra of [SCH06] J0359+2009 B. This wide substellar companion is demonstrating extreme Hα accretion variability. Spectroscopic data like these are important to obtain when an edge-on disk around a brown dwarf can mimic the expected photospheric properties of a planet. Moderate-resolution spectroscopy of PMCs opens the possibility of identifying emission lines associated with accretion from circumplanetary disks which would provide important clues about the formation routes, mass accretion rates, circumplanetary disk structure, and even possible moon-forming capabilities of these wide-orbit companions.

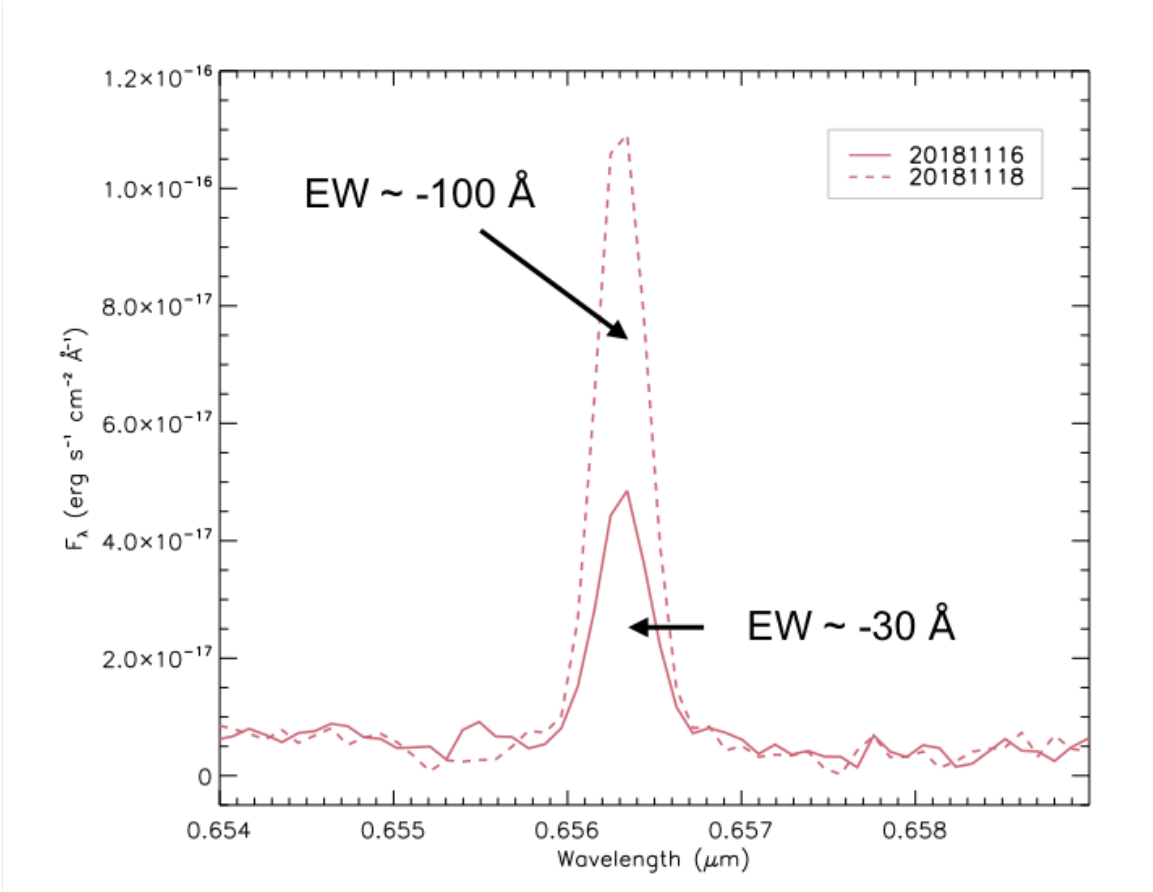

Figure 5.3: Preliminary extracted flux calibrated HET/LRS2 optical spectra of [SCH06] J0359+2009 B at Hα. There is a $\sim$70 Å difference in equivalent width in the Hα emission line between the two nights of observations potentially indicating active accretion.

the properties of known ones. I actively worked to build the sample of wide-orbit PMCs through the development of an automated pipeline to search for PMCs in archival *Spitzer*/IRAC images. My point spread function subtraction framework accurately model and subtracts the flux of bright primary stars, taking advantage of *Spitzer*'s extraordinary sensitivity in the mid-infrared to study wide low-mass companions near the diffraction-limit.

In Chapter 2, I demonstrated that my framework to model the IRAC PSF was successful at recovering known or candidate companions at a wide range of projected separations from their hosts. I built an 11-member sample of systems to process through my pipeline, all with low-mass companions previously discovered or confirmed in the star-forming regions of Chameleon I, Taurus-Auriga, and Upper Scorpius. My reprocessing of the IRAC images yielded detection of all 11 system primaries, six confirmed low-mass companions, and two candidate companions. In addition, five of the companions had [3.6]–[8.0] colors more than 3-σ above their expected intrinsic photosphere color and thus are candidate disk hosts. I showed that my framework was sensitive to companion masses as low as 1 $M_{\rm Jup}$ at 5 Myr. The initial demonstration of my pipeline resulted in the confirmation of a new wide-orbit companion, [SCH06] J0359+2009 B, with a mass near the planet–brown-dwarf boundary. I measured a mid-infrared excess for the companion, concluding that it has a circumsubstellar disk. Based on the primary age and *Gaia* parallactic distance, and the companion's best-fit SED ($T_{\rm eff} = 2400$ K), I estimated the companion's projected separation to be $\rho = 540$ au and inferred its mass to be $20 \pm 5\ M_{\rm Jup}$, making it an older analog of ultrawide brown dwarf pairs like FU Tau, SR 12 c, USco 1621 B, and USco 1556 B. The extremely low total mass and wide separation of binaries such as [SCH06] J0359+2009 are difficult to explain with current brown dwarf formation models, making each discovery an important test of any new theory for brown dwarf origins.

In Chapter 3, I processed the remaining wide PMC systems with IRAC images through my PSF-fitting framework to resolve their companions in the mid-infrared. The new sample of 9 wide-orbit PMC systems with companions were on average fainter and closer-in than the sample examined in the previous chapter. I detected 8 out of 9 companions in at least one IRAC channel, 5 of which were resolved for the first time in the mid-infrared. Five of the companions had [3.6]–

[8.0] colors more than 3-σ above their expected intrinsic photosphere color, four of which were previously known as candidate disk hosts and one that had not been identified. By using *Gaia* parallactic distances for the primary stars in this sample, their reported ages, and BT-Settl evolutionary models, I found that my framework was sensitivity to companions of masses down to 10 $M_{\rm Jup}$ within the IRAC PSF core ($< 5''$), and down to 1 $M_{\rm Jup}$ in the IRAC PSF wings ($> 5''$). I resolved AB Pic b in its IRAC images, using the newly measured photometry and its updated system age of 13 Myr (Booth et al. 2021) to estimate its mass at $M = 11 \pm 1\ M_{\rm Jup}$, placing the companion firmly below the deuterium-burning limit. I also measured an 8.0 μm excess for ROXs 42B b, a companion not thought to harbor a disk due to a lack of observed emission line accretion signatures. Finally, I found for our sample from Martinez & Kraus (2019) (see Chapter 2) and this sample that $67\% \pm 16\%$ of young (<15 Myr) wide-orbit PMCs harbor disks. Combined with past detections of disk indicators to wide-orbit PMCs, I found a global young disk fraction of $56\% \pm 12\%$, signifying that both accreting and non-accreting PMC disks are very common. My MCMC-based PSF fitter is finally opening up a regime of parameter space that has yet to be studied in detail and will reveal low-mass companions, whether they have disks, and the properties of those disks.

In Chapter 4, I scaled up the search for wide PMCs from samples of ∼10 to samples of a few hundred. I reported the results from a general search for Jupiter-like companions on wide orbits (>50 au) around members of the Taurus star-forming region (τ∼2 Myr, d∼145 pc; Torres et al. 2008). I searched for these wide companions using my *Spitzer*/IRAC PSF-subtraction infrastructure, adding an automated method to also signal the presence of significant positive residuals post-primary PSF subtraction in a target's images. In the sample of 209 stars, I found 11 systems of interest that appear to harbor candidate companions or have extended residual flux remaining after primary PSF subtraction. I reported the discovery of a $\rho = 2\farcs98$ (780 au) companion to 2MASS J05160577+2236151. I inferred the companion mass to be $M = 30\ M_{\rm Jup}$ based on its brightness and the primary's model-derived age of 5 Myr. My survey was up to 93% complete to 5 $M_{\rm Jup}$ companions at ∼1000 au, and from my survey completeness I constrained the frequency of 0.5–30 $M_{\rm Jup}$ companions on semi-major axes of 50–5000 au to <3.7% at a 95% confidence level. The well-constrained age of the Taurus complex, along with the moderate con-

trasts and wide separations of the companions will make them prime targets for detailed follow-up characterization via spectroscopy, which would provide valuable insights for exoplanet atmosphere models at young ages.

At the outset of my Ph.D., my goal was to better understand the origins of wide-orbit planetary-mass and substellar companions through a comprehensive thesis project that I built from the ground up. I developed the infrastructure to search for new PMC systems; I leveraged existing mid-infrared data sets to determine the disk properties of the small number of wide PMC systems currently known; I expanded my framework to accommodate larger samples to study wide companion systems on a statistical basis. My thesis has opened up a new regime of parameter space for the study of wide-orbit PMCs that is only just beginning to be studied in detail, discovering planetary-mass companions in their birth environments and revealing their circum(sub)stellar disks. I have shown that my analysis techniques are scaleable and adaptable, and there is a straightforward path to processing sample sizes of thousands. Previous analyses of archival *Spitzer*/IRAC images have searched for wide companions in young moving groups that are closer ($<$100 pc) and older ($>$10 Myr) than the regions I studied (e.g., Durkan et al. 2016; Baron et al. 2018). Although they were able to take advantage of the well-behaved IRAC PSF wings at $>>\lambda/D$ when searching for wide companions, they do so when the contrast between primary star and companion is more severe. My work is a complement to AO-imaging surveys that probe mostly solar system scales.

The global disk frequency is $56\% \pm 12\%$ for young ($<$15 Myr) wide companions with masses near the deuterium-burning limit. Hence, wide PMCs frequently harbor disks that govern fundamental aspects of planet formation, such as accretion onto the young planet or the conditions for satellite formation. This offers an opportunity to investigate disk evolution and dispersal in low-mass companions to stars. My thesis has not only discovered new wide PMC systems with disk-bearing companions, but also identified evidence of circum(sub)stellar disks around known companions. Since the disk fraction is high, the opportunity arises to find more circum(sub)stellar disks and determining whether their properties (e.g., mass, size, lifetime) are more consistent with formation via fragmentation of a molecular or via the accretion of circumstellar disk material from its host.

Simulations of gravitational instability (GI) predict circumplanetary disks to be

truncated to 1/3 of the companion Hill radius (Ayliffe & Bate 2009; Shabram & Boley 2013) and luminous at radio wavelengths (Shabram & Boley 2013; Zhu et al. 2016), potentially observable with ALMA. Searches for this disk emission have yielded mostly upper limits (Wu et al. 2017), which suggests wide-orbit PMCs have smaller, hotter disks. This implies that dynamical interactions are important in the formation of PMCs to truncate their disks if they formed via GI. On the other hand, the dust in planet-forming disks of binary stars have been shown to also be smaller just because of grain growth and radial drift (Zagaria et al. 2021). The increasing likelihood that the disks surrounding wide-orbit PMCs are compact and optically thick, and thus easier to study in the mid-infrared, highlights the importance of leveraging *Spitzer* to motivate future observations of PMC systems in the *JWST* era.

The frequency of 0.5–30 $M_{\rm Jup}$ companions on semi-major axes of 50–5000 au is $<$3.7% at a 95% confidence level. While I am continuing to vet 11 possible candidate companions in the IRAC images of Taurus members, it is plausible that some candidates will eventually be confirmed. So far I have not found any candidate PMCs with $\rho >$1000 au, potentially signally that binary star formation mechanism is not the dominant pathway. This upper limit is consistent with the findings of previous multiplicity surveys of young star-forming regions for substellar companions (e.g., Ireland et al. 2011; Lafrenière et al. 2014), though the frequency rates for planets ($<$13 $M_{\rm Jup}$) on wider orbits ($>$50 au) from direct-imaging surveys are much less constrained ($<$3–20%; Durkan et al. 2016; Baron et al. 2018; Wallace et al. 2020).

Yet for now, adding a few more wide PMC systems does not adequately increase the low-mass companion sample enough to determine the functional forms of their companion mass or semi-major axis distributions. Analyzing the thousands of young stars within the entire *Spitzer*/IRAC archive would potentially reveal hundreds of new wide companions, allowing for the empirical tests necessary to unite theory and observations.

Despite the short-comings in hypothesized avenues of PMC formation, the final determination of which physical process describes their primary formation pathway will require a statistically robust sample of wide-orbit PMC systems from which demographics can be obtained. My thesis has developed the framework

to efficiently build this sample, and in the absence of new discoveries, place constraints on the frequency of planets on wide orbits. I will continue to build upon this work to reveal the demographics of wide-orbit PMCs from which better constraints on the models of extreme binary star and planet formation will emerge, ultimately enhancing our understanding of where these systems come from, how they evolve, and where they fit into the paradigm of star and planet formation.

Bibliography

Adame, L., Calvet, N., Luhman, K. L., et al. 2011, ApJ, 726, L3

Adams, F. C., Proszkow, E. M., Fatuzzo, M., & Myers, P. C. 2006, ApJ, 641, 504

Adams, F. C., Ruden, S. P., & Shu, F. H. 1989, ApJ, 347, 959

Alibert, Y., Mordasini, C., Benz, W., & Winisdoerffer, C. 2005a, A&A, 434, 343

Alibert, Y., Mousis, O., Mordasini, C., & Benz, W. 2005b, ApJ, 626, L57

Allard, F., Hauschildt, P. H., Alexander, D. R., Tamanai, A., & Schweitzer, A. 2001, ApJ, 556, 357

Allard, F., Homeier, D., & Freytag, B. 2012, Philosophical Transactions of the Royal Society of London Series A, 370, 2765

Aller, K. M., Kraus, A. L., Liu, M. C., et al. 2013, ApJ, 773, 63

Allers, K. N., Liu, M. C., Dupuy, T. J., & Cushing, M. C. 2010, ApJ, 715, 561

Alves de Oliveira, C., Moraux, E., Bouvier, J., et al. 2010, A&A, 515, A75

Andre, P., Ward-Thompson, D., & Barsony, M. 1993, ApJ, 406, 122

Andrews, S. M., Rosenfeld, K. A., Kraus, A. L., & Wilner, D. J. 2013, ApJ, 771, 129

Ayliffe, B. A., & Bate, M. R. 2009, MNRAS, 397, 657

Bailer-Jones, C. A. L., Rybizki, J., Fouesneau, M., Demleitner, M., & Andrae, R. 2021, AJ, 161, 147

Bailer-Jones, C. A. L., Rybizki, J., Fouesneau, M., Mantelet, G., & Andrae, R. 2018, AJ, 156, 58

Bailey, V., Meshkat, T., Reiter, M., et al. 2014, ApJ, 780, L4

Barenfeld, S. A., Carpenter, J. M., Ricci, L., & Isella, A. 2016, ApJ, 827, 142

Barman, T. S., Macintosh, B., Konopacky, Q. M., & Marois, C. 2011, ApJ, 733, 65

Baron, F., Artigau, É., Rameau, J., et al. 2018, AJ, 156, 137

Barsony, M. 1994, in Astronomical Society of the Pacific Conference Series, Vol. 65, Clouds, Cores, and Low Mass Stars, ed. D. P. Clemens & R. Barvainis, 197

Bate, M. R. 2005, MNRAS, 363, 363

Batten, A. H. 1973, Binary and multiple systems of stars

Béjar, V. J. S., Zapatero Osorio, M. R., Pérez-Garrido, A., et al. 2008, ApJ, 673, L185

Bell, C. P. M., Mamajek, E. E., & Naylor, T. 2015, MNRAS, 454, 593

Blaauw, A. 1956, ApJ, 123, 408

Bodenheimer, P., & Burkert, A. 2001, in IAU Symposium, Vol. 200, The Formation of Binary Stars, ed. H. Zinnecker & R. Mathieu, 13

Boley, A. C. 2009, ApJ, 695, L53

Bonavita, M., Chauvin, G., Desidera, S., et al. 2012, A&A, 537, A67

Bonnefoy, M., Chauvin, G., Lagrange, A. M., et al. 2014, A&A, 562, A127

Bonnefoy, M., Chauvin, G., Rojo, P., et al. 2010, A&A, 512, A52

Bonnefoy, M., Boccaletti, A., Lagrange, A. M., et al. 2013, A&A, 555, A107

Bonnell, I. A., & Bate, M. R. 1994a, MNRAS, 269, L45

—. 1994b, MNRAS, 271, 999

Booth, M., del Burgo, C., & Hambaryan, V. V. 2021, MNRAS, 500, 5552

Borucki, W. J., Koch, D., Basri, G., et al. 2010, Science, 327, 977

Boss, A. P. 1988, ApJ, 331, 370

—. 2011, ApJ, 731, 74

Bowler, B. P. 2016, PASP, 128, 102001

Bowler, B. P., & Hillenbrand, L. A. 2015, ApJ, 811, L30

Bowler, B. P., Liu, M. C., Dupuy, T. J., & Cushing, M. C. 2010, ApJ, 723, 850

Bowler, B. P., Liu, M. C., Kraus, A. L., & Mann, A. W. 2014, ApJ, 784, 65

Bowler, B. P., Liu, M. C., Kraus, A. L., Mann, A. W., & Ireland, M. J. 2011, ApJ, 743, 148

Bowler, B. P., Kraus, A. L., Bryan, M. L., et al. 2017, AJ, 154, 165

Boyd, D. F. A., & Whitworth, A. P. 2005, A&A, 430, 1059

Brandt, T. D., McElwain, M. W., Turner, E. L., et al. 2014, ApJ, 794, 159

Bryan, M. L., Bowler, B. P., Knutson, H. A., et al. 2016, ApJ, 827, 100

Bryan, M. L., Ginzburg, S., Chiang, E., et al. 2020, ApJ, 905, 37

Bulger, J., Patience, J., Ward-Duong, K., et al. 2014, A&A, 570, A29

Burkert, A., Bate, M. R., & Bodenheimer, P. 1997, MNRAS, 289, 497

Burrows, A., Marley, M., Hubbard, W. B., et al. 1997, ApJ, 491, 856

Caceres, C., Hardy, A., Schreiber, M. R., et al. 2015, ApJ, 806, L22

Cameron, A. G. W. 1978, Moon and Planets, 18, 5

Carpenter, J. M., Mamajek, E. E., Hillenbrand, L. A., & Meyer, M. R. 2006, ApJ, 651, L49

Carson, J. C., Eikenberry, S. S., Smith, J. J., & Cordes, J. M. 2006, AJ, 132, 1146

Chabrier, G., Baraffe, I., Allard, F., & Hauschildt, P. 2000a, ApJ, 542, L119

—. 2000b, ApJ, 542, 464

Chambers, K. C., Magnier, E. A., Metcalfe, N., et al. 2016, ArXiv e-prints, arXiv:1612.05560

Chauvin, G., Lagrange, A.-M., Dumas, C., et al. 2004, A&A, 425, L29

Chauvin, G., Lagrange, A. M., Dumas, C., et al. 2005a, A&A, 438, L25

Chauvin, G., Lagrange, A. M., Zuckerman, B., et al. 2005b, A&A, 438, L29

Chauvin, G., Lagrange, A. M., Bonavita, M., et al. 2010, A&A, 509, A52

Christiansen, J. L., Clarke, B. D., Burke, C. J., et al. 2020, AJ, 160, 159

Cieza, L., Padgett, D. L., Stapelfeldt, K. R., et al. 2007, ApJ, 667, 308

Cieza, L. A., Padgett, D. L., Allen, L. E., et al. 2009, ApJ, 696, L84

Cumming, A., Butler, R. P., Marcy, G. W., et al. 2008, PASP, 120, 531

Currie, T., Daemgen, S., Debes, J., et al. 2014, ApJ, 780, L30

Cutri, R. M., Skrutskie, M. F., van Dyk, S., et al. 2003, VizieR Online Data Catalog, 2246

Cutri, R. M., Wright, E. L., Conrow, T., et al. 2021, VizieR Online Data Catalog, II/328

Daemgen, S., Bonavita, M., Jayawardhana, R., Lafrenière, D., & Janson, M. 2015, ApJ, 799, 155

de Zeeuw, P. T., Hoogerwerf, R., de Bruijne, J. H. J., Brown, A. G. A., & Blaauw, A. 1999, AJ, 117, 354

Deacon, N. R., Schlieder, J. E., & Murphy, S. J. 2016, MNRAS, 457, 3191

Deming, D., Wilkins, A., McCullough, P., et al. 2013, ApJ, 774, 95

Dodson-Robinson, S. E., Bodenheimer, P., Laughlin, G., et al. 2008, ApJ, 688, L99

Dodson-Robinson, S. E., Veras, D., Ford, E. B., & Beichman, C. A. 2009, ApJ, 707, 79

Dopita, M. A. 1978, ApJS, 37, 117

Dullemond, C. P., & Dominik, C. 2004, in Astronomical Society of the Pacific Conference Series, Vol. 321, Extrasolar Planets: Today and Tomorrow, ed. J. Beaulieu, A. Lecavelier Des Etangs, & C. Terquem, 361

Dullemond, C. P., Hollenbach, D., Kamp, I., & D'Alessio, P. 2007, in Protostars and Planets V, ed. B. Reipurth, D. Jewitt, & K. Keil, 555

Dunham, M. M., Allen, L. E., Evans, Neal J., I., et al. 2015, ApJS, 220, 11

Dupuy, T. J., & Liu, M. C. 2012, ApJS, 201, 19

Dupuy, T. J., Liu, M. C., Bowler, B. P., et al. 2010, ApJ, 721, 1725

Duquennoy, A., & Mayor, M. 1991, A&A, 500, 337

Durkan, S., Janson, M., & Carson, J. C. 2016, ApJ, 824, 58

Eisner, J. A. 2015, ApJ, 803, L4

Epchtein, N., de Batz, B., Capoani, L., et al. 1997, The Messenger, 87, 27

Ercolano, B., & Pascucci, I. 2017, Royal Society Open Science, 4, 170114

Espaillat, C., Ingleby, L., Hernández, J., et al. 2012, ApJ, 747, 103

Esplin, T. L., & Luhman, K. L. 2017, AJ, 154, 134

—. 2020, AJ, 159, 282

Esplin, T. L., Luhman, K. L., & Mamajek, E. E. 2014, ApJ, 784, 126

Evans, II, N. J., Dunham, M. M., Jørgensen, J. K., et al. 2009, ApJS, 181, 321

Faherty, J. K., Riedel, A. R., Cruz, K. L., et al. 2016, ApJS, 225, 10

Fazio, G. G., Hora, J. L., Allen, L. E., et al. 2004, ApJS, 154, 10

Feiden, G. A. 2016, A&A, 593, A99

Filippazzo, J. C., Rice, E. L., Faherty, J., et al. 2015, ApJ, 810, 158

Fitzpatrick, E. L. 1999, PASP, 111, 63

Gaia Collaboration, Brown, A. G. A., Vallenari, A., et al. 2018, A&A, 616, A1

—. 2021, A&A, 649, A1

Gammie, C. F. 2001, ApJ, 553, 174

Ginski, C., Schmidt, T. O. B., Mugrauer, M., et al. 2014, MNRAS, 444, 2280

Goodwin, S. P., Whitworth, A. P., & Ward-Thompson, D. 2004, A&A, 414, 633

Gully-Santiago, M. A., Herczeg, G. J., Czekala, I., et al. 2017, ApJ, 836, 200

Günther, H. M., Cody, A. M., Covey, K. R., et al. 2014, AJ, 148, 122

Gutermuth, R. A., Megeath, S. T., Myers, P. C., et al. 2009, ApJS, 184, 18

Haffert, S. Y., Bohn, A. J., de Boer, J., et al. 2019, Nature Astronomy, 3, 749

Haisch, Karl E., J., Lada, E. A., & Lada, C. J. 2001, ApJ, 553, L153

Hartmann, L. 1998, Accretion Processes in Star Formation

Hatzes, A. P., & Rauer, H. 2015, ApJ, 810, L25

Heintz, W. D. 1969, JRASC, 63, 275

Herbig, G. H. 1977a, ApJ, 217, 693

—. 1977b, ApJ, 214, 747

Herczeg, G. J., & Hillenbrand, L. A. 2014, ApJ, 786, 97

Hillenbrand, L. A. 2005, arXiv e-prints, astro

Hoffman, W. F. 2005, in Technical Report

Høg, E., Fabricius, C., Makarov, V. V., et al. 2000, A&A, 355, L27

Hollenbach, D. J., Yorke, H. W., & Johnstone, D. 2000, in Protostars and Planets IV, ed. V. Mannings, A. P. Boss, & S. S. Russell, 401–428

Houck, J. R., Roellig, T. L., Van Cleve, J., et al. 2004, in Society of Photo-Optical Instrumentation Engineers (SPIE) Conference Series, Vol. 5487, Optical, Infrared, and Millimeter Space Telescopes, ed. J. C. Mather, 62–76

Hubickyj, O., Bodenheimer, P., & Lissauer, J. J. 2005, Icarus, 179, 415

Ingalls, J. G., Krick, J. E., Carey, S. J., et al. 2016, AJ, 152, 44

Ireland, M. J., Kraus, A., Martinache, F., Law, N., & Hillenbrand, L. A. 2011, ApJ, 726, 113

Itoh, Y., Hayashi, M., Tamura, M., et al. 2005, ApJ, 620, 984

Janson, M., Lafrenière, D., Jayawardhana, R., et al. 2013, ApJ, 773, 170

Janson, M., Quanz, S. P., Carson, J. C., et al. 2015, A&A, 574, A120

Joergens, V., Bonnefoy, M., Liu, Y., et al. 2013, A&A, 558, L7

Johansen, A., & Youdin, A. 2007, ApJ, 662, 627

Kaiser, N., Aussel, H., Burke, B. E., et al. 2002, in Proc. SPIE, Vol. 4836, Survey and Other Telescope Technologies and Discoveries, ed. J. A. Tyson & S. Wolff, 154–164

Kaisler, D., Zuckerman, B., & Becklin, E. Macintosh, B. 2003, in Astronomical Society of the Pacific Conference Series, Vol. 294, Scientific Frontiers in Research on Extrasolar Planets, ed. D. Deming & S. Seager, 91–94

Keppler, M., Benisty, M., Müller, A., et al. 2018, A&A, 617, A44

Kirkpatrick, J. D., Barman, T. S., Burgasser, A. J., et al. 2006, ApJ, 639, 1120

Konopacky, Q. M., Barman, T. S., Macintosh, B. A., & Marois, C. 2013, Science, 339, 1398

Kratter, K. M., Murray-Clay, R. A., & Youdin, A. N. 2010, ApJ, 710, 1375

Kraus, A. L., Andrews, S. M., Bowler, B. P., et al. 2015, ApJ, 798, L23

Kraus, A. L., Herczeg, G. J., Rizzuto, A. C., et al. 2017, ApJ, 838, 150

Kraus, A. L., & Hillenbrand, L. A. 2007, ApJ, 662, 413

—. 2009a, ApJ, 703, 1511

—. 2009b, ApJ, 704, 531

—. 2012, ApJ, 757, 141

Kraus, A. L., Ireland, M. J., Cieza, L. A., et al. 2014a, ApJ, 781, 20

Kraus, A. L., Ireland, M. J., Martinache, F., & Hillenbrand, L. A. 2011, ApJ, 731, 8

Kraus, A. L., Shkolnik, E. L., Allers, K. N., & Liu, M. C. 2014b, AJ, 147, 146

Kreidberg, L., Bean, J. L., Désert, J.-M., et al. 2014, Nature, 505, 69

Krolikowski, D. M., Kraus, A. L., & Rizzuto, A. C. 2021, arXiv e-prints, arXiv:2105.13370

Kuzuhara, M., Tamura, M., Ishii, M., et al. 2011, AJ, 141, 119

Kuzuhara, M., Tamura, M., Kudo, T., et al. 2013, ApJ, 774, 11

Lachapelle, F.-R., Lafrenière, D., Gagné, J., et al. 2015, ApJ, 802, 61

Lada, C. J. 1987, in Star Forming Regions, ed. M. Peimbert & J. Jugaku, Vol. 115, 1

Lafrenière, D., Jayawardhana, R., Brandeker, A., Ahmic, M., & van Kerkwijk, M. H. 2008a, ApJ, 683, 844

Lafrenière, D., Jayawardhana, R., & van Kerkwijk, M. H. 2008b, ApJ, 689, L153

Lafrenière, D., Jayawardhana, R., van Kerkwijk, M. H., Brandeker, A., & Janson, M. 2014, ApJ, 785, 47

Lafrenière, D., Marois, C., Doyon, R., & Barman, T. 2009, ApJ, 694, L148

Lafrenière, D., Marois, C., Doyon, R., Nadeau, D., & Artigau, É. 2007, ApJ, 660, 770

Lambrechts, M., & Johansen, A. 2012, A&A, 544, A32

Laughlin, G., & Korchagin, V. 1996, ApJ, 460, 855

Lawrence, A., Warren, S. J., Almaini, O., et al. 2007, MNRAS, 379, 1599

—. 2012, VizieR Online Data Catalog, 2314

Leggett, S. K., Saumon, D., Albert, L., et al. 2008, ApJ, 682, 1256

Lewis, J. S. 1974, Science, 186, 440

Liu, M. C., Dupuy, T. J., & Allers, K. N. 2016, ApJ, 833, 96

Looper, D. L., Kirkpatrick, J. D., Cutri, R. M., et al. 2008, ApJ, 686, 528

Low, C., & Lynden-Bell, D. 1976, MNRAS, 176, 367

Lubow, S. H., Seibert, M., & Artymowicz, P. 1999, ApJ, 526, 1001

Luhman, K. L. 2004, ApJ, 602, 816

Luhman, K. L., Allen, P. R., Espaillat, C., Hartmann, L., & Calvet, N. 2010, ApJS, 186, 111

Luhman, K. L., & Esplin, T. L. 2020, AJ, 160, 44

Luhman, K. L., & Mamajek, E. E. 2012, ApJ, 758, 31

Luhman, K. L., Mamajek, E. E., Allen, P. R., Muench, A. A., & Finkbeiner, D. P. 2009, ApJ, 691, 1265

Luhman, K. L., Wilson, J. C., Brandner, W., et al. 2006, ApJ, 649, 894

MacGregor, M. A., Wilner, D. J., Czekala, I., et al. 2017, ApJ, 835, 17

Marengo, M., Megeath, S. T., Fazio, G. G., et al. 2006, ApJ, 647, 1437

Marocco, F., Eisenhardt, P. R. M., Fowler, J. W., et al. 2020, VizieR Online Data Catalog, II/365

Marois, C. 2010, in In the Spirit of Lyot 2010, ed. A. Boccaletti, E18

Marois, C., Macintosh, B., Barman, T., et al. 2008, Science, 322, 1348

Marois, C., Zuckerman, B., Konopacky, Q. M., Macintosh, B., & Barman, T. 2010, Nature, 468, 1080

Martin, R. G., Lubow, S. H., Pringle, J. E., & Wyatt, M. C. 2007, MNRAS, 378, 1589

Martinez, R. A., & Kraus, A. L. 2019, AJ, 158, 134

Mayor, M., & Queloz, D. 1995, Nature, 378, 355

Metchev, S., Marois, C., & Zuckerman, B. 2009, ApJ, 705, L204

Metchev, S. A., & Hillenbrand, L. A. 2006, ApJ, 651, 1166

Meyer, M. R., Beckwith, S. V. W., Herbst, T. M., & Robberto, M. 1997, ApJ, 489, L173

Miles-Páez, P. A., Metchev, S., Luhman, K. L., Marengo, M., & Hulsebus, A. 2017, AJ, 154, 262

Miret-Roig, N., Antoja, T., Romero-Gómez, M., & Figueras, F. 2018, A&A, 615, A51

Mohanty, S., Jayawardhana, R., Huélamo, N., & Mamajek, E. 2007, ApJ, 657, 1064

Mordasini, C. 2013, A&A, 558, A113

Müller, A., Keppler, M., Henning, T., et al. 2018, A&A, 617, L2

Myers, P. C., & Ladd, E. F. 1993, ApJ, 413, L47

Nagasawa, M., & Ida, S. 2011, ApJ, 742, 72

Newton, E. R., Mann, A. W., Tofflemire, B. M., et al. 2019, ApJ, 880, L17

Nielsen, E. L., De Rosa, R. J., Macintosh, B., et al. 2019, AJ, 158, 13

Öberg, K. I., Murray-Clay, R., & Bergin, E. A. 2011, ApJ, 743, L16

Offner, S. S. R., Kratter, K. M., Matzner, C. D., Krumholz, M. R., & Klein, R. I. 2010, ApJ, 725, 1485

Ormel, C. W., & Klahr, H. H. 2010, A&A, 520, A43

Padgett, D. L., Cieza, L., Stapelfeldt, K. R., et al. 2006, ApJ, 645, 1283

Patience, J., King, R. R., de Rosa, R. J., & Marois, C. 2010, A&A, 517, A76

Patten, B. M., Stauffer, J. R., Burrows, A., et al. 2006, ApJ, 651, 502

Pearce, L. A., Kraus, A. L., Dupuy, T. J., et al. 2019, AJ, 157, 71

Pecaut, M. J., Mamajek, E. E., & Bubar, E. J. 2012, ApJ, 746, 154

Peneva, S. P., Semkov, E. H., Munari, U., & Birkle, K. 2010, A&A, 515, A24

Pepliński, A., Artymowicz, P., & Mellema, G. 2008, MNRAS, 387, 1063

Pérez, S., Marino, S., Casassus, S., et al. 2019, MNRAS, 488, 1005

Petrus, S., Bonnefoy, M., Chauvin, G., et al. 2020, arXiv e-prints, arXiv:2012.02798

Pollack, J. B., Hubickyj, O., Bodenheimer, P., et al. 1996, Icarus, 124, 62

Preibisch, T., Brown, A. G. A., Bridges, T., Guenther, E., & Zinnecker, H. 2002, AJ, 124, 404

Preibisch, T., Guenther, E., Zinnecker, H., et al. 1998, A&A, 333, 619

Raghavan, D., McAlister, H. A., Henry, T. J., et al. 2010, ApJS, 190, 1

Rameau, J., Chauvin, G., Lagrange, A. M., et al. 2013, A&A, 553, A60

Rebull, L. M., Koenig, X. P., Padgett, D. L., et al. 2011, ApJS, 196, 4

Reggiani, M., Meyer, M. R., Chauvin, G., et al. 2016, A&A, 586, A147

Reipurth, B. 1989, Nature, 340, 42

Rice, W. K. M., & Armitage, P. J. 2003, ApJ, 598, L55

Safronov, V. S. 1969, Evoliutsiia doplanetnogo oblaka.

—. 1972, Evolution of the protoplanetary cloud and formation of the earth and planets.

Santamaría-Miranda, A., Cáceres, C., Schreiber, M. R., et al. 2018, MNRAS, 475, 2994

Scally, A., & Clarke, C. 2001, MNRAS, 325, 449

Scharf, C., & Menou, K. 2009, ApJ, 693, L113

Schlafly, E. F., Green, G., Finkbeiner, D. P., et al. 2014, ApJ, 789, 15

Schmidt, T. O. B., Neuhäuser, R., Seifahrt, A., et al. 2008, A&A, 491, 311

Schneider, J., Dedieu, C., Le Sidaner, P., Savalle, R., & Zolotukhin, I. 2011, A&A, 532, A79

Scholz, A., Stelzer, B., Costigan, G., et al. 2012, MNRAS, 419, 1271

Schwarz, H., Ginski, C., de Kok, R. J., et al. 2016, A&A, 593, A74

Seifahrt, A., Neuhäuser, R., & Hauschildt, P. H. 2007, A&A, 463, 309

Shabram, M., & Boley, A. C. 2013, ApJ, 767, 63

Shu, F. H., Adams, F. C., & Lizano, S. 1987, ARA&A, 25, 23

Silk, J. 1977, ApJ, 214, 152

Skemer, A. J., Morley, C. V., Zimmerman, N. T., et al. 2016, ApJ, 817, 166

Slesnick, C. L., Carpenter, J. M., Hillenbrand, L. A., & Mamajek, E. E. 2006, AJ, 132, 2665

Song, I., Zuckerman, B., & Bessell, M. S. 2003, ApJ, 599, 342

Spiegel, D. S., & Burrows, A. 2012, ApJ, 745, 174

Stamatellos, D., & Whitworth, A. P. 2009, MNRAS, 392, 413

Stamatellos, D., Whitworth, A. P., & Hubber, D. A. 2011, ApJ, 730, 32

Stelzer, B., Scholz, A., Argiroffi, C., & Micela, G. 2010, MNRAS, 408, 1095

Stevenson, D. J., & Lunine, J. I. 1988, Icarus, 75, 146

Thompson, S. E., Coughlin, J. L., Hoffman, K., et al. 2018, ApJS, 235, 38

Tobin, J. J., Looney, L. W., Li, Z.-Y., et al. 2016, ApJ, 818, 73

Todorov, K., Luhman, K. L., & McLeod, K. K. 2010, ApJ, 714, L84

Todorov, K. O., Luhman, K. L., Konopacky, Q. M., et al. 2014, ApJ, 788, 40

Tohline, J. E. 2002, ARA&A, 40, 349

Tomida, K., Tomisaka, K., Matsumoto, T., et al. 2013, ApJ, 763, 6

Toomre, A. 1964, ApJ, 139, 1217

Torres, C. A. O., Quast, G. R., Melo, C. H. F., & Sterzik, M. F. 2008, Young Nearby Loose Associations, ed. B. Reipurth, Vol. 5, 757

Torres, R. M., Loinard, L., Mioduszewski, A. J., & Rodríguez, L. F. 2009, ApJ, 698, 242

Valenti, J. A., Basri, G., & Johns, C. M. 1993, AJ, 106, 2024

van Belle, G. T., & von Braun, K. 2009, ApJ, 694, 1085

Veras, D., & Armitage, P. J. 2004, MNRAS, 347, 613

Veras, D., Crepp, J. R., & Ford, E. B. 2009, ApJ, 696, 1600

Voirin, J., Manara, C. F., & Prusti, T. 2018, A&A, 610, A64

Vorobyov, E. I. 2013, A&A, 552, A129

Wagner, K., Apai, D., & Kratter, K. M. 2019, ApJ, 877, 46

Wakeford, H. R., Sing, D. K., Kataria, T., et al. 2017, Science, 356, 628

Wallace, A. L., Kammerer, J., Ireland, M. J., et al. 2020, MNRAS, 498, 1382

Ward, W. R. 1997, Icarus, 126, 261

Watson, D. M., Leisenring, J. M., Furlan, E., et al. 2009, ApJS, 180, 84

Werner, M. W., Roellig, T. L., Low, F. J., et al. 2004, ApJS, 154, 1

Wichmann, R., Krautter, J., Schmitt, J. H. M. M., et al. 1996, A&A, 312, 439

Woitke, P., & Helling, C. 2004, A&A, 414, 335

Wolff, S. G., Ménard, F., Caceres, C., et al. 2017, AJ, 154, 26

Wright, J. T., Fakhouri, O., Marcy, G. W., et al. 2011, PASP, 123, 412

Wu, Y.-L., Close, L. M., Eisner, J. A., & Sheehan, P. D. 2017, AJ, 154, 234

Wu, Y.-L., & Sheehan, P. D. 2017, ApJ, 846, L26

Wu, Y.-L., Close, L. M., Males, J. R., et al. 2015, ApJ, 807, L13

Wu, Y.-L., Bowler, B. P., Sheehan, P. D., et al. 2020, AJ, 159, 229

Youdin, A. N., & Goodman, J. 2005, ApJ, 620, 459

Zagaria, F., Rosotti, G. P., & Lodato, G. 2021, arXiv e-prints, arXiv:2107.05268

Zhou, Y., Herczeg, G. J., Kraus, A. L., Metchev, S., & Cruz, K. L. 2014, The Astrophysical Journal Letters, 783, L17

Zhou, Y., Bowler, B. P., Wagner, K. R., et al. 2021, AJ, 161, 244

Zhu, Z. 2015, ApJ, 799, 16

Zhu, Z., Ju, W., & Stone, J. M. 2016, ApJ, 832, 193